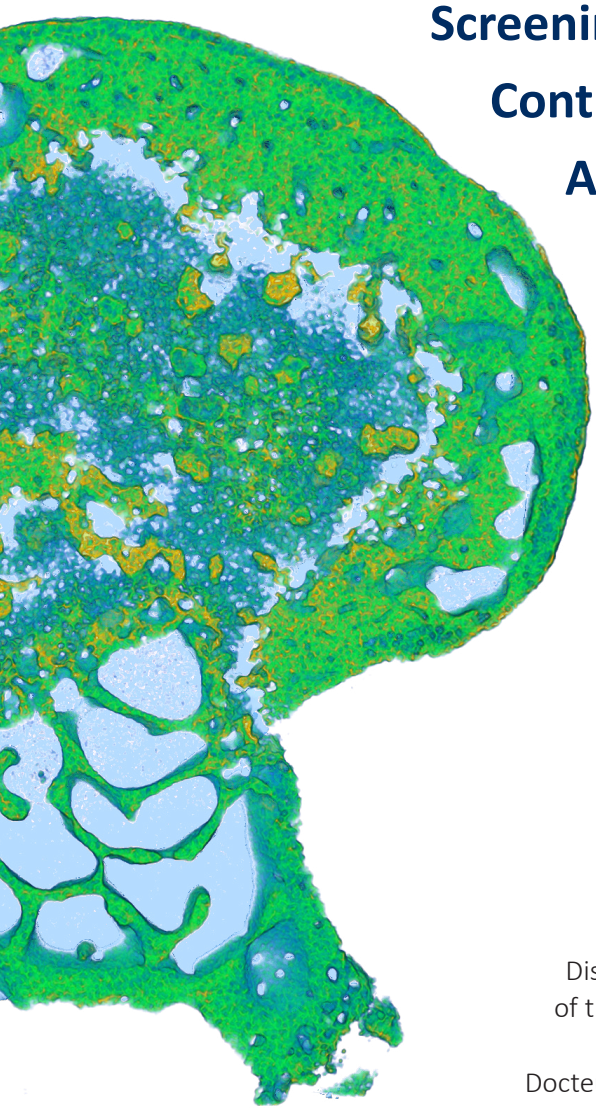
KU LEUVEN
ARENBERG DOCTORAL SCHOOL
FACULTY OF SCIENCE

UCLouvain
ECOLE POLYTECHNIQUE DE LOUVAIN



Screening and Development of Contrast-Enhancing Staining Agents for CECT Imaging

Sarah Vangrunderbeeck

Supervisors:
Prof. Wim De Borggraeve
Prof. Greet Kerckhofs

Dissertation presented in the partial fulfilment of the requirements for the joint PhD degree of Doctor of Science (PhD): Chemistry & Docteur en Sciences de l'Ingénieur et Technologie

July 2023

SCREENING AND DEVELOPMENT OF CONTRAST-ENHANCING STAINING AGENTS FOR CECT IMAGING

Sarah VANGRUNDERBEECK

Supervisors:

Prof. Wim De Borggraeve
Prof. Greet Kerckhofs

Members of the Examination Committee:

Prof. Mario Smet
Prof. Catherine Behets Wydemans
Prof. Tatjana Parac-Vogt
Prof. Mark Grinstaff
Prof. Erik Nies, Chairman

Dissertation presented in the partial fulfilment of the requirements for the joint PhD degree of Doctor of Science (PhD): Chemistry & Docteur en Sciences de l'Ingénieur et Technologie

July 2023

© 2023 Sarah Vangrunderbeeck
Uitgegeven in eigen beheer, Sarah Vangrunderbeeck, Leuven, Belgium

Alle rechten voorbehouden. Niets uit deze uitgave mag worden vermenigvuldigd en/of openbaar gemaakt worden door middel van druk, fotokopie, microfilm, elektronisch of op welke andere wijze ook zonder voorafgaandelijke schriftelijke toestemming van de uitgever.

All rights reserved. No part of the publication may be reproduced in any form by print, photoprint, microfilm, electronic or any other means without written permission from the publisher.

SUMMARY

The visualization of the composition and the spatial organization of tissues is of paramount importance to better understand their functioning and the impact of a disease. Microfocus X-ray computed tomography (microCT) is a valuable tool for 3D imaging to complement classical 2D histological imaging techniques. In the last two decades, the incorporation of contrast-enhancing staining agents (CESAs) has augmented the applicability of microCT for soft tissue imaging, which is referred to as contrast-enhanced computed tomography (CECT). This dissertation aspires to contribute to this field by investigating the potential of existing compounds as CESAs and by developing novel CESAs, which are capable to discern between tissue constituents, while avoiding tissue deformation. The fundamental insights obtained in this work enable the investigation of tissues in 3D at high resolution, thereby facilitating research in the fields of biology and medicine.

This dissertation opens with an overview of the state-of-the-art literature concerning CESAs for *ex vivo* CECT imaging, focusing on musculoskeletal tissues. The progress made in the field is discussed, along with the challenges that need to be overcome to improve the widespread use of CECT for X-ray based histology. A deeper understanding of the staining mechanism coupled with the development of CESAs with well-known tissue affinities are key to advance the field of CECT.

The next three chapters cover the synthesis of a wide range of CESAs and the assessment of their potential to visualize soft tissues *via* CECT.

First, polyoxometalates were explored for imaging murine bone marrow and kidney. Monolacunary Wells-Dawson polyoxometalate combined with LiCl showed good tissue penetration and resulted in high contrast enhancement without inducing substantial tissue shrinkage. CECT images of the long bones allowed distinction between mineralized bone, bone marrow adipose tissue, and vasculature. Similarly, renal pelvis, papilla, inner and outer medulla, and cortex could be discerned in the obtained images.

Second, novel cationic iodine-based CESAs of different iodine content and charge density were designed to improve glycosaminoglycan (GAG) detection, while existing synthetic procedures were optimized in terms of efficiency and sustainability. Time-lapsed staining experiments of osteochondral plugs

revealed that contrast enhancement was positively correlated with the staining time, and the CESA concentration, iodine content and positive charge density. Moreover, the spatial distribution of the CESA at diffusion equilibrium was consistent with the depth-wise GAG concentration in healthy cartilage. CA8+6I, a CESA with the highest tested charge density and iodine content, was found to have the highest GAG affinity, while CA4+6I, a CESA with mediocre charge density and iodine content, appears to have the highest sensitivity to detect variations in the GAG concentration.

Third, novel CESAs were designed for protein-specific imaging. Moving away from antibodies as detecting probes, short peptide sequences were first explored. By means of phage display, a peptide sequence showing affinity towards keyhole limpet hemocyanin (KLH) was identified, but did not bind specifically to KLH as evaluated by ELISA. Increasing the avidity of this peptide-based probe could lead to better binding, and hence serve as a good alternative for antibody-based labeling. Secondly, X-ray attenuating revealing agents were developed for 3D immunostaining by CECT. Although the revealing agents based on 3,3'-diaminobenizidine and tyramine were successfully synthesized, their poor water solubility hampered their use to detect antibody-labeled proteins. Improving the water solubility of revealing agents would be a next step towards increasing their efficacy.

Overall, this dissertation investigated the potential of existing and entirely new compounds to be used as CESAs for the general visualization of soft tissues as well as for targeted imaging. This work paves the way for the application of CECT as a tool for X-ray based histology at high resolution, complementary to classical 2D histology.

SAMENVATTING

De visualisatie van de samenstelling en de ruimtelijke organisatie van weefsels is van groot belang om de werking ervan en de impact van een ziekte beter te begrijpen. Microfocus X-stralen computertomografie (microCT) is een waardevolle techniek voor 3D beeldvorming als aanvulling op klassieke 2D histologische beeldvormingstechnieken. De integratie van contrastverhogende kleurstoffen (CESAs) heeft de toepasbaarheid van microCT voor beeldvorming van zachte weefsels in de laatste twee decennia verder uitgebreid. Deze techniek is beter gekend als contrastverhogende computertomografie (CECT). Dit proefschrift streeft ernaar een bijdrage te leveren door, enerzijds, bestaande verbindingen te onderzoeken als potentiële CESAs, en anderzijds, door nieuwe CESAs te ontwikkelen. Het gebruik van CESAs laat toe een onderscheid te maken tussen weefselbestanddelen terwijl weefselvervorming vermeden wordt. De fundamentele inzichten uit dit onderzoek laten toe zachte weefsels in 3D met hoge resolutie te bestuderen, waardoor het onderzoek naar weefsels in het gebied van biologie en geneeskunde vergemakkelijkt wordt.

Dit proefschrift geeft eerst een overzicht van de meest recente literatuur over CESAs voor *ex vivo* CECT, met de nadruk op musculoskeletale weefsels. De vooruitgang in het veld wordt besproken, evenals de uitdagingen die overwonnen dienen te worden ter bevordering van het grootschalige gebruik van CECT voor X-stralen gebaseerde histologie. Een grondiger begrip van de interacties tussen CESAs en het weefsel, in combinatie met de ontwikkeling van CESAs met gekende weefselaffiniteiten, zijn essentieel om het veld van CECT vooruit te helpen.

De volgende drie hoofdstukken behandelen de synthese van diverse CESAs en de beoordeling van hun potentieel om weefsels te visualiseren *via* CECT.

Eerst werden polyoxometalaten onderzocht voor de beeldvorming van het beenmerg en de nieren van muizen. Monolacunair Wells-Dawson polyoxometalaat in combinatie met LiCl vertoonde een goede weefselpenetratie en resulteerde in een verhoogd contrast zonder aanzienlijke weefselkrimping. In CECT beelden kon een onderscheid gemaakt worden tussen gemineraliseerd bot, beenmerg-vetweefsel en bloedvaten. Tevens konden de nieren, het nierbekken, de papillen, het binnenste en buitenste merg en de cortex worden onderscheiden.

Ten tweede werden nieuwe kationische jood-gebaseerde CESAs ontworpen met een verschillende ladingsdichtheid en joodgehalte om de detectie van glycosaminoglycanen (GAGs) te bevorderen. Tegelijkertijd werden bestaande synthetische procedures geoptimaliseerd in functie van efficiëntie en duurzaamheid. Experimenten waarbij osteochondrale pluggen verrijkt werden met CESA over tijd toonden aan dat contrastverhoging positief gecorreleerd was met de tijd, de CESA concentratie, het joodgehalte en de positieve ladingsdichtheid van de CESA. De ruimtelijke verdeling van de CESA bij diffusie evenwicht was bovendien consistent met de diepte-afhankelijke GAG concentratie in gezond kraakbeen. CA8+6I, een CESA met de hoogste ladingsdichtheid en joodgehalte in dit werk, bleek de hoogste GAG-affiniteit te vertonen. Overigens bleek CA4+6I, een CESA met middelmatige ladingsdichtheid en joodgehalte, de hoogste gevoeligheid te vertonen voor de detectie van variaties in de GAG-concentratie.

Ten derde werden nieuwe CESAs ontworpen voor proteïne-specifieke beeldvorming. In een eerste onderdeel werden korte peptidesequenties onderzocht als detecterende eenheden in plaats van vaak gebruikte antilichamen. Door middel van *phage display* werd een peptidesequentie met affiniteit voor *keyhole limpet hemocyanine* (KLH) geïdentificeerd, maar deze bleek niet specifiek te binden aan KLH op basis van evaluatie met ELISA. Het verhogen van de aviditeit van deze peptide-gebaseerde CESA zou kunnen leiden tot een betere binding waardoor het als een waardig alternatief kan fungeren voor antilichaam-gebaseerd labelen. In een tweede onderdeel werden er X-straal verzwakkende merkerstoffen ontwikkeld voor 3D immuno-gebaseerde CECT. Hoewel de merkerstoffen op basis van 3,3'-diaminobenizidine en tyramine succesvol werden gesynthetiseerd, belemmerde hun slechte wateroplosbaarheid de detectie van proteïnen gelabeld met antilichamen. Verbetering van hun wateroplosbaarheid zou een volgende stap zijn om de doeltreffendheid ervan te verbeteren.

In dit doctoraat werd het gebruik van bestaande en geheel nieuwe verbindingen als CESAs onderzocht voor, enerzijds, de algemene visualisatie van zachte weefsels en, anderzijds, de gerichte beeldvorming van specifieke weefselonderdelen. De behaalde resultaten helpen een weg te banen voor de toepassing van CECT als methode voor X-stralen gebaseerde histologie, als aanvulling op klassieke 2D histologie.

LIST OF ABBREVIATIONS

2D	two-dimensional
3D	three-dimensional
4D	four-dimensional
Ab	antibody
AC	articular cartilage
ASAP-MS	atmospheric solids analysis probe mass spectrometry
Aq.	aqueous
BMAT	bone marrow adipose tissue
Boc_2O	di-*tert*-butyl dicarbonate
BSA	bovine serum albumin
CA	contrast agent
CA1+	2-(3-acetamido-2,4,6-triiodobenzamido)ethan-1-aminium chloride
CA4+3I	2,2'-((5-amino-2,4,6-triiodoisophthaloyl)-bis(azanediyl))bis(propane-1,3-diaminium), chloride salt
CA4+6I	5,5'-[malonylbis(azanediyl)]bis[*N1,N3*-bis(2-aminoethyl)-2,4,6-triiodoisophthalamide], chloride salt
CA8+6I	2,2',2'',2'''-((5,5'-(malonylbis(azanediyl))bis(2,4,6-triiodoisophthaloyl))tetrakis(azanediyl))tetrakis(propane-1,3-diaminium), chloride salt
CARD	catalyzed reporter deposition
cat.	catalytic amount
CECT	contrast-enhanced computed tomography
CESA	contrast-enhancing staining agent
CIH	chromogenic immunohistochemistry
CS	compton scattering
CT	X-ray computed tomography
CuAAC	copper(I)-catalyzed alkyne-azide cycloaddition
CZ	calcified zone (of cartilage)
Da	dalton
DAB	3,3'-diaminobenzidine
DCC	dicyclohexylcarbodiimide
DCM	dichloromethane
df	degrees of freedom (in statistics)
DIPEA	*N,N*'-diisopropylethylamine
DMA	*N,N*-dimethylacetamide
DMAP	4-dimethylaminopyridine

DMF	*N,N*-dimethylformamide
DMMB assay	1,9-dimethylmethylene blue assay
DMSO	dimethyl sulfoxide
DNA	deoxyribonucleic acid
e.g.	exempli gratia *(Latin)*
ECM	extracellular matrix
EDTA	ethylenediaminetetraacetic acid
ELISA	enzyme-linked immunosorbent assay
EPIC-microCT	equilibrium partitioning of an anionic contrast agent *via* microCT
eq.	equation
equiv	molar equivalents
ESI	electrospray ionization
et al.	et alii / et aliae *(Latin)*
etc.	et cetera *(Latin)*
Fab	antigen-binding fragment
GAG	glycosaminoglycan
GV	gray value
h	hours
HBTU	2-(1*H*-Benzotriazole-1-yl)-1,1,3,3-tetramethyluronium hexafluorophosphate
Hf-WD POM	hafnium-substituted Wells-Dawson polyoxometalate
HPLC	high-performance liquid chromatography
h_r	hydrodynamic radius
HR-MS	high-resolution mass spectrometry
HRP	horseradish peroxidase
HSE	health, safety and evironment
i.e.	id est (*Latin*)
I_2KI	Lugol's iodine
IF	immunofluorescence
IHC	immunohistochemistry
IR	infrared
KLH	keyhole limpet hemocyanin
kVp	X-ray tube voltage
LC-MS	liquid chromatography – mass spectrometry
LM	light microscopy
LMS	least square means (in statistics)
LR-MS	low resolution mass spectrometry
MANOVA	multivariate Analysis of variance

microCT	X-ray microfocus computed tomography
Mono-WD POM	monolacunary Wells-Dawson polyoxometalate
MP	melting point
MPLC	medium pressure liquid chromatography
MRI	magnetic resonance imaging
MS	mass spectrometry
MWCO	molecular weight cut-off (membrane characteristic)
MZ	middle zone (of cartilage)
nanoCT	X-ray nanofocus computed tomography
N-Boc DAB	*N*,*N*',*N*'',*N*'''-tetrakis(*tert*-butyloxycarbonyl)-3,3'-diamino-benzidine
NIS	*N*-iodosuccinimide
NMR	nuclear magnetic resonance
NP	nanoparticle
ns	not significant (in statistics)
OA	osteoarthritis
OD	optical density
p	significance level (in statistics)
p3L15	phage display library that expresses 15-mer peptides in the pIII coat protein
PBS	phosphate buffered saline
PE	photoelectric effect
PEG	polyethylene glycol
PG	proteoglycan
phage	filamentous M13 bacteriophage
PMA	phosphomolybdic acid
ppm	parts per million
POM	polyoxometalate
PTA	phosphotungstic acid
RMSE	root mean square error (in statistics)
RP-HPLC	reversed-phase high-performance liquid chromatography
RS	rayleigh scattering
rt	room temperature
sd	standard deviation (in statistics)
SPR	surface plasmon resonance
SR	synchrotron radiation
SZ	superficial zone (of cartilage)
t	time

Boc-*N*-amido-PEG3-acid	2,2-dimethyl-4-oxo-3,8,11,14-tetraoxa-5-azaheptadecan-17-oic acid
TFA	trifluoroacetic acid
THF	tetrahydrofuran
THPTA	tris(3-hydroxypropyltriazolylmethyl)amine
TLC	thin layer chromatography
TMB	3,3',5,5'-tetramethylbenzidine
Tri-WD POM	trilacunary Wells-Dawson polyoxometalate
$TsOH.H_2O$	p-toluenesulfonic acid monohydrate
tyramine	2-(4-hydroxyphenyl)ethylamine
UV	ultraviolet
v	wavenumber (cm^{-1}, in IR spectroscopy)
vs.	Versus (*Latin*)
WD	Wells-Dawson (type of POM)
α	threshold significance level (in statistics) or maximum gray value (in diffusion)
δ	chemical shift (ppm, in NMR spectroscopy) or equilibrium time (in diffusion)
τ	penetration rate constant
μ	linear attenuation coefficient
η^2	measure of effect size (in statistics)

Pseudo-elemental symbols

Asc	ascorbate
Boc	*tert*-butyloxycarbonyl
Et	ethyl
Me	methyl
Ms	mesyl, methanesulfonyl
R	any carbon group
TBDMS	*tert*-butyldimethylsilyl
Tf	triflyl, trifluoromethylsulfonyl
Ts	tosyl, toluenesulfonyl

PREFACE

Fueled by an insatiable curiosity and a profound sense of wonder, I decided to immerse myself in the realm of exact sciences. More specifically, in one of the most beautiful fields of exact sciences: chemistry. Throughout my studies, I started seeing chemistry as a toolbox to also tackle challenges in other fields of science. My desire to discover and to contribute something of value convinced me to embark on this scientific challenge: a PhD. As I am convinced interdisciplinary research is crucial to obtain groundbreaking insights, I decided to pursue a joint PhD at the intersection of organic chemistry and biomedical engineering.

A PhD is an adventurous journey, which enabled me to meet my desire to understand the ultimate nature of things. The scientific experiments, discussions and insights I encounter during this journey were enlightening, interesting and joyful, although sometimes frustrating. Doing science shaped my critical mindset and strengthened my fascination, curiosity, perseverance, resilience and patience. Yet, doing a PhD is more than doing science. The journey by which results were acquired and skills were mastered is at least as interesting. The PhD path encouraged me to turn fears into challenges, to step out of my comfort zone and see failures as opportunities to learn rather than as shortcomings. Hence, my endeavors not only granted me knowledge, but also wisdom. I could not agree more with Socrates' words:

Wonder is the beginning of wisdom.

I hope that the artwork adorning the cover of this booklet has sparked your curiosity and sense of wonder. Without further delay, allow me to reveal its contents — a CECT cross-section of a murine femur, which was stained with monolacunary Wells-Dawson polyoxometalate upon microCT imaging. The staining enables the visualization of the bone marrow, displayed in dark blue, while the bone structure is simultaneously visible in predominant green hues.

Sarah Vangrunderbeeck
Hoeilaart, June 2023

ACKNOWLEDGEMENTS - DANKWOORD

"Which is more important." asked big Panda,
"the journey or the destination?"
"The company." Said Tiny Dragon. – James Norbury

Based on my personal experience, doing research is a collaborative effort. I am very lucky and grateful for the people that contributed to this work in a direct or indirect way, some during the past year, others far beyond. This section is dedicated to all the journeymen and women along my path, who helped me grow not only as a scientist but also as a person. Let's go!

Eerst en vooral wil ik mijn dankbaarheid uiten tot de promotor die me al het langst heeft gevolgd op mijn wetenschappelijke pad, **Prof. Wim De Borggraeve.** Ik herinner me mijn enthousiasme toen ik mijn masterthesis mocht volbrengen in MolDesignS. Ik wil je enorm bedanken voor het vertrouwen en de kans die ik kreeg om nadien mijn onderzoekscarrière verder uit te bouwen als doctoraatsstudent. Bedankt voor je continue beschikbaarheid, constructieve feedback, de mogelijkheid om naar het buitenland te gaan en vooral het duwtje in de rug dat ik daarbij nodig had. Tijdens deze jaren maakte je me duidelijk dat je in mij geloofde, ook al deed ik dat zelf niet altijd. De kalmte die je uitstraalt en je gedisciplineerde, vriendelijke aanpak apprecieer ik enorm.

"Twee weten meer dan één" kan ik alleen maar beamen. Ik had het geluk begeleid te worden door niet enkel één maar twee promotoren. Over contrast gesproken. **Prof. Greet Kerckhofs**, ik herinner me onze eerste ontmoeting als de dag van gisteren door je enthousiaste, warme omgang en 'Oh, kijk hier, zo'n schoon beelden'. Bedankt om in me te geloven, mijn kritische geest uit te dagen en de goede opvolging. Bedankt voor het aanreiken van buitenlandse trippen en de oprechte gesprekken. Je passie voor wetenschap en authenticiteit vind ik inspirerend. Merci Greet!!!!!

I would like to thank **Prof. Mario Smet** and **Prof. Catherine Behets** for their membership of my supervisory committee. Thank you for your availability and the valuable input during the course of my research. Furthermore, I would like to thank **Prof. Tatjana Vogt** for being part of the examination committee and **Prof. Erik Nies** as chairman of the doctoral jury. Thank you all for your willingness to assess the quality of this work.

I am very grateful to **Prof. Mark Grinstaff** for hosting me in his interdisciplinary lab at Boston University. Thank you for being such an approachable group leader, for being part of my examination committee, for sharing your knowledge at all possible times and for challenging/inspiring me to think about scientific questions from different perspectives. Moreover, I am thankful for the overall very agreeable five months in the Grinstaff group.

Engaging in multiple research groups has afforded me the opportunity to be surrounded by numerous colleagues, each contributing in their unique way, making my work an enjoyable experience. I am grateful to my colleagues who assisted me in finding solutions to my inquiries, who patiently heard me out when experiments didn't go as planned, who aided in bringing order in my (sometimes chaotic) thoughts and who have acquired the skills to react appropriately to my occasionally abrupt expressions in the lab (read: (non-)ignoring my dramatic outbursts when I ~~occasionally~~ knocked something over or dropped it).

Beginnen doe ik graag met **Cedrick**, wie me trainde als chemist, alsook mijn efficiëntie (in de mate van het mogelijke) sterk heeft aangesterkt. Bedankt vriendschap voor de behulpzaamheid, de fijne gesprekken, je enthousiasme en energie die de labodagen opfleurden. Ik zal de manier waarop je vrolijk Deense liedjes door de boxen van het labo liet knallen als ook je snelle - haast opgejaagde - wandelpassen door de gangen van F niet snel vergeten. Ik heb genoten van alle momenten - zelfs reikend tot Denemarken - die we samen doorbrachten en ik bewonder je drive en doorzettingsvermogen. **Philippe**, sinds 2011 (!) samen op de aulabanken, tot samen doctoreren in MolDesignS. Ik waardeer je gestructureerde aanpak en bijdrage om ons labo qua technologie te verhogen in niveau als *Head of Innovation*. Al moet ik eerlijk zijn dat ik RGR in het lab niet miste. Gelukkig was er **thomas** om samen tegengewicht te bieden om de youtube autoplayer niet enkel bizarre muziekkeuzes te laten knallen door de boxen. Misschien hebben we wel gewonnen met *Blue Monday.* Hoewel? Bedankt om naast goeie muziek ons lab te verrijken met een toffe sfeer, je vrolijkheid en reisverhalen. Ik bewonder de hoedanigheid waarmee je efficiënt *scientific output* genereerde en steeds chill en behulpzaam was. **Laurens**, *the Gelator*, steeds paraat voor een fijne babbel. Bedankt om van *Afternoon Tea Scones* een jaarlijkse traditie te hebben gemaakt als ook om de zorg voor de lyofillisator ter harte te hebben genomen, de overname liep gesmeerd. **Dries**, bedankt om me te hebben betrokken in de wereld van de medchem en je behulpzaamheid. Ik koester onze fijne

gesprekken in het lab. **Seger**, ik kan me er niet van ontdoen dat er iets mysterieus rond jou hangt. Jammer dat we het labo niet langer deelden, ik ben er haast van overtuigd dat we vriendschappelijk zouden klikken gezien de gedeelde interesses en gemeenschappelijke vrienden. Ik hou je aan het - ondanks het vele uitstellen - afspreken. **Joa**, de baken - niet enkel qua literatuurlegende maar steeds meer en meer qua standvastigheid - van MolDesignS. Ik bewonder je onuitputtelijk interesse, verregaande behulpzaamheid en afwezigheid van vooroordelen naar mensen. Een enorme merci voor je luisterend oor en onze gedeelde fijne momenten tot nu toe alsook je welklinkend accent. Dat brengt me bij een andere collega die niet vreemd is van nocturale schrijfsessies. **Rik**, opmerkelijk hoe onze band gestaag maar zeker groeide van mede-thesis-student naar collega tot vriend. Bewonderingswaardig hoe beargumenteerd en gepassioneerd jij de meest complexe dingen haarfijn en gedetailleerd kunt overbrengen. Je wijze raad 'als ge het niet weet, moet ge doen alsof ge het weet' in praktijk omzetten aanschouw ik nog steeds als uitdagend, desalniettemin waardevol. Bedankt voor je paraatheid, de fijne babbels en gezellige wandelingen gekoppeld aan minutieus spotten van vogels (BirdNET!). Het jaar 2017 was zeer vruchtbaar voor MolDesignS, gezien het niet één, niet twee maar wel drie nieuwe doctoraatsstudenten voortbracht. **Gert**, heel fijn om een gelijklopend pad met jou te hebben bewandeld. Van samen thesissen, FWO aanvragen tot het delen van stress (ik herinner me nog levendig je geijsbeer in de Egmondlaan) dezelfde bureau, tweekamerreactoren en zelfs een poster. Al was het uitdagend, het gaf me voldoening wanneer ik er in slaagde je pessimistische blik te optimaliseren en oordelen te verzachten. Bedankt voor je steun, paraatheid en vriendschap. Dan komen we bij mijn buur in onze bureau: **Ruben**. Het deed deugd om het gevoel van soms *de vreemde eend in de bijt,* getekend door interdisciplinair onderzoek, te kunnen delen alsook de interesse in *Scicom*. Bedankt voor de fijne gesprekken en bereidwilligheid steeds te willen helpen met de meest uiteenlopende zaken. Ik bewonder je altruïsme en de manier waarop je meerdere projecten gelijktijdig en efficiënt kan runnen. **Lauren**, de liefste achterbuur in onze bureau, merci voor de fijne babbels en je bijdrage aan de fijne sfeer in het lab maar vooral de vriendschap. Bedankt om ons lab te doen opfleuren door het organiseren van socials, sportiviteiten en mee een punt te maken van *lunch* (liefst niet te hard afwijkend van 12u30). Het belang dat je hecht aan de staat van het lab siert je. I was very happy the *girlpower* improved over the years. **Carlotta**, thank you for vibrant Italian personality that energizes our lab as well as your contribution to its organization and general well-being. I value our mutual

admiration for Prince. **Bingyu**, who always makes me smile. Thanks for bringing joy, Chinese hot pot and a ton of pictures to our group. **Reza** and **Armir**, it's a pleasure having you guys around in the lab. Vervolgens zou ik graag mijn waardering uitspreken voor de studenten die ik begeleid heb. Bedankt voor jullie bijdrage aan dit werk, het was me een genoegen om jullie te zien groeien in het wetenschappelijk denken. **Alberto**, thank you for your efforts to keep on going despite the challenges encountered during the synthesis (including yellow splashes on your shoes). **Renée**, bedankt voor je bijdrage aan het vierde hoofdstuk van dit werk. Je goedlachsheid en gestructureerde aanpak maakte het een plezier om met jou samen te werken.

Timmie, hoe kan ik zo'n karakter eer aandoen in slechts één paragraaf? Haast onmogelijk. Het is me een waar genoegen van kortbij je groeiproces te hebben mogen gevolgd van biochemist naar chemist naar de interdisciplinaire wetenschapper die je vandaag bent. Het siert je enorm dat je geen enkele discipline lijkt te schuwen en met je brede glimlach uitdagingen ter harte neemt. Je energiepijl oogt vaak onuitputbaar; het is me een raadsel hoe je meer dan 24u in een dag kan vinden om je planning te volbrengen - naast het verslinden van wetenschappelijke boeken, je beestenboel in bedwang te houden en non-stop beoefenen van klassieke muziek in je hoofd. Die energie breng je maar al te graag over, liefst al *babbelend*, via elk mogelijk kanaal, ongeacht tijdstip en plaats. Je berichten als *Ik heb nog eens nagedacht* op ontiegelijk vroege uren in het weekend en het delen van *The absence of evidence is not evidence of absence.* uit je boek statistiek tijdens je verlof zijn slechts een blijk van de enorme gedrevenheid en passie waarmee je aan wetenschap doet. Oneliners als *Hallo! Oeps! Spannend! Mooi hè!* staan in mijn geheugen gegrift. Je fleurt en kleurt (letterlijk) het labo met je aanwezig. Bedankt voor je onvervangbare bijdrage aan dit werk, mee in het bootje van de CESAs te varen en de golven te bedwingen. Bovenal bedankt voor je vriendschap, je oprechte interesse en je openheid. Met veel plezier kom ik binnenkort graag je boerderij bewonderen, thee oogsten en piano spelen in Lievegem. Hoewel ik eerlijkheidshalve twijfel(de) over deze uitspraak: mijn WhatsApp staat voor jou nooit op *mute*.

I would like to express my deepest appreciation to all other members of MoldesignS with whom I had the pleasure of sharing office and lab space: **Soultan**, **Carmen**, **Koen**, **Johannes**, **Vidmantas**, **Mei**, **Ermal**, **Sam**, **Seba**, **Dimitri**, **Jef**, **Alberto**, **Stijn**, **Margaux**, **Julie**, **Jelena**, **Ilan**, **Tibo**, **Carlotta S**,

Gianluca, **Robin**, **Barbara**, **Wouter**, **Tim DB**, **Daan** and **Steff**. Hoewel we nooit echt het labo gedeeld hebben mag **Klaas** zeker niet ontbreken.

Woorden van dank gaan uit naar de collega's die het reilen en zeilen van den F onder controle houden. De eeuwig jong van geest zijnde kapitein **Raf**, bedankt om het schip op koers te houden en de uiterst aangename praatjes. Groetjes aan Aline & Mathieu! Bedankt **Bart** voor je behulpzaamheid en het draaiende houden van onze favoriete meettoestellen, **Paul**, **Dirk** en **Gerrit** voor de uitstekende logistieke hulp, **Greet**, **Ann**, en **Evy** voor de administratieve bijstand, **Karel** voor de hulp bij NMR experimenten, **Dominik** voor de aangename shopervaringen en de **schoonmaakploeg** voor het keurig houden van den F.

To my colleagues from the neighboring labs in the F building, I want to extend a special word of thanks for your kindness, helpfulness, and the delightful chats we had in between our work. These exchanges not only brightened up my days but also created a supportive environment of sharing knowledge. Thanks to **Matthi**, **Mops**, **Winnie**, **Horsten**, **Martijn**, **Tom**, **Jasper**, **Max**, **Sem**, **Felien**, **Brent**, **Demian**, **Yenthel**, **Stijn** (al voelt het bijna raar om u hier op te noemen), **Pavel**, **Upendra**, **Gerardo**, **Guglielmo**, **Monica**, **Serena**, **Prabhat**, **Alexandra** and **Jens**. **Jakob**, ik koester de fijne tijden die we hebben beleefd op de aulabanken en bewonder je DIY-oplossingen en ideeën. Merci voor de fijne lunchpauzes!

Next, I transition to my colleagues within the **ContrasT Team**. **Sébastien**, I would like to express my gratitude for the enjoyable teamwork, imparting me with expertise in microCT, your valuable perspectives as an engineer and your effective approach in accomplishing projects successfully. Good luck with your MyCellHub adventures; I observe with wide, admiring eyes its robust evolution. **Lisa**, de rust zelve, kompaan sinds het prille begin. Ik herinner me nog zeer goed hoe we samen, met knikkende knieën, ons naar Woluwe begaven voor het inoefenen van ons FNRS/FWO overtuigingspraatje. Bedankt voor de fijne babbels en je behulpzaamheid. De komst van **Arne** ging gepaard met een toename in zowel efficiëntie (HistoWindow! Normalization!) als sfeer. Ik moet luidop lachen als ik scrol doorheen onze chat, rijkelijk gevuld met GIFs. Bedankt voor je paraatheid en hulp bij het maken van de afbeelding op deze cover! **Gregory**, thank you so much for your diverse contributions to the team ranging from organizing workshops, managing our beloved Nanotom, cab rides to LLN, sharing your Avizo master skill to sending *Happy*

Women's Day e-mails. It is a true pleasure to have you as a colleague. The team was further enriched with the arrival of **Delia**. I appreciate the excellent collaboration we've had. Our meetings frequently transformed into enjoyable conversations which helped ease my frustrations regarding precipitating compounds. I'm thankful for the laughter we shared during our "stay serious" games and for exchanging stories about mountain travelling. **Camille**, thanks for your enthusiasm and positive attitude, which contributes to a well-organized and pleasant group environment. Thank you for addressing all my inquiries regarding ~~frustrating~~ UCLouvain admin. Good luck with your imminent PhD Defense and future endeavors. De multidisciplinariteit van ons team werd tot een *next level* gebracht met de komst van **Victor**. Bedankt voor het vertalen van onze wensen in scripts en een reddingsbootje te delen van gestrande kajakkers.

I would like to extend my sincere gratitude to all the fellow members of ContrasT Team for the interesting discussions and experimental support: **Maïté**, **Lara**, **Kaveh**, **Carla**, **Karem**, **Walid**, **Pierre** and **Jeroen**. The research performed in this work benefited from the help of **Catherine Rasse**, statistical consultant of the Service de Méthodologie et Calcul Statistique. Thank you for your kind help, **Catherine**.

I am eternally thankful to all the people I have met and who have warmly welcomed and embraced me throughout my time in Boston. The experience was truly extraordinary. It was great being part of the **Orchard buddies** and Grinstaff group for five months. I am incredibly fortunate to have crossed paths with someone as remarkable as **Paola**, my friend. We embarked on a mutual exciting journey, exploring houses and furniture, and even searching for the perfect roommates. Thank you so much for all the support, adventures, friendship and laughter. I extend my appreciation to **Ceci** and **Fede** for their unwavering support, encouragement, companionship and positive energy. From movie nights, snow diving, basement parties to cooking together, your presence has brought warmth and joy to our shared living space. I would like to express my sincere gratitude to **Mareike** for being a lovely roommate and teaching me about strabismus. Together, we have created a home away from home, where cultural differences were celebrated, and friendships were forged. Our shared experiences and diverse backgrounds have enriched my understanding of the world. **Stijn**, *partner in crime* voor spontane avonturen, concertjes, toerist-uitjes. Merci voor de vriendschap en de onvergetelijke momenten die we beleefden in dat gekke land. Graag vul ik het lijstje aan met

Justine, **Valentina**, **Erik**, **Adrianna** (uitstekende kapitein), **Alexander**, **Wouter**, **David**, **Pierre**, **Thomas** and **Sneha.**

Anisha, I have very fond memories of the time we spent coring. I remember our laughter while placing the finicky wooden blocks to stabilize the drill, with or without zip ties. Thinking of 'dust in the wind' and 'I'm back. Maybe there was no need to vocalize that' makes me smile. Thank you for the moments of joy, scientific talks and deep conversations. I am grateful I could enjoy your optimism, kindness, helpfulness and good-heartedness on a daily basis. Your presence has enriched my US experience. Furthermore I would like to extend my sincere gratitude to the following **Grinstaff** fellows who helped me with my experimental work and answered all my questions: **Zach**, **Jack**, **Christian** and **Matt**. **Aaron**, I want to express my gratitude for the delightful and deep conversations we have had. Additionally, I would like to thank you for warmly welcoming me at your place and kind help to drive me to the airport. **Mariam**, thank you for your kind help with handling the administrative aspects of my stay.

Pfjoew, en dat waren dan nog enkel maar collega's en personen die ik indirect heb leren kennen via dit doctoraatsavontuur. We zijn er nog niet! Ik zou graag nog mensen willen bedanken die me nauw aan het hart liggen en me hebben geholpen me weg te trekken uit de PhD bubbel en steun hebben geboden tijdens de afgelopen jaren, en in het bijzonder de afgelopen maanden. Maar vooraleer ik dat doe wil ik graag mijn dankbaarheid uiten voor de **muziek** van enkele favoriete bands die me een drive, plezier, mooiheid en het afgelopen jaar zelfs steun, brachten: Arcade Fire, Balthazar, Intergalactic Lovers en The National (al kan ik hier nog even blijven doorgaan). Ik heb het geluk omringd te zijn met de meest fantastische **vrienden en familie**. Dankzij hun vriendschap, steun en liefde sta ik waar ik nu sta. Ik kan niet voldoende benadrukken dat mijn veerkracht en levenslust mede aan hen te danken is. Hoewel ik met plezier de uitgebreidheid van mijn dankwoord zou willen doortrekken naar de volgende paragrafen, vrees ik dat het me te ver gaat brengen. Ik zou niet willen dat u, als lezer, niet eens toe geraakt aan het lezen van het eigenlijke wetenschappelijke werk.

Mijn langstdurende vrienden, **Sofie** (mijn rots), **Glennemans** (van lessenaar-, naar aula- tot zelfs PhD- en filosofie-buddy) en **Astrid**, bedankt voor die onvoorwaardelijke vriendschap en jullie steun. Het voelt bijzonder te weten dat ik ALTIJD op jullie kan rekenen. Sofieke, bedankt om me zo mijn hele leven

(zo voelt het althans) bij te staan met je gouden hart en mooiste woorden. Bedankt lieve kazouvrienden, met in het bijzonder **Charlotte** (met de mooiste beeldspraak), **Niels**, **Ann-Sophie**, **Marlies**, **Lieve**, **Elisabeth, Sofie**, **Wibert**, **Sarah**, **Anke**, **Tomas**, **Elize**, **Hanne**, **Elien**, **Kobe** en ook **Ine** en **Celine.** En natuurlijk ook leuke **Marie**. Nauw aansluitend in dit rijtje zijn **Pieter** en **Laura**. Jullie aanwezigheid maakte het afgelopen jaar dragelijker en warmer, enorm veel dank. **Karlien** en **Andreas**, flirtend met de grens tussen vrienden/familie. **Karrie**, vriendinneke, bedankt om streng maar rechtvaardig op te treden wanneer ik té veel werkte, je steunende woorden en de babbels – die steeds oneindig kunnen blijven doorgaan. **Dré**, positivo, bedankt voor de onvoorwaardelijke vriendschap, de MTB- & kampeeruitjes, je mopjes (hoewel?) en zoveel meer. De herinneringen, getekend met een gouden randje, aan onze vierhoeksverhouding (ree! da's toch handig! rollende ogen!) koester ik met heel mijn hart. Bedankt om me het afgelopen jaar thuis te doen voelen wanneer ik verdwaalde. Bedankt om mee te dragen. **Charrie**, jij hebt een heel speciaal plekje in mijn hart. Je weet me soms beter te begrijpen dan ikzelf en je woorden kunnen me als geen ander raken en troosten. Bedankt voor die mooie vriendschap, op naar de 10 jaar die we samen met **Freekie** zullen vieren! **Woutie**, ik koester onze vriendschap die zelfs verder werd gezet en glorieus gevierd aan de overkant van de oceaan. Merci voor alle kleine en grote avonturen, de eindeloze babbels en last-minute plannen. **Elienos**, die de gekste kronkels in mijn hoofd kan begrijpen als geen ander. Bedankt voor uw loopvibes, lachvibes (gieren!), yolovibes en alle steun. De olijfboom pronkt met trots op mijn terras. Verder wil ik graag **Rany, Femke, Louise** en **Hanne** bedanken voor hun bijzondere aanwezigheid het afgelopen jaar. Bedankt voor alle steun en mooie - soms ontroerende - momenten. Uiteraard mogen **Liz** en **Flo** hier niet ontbreken.

Het afgelopen jaar was het meest bijzondere jaar tot nu toe, getekend door diep gemis en verdriet maar ook door de meest uiteenlopende warme ontmoetingen en verdiepende vriendschappen. De meest knuffelbare bij uitstek - **NAHY**. **Stijn**, hier vind ik u beter passen. Favoriete kuddedier, lijmen kan hij als geen ander. Bedankt voor je fundamentele blik, interessante inzichten en diepe gesprekken. En knuffels! Nog meer bedankt om samen met **Amy** me een thuis te bieden en zijn waar ik om het even wanneer steeds kan neerdwarrelen en innestelen, gepaard gaan met de meest verrukkelijke avondmalen uit mijn leven. Liefste **Amy**, jij kan als geen ander de meest holistische antwoorden bieden op vragen, ingaan op/bedenken van de meest vrolijke, soms impulsieve plannen en steunende knuffels en zinnen bieden

wanneer ik niet uit mijn woorden geraak. Van onschatbare waarde. **Rhea**, gepassioneerd en enthousiast, favoriete hyperintellectuele speelse wereldvogel. Bedankt voor je grote hart, alle eindeloze inzichtrijke gesprekken, gemsgewijze sprongen op de meest uiteenlopende plekken en steun op mijn meest breekbare momenten. Bedankt, liefste nahy, voor de warmte en voor het in me planten van inspirerende zaadjes.

Mama, papa, bedankt voor het warme nest waar ik ten alle tijden naartoe kan vliegen, en tegelijkertijd alle ondersteuning krijg om mijn (~~liefst geknipte~~) vleugels uit te spreiden (onder jullie ~~bezorgd~~ ~~toeziend~~ nabij oog) – ook al reiken mijn vluchten verder en zijn ze van meer avontuurlijke aard dan jullie believen. Ik kan jullie niet genoeg bedanken voor jullie onvoorwaardelijke steun en alle kansen die jullie me gegeven hebben. **Pappie**, bedankt voor je positieve ingesteldheid, je humor (hoewel?), je relativeringsvermogen en aanzienlijke veerkracht. Liefste **mamake**, bedankt voor alle zorgen, lieve woorden en steun. Wat ben ik toch een gelukzak met zo'n ouders. **Lauren**, onze band is op zijn minst uniek te noemen, zonder twijfel ben je één van de belangrijkste personen in mijn leven. Bedankt om altijd klaar te staan (echt altijd), me te helpen met de gekste dingen en praktisch dagelijkse bellekes. **Sien**, bedankt om zo'n lieve zus te zijn en om het kind in mij nog altijd graag naar boven te laten komen. **Moeke**, bedankt om ten alle tijden met veel zorg voor me klaar te staan en me overal naartoe te brengen. **Vake**, wat zou ik je graag zien glunderen. Bedankt voor je zotste verhalen en alle avonturen die we beleefd hebben. Wie er zeker niet mag ontbreken is **Titi**. Jouw bijdrage aan mijn studiecarrière zal ik nooit onderschatten. Bedankt voor al je steun, het lekkere eten en de fijne wandelingen en nog zoveel meer. Het lijstje vervolledigen doe ik met **Veke**, ~~zo goed~~ als familie. Niemand anders dan jij kan ons beter inschatten en bijstaan met raad en daad. Merci om me (last-minute) steeds uit de nood te helpen.

Allerleukste **neven en nichten**, ik voel me vereerd deel uit te maken van zo'n toffe bende. **Opa** en **Oma** zouden terecht fier zijn. Hoe kan het ook anders. Bedankt voor die gezellige samenkomsten waar ik zo van geniet; ik ben met mijn gat in de boter gevallen. Merci **Marijke**, ik voel me steeds zo thuis bij u.

Lieve **Mie**, ik ben je dankbaar voor het openstellen van je tuin en huis voor de Ferdinand Verbiestclub, inclusief het mogelijk maken van mijn eigen bureauruimte, maar vooral voor alle warme momenten. **Paul** en **Caro**, dankjulliewel voor de fijne tijden in het geliefde Rooi. Het doet me deugd te

weten dat ik steeds op jullie kan rekenen. **Anneleen**, de gouden rand van afgelopen jaar is zonder enige twijfel onze speciale band. Te veel om in woorden te vatten waarvoor ik je dankbaar ben. Bedankt voor - alles. Mijn oogappels **Lucas** en **Tiago** verdienen hier een mooie plek, samen met **Eduardo**. Ik kijk uit naar meer zussenmomenten samen met **Lore**, jij vrolijke, goedhartige en speelse spring-int-veld. Dikke merci voor onze meer-dan-familie-band. Bedankt om me samen met lieveling **Noah** thuis te doen voelen in jullie aanwezigheid.

In het kader van dit doctoraatsavontuur, en ver daarbuiten, is **Hannes** de persoon bij uitstek die ik wil bedanken. Zonder hem zou dit doctoraat er niet gestaan hebben zoals het er nu staat. Hij was het die me heeft verdragen de afgelopen jaren. Hij was het die wachtte met eten toen ik - weeral - later thuis kwam van het labo. Hij was het die geïnteresseerd bleef luisteren naar mijn presentaties en zelfs een geïmproviseerd publiek van chemici knutselde. Hij was het die me enkele minuten voor elke presentatie of belangrijke meeting succes stuurde. Hij was het die me steunende woorden toefluisterde wanneer mijn onzekerheden de overhand namen. Hij was het die me liet gaan voor mijn Amerikaans avontuur, me kwam opzoeken voor de allermooiste tijd samen, en me zelfs in alles ondersteunde. (Al had je liever niet dat ik niet vertrok - je wederkerig opduikende pruillip naarmate het avontuur concreter werd staat op mijn netvlies gebrand). Bewonderingswaardig hoeveel je voor me deed, geduld je had en interesse je toonde. Bedankt om mijn grootste supporter en mijn klankbord op elke minuut van de dag geweest te zijn. Bedankt om zonder woorden aan te voelen wat ik nodig had. Bedankt voor je paraatheid en hulp, je capaciteit om met me samen te hebben geleefd in tijden van stress, chaos en rusteloosheid. Bedankt om van mijn omgeving ook jouw omgeving te hebben gemaakt. Bedankt om samen met me te groeien. Bedankt voor de onvoorwaardelijke steun en diepe gesprekken. Bedankt voor die ontzettend mooie liefde.

Het is moeilijk onder woorden te brengen hoe het voelt om te leven zonder je fysieke aanwezigheid.

De spijt en schuld die ik voel van alle avonden waarin mijn perfectionisme/ plichtsbewustzijn het werk verkoos boven tijd voor ons samen, maakte het me de laatste maanden erg lastig om het schrijfproces te hervatten. Het lukte, weliswaar bijzonder moeizaam, maar ik hield in mijn achterhoofd dat je het niet anders zou gewild hebben. Het voelt zo paradoxaal en oneerlijk. Ik zou op

dit eigenlijke moment er ALLES voor over hebben om je te kunnen bellen om te zeggen dat ik mijn laatste woorden aan het neerschrijven ben. Nog liever zou ik graag je blik, met je waarschijnlijk fonkelende ogen, willen zien op de dag van mijn publieke verdediging. Die dag zou voor jou, minstens evenveel, of misschien zelfs nog meer dan voor mij, een feest geweest zijn.

Onwezenlijk. Absurd. Hard.

Hoe hard het ook in mijn natuur zit, en misschien zelfs iets te veel, om 'je best te doen' en 'goed te werken', des te hard doe ik mijn best om voortaan anders naar het leven te kijken, want er is zoveel meer dan werk, verplichtingen en voldoen aan verwachtingen.

Zoekend naar nieuwe evenwichten, ben ik je ontzettend dankbaar voor je levenslessen en alles wat je voor me deed, lieve Hannes. Je bedanken voelt niet als voldoende, liever draag ik je waarden vanbinnen met me mee, altijd en overal. Voor eeuwig in mijn hart, voor eeuwig in mijn gedachten, voor eeuwig in mijn leven.

Sarah
Kortenberg, Juni 2023

Courage is the most important of all the virtues because without courage, you can't practice any other virtue consistently – Maya Angelou

XX

TABLE OF CONTENTS

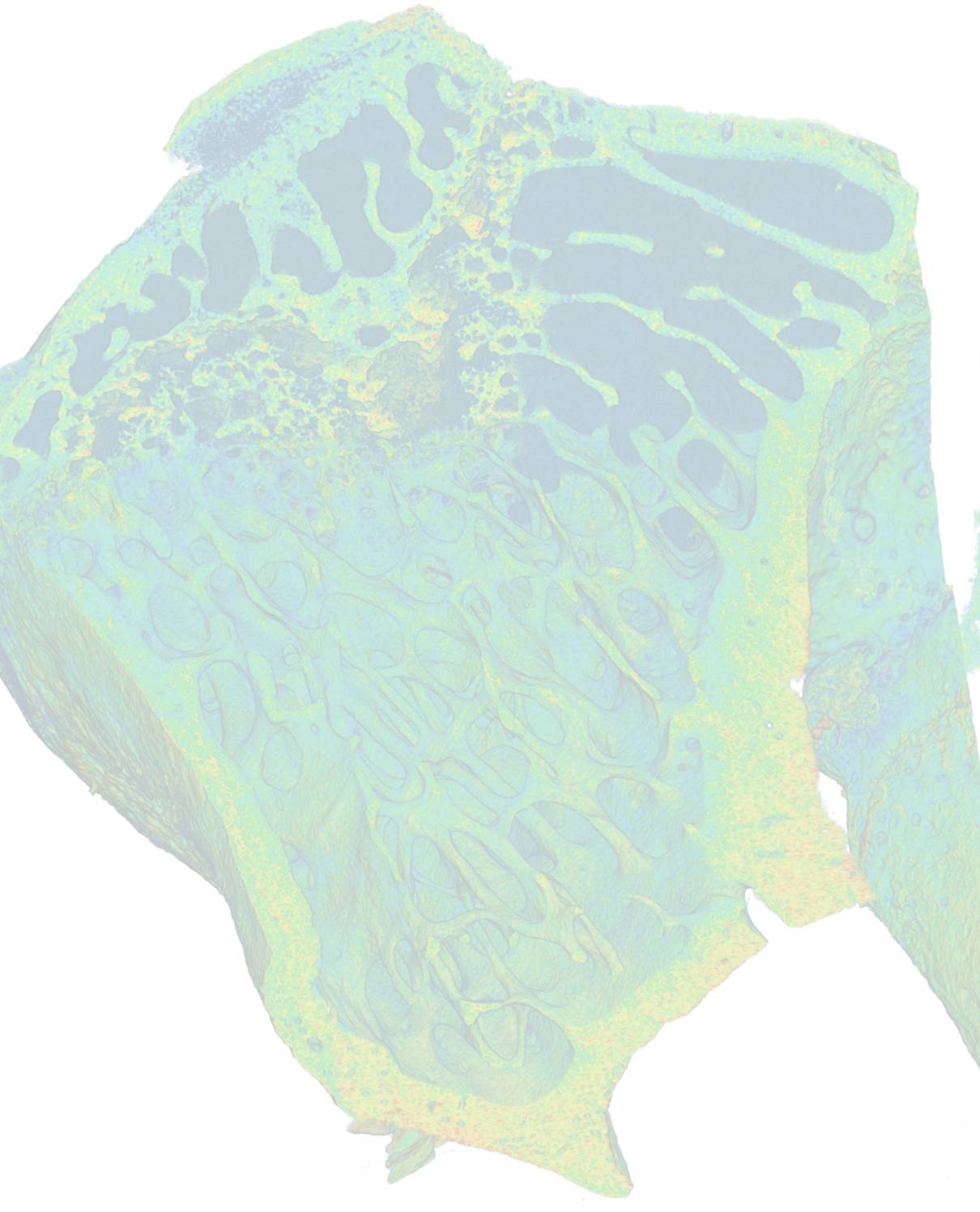
SUMMARY I
SAMENVATTING III
LIST OF ABBREVIATIONS V
PREFACE IX
ACKNOWLEDGEMENTS - DANKWOORD X
TABLE OF CONTENTS XXI
CHAPTER 1 Overview 1
1.1 Context 2
1.2 X-ray micro-computed tomography 3
1.3 Dissertation overview – guide for the reader 3
CHAPTER 2 Introduction 7
2.1 Introduction 8
2.2 Need for contrast enhancement 9
2.3 First exploratory studies on contrast-enhanced microCT 10
2.4 Contrast-enhanced microCT for cartilage 13
2.5 Contrast-enhanced microCT for the bone marrow compartment . 16
2.6 Contrast-enhanced microCT for muscle tissue 17
2.7 Contrast-enhanced microCT for tendons and ligaments 18
2.8 Remaining challenges 19
2.9 Conclusions 20
CHAPTER 3 Polyoxometalates as CESAs 23
3.1 Introduction 24
3.2 Objectives 24
3.3 Properties of POMs 25
3.4 CECT imaging 25
3.5 Stability and speciation of POMs 32

3.6 Conclusion 36
CHAPTER 4 Cationic CESAs 39
4.1 Introduction 40
4.1.1 Osteoarthritis 40
4.1.2 Articular cartilage 41
4.1.3 Cationic CESAs for cartilage imaging 44
4.2 Objectives 45
4.3 Synthesis of cationic CESAs 46
4.3.1 Synthesis of CA4+6I 46
4.3.2 Synthesis of CA8+6I 48
4.3.3 Synthesis of CA4+3I 50
4.4 Evaluation of X-ray attenuation of the CESA solutions 51
4.5 Diffusive behavior of cationic CESAs through AC 52
4.6 Staining of osteochondral plugs with cationic CESAs 53
4.6.1 Descriptive data analysis 55
4.6.2 Diffusion analysis 64
4.6.3 Multivariate Analysis of Variance 67
4.6.4 Preferred staining condition 72
4.7 Conclusions 73
CHAPTER 5 Protein-specific CECT 77
5.1 Introduction 78
5.2 Objectives and general strategy 81
5.3 Development of a protocol to improve tissue penetration 82
5.4 Development of a peptide-based targeting probe 82
5.4.1 Ab-based probes 82
5.4.2 Peptide-based probes 83
5.4.3 Selection of KLH-specific phage clones by phage display 86

5.4.4 Affinity comparison between phage clone and isolated peptide 89
5.5 Development of an X-ray attenuating substrate for HRP 91
5.5.1 Iodination of 3,3'-diaminobenzidine 92
5.5.2 Attachment of an X-ray attenuating core to DAB 94
5.5.3 Screening of commercially available iodinated tyrosine analogues 95
5.5.4 Attachment of an X-ray attenuating core to tyramine 97
5.6 Conclusions 104
CHAPTER 6 Conclusions & Outlook 109
6.1 Polyoxometalates as CESAs 110
6.2 Cationic CESAs 112
6.3 Development of protein-specific contrast-enhancing staining agents 113
6.4 Future of *ex vivo* CECT 116
CHAPTER 7 Experimental Section 119
7.1 Chemical safety considerations 120
7.2 General experimental information 122
7.2.1 General information 122
7.2.2 Purification equipment 122
7.2.3 Analytical equipment 123
7.3 Chapter 3 POM screening – Experimental 127
7.3.1 Materials 127
7.3.2 Microfocus X-ray computed tomography 128
7.3.3 Statistical analysis 131
7.4 Chapter 4 Cationic CESAs – Experimental 131
7.4.1 Synthesis 131
7.4.2 Materials 142

7.4.3 Microfocus X-ray computed tomography 144
7.4.4 NaI calibration curve for iodine concentration determination 145
7.4.5 Staining of osteochondral plugs with cationic CESAs 147
7.4.6 Descriptive data analysis 148
7.4.7 Diffusion analysis 148
7.4.8 Statistical data analysis (MANOVA) 151
7.4.9 Supplementary figures 151
7.5 Chapter 5 Protein-specific CECT – Experimental 155
7.5.1 Synthesis 155
7.5.2 Phage display library 163
7.5.3 Phage display protocol 164
7.5.4 Elisa protocol for the identified phage clones 165
7.5.5 Elisa protocol for the comparison of phage & peptide insert 166
7.5.6 Protocol for staining kidneys with compounds 3.6, 3.7 or 3.14 167
7.5.7 Microfocus X-ray computed tomography 168
Appendix A 171
A.1 Introduction 172
A.2 Instrumentation and parameters 172
A.3 Principles of X-ray attenuation 175
A.3.1 Photoelectric effect (PE) 178
A.3.2 Compton scattering (CS) 179
A.3.3 Rayleigh scattering (RS) 179
A.4 Measurement of attenuation 180
A.4.1 Gray value 180
A.4.2 Hounsfield unit 180

Appendix B..... 183
REFERENCES 186
PUBLICATIONS & PRESENTATIONS..... 210



CHAPTER 1

Overview

1.1 Context

Throughout this dissertation, *ex vivo* microfocus X-ray computed tomography (microCT) has been used to evaluate compounds as contrast-enhancing staining agents (CESAs) for contrast-enhanced microCT (CECT) imaging. X-ray computed tomography (CT) is a 3D imaging modality that was introduced in the early 1970s.[1] Herein, the penetration power of X-rays is exploited to create two-dimensional (2D) radiographs (projections) of a sample at sequential angles. X-rays are a form of electromagnetic radiation with a wavelength in the short range of the electromagnetic spectrum, from 0.01 to 10 nm. A reconstruction algorithm then compiles these radiographs into a volume, which consists of a stack of 2D reconstructed sectional slices. As a result, the sample is visualized as a 3D volume that can be virtually sliced in any desired direction and orientation. A concise theoretical background microCT is given in Appendix A. This background serves to understand the principles of microCT and the parameters used in this work.

X-rays that pass through an object can be absorbed or deflected (*i.e.* attenuation), which results in a change of intensity and phase. Attenuation contrast imaging is based on the change in X-ray intensity. X-ray attenuation depends on the atomic number of the atoms present in the material, the physical density of the material and the energy of the X-ray beam. Soft tissues (such as muscles, adipose tissue) are hard to visualize by microCT due to the lack of atoms with a high atomic number. On the contrary, hard tissues (such as bone) are easily visualized due to the presence of calcium. In order to enhance their X-ray attenuation, soft tissues are stained with contrast agents (CAs). These CAs contain atoms of high atomic number, such as iodine or tungsten. In this work, we focus on CAs for *ex vivo* imaging of biological tissues. Herein, tissues are stained through passive diffusion by immersing them in a solution containing a CA. We call this type of CAs 'contrast-enhancing staining agents' (CESAs). As a result, the tissue is rendered X-ray attenuating, which allows visualization of its inner structure.

Ex vivo CECT of biological tissues is a modern field. The very first reports focusing on the use of commercially available compounds as CESAs for soft tissue visualization go back to only 15 years ago. Still today, the development of novel staining procedures heavily relies on trial-and-error approaches and anecdotal knowledge. A good example is the use of Lugol's iodine (aqueous solution of I_2KI), which has been used as a disinfectant and a colorimetric dye amongst others. Meanwhile, various literature reports exist on the use of

Lugol's iodine as a CESA to stain a wide variety of soft tissues. Nevertheless, deciding on the required volume, concentration and staining time is still not an easy feat. Screening of current literature can provide a first indication, however, guidelines to select an optimal condition are desirable.

Despite the widespread use of CESAs in research, the mechanism of staining is still poorly understood. In recent years, knowledge on staining mechanisms gained more interest in literature.[2, 3] Problems associated with staining were the main driving force to better understand the mechanism. In this way, researchers hope to overcome issues such as limited penetration depth and tissue shrinkage.[4]

1.2 X-ray micro-computed tomography

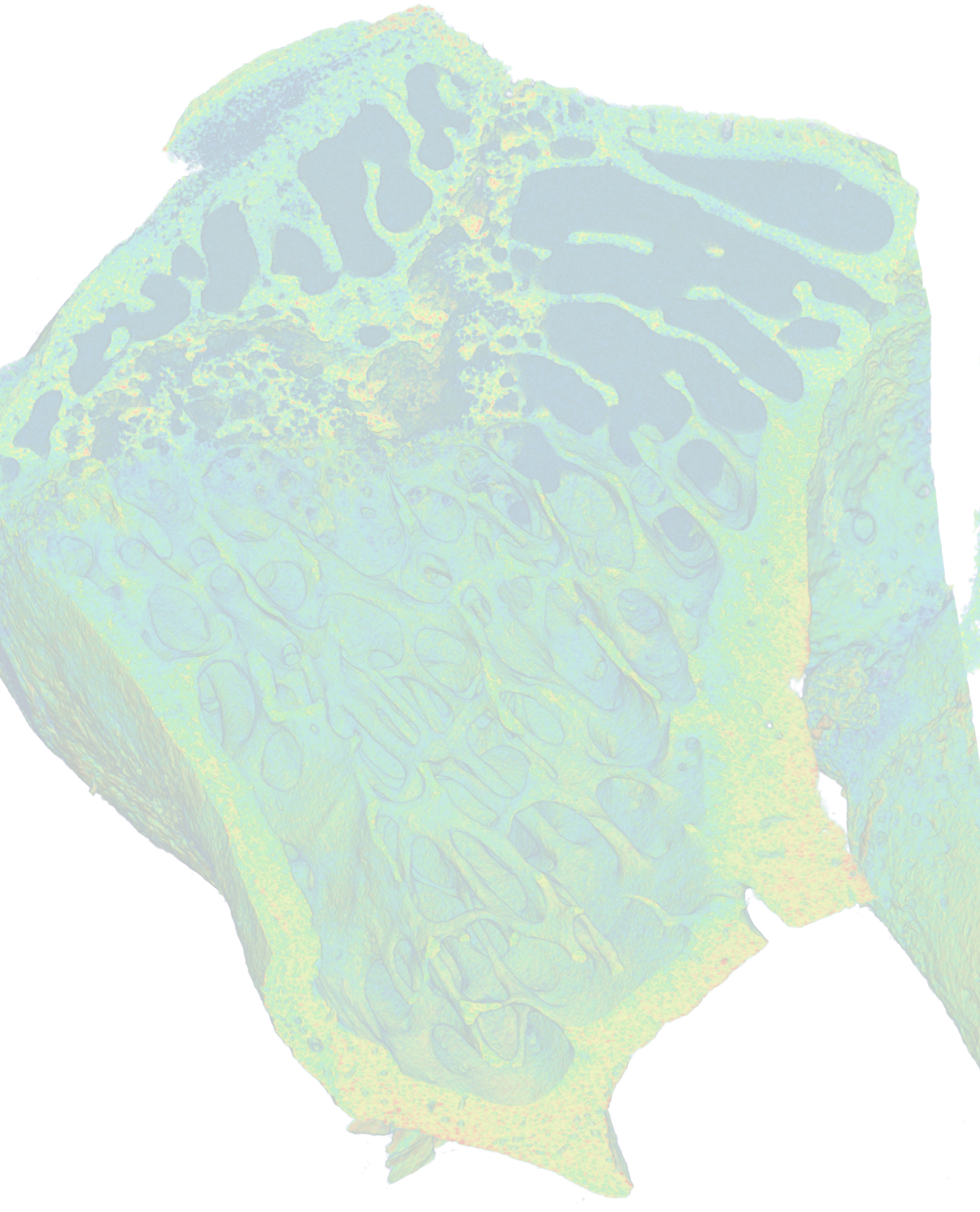
MicroCT has proven to be a very powerful tool for 3D imaging of mineralized samples, in many biomedical fields.[5] Thanks to the penetrating power of X-rays, microCT provides a 3D density map of the samples *(a)*. High resolution microCT scans are achievable (< 1 µm voxel size) *(b)* and a high field of view to voxel size ratio can be obtained nowadays *(c)*. Additionally, the workload for sample preparation before imaging is substantially lower compared to other histological assessment techniques, and fast image acquisition and volume reconstruction times are feasible by means of the current high-resolution microCT devices, justifying the higher throughput potential of this technology *(d, e)*. While one of the major advantages of microCT is its non-destructive character (no need for cutting samples) *(f)*, a considerable limitation of this technology is its lack of specificity for different soft tissue types. Indeed, X-ray imaging techniques are suitable to investigate strongly absorbing samples, such as mineralized tissues, but struggle with discriminating non-mineralized or soft biological tissues that have similar or weak X-ray absorbing properties. Consequently, it can be challenging to differentiate between soft tissues on X-ray radiographs and reconstructed microCT images.

1.3 Dissertation overview – guide for the reader

This dissertation aspires to contribute to the field of CESAs for CECT imaging, with a particular focus on the visualization of the internal structure of biological tissues. The overarching objective of this dissertation is to develop novel compounds to be used as CESAs for staining tissue constituents, hence increasing their visibility in CECT imaging. In doing so, tissue constituents can

be distinguished based on differences in X-ray attenuation stemming from diverse CESA affinities. The ultimate goal is to provide researchers a valuable instrument to investigate the 3D composition of biological tissues and the spatial organization of its constituents.

The first chapter provides an overview of the state-of-the-art literature concerning CESAs for *ex vivo* CECT imaging. In addition, this chapter discusses the progress made in the field as well as the challenges that need to be overcome to improve its widespread use. A concise theoretical background on microCT is given in Appendix A to help the reader to understand some general principles. In what follows, three different CESA stories are presented. Especially noteworthy about the chronological structure of this dissertation is the trend to image in a more specific, targeted way. The reader will first encounter the screening of polyoxometalates (POMs) for imaging soft tissues. Herein, aqueous solutions of different POM species were evaluated to visualize murine bone marrow and kidney. Next, a report is presented on the synthesis and evaluation of cationic iodine-based CESAs for cartilage imaging. Optimization of existing synthesis procedures are described, as well as the development of new CESAs and their evaluation for staining articular cartilage at different cartilage depths. Lastly, in chapter 5 we aimed to develop procedures to perform 3D protein-specific staining. This chapter focuses on one hand on the development of a labelling protocol, and on the other hand on the synthesis of X-ray attenuating probes. Chapter 6 provides concluding remarks and future challenges the field faces to move from trial-and-error approaches towards a more directed development of novel CESAs. Details on the methods used and experimental details of the work performed in this dissertation are given in chapter 7.



CHAPTER 2

Introduction

Contrast-enhanced microCT of biological tissues

The content of this chapter is based on:

Contrast-Enhanced MicroCT for Virtual 3D Anatomical Pathology of Biological Tissues: a Literature Review

de Bournonville, S.; Vangrunderbeeck, S.; Kerckhofs, G. *Contrast Media Mol. Imaging*. **2019**, 8617406. doi: 10.1155/2019/8617406

and was partly adapted and reproduced under the Creative Commons Attribution 4.0 International License.

Credit authorship contribution statement

Sébastien de Bournonville: Conceptualization, Investigation, Writing – Original Draft, Writing – Review & Editing, Funding acquisition. **Sarah Vangrunderbeeck:** Investigation, Writing – Original Draft, Writing – Review & Editing. **Greet Kerckhofs**: Conceptualization, Writing – Review & Editing, Funding acquisition, Supervision.

2.1 Introduction

Biological tissues have a complex composition and microstructural organization, and hence an inherent spatial heterogeneity. Understanding the spatial organization of the tissue constituents, such as proteins, cells or extracellular matrix (ECM), is paramount in elucidation their role in both healthy and diseased condition. Since decades, the gold standard for the evaluation and characterization of biological tissues in the field of biomedical sciences is histological assessment by optical microscopy, which involves tissue embedding and sectioning with subsequent colorimetric, immunohistochemical (IHC) or immunofluorescent (IF) staining and microscopic evaluation. Thanks to the broad range of class-specific (DNA, proteins, lipids or carbohydrates) dyes it is considered a highly versatile screening technique. Out of a single sample, a significantly high amount of qualitative and quantitative characteristics of different kind of tissues can be obtained.[6] Although having a highly discriminative power on both the tissue and cellular level, classical two-dimensional (2D) histological assessment remains a challenging, time-consuming and costly technique.[7] If the tissue is mineralized, decalcification might be required before slicing (which can take more than one week depending on the sample size). Moreover, depending on the dimensions and heterogeneity of the tissue, a large number of slices might be required for a sufficient spatial analysis of the sample. In addition, slicing the sample can only be performed under a restricted sectioning orientation and is subject to processing glitches and distortions. After staining the slices, the sections are typically assessed under a light microscope. This results in a stack of 2D microscopy images, representing the three-dimensional (3D) arrangement of the sample. While the individual slices are of high quality (highly selective stains, high in-plane spatial and contrast resolution), the resolution along the third dimension in space is often limited due to the restricted number of sections that can be realistically be sliced and imaged for one sample.[8] These drawbacks play an important role in the spatial assessment of highly heterogeneous tissues (*e.g.* trabecular bone, vascular networks, *etc.*), as well as in quantifying the spatial inter-relationship between different tissues within one sample.

For heterogeneous tissues, an ideal alternative 3D visualization technique should allow to *(a)* provide full 3D information and *(b)* provide sufficient spatial and contrast resolution for the structures of interest, while *(c)* allowing a broad field of view along any direction of the volume and *(d)* reducing the workload for sample preparation. Additionally, it should *(e)* increase the

throughput, *(f)* provide a wide range of specific stains with sufficient contrast and *(g)* limit the destructiveness of the methodology to the samples, as not to harm the tissue integrity nor hamper the complementarity with histological assessment or other biochemical assays. MicroCT is a technique that has been on the rise in recent years and largely meets these requirements.

2.2 Need for contrast enhancement

The introduction of radio-opaque contrast agents (CA) enabled high-resolution microCT to become an important tool in biomedical imaging. CAs consist of atoms of high atomic number and are used to stain soft tissues. As a result, the radiodensity will increase, which enhances differentiation among different tissues. Contrast enhancement by means of CAs for microCT imaging is known as contrast-enhanced microCT (CECT). CAs for microCT imaging of biological tissues fall apart in roughly two categories: (1) perfusion contrast agents for *in vivo* or *ex vivo* vasculature imaging, and (2) contrast-enhancing staining agents (CESAs) for *ex vivo* imaging of biological tissues.[9] The latter category has sparked our interest to develop 'X-ray based 3D histology'. Herein, biological tissues are stained through passive diffusion by immersion in a solution containing a CESA. Because of the interactions of the CESA , the tissue is rendered X-ray attenuating, which allows visualization of the microstructure by microCT.

As reviewed further in this chapter, different CESAs have recently been reported for CECT imaging of specific soft tissues (g). However, care should be taken that both the staining protocol and the image acquisition setup do not compromise the non-destructive character of the methodology. Hence, the protocol should not have any effect on the tissue integrity. Ultimately, CECT should be complementary with subsequent biochemical assays, while maintaining good image quality.

Although the focus of this dissertation is on attenuation contrast imaging, we would like to briefly mention that alternative X-ray based imaging techniques also exist, which enable contrast enhancement differently. Dual energy X-ray imaging, on the one hand, could be used to distinguish two compounds with a similar attenuation, but with a different K-edge (*i.e.* inner electron shell binding energy). In this context, imaging at two different X-ray energies (before and after the specific K-edge), allows to enhance the contrast of specific CESAs.[10] Phase contrast X-ray CT, on the other hand, provides

information concerning changes in the phase of an X-ray beam that passes through an object. Typically, this technique is applied to visualize objects containing components with similar attenuation characteristics. It can be used to, for example, enhance edges, which allows a better visualization of soft tissues. [11, 12] In contrast to the aforementioned imaging techniques, which require highly dedicated hard- and software, CECT is a more commonly used and affordable technique.

2.3 First exploratory studies on contrast-enhanced microCT

The very first reports focusing on the use of commercially available compounds as CESAs for CECT visualization of soft tissues go back to only about 15 years ago. Johnson *et al*.[13], Litzlbauer *et al.*[14] and Ribi *et al*.[15] used OsO_4, a highly toxic stain, on mouse embryos, pig lungs and honey bees respectively, to enable their virtual 3D anatomical analyses using CECT. Few years later, Brian D. Metscher and his group went one step further by exhaustively investigating the staining potential of several commercially available compounds as CESAs for different sample types.[16, 17] Their research about different sample fixations and staining protocols gave birth to the very first protocols for soft tissue CECT. Metscher and co-workers demonstrated the use of very simple and versatile staining methods for quantitative volumetric imaging of animal soft tissues. They investigated which fixation method is preferred for better imaging results, depending on the tissue type and the CESA used. This research also confirmed that Lugol's iodine (I_2KI) and phosphotungstic acid (PTA) could be used for a broad range of CECT applications. The main advantages of these two CESAs are the simplicity of sample preparation and their safer nature compared to OsO_4. However, it should be noted that these studies only investigated the staining potential of the CESAs for visualizing different soft tissues, without studying the potential destructiveness of the CESAs themselves on the tissues, nor their binding mechanisms. From then on, more exploratory studies were performed to investigate the staining potential of new compounds.[18-20] In 2013, Pauwels *et al.* reported an elaborate tissue-directed screening study of different compounds to be used as CESAs.[21] While this study reported various CESAs for soft tissue imaging, most of the staining solutions used had a higher osmolality than the biological samples, which could harm the samples due to tissue shrinkage. Moreover, the tissue-specific binding mechanisms still remained to be better understood. Other work focused on the validation of the method

against established gold standards like (immuno)histological assessment by optical microscopy.[22]

In what follows, we will discuss several studies that paved the way for CECT-based virtual 3D anatomical pathology. Educated opinions on aspects to consider will be given, as well as on remaining challenges and future perspectives. Over the years, microCT has become a standard imaging technique for 3D structural analysis of bone and mineralized tissues. As a result, a majority of the studies that have reported on the use of CESAs for CECT imaging have been performed with regards to the musculoskeletal system. Hence, we will mainly focus on musculoskeletal tissues. Table 2.1 provides an overview of the CESAs that have been reported for attenuation X-ray CT imaging, organized by type of tissue.

Table 2.1 Reported CESAs for musculoskeletal tissues.

Tissue	CESAs & references	Remarks & added value of CECT
Cartilage	• Anionic CESA ○ Ioxaglate/Hexabrix® [23-31] ○ Iothalamate/Cysto Conray® II [23, 28, 29, 32, 33] ○ Gadopentetate/Magnevist® [25, 34-38] ○ NaI [36, 37] • Cationic CESA ○ CA4+ [8, 23, 25, 31, 32, 39-72] ○ CA2+ [23, 50] ○ CA1+ [23] ○ Gd^{3+} [35] • Nonionic iodinated CESA ○ Iopromide/Ultravist® [30] ○ Iodixanol/Visipaque® [36, 69] ○ Iohexol/Omnipaque™ [73] ○ Ioversol/Optiray® [74] ○ Iomeprol/Iomeron300® [74] ○ Gadoteridol/ProHance® [35, 42] ○ Gadodiamide/Omniscan™ [36, 37] • Ta_2O_5 NP [47, 56] • PMA [75] • PTA [75-81] • Hf-WD POM [22] (Fig. 1A) • Uranyl acetate [82]	Electrostatic interactions between anionic or cationic CESAs and the GAGs in the cartilage enable visualization of the GAG distribution in the cartilage matrix. POM CESAs are reported to bind to collagen, enabling structural analysis of the cartilage tissue and, in case of sufficiently high spatial resolution, imaging of individual chondrocytes. Uranyl acetate is known to bind collagen and was reported in one single study for cartilage imaging.

Bone marrow compartment	Hf-WD POM [22] Mono-WD POM[83]	Enables simultaneous visualization and structural quantification of adipocytes, vasculature and mineralized tissues.
Muscle	• PTA [17, 21, 84] • I_2KI [17, 85, 86] • PMA [21] • $HgCl_2$ [21] • Na_2WO_4 [21] • $(NH_4)_2MoO_4$ [21]	CECT images can serve as input for computational models to study biomechanical properties. PTA, PMA, I_2KI, $HgCl_2$, Na_2WO_4 and $(NH_4)_2MoO_4$ have high osmolality compared to biological tissues, and hence induce tissue shrinkage.
Bone marrow adiposity	• OsO_4 [87, 88]	OsO_4 is highly toxic and requires a two-step scanning protocol.
Tendons and ligaments	• PTA [21, 89-91] • I_2KI [89-91] • Iomeprol/Imeron® [92] • PMA [21, 89] • $(NH_4)_2MoO_4$ [21] • $Ba(ClO_3)_2$ [21] • $HgCl_2$ [21] • Na_2WO_4 [21] • $BaCl_2$ [21] • $Pb(NO_3)_2$ [21]	Same remarks as for muscle tissue for PTA, I2KI, PMA, $HgCl_2$, Na_2WO_4, $(NH_4)_2MoO_4$, $BaCl_2$ and $Ba(ClO_3)_2$

2.4 Contrast-enhanced microCT for cartilage

The musculoskeletal system ensures locomotion, protection and stability of the body. To fulfil its functions, this system is mainly composed of different tissues: long and flat bones, cartilage, muscles, tendons, ligaments and other connective tissues. The visual assessment and structural analysis of these tissues is relevant for different fields (*i.e.* regenerative medicine, drug development, early detection of pathologies, developmental biology, *etc.*). Cartilage is one of the most studied musculoskeletal tissues with regards to CECT imaging and pathologies (osteoarthritis and rheumatoid arthritis). It is

composed of a collagenous matrix that is rich in glycosaminoglycan (GAG) polysaccharide chains. Because of these GAGs, cartilage tissue possesses a negative charge density. As a consequence of its specific composition, iodinated CESAs for cartilage can be classified in three groups: anionic, cationic and non-ionic iodinated CESAs. Besides, some metal-based CESAs were also reported in literature for cartilage imaging.

For the first group of CESAs, equilibrium partitioning of an anionic contrast agent *via* microCT (EPIC-microCT) has been described to study the morphology and composition of cartilage.[24] EPIC-microCT is a methodology in which a tissue sample is equilibrated in a solution of an anionic CESA. It relies on the inverse distribution of anionic CESAs to the fixed negatively charged GAGs due to electrostatic repulsion. As a result, the cartilage is visualized as a negative contrast since the surrounding tissue receives a higher gray value in the reconstructed images. Over the past years, several commercially available iodinated anionic CESAs (*e.g.* iothalamate (Cysto-Conray® II) and ioxaglate (Hexabrix®)), which were originally developed for *in vivo* cardiovascular and urological imaging, have been studied for both qualitatively and quantitatively assessment of the cartilage morphology.[24, 28, 29, 41, 93, 94] Similar inverse distribution to GAGs of gadopentate (Magnevist®) was also reported.[25, 34, 35] Gadopentate is a gadolinium-based CA for MRI, which was also adopted as a CESA for X-ray CT. The major disadvantage of anionic CESAs is the high concentrations required in order to obtain a sufficient contrast-to-noise ratio.[61] Furthermore, the contrast and the overall quality of the images might no longer be sufficient for accurate quantification of the GAG content in case of low GAG concentrations (*e.g.* in engineered cartilage).[95]

To improve the potential of electrostatic interactions between the CESA and the GAGs within the cartilage, iodinated cationic CESAs have been developed, which attract rather than repel GAGs, compared to anionic CESAs. The synthesis and evaluation of such iodine-based, positively charged compounds was first described by the Grinstaff group.[23, 69] Soon after, a CESA with a net positive charge of four (CA4+) was reported, which showed a higher uptake ratio in the deeper zones of the cartilage tissue and, therefore, generated higher X-ray attenuation of the cartilage tissue at lower concentrations compared to anionic CESAs.[25, 32, 53, 61, 67, 69] Moreover, the higher equilibrium concentration of CA4+ resulted in an increased sensitivity to the GAG content. Hence, a more specific imaging of the cartilage tissue was obtained, along with a more precise tissue differentiation.[8, 31, 32, 40, 53-55, 57, 61, 63, 69] Likewise, bovine

articular cartilage stained with Gd^{3+} was found to positively correlate with the GAGs in the cartilage matrix.[35] Furthermore, it has been demonstrated in *ex vivo* bovine, murine, equine and human cartilage that the increased X-ray attenuation, induced by CA4+, showed a positive trend with the equilibrium compressive modulus and a negative trend with the coefficient of friction.[8, 31, 46, 54, 55, 58, 60, 68, 69] These mechanical properties are frequently examined because they are important indicators of cartilage health and functional performance. Moreover, X-ray attenuation conferred by CA4+ was correlated with the cartilage compressive stiffness, subchondral bone properties, and trabecular network factors in human articular cartilage.[54, 62] Dual energy CT studies using CA4+ and gadoteridol (neutral) declared an improved GAG sensitivity of CA4+ when normalized with gadoteridol partition.[43, 44, 51, 52, 64, 66, 72, 96] For the same reason, an improved correlation of X-ray attenuation (CA4+) with equilibrium modulus was reported.[42, 52, 60, 64] One limitation of using CA4+ is, however, the considerably longer time required to reach diffusion equilibrium in comparison with anionic CESAs.[61, 69] The Grinstaff group also reported surface-modified tantalum oxide nanoparticles (Ta_2O_5 NPs) for cartilage imaging. More specifically, the surface of Ta_2O_5 NPs were decorated with phosphonate/PEG (neutral), ammonium (cationic) or carboxylate (anionic) functional groups, and subsequently used for *ex vivo* imaging of murine and human articular cartilage.[47, 56] Among these, the cationic NPs most closely reflect the GAG distribution within the cartilage matrix, both in healthy and osteoarthritic samples.

Besides ionic CESAs, several non-ionic CESA were also explored for cartilage imaging. The main limitation of non-ionic CESAs (such as iopromide (Ultravist®)) is the absence of correlation between the GAG content and the X-ray attenuation.[30] Instead, these types of CESAs are rather used to reflect the water content in the cartilage matrix.

PTA, originally used in histological staining, has been described for cartilage X-ray imaging because of its attractive interactions with type II collagen in an acidic environment (Figure 2.1B).[75-81] More specifically, Nieminen and Saarakkala distinguished superficial, middle and deep zones of PTA-stained articular cartilage based on the differences in collagen density.[53, 75] In addition, visualization and characterization of chondrocytes in articular cartilage stained with PTA was reported, which was validated by comparison with alternative microscopy methods.[78, 80] PTA, being a polyanion, is thought to bind with collagen in an electrostatic way.[97] In addition, Nemetschek *et al.*

hypothesized the formation of an intersubfibrillar binding of PTA with collagen fibers.[98]

Similarly to PTA, a hafnium-based Wells-Dawson polyoxometalate (Hf-WD POM) was hypothesized to bind collagen, and has been used for CECT visualization of the cartilage tissue within human osteochondral samples, though within a neutral, non-acidic environment (Figure 2.1A).[22] Interestingly, individual lacunae could also be visualized within the cartilage matrix.

All things considered, CA4+ and related cationic CESAs are highly promising for quantitative cartilage CECT imaging because of their high affinity and sensitivity to GAGs, making functional imaging of the cartilage tissue possible.

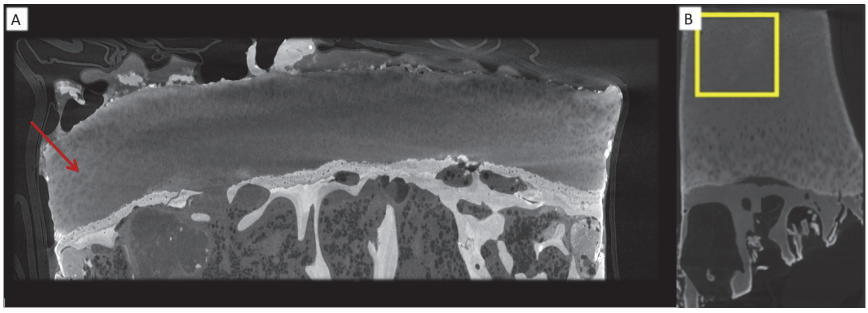


Figure 2.1 CECT of cartilage samples with POM staining. **A** Typical Hf-WD POM-based CECT longitudinal section of an osteochondral sample of a human femoral head, clearly showing the individual chondrocyte lacunae within the articular cartilage layer, as indicated by the red arrow. **B** CECT longitudinal section of an osteochondral sample stained with PTA (Image from Nieminen H.J. *et al.*, reference [78], reused under Creative Commons license CC BY-NC-ND 4.0).

2.5 Contrast-enhanced microCT for the bone marrow compartment

Bone organs are not only composed of mineralized tissues, but they also contain non-mineralized, soft tissues like bone marrow adipose tissue and vasculature. Thanks to the reaction of OsO_4 with olefinic sites in unsaturated lipids, Scheller *et al.* reported the use of this CESA for microCT imaging of the bone marrow adipose tissue (BMAT) in long bones of mice.[87, 88, 99] Using the reconstructed 3D images, they could quantify region-specific adiposity, which revealed the regulated and constitutive BMAT formation. Moreover, individual adipocytes were visible and diameters could be calculated. They also unveiled the importance of BMAT in bone remodeling. Notwithstanding

the widespread use of OsO_4 as a staining dye for unsaturated lipids, it is highly toxic and has a limited tissue penetration capability.[16] Additionally, studying correlation between BMAT distribution and calcified bone architecture requires a two-step scanning protocol: before and after bone decalcification.

A recent study within our group reported the simultaneous visualization of mineralized and soft structures within bones utilizing Hf-WD POM as CESA.[22] Thanks to the combination of the hydrophobic behavior of adipocytes and the binding of Hf-WD POM to the bone marrow tissue, Kerckhofs *et al.* were able to visualize the bone marrow adipocytes at the single cell level, using high resolution microCT scanning. This not only allowed to quantify the volume fraction of BMAT within the bone, but it also enabled the quantification of the adipocyte number/density and diameter. Additionally, the vascular network could be visualized and discriminated from the other tissues, allowing full 3D blood vessel network assessment (*i.e.* branching analysis and spatial distribution). Recently, monolacunary Wells-Dawson POM (Mono-WD POM) was reported to result in the same contrast enhancement and tissue penetration for murine bone marrow CECT imaging as Hf-WD POM.[83] Since WD-POM based CECT provides additional data to standard histomorphometry, with more spatial information, it could offer novel insights in the complex mechanisms of normal bone development and bone pathologies.

2.6 Contrast-enhanced microCT for muscle tissue

A substantial amount of CECT studies have reported the 3D visualization and structural assessment (muscle volume, fiber orientation and thickness, etc.) of muscle tissue. Based on this type of assessment, CECT not only allowed to better understand muscle function and development, but also to evaluate structural changes due to diseases. Similarly to magnetic resonance imaging, CECT of muscles could serve as input for computational modelling,[100, 101] which could be valuable as complementary tool or validation for *in situ* loading studies, where displacements can be experimentally quantified to reverse engineer stress distributions.[100] Furthermore, a sufficiently high spatial image resolution should provide the feasibility of visualization, quantification and modelling of individual muscle fibers.

For muscle tissue, Lugol's iodine (I_2KI), PMA and PTA are the most frequently reported CESAs.[17, 21, 84-86] Although these CESAs provide very good staining of

this type of tissues (and collagenous soft tissues in general), several studies reported shrinkage of the samples induced.[89, 102, 103] Tissue shrinkage is mainly caused by an acidic and/or hypertonic staining solution. Recently, a staining protocol using a buffered solution of Lugol's iodine has been reported, which shows reduced shrinkage artifacts in case of stained human fetuses.[4] This observation has led the authors to conclude that the pH rather than the osmolality of the solution is the key factor in tissue shrinkage. Shrinkage of the samples is a crucial effect that needs to be avoided or minimized when using CECT on soft tissues, as it changes the tissue morphology and integrity significantly, eliminating correct structural analysis and CECT image-based modelling. Consequently, analysis of the CECT data could be biased. Additionally, shrinkage damages the samples and the complementarity of CECT to other biochemical assays can thus be hampered.

2.7 Contrast-enhanced microCT for tendons and ligaments

In the musculoskeletal system, tendons and ligaments play an important role in motion and stability. They are mostly composed of collagen type I and have a highly fibrous structure. Several studies reported the use of iodine based CESAs (I_2KI, iomeprol) or PTA for the 3D visualization of these collagenous tissues.[21, 89, 90, 92] Rossetti *et al.* showed a proper example of using CECT as a complementary 3D imaging tool to micromechanical, compositional and proteomic methods in order to investigate the physiological functions of the bone-tendon insertion.[92] Shearer *et al.* and Balint *et al.* highlighted that I_2KI staining allows 3D imaging of ligaments and tendons, but they did not succeed in obtaining sufficient contrast for the individual fascicles as only the edge were visible on the images. Moreover, this CESA invoked observable tissue deformation and shrinkage.[89, 91] Sartori *et al.* have shown that PTA is able to reveal the individual fibers of the tendon, provided a sufficiently high spatial image and contrast resolution.[90] By microCT scanning a demineralized PTA stained Achilles tendon enthesis, they were able to visualize the collagen fiber bundles in the tendon down to a diameter of 3 µm. Consequently, they were able to not only visualize the tendon insertion point, but they also succeeded in making a structural quantification of the fiber thickness distribution and volume. Again, a known limitation of PTA is its acidic nature, inducing tissue shrinkage upon staining. When quantifying the structural parameters of the collagenous fibers in tendon or ligament tissue, this shrinkage will induce a significant bias. Additionally, in case the biomechanical properties of these

fibrous tissues were to be assessed by functional *in situ* testing (*e.g. in situ* loading of tendons within the microCT device, referred to as 4D microCT), the destructive character of these CESAs would be an important limitation. All things considered, there is still a pending need for a proper non-destructive CESA for CECT assessment of fibrous tissues, like tendons and ligaments.

2.8 Remaining challenges

Despite the substantial amount of advances in the field of CECT imaging for virtual 3D anatomical pathology and structural quantification of different biological tissues, some key challenges still remain to be overcome. One of the main limitations in the field is related to the tradeoff between sample size and voxel size. The smaller the desired voxel size generally implies adopting a smaller sample size due to a smaller field of view on the detector of a microCT device. This limitation can hamper the visualization of individual cells within an entire tissue. Using OsO_4, an adipocyte-specific CESA, Scheller *et al.* were able to image overall adiposity within murine long bones, but they could not perform single cell analysis due to the limited spatial image resolution.[22, 87] In order to visualize and analyze individual adipocytes, Kerckhofs *et al*. focused on the analysis of the metaphysis of the bones only, which allowed to increase the spatial image resolution.[22] The same applies for the collagen fibers in tendons or ligaments; only with sufficiently high spatial image resolution, these feature could be visualized.[90] This shows the need of not only a suitable CESA for good contrast, but also of sufficiently high spatial image resolution.

Another challenge in the field is related to the *ex vivo* CECT imaging and microstructural analysis of vascular networks. Once harvested, the vascularized networks within a sample are mostly in contact with air causing possible leakage of the injected CESA. Hence, the use of perfusion CESAs, as for *in vivo* microCT, is challenging. Additionally, casting techniques have shown their potential for visualizing blood vessels and measuring their volume.[104-106] Even though large vessels could be easily imaged, these techniques suffer from the inherently low blood flow in capillaries rendering them invisible for microCT. Staining vasculature by passive diffusion of CESAs has also been reported, though less common. A more rigorous review of the literature on *ex vivo* CECT of vasculature can be found in reference [107].

Finally, examples of targeted imaging using cell-, protein-specific CESAs are reported in literature, which mostly focus on *in vivo* imaging. Although

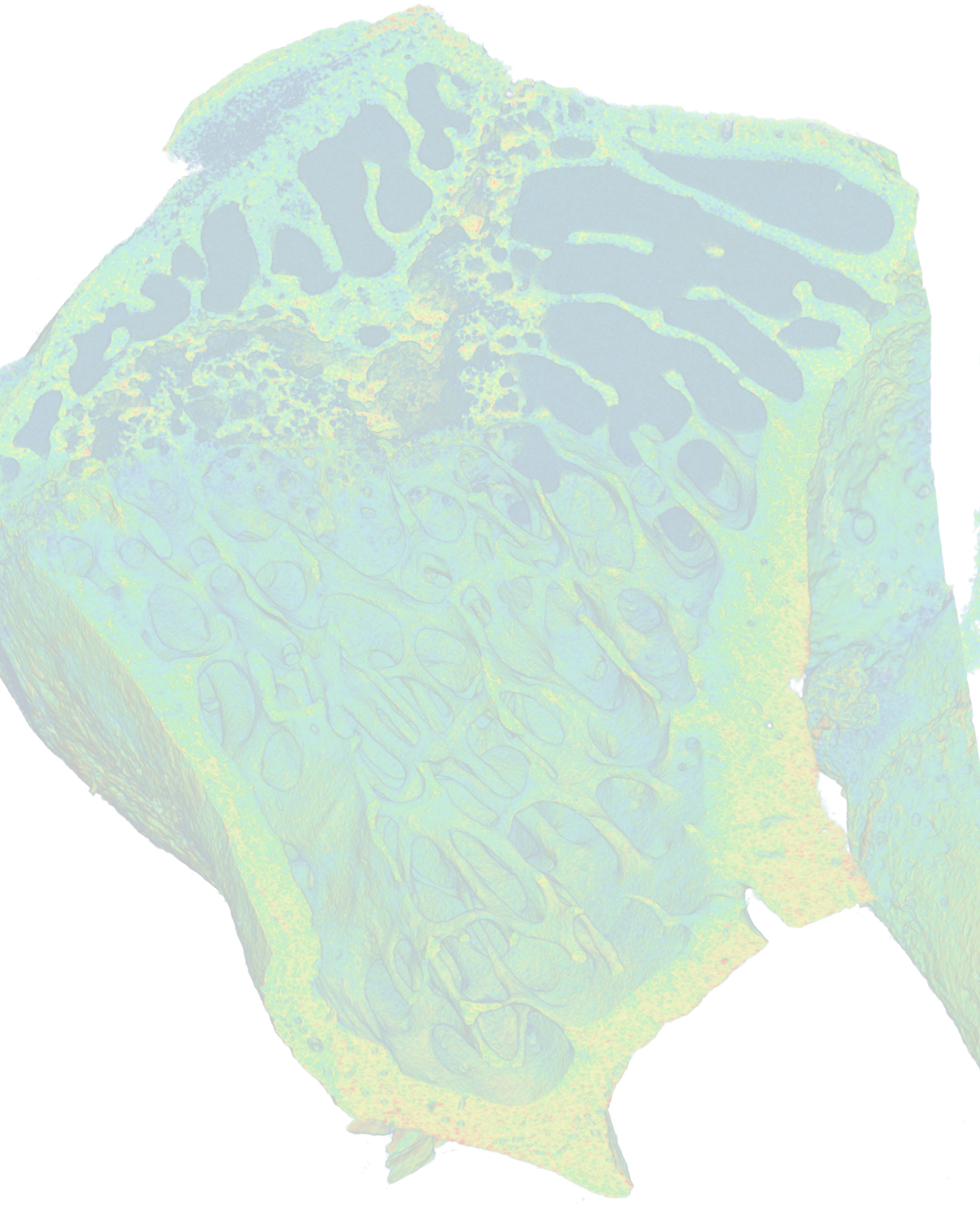
advances have been reported in the last decade, clinical translation is hampered due to challenges related to the required high CA concentration, retention time, unspecific bio distribution and toxicity. Literature regarding protein-specific CESAs for *ex vivo* microCT is scarce and underdeveloped. In general, two major approaches for *ex vivo* targeted imaging are reported. The first approach is based on enzyme metallography, which is an immunodetection staining method using labelled antibodies.[108] The second approach uses metal nanoparticles with surface modifications for targeting purposes. [109, 110] For a brief discussion on targeted *ex vivo* X-ray imaging, the reader is referred to the introduction of chapter 3 (Section 3.1). 3D high-resolution targeted CECT can be highly valuable as it could reveal relevant information about the spatial distribution of specific proteins within heterogeneous tissues.

2.9 Conclusions

Histologists have been working on stains for microscopy for more than 400 years since Anton Van Leeuwenhoek stained protozoans using saffron extract in the 1600's.[111] Regardless being a young field, CECT has a high potential within biomedical research because of its minimally destructive character and its possibility to produce 3D datasets. There is a strong need for this type of 3D imaging methodology for structural analysis of biological tissues, especially in the case of heterogeneous tissues. Nevertheless, it still requires further improvement and optimization of staining protocols as well as validation of currently used CESAs. In this chapter, a non-exhaustive review of the current state-of-the art in the field of CECT imaging was given, with a focus on musculoskeletal tissues. While CECT imaging of other tissue types have been reviewed (brain and nervous tissues,[112] cardiovascular system,[107] etc.), we focused here on musculoskeletal tissues, as for these tissues most of the progress in the field has been made.

Although there has been quite some progress in the applicability of CECT for the quantitative 3D assessment of biological tissues (*i.e.* quantitative virtual 3D anatomical pathology), the global acceptance of this innovative technology within the biomedical field is still challenging. There are several limitations that need to be overcome to adopt quantitative virtual 3D anatomical pathology based on CECT as a standardly used technique, complementary to histological assessment based on optical microscopy. The destructiveness of the CESAs and scanning protocols *(1)* should be reduced as much as possible to ensure that the tissue integrity is not harmed, and hence, to avoid biased

structural analysis. Moreover, the technique should be complementary to other assays (*e.g.* optical microscopy) and functional testing such as 4D microCT. The specificity of the CESAs *(2)* and their binding mechanisms to the tissues should be more deeply understood to allow appropriate interpretation of the results, and novel CESAs should be developed that have cell/protein-specific binding capacities. Standard operating procedures *(3)* for sample preparation, staining and acquisition should be developed to increase the comparability, the ability to share and the reproducibility of the results. Indeed, optimization of the staining parameters such as concentration and staining time *(4)*, for every tissue type is of substantial importance to maximize the CESA tissue penetration, and thus staining, and minimize potential tissue shrinkage. Overcoming these limitations will be crucial to move the field of CECT imaging one step further towards a standardly accepted tool for quantitative virtual 3D anatomical pathology.



CHAPTER 3

Polyoxometalates as CESAs

Exploring polyoxometalates for microCT imaging of biological tissues

The content of this chapter is based on:

Exploring Polyoxometalates as Non-Destructive Staining Agents for Contrast-Enhanced Microfocus Computed Tomography of Biological Tissues

De Bournonville, S.; Vangrunderbeeck, S.; Ly, H. G. T.; Geeroms, C.; De Borggraeve, W. M.; Parac-Vogt, T. N.; Kerckhofs, G. *Acta Biomater.* **2020**, *105*, 253-262. doi: 10.1016/j.actbio.2020.01.038

and was reproduced with permission from Elsevier.
Copyright © 2020

Credit authorship contribution statement

Sébastien de Bournonville: Conceptualization, Data curation, Formal analysis, Funding acquisition, Writing - original draft, Writing - review & editing. **Sarah Vangrunderbeeck:** Conceptualization, Investigation, Data curation, Formal analysis, Writing - original draft, Writing - review & editing. **Hong Giang T. Ly:** Investigation, Writing - original draft, Writing - review & editing. **Carla Geeroms:** Investigation, Writing - review & editing. **Wim M. De Borggraeve:** Data curation, Formal analysis, Supervision, Funding acquisition, Writing - review & editing. **Tatjana N. Parac-Vogt:** Data curation, Formal analysis, Supervision, Writing - review & editing. **Greet Kerckhofs:** Conceptualization, Data curation, Formal analysis, Supervision, Funding acquisition, Writing - original draft, Writing - review & editing.

3.1 Introduction

A considerable number of the reported CESAs are destructive towards the tissue sample or hazardous to work with, preventing subsequent (immuno)-histological assessment.[20, 87, 88, 102, 103, 113] Moreover, several of these have been discovered by trial-and-error screening of commercially available chemical compounds containing an X-ray opaque element, consequently lacking knowledge about the exact binding mechanism.[17, 21]

Polyoxometalates (POMs) represent a group of clusters consisting of early transition metals (typically V, Mo, W) in their highest oxidation state that are bridged by oxide anions. Besides the Keggin structure, the Wells-Dawson POM is among the best studied phosphotungstate POM. Under mildly alkaline conditions, a controlled removal of one tungsten-oxygen unit from the Wells-Dawson POM structure can be achieved, resulting in a lacunary isomer, which can be substituted with various metals (*e.g.* hafnium, zirconium).

In a previous study, we have tested and validated the hafnium-substituted Wells-Dawson POM $[Hf(\alpha_2\text{-}P_2W_{17}O_{61})_2]^{16-}$ (Hf-WD POM) as a new X-ray attenuating CESA for the visualization of soft skeletal tissues.[22] Hf-WD POM was compared with phosphotungstic acid (PTA), which has often been reported for 3D visualization of multiple soft biological tissues using CECT.[16, 21, 77] Because of its strongly acidic nature, PTA affects the tissue integrity.[102, 114, 115] Hf-WD POM-based CECT, however, allows simultaneous 3D multi-tissue visualization and characterization in murine long bones of the mineralized bone, bone marrow vasculature and adipose tissue, while precluding tissue shrinkage. Indeed, phosphate-buffered saline (PBS) solutions of Hf-WD POM are characterized by a nearly neutral pH. Alterations of the tissue integrity of the stained samples were not observed, enabling subsequent (immuno)-histological processing and staining, as well as assessment of the spatial distribution of the different tissues and their interrelationship.[22]

3.2 Objectives

The application Hf-WD POM as a CESA, characterized by minimal tissue destruction upon staining, is a valuable approach to visualize murine bone marrow in 3D. For this reason, we were curious to explore related POM species as CESAs.

The multistep synthesis of Hf-WD POM involves different intermediates. The latter, in turn, could be interesting CESA candidates since they are more cost-effective, more straightforward and less time-consuming to synthesize. Our aim is here to investigate the potential of different WD POMs for staining soft tissues. These compounds should be minimally destructive to the tissue and stable under physiological conditions, while providing X-ray attenuation to the constituents to enable 3D visualization by microCT. Ideally, we would like to differentiate between tissue constituents based on differences in X-ray attenuation.

In this chapter, four different WD POM species were evaluated as CESAs using murine long bones and kidneys. The tissue penetration was evaluated based on comparison of CECT images of kidneys. Phosphorus nuclear magnetic resonance (^{31}P NMR) spectroscopy was used to study the effect of the buffer solution, staining time, and the influence of the long bones or kidneys on the stability of the POMs.

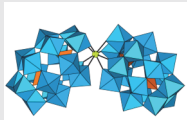
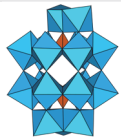
3.3 Properties of POMs

The structures of the POMs that were evaluated as CESAs are shown in Table 3.1.The table also summarizes the pH values measured of the different POMs upon dissolution of 35.0 mg/mL in PBS. The pH of all the POM solutions showed to be much closer to physiological pH (or were significantly less acidic) than the pH of the PTA solution. The PBS solutions of Parent-WD POM and Hf-WD POM were slightly acidic, while the Tri-WD POM solution was slightly basic.

3.4 CECT imaging

To assess the staining potential of the different POMs, we determined the contrast difference between different types of tissue in murine long bones after 48 hours of staining by immersion, as well as the extent of penetration within murine kidneys at different staining times (4 days and 10 days). Representative CECT images of the long bones and kidneys are given in Figure 3.1, while Figure 3.2 presents the quantification of the contrast difference between the features in the cortical bone and bone marrow compartment of the long bone, and the extent of penetration through the kidneys. Samples in

Table 3.1 Chemical structure, charge and pH of the POM species dissolved in PBS (35.0 mg/mL).

		Hf-WD POM	Parent-WD POM	Mono-WD POM	Tri-WD POM	PTA
Structure						
Charge	POM	-20	-6	-10	-12	-3
	Metal	+4	0	0	0	0
	Net	-16	-6	-10	-12	-3
pH		6.73	6.42	7.15	8.18	1.82

PBS were used as a negative control for contrast enhancement (but not for penetration). Samples stained with PTA were used as a positive control, since the potential of this CESA for soft tissue staining has been shown in the literature.[17, 102] Low contrast differences between cortical bone and bone marrow tissue indicate good staining of the bone marrow tissue by the CESA (Figure 3.2A). High contrast differences between bone marrow tissue and adipocytes indicate good staining of the bone marrow tissue (since the POMs are repelled by the adipocytes) (Figure 3.2B).[22] Low contrast differences between the edge and the middle of the kidneys (Figure 3.2C) indicate good penetration of the CESA through the tissue and, therefore a more homogeneous staining.

A clear contrast enhancement of both bone marrow and kidney tissue was observed for most of the CESAs compared to the unstained reference material (PBS). Tri-WD POM showed the worst contrast enhancement, as qualitatively confirmed on the reconstructed CECT images (Figure 3.1), and quantitatively determined in Figure 3.2A and Figure 3.2B. Distinct structures within the bone marrow of the long bone (bone marrow tissue or adipocytes) or within the

kidney tissue (*i.e.* blood vessels, porosities, *etc.*) were difficult to identify. On the contrary, long bones stained with Parent-WD POM, Mono-WD POM, and Hf-WD POM performed similarly to PTA in terms of contrast enhancement (Figure 3.2A and Figure 3.2B). Reconstructed CECT images of the long bones stained with these CESAs provided the differentiation of distinct skeletal tissues: mineralized bone, bone marrow adipose tissue and vasculature. Similarly, substructures of kidneys could be revealed, such as: renal pelvis, papilla, inner and outer medulla and cortex. Related to the diffusion dynamics, Parent-WD POM behaved similarly to PTA, which is known to have a relatively slow penetration through soft tissues (Figure 3.1 and Figure 3.2C-D).[17] These, both non-lacunary, POMs failed to penetrate the inside the core of the kidneys. In contrast, Mono-WD POM and Hf-WD POM showed a faster penetration within the tissue. Although it seems counterintuitive, the

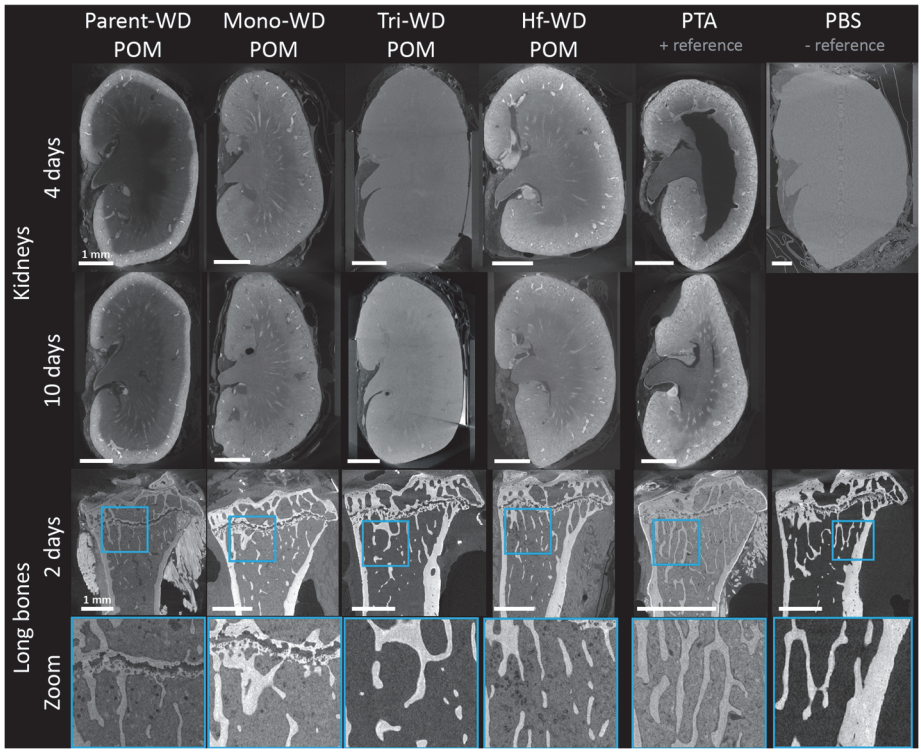


Figure 3.1 CECT images of murine tibiae and kidneys stained with the different POMs. Typical coronal CECT slices of kidneys (rows 1 and 2) and tibiae (row 3 and 4) stained with different POM species (columns: Parent WD POM, Mono-WD POM, Tri-WD POM, Hf-WD POM and PTA (positive control)) and PBS (negative control) for different staining times. Scale bar = 1 mm.

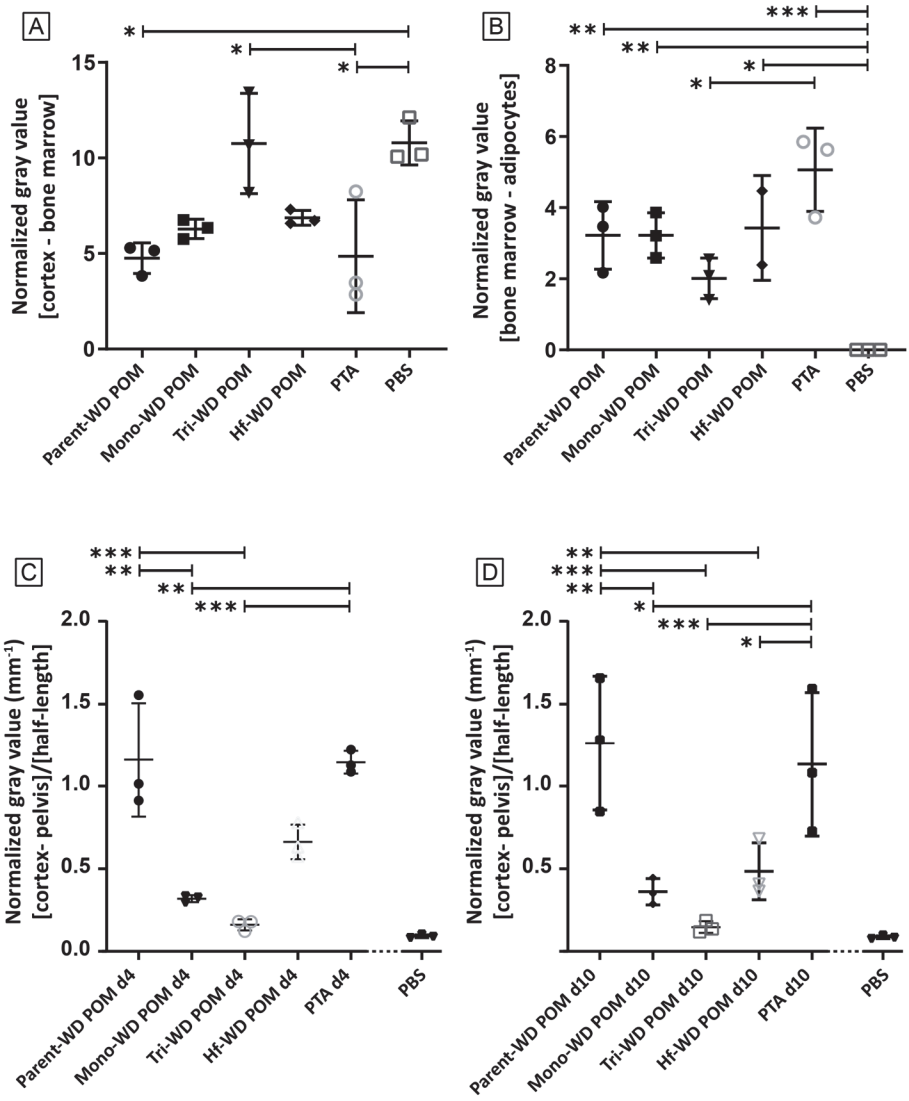


Figure 3.2 Quantitative assessment of the contrast difference in the CECT images of tibiae and kidneys stained with different POMs for different staining times; values are given in normalized gray values. **A** Quantification of the contrast difference between cortical bone and bone marrow tissue for all tibiae. **B** Quantification of the contrast difference between bone marrow tissue and adipocytes for all tibiae. **C-D** Quantification of the contrast difference between the renal cortex and the renal pelvis (middle) of the kidneys that were stained for 4 days (C) and 10 days (D), divided by half the length of the kidney, for all the kidneys; values are given in normalized gray values per millimeter.

obtained data suggest that the penetration rate improves if the POM structure contains a lacuna. Because of the small difference in gray value at the renal cortex and renal pelvis, Tri-WD POM seemed to show a very good diffusion (Figure 3.2C-D). However, the negative control PBS also shows a small difference. As noted above, Tri-WD POM was not able to increase the contrast of soft tissues (Figure 3.2A-B), which is reflected in about the same gray value at the renal pelvis and renal cortex. In addition, tissue shrinkage was only observed for PTA-stained samples, and this due to the acidic nature of PTA. Tissue shrinkage strongly affects tissue integrity and prevents structural and volumetric analyses.[102]

In general, excellent results, both in terms of contrast enhancement and tissue penetration, were achieved with Mono-WD POM and Hf-WD POM. Whereas tissues stained with Mono-WD POM and Hf-WD POM give rise to about the same degree of contrast enhancement, a lower solubility was observed in PBS for Mono-WD POM compared to Hf-WD POM. Therefore, we decided to further improve the solubility of Mono-WD POM in PBS. This is worthwhile since Mono-WD POM is an intermediate in the synthesis of Hf-WD POM, hence it is easier to prepare. The synthesis of Mono-WD-POM is more cost-efficient and less time-consuming, making it the preferred CESA. Addition of LiCl to the staining solution increased the solubility of Mono-WD POM because of the presence of the added Li^+ ions.[116, 117] Since Mono-WD POM was synthesized as a potassium salt, the effect of the presence of Li^+ ions was studied for an increasing molar ratio of lithium to potassium, using PBS as the solvent. In the presence of 35.0 mg/mL Mono-WD POM, three conditions were selected based on a molar ratio of lithium to potassium of 1:1, 1:3 and 1:13, corresponding to a LiCl concentration of 3.0 mg/mL, 9.1 mg/mL and 39.5 mg/mL respectively. A sample immersed in a PBS solution solely containing 39.5 mg/mL LiCl was used as a negative control. Representative CECT images of the long bones are given in Figure 3.3A-D, while Figure 3.3E-F present the quantification of the contrast difference between the features in the cortical bone and bone marrow compartment.

The CECT images of the long bones stained with Mono-WD POM in Figure 3.3A-D appear to indicate an increased contrast of the bone marrow with increasing LiCl concentrations, which was quantitatively validated in Figure 3.3E-F. Indeed, the lower contrast difference between cortical bone and bone marrow for the sample stained with Mono-WD POM in the presence of 39.5 mg/mL LiCl, compared to the samples stained with a lower LiCl concentration,

confirms the improved bone marrow staining. Likewise, the improved staining is also reflected in the higher contrast difference between bone marrow and adipocytes for increased LiCl concentrations.

Despite the increased bone marrow contrast, shrinkage was observed as cavities in the bone marrow tissue for samples stained with Mono-WD POM and high LiCl concentrations (Figure 3.3A, Figure 3.3C and Figure 3.3D). The observed tissue shrinkage is caused by dehydration of the soft tissue, which we hypothesize is due to the hypertonicity of these staining solutions.[103, 118, 119] PBS buffer, which is isotonic, was used to prepare the staining solutions. Addition of Mono-WD POM and LiCl increases the ionic strength, resulting in hypertonic staining solutions (> 312 mOsm/L), justified by the calculated osmolarities in Table 3.2.[120] The degree of tissue shrinkage and the correlated harm of tissue integrity is an important consideration for morphometric and volumetric analyses. Therefore, we selected Mono-WD POM with 3.0 mg/mL LiCl dissolved in PBS as the preferred condition for long bone staining as the contrast of bone marrow was increased without the observation of substantial tissue shrinkage. The development of isotonic staining solutions, *e.g.* through replacement of PBS by a solution of lower ionic strength, will be the focus of future studies.

Table 3.2 pH and calculated osmolarity of Mono-WD POM solutions containing LiCl, dissolved in PBS.

	3.0 mg/mL LiCl + MonoWD-POM	9.1 mg/mL LiCl + MonoWD-POM	39.5 mg/mL LiCl + MonoWD-POM
pH	6.78	6.73	6.37
calculated osmolarity in PBS (mOsm/L)	553	841	2275

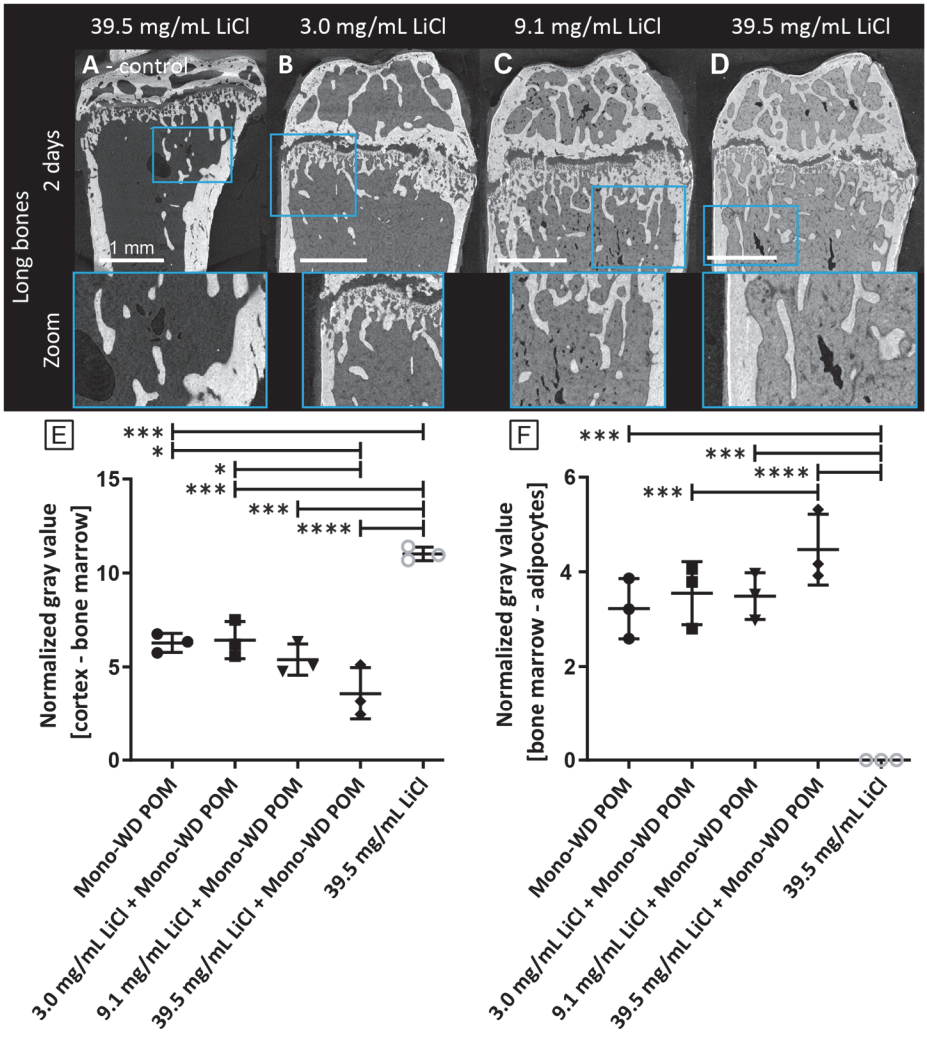


Figure 3.3 CECT images and quantitative assessment of murine tibia and femurs stained with Mono-WD POM dissolved in PBS in the presence of LiCl. **A** CECT image of a murine tibia, displayed in the coronal view, submerged in a solution of 39.5 mg/mL LiCl for 48 hours in PBS. Control sample, absence of Mono-WD POM. **B-D** CECT images of murine femurs, displayed in the coronal view, stained for 48 hours with Mono-WD POM (35.0 mg/mL) in PBS in the presence of variable concentrations of LiCl. Scale bar = 1 mm. **E** Quantification of the contrast difference between cortical bone and bone marrow tissue for all the long bones; values are given in normalized gray values. **F** Quantification of the contrast difference between bone marrow tissue and adipocytes for all the long bones; values are given in normalized gray values.

3.5 Stability and speciation of POMs

The structural integrity of POMs in aqueous solution is highly dependent on pH, temperature, time and concentration.[121-124] Therefore, apart from their staining potential, their stability under the experimental conditions used for the staining experiments was also investigated. Due to the presence of phosphorus atoms in POMs, ^{31}P NMR spectroscopy is a powerful technique for their characterization in solution.

The ^{31}P NMR spectrum of PTA dissolved in PBS showed a singlet at -14.98 ppm (Figure 3.4A-B) at low pH values. Indeed, after dissolution of PTA in PBS, the pH of the solution reached 1.82 (Table 3.1), and resulted in a partial decomposition of PTA as indicated by the additional singlets at -12.27 ppm, -12.75 ppm and -12.86 ppm.[125, 126] After staining of a kidney, the ^{31}P NMR spectrum of the staining solution showed disappearance of the singlet at -14.98 ppm and appearance of a broad singlet at -10.73 ppm (Figure 3.4C-D), which could be attributed to the base decomposition of PTA to monolacunary α-Keggin type POM.[122, 127] After long bone staining only a singlet at -11.52 ppm was detected in the ^{31}P NMR spectrum of the staining solution (Figure 3.4E), which could be most likely attributed to monolacunary α-Keggin type POM that is coordinated to Ca^{2+} ions in the mineralized bone (*vide infra*).

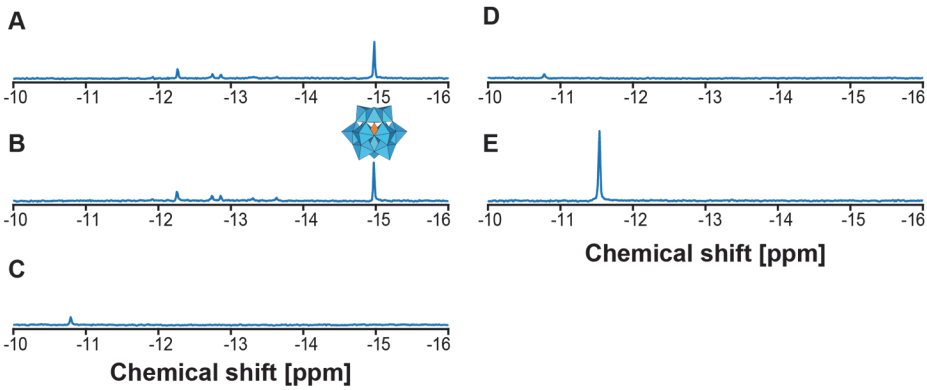


Figure 3.4 ^{31}P NMR spectra of PTA in the absence and presence of a kidney or tibia in PBS for different staining times. Spectrum of a PTA solution in PBS **A** after dissolution. **B** after 17 days in PBS. **C** after 4 days of staining a kidney. **D** after 10 days of staining a kidney. **E** after 2 days of staining a tibia.

Mono-WD POM (showing singlets at -6.97 ppm and -14.14 ppm in the ^{31}P NMR spectrum, $\Delta\delta$ = 7.17 ppm) was stable in PBS both in the absence and presence of a kidney or a long bone (Figure 3.5A-E).[128] After 4 days of staining a kidney and 2 days of staining a long bone, the amount of Mono-WD POM in the staining solution decreased in both cases (Figure 3.5C and Figure 3.5E). In the presence of the bone, the difference in chemical shift ($\Delta\delta$) between two phosphorus atoms was reduced from 7.17 ppm to 6.54 ppm (Figure 3.5E). The shift of the ^{31}P NMR singlets of Mono-WD POM after long bone staining could be attributed to the presence of Ca^{2+} ions in the mineralized bone. We hypothesized that Ca^{2+} ions in the mineralized bone interact with the open lacunary site in the POM, thereby influencing the chemical shift of the ^{31}P NMR singlets.[129] To confirm this, ^{31}P NMR spectra of 1 mL-samples containing 35.0 mg Mono-WD POM and 0.2 M $Ca(NO_3)_2$ or $CaCl_2$ were recorded (Figure 3.5F-G). As expected, when Ca^{2+} ions were added to the staining solution the chemical shift of the ^{31}P NMR singlets of Mono-WD POM changed in the same way as in Figure 3.5E. This change in chemical shift indicates that Ca^{2+} ions

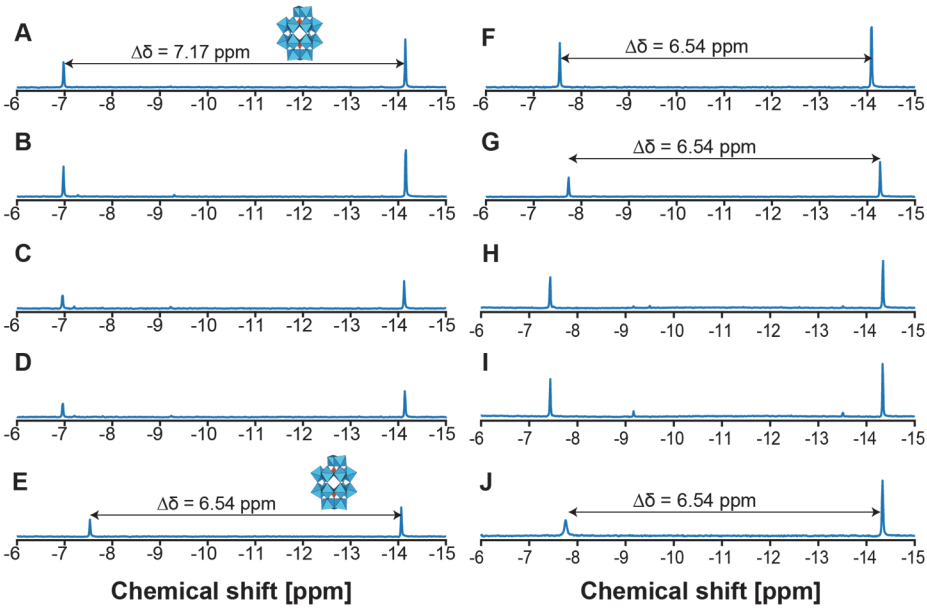


Figure 3.5 ^{31}P NMR spectra of Mono-WD POM in PBS, before and after staining of kidney or bone and in the presence of 3.0 mg/mL LiCl. Spectrum of a Mono-WD POM solution in PBS **A** after dissolution. **B** after 17 days. **C** after 4 days of staining a kidney. **D** after 10 days of staining a kidney. **E** after 2 days of staining a tibia. **F** in the presence of $Ca(NO_3)_2$ and **G** $CaCl_2$. Spectrum of a Mono-WD POM with 3.0 mg/mL LiCl solution in PBS **H** after dissolution. **I** after 17 days. **J** after 2 days of staining a femur.

indeed interact with Mono-WD POM, most likely via coordination to its open lacunary site.

Mono-WD POM in the presence of 3.0 mg/mL LiCl was stable in PBS, exhibiting singlets at -7.43 ppm and -14.34 ppm in the ^{31}P NMR spectrum (Δδ = 6.91 ppm, Figure 3.5H-I). The decrease in both the chemical shift of the ^{31}P singlets and the distance between these singlets in the presence of LiCl, compared to the solution without LiCl, could be attributed to the increased ionic strength of the solution.[130] After long bone staining, the ^{31}P NMR spectrum of the staining solution showed a further reduction of the difference in chemical shift between the two characteristic singlets to 6.54 ppm, which is the same as in Figure 3.5E-G (Figure 3.5J). Again, the decrease in the difference in chemical shift could be attributed to the coordination of Mono-WD POM with Ca^{2+} ions of the mineralized bone.

Dissolved in PBS, Hf-WD POM showed singlets at -9.40 ppm and -14.02 ppm in the ^{31}P NMR spectrum (Δδ = 4.62 ppm, Figure 3.6A-B).[128] In addition, singlets at -7.17 ppm and -14.33 ppm (Δδ = 7.17 ppm) were observed, which could be attributed to the dissociation of the 1:2 Hf-WD POM into Mono-WD POM and 1:1 Hf-WD POM in PBS. After 4 days of kidney staining, the integrated values of the singlets corresponding to 1:2 Hf-WD POM decreased (Figure 3.6C), and decreased even more when staining was prolonged for six additional days,

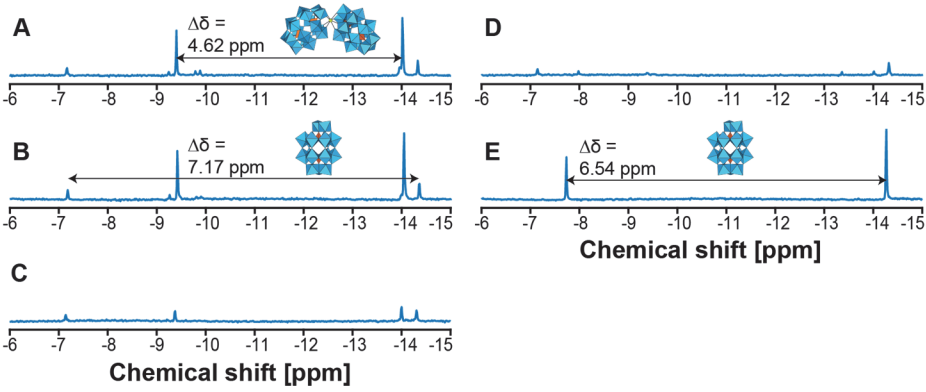


Figure 3.6 ^{31}P NMR spectra of Hf-WD POM in the absence and presence of kidney or a tibia in PBS. Spectrum of an Hf-WD POM solution in PBS **A** after dissolution. **B** after 17 days in PBS. **C** after 4 days of staining a kidney. **D** after 10 days of staining a kidney. **E** after 2 days of staining a tibia.

albeit only slightly (Figure 3.6D). The singlets at -7.17 ppm and -14.33 ppm were still observed in the staining solution after kidney staining. After long bone staining, the ^{31}P NMR spectrum of the staining solution solely showed singlets at -7.73 ppm and -14.27 ppm (Δδ = 6.54 ppm), which could be ascribed to the presence of Mono-WD POM (Figure 3.6E). Similarly to other cases discussed above, the chemical shift change due to the presence of Ca^{2+} ions in mineralized bone was observed.

The ^{31}P NMR spectrum of Parent-WD POM dissolved in PBS showed singlets at -12.96 (α-Parent-WD POM), -11.46 ppm (β-Parent-WD POM) and -12.23 ppm (β-Parent-WD POM).[128] Moreover, singlets at -7.17 ppm and -14.34 ppm (Δδ = 7.17 ppm) were also detected, which could be explained by the conversion of Parent-WD POM into Mono-WD POM (Figure 3.7A-B). The ^{31}P NMR spectrum of the staining solution after kidney staining only showed singlets that are most likely originating from Mono-WD POM (Figure 3.7C-D); signals corresponding to Parent-WD POM disappeared. After long bone staining, the singlets corresponding to Parent-WD POM were not observed in the ^{31}P NMR spectrum of the staining solution. Nonetheless, singlets at -7.74 ppm and -14.28 ppm (Δδ = 6.54 ppm) appeared in the ^{31}P NMR spectrum, which probably results from the presence of Ca^{2+}-coordinated Mono-WD POM (Figure 3.7E).

Finally, PBS solutions containing Tri-WD POM were analyzed by ^{13}P NMR. Characteristic resonance signals of Tri-WD POM were not observed, indicating that Tri-WD POM is not stable in PBS (data not shown). Since contrast enhancement was observed neither for kidney, nor for long bone, Tri-WD POM was not considered as a suitable CESA.

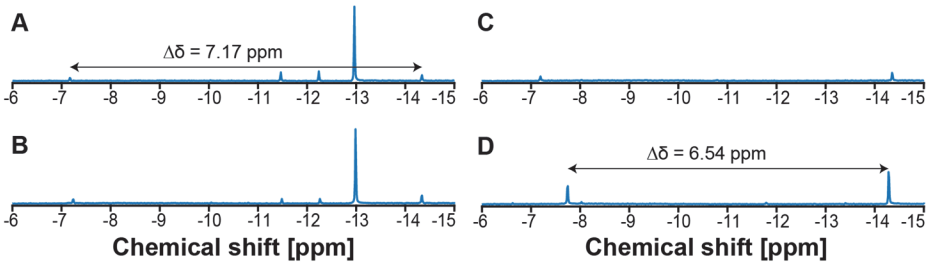


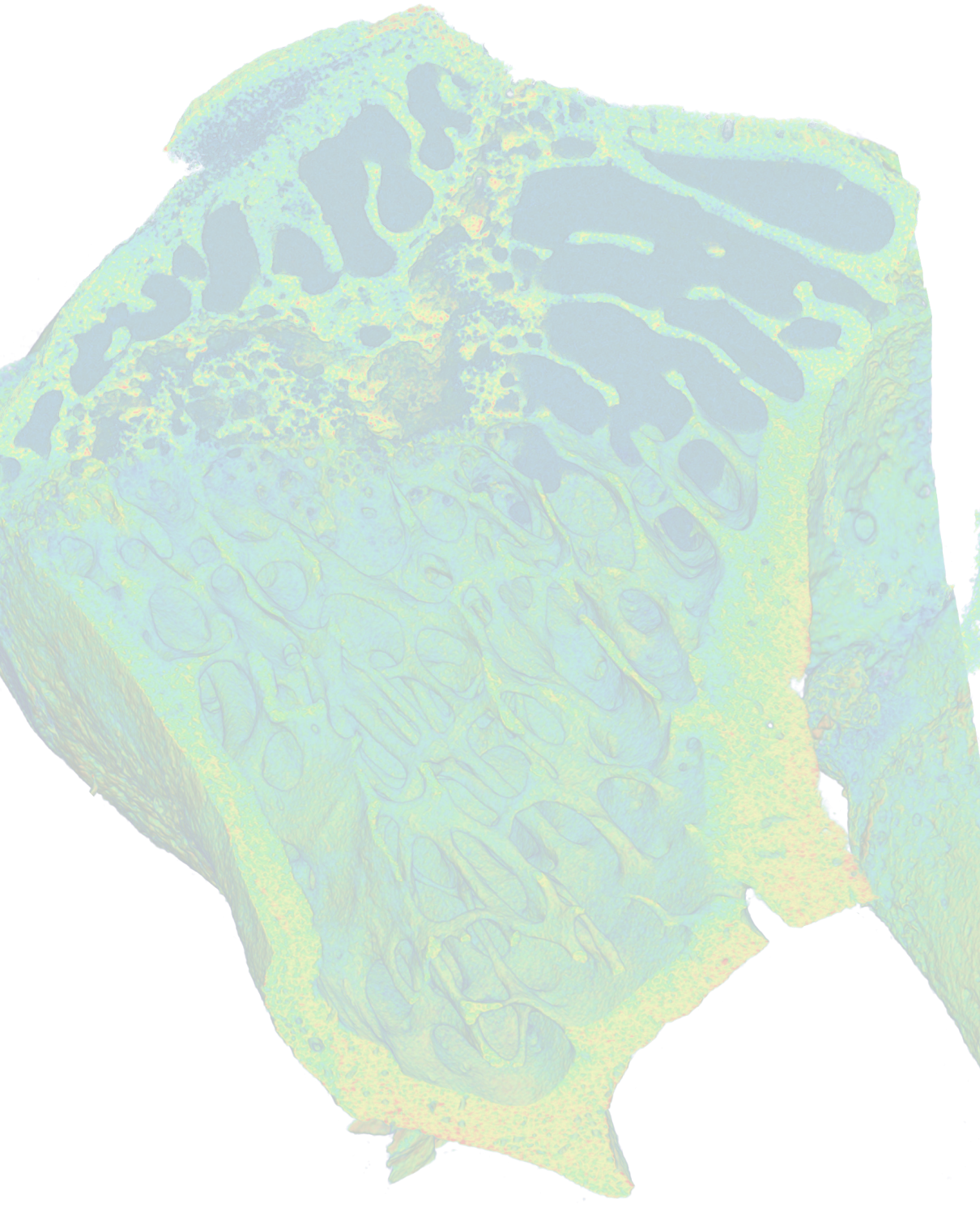
Figure 3.7 ^{31}P NMR spectra of Parent-WD POM in the absence and presence of kidney or tibia in PBS. Spectrum of a Parent-WD POM solution in PBS **A** after dissolution. **B** after 17 days in PBS. **C** after 4 days of staining a kidney. **D** after 10 days of staining a kidney. **E** after 2 days of staining a tibia.

In general, the ^{31}P NMR spectra of the different WD POMs indicate Mono-WD POM to be the most stable species in PBS. Indeed, PBS solutions of Parent-WD POM and Hf-WD POM were shown to partially convert and dissociate, respectively, into Mono-WD POM. The CECT images (Figure 3.1 and Figure 3.3) showed effective soft tissue contrast enhancement for these three WD species, while almost no contrast enhancement was observed for Tri-WD POM. Taken together the data obtained from the CECT images and ^{31}P NMR experiments, 35.0 mg/mL Mono-WD POM in combination with 3.0 mg/mL LiCl is concluded to be the most suitable CESA for imaging soft tissue as it is the most stable in PBS and shows high contrast enhancement.

3.6 Conclusion

In this work, four WD POM species were screened for their potential as CESAs for soft tissue visualization using CECT. The different WD POMs were compared to PTA, which is both a commonly used CESA and dye in 2D histological assessment. The POMs were dissolved in PBS at equal concentrations and subsequently used to stain murine long bones and kidneys for CECT imaging. Quantification of the contrast enhancement by POM staining indicated that Tri-WD POM was not a suitable CESA. ^{31}P NMR measurements of the staining solutions performed before and after staining revealed that: (1) calcium ions interact with lacunary POM structures and induce a shift in the ^{31}P NMR resonance signals, (2) Mono-WD POM is the most stable POM type in PBS since Parent-WD POM and Hf-WD POM convert and dissociate, respectively, to it. Finally, Mono-WD POM and Hf-WD POM species showed the best diffusion and overall staining of soft tissues. Therefore, we concluded that Mono-WD POM is the most suitable CESA of the screened POM species in terms of (1) contrast-enhancement, (2) penetration through the tissue, (3) non-destructiveness (physiological pH), (4) chemical stability, and (5) ease of synthesis, leading to a lower production cost in comparison with Hf-WD POM. This work was further strengthened by improving the staining properties of Mono-WD POM through addition of LiCl to the staining solution in order to increase its solubility. We conclude that Mono-WD POM (35.0 mg/mL) with 3.0 mg/mL LiCl, dissolved in PBS, results in high contrast enhancement of soft tissue without inducing substantial tissue shrinkage. Although improving the contrast, tissue shrinkage was observed for long bones that were stained with Mono-WD POM solutions containing a higher concentration of LiCl (> 3.0 mg/mL). Therefore, the development of isotonic staining solutions containing CESAs that match the pH levels of biological tissues will be the focus of future research.

CECT using Mono-WD POM with LiCl demonstrates the potential of virtual 3D histology of biological tissues, as it provides additional spatial information, compared to histological assessment by optical microscopy. Given the complexity of biological tissues, precise imaging and the additional 3D information could provide novel insights in tissue development and disease, which is valuable for both basic research and disease diagnosis.



CHAPTER 4

Cationic CESAs

Development of cationic iodinated CESAs for microCT imaging of articular cartilage

The content of this chapter is based on:

Manuscript in preparation, **2023**

Vangrunderbeeck, S.; Diepvens, R.; Balcaen, T.; Joenathan, A.; Kerckhofs, G.; Grinstaff, M.; De Borggraeve, W.M.

Credit authorship contribution statement

Sarah Vangrunderbeeck: Conceptualization, Investigation, Formal analysis, Data curation, Writing – original draft, Writing – Review & Editing, Visualization, Project administration. **Renée Diepvens**: Investigation, Formal analysis. **Tim Balcaen**: Formal analysis, Data Curation. **Anisha Joenathan**: Investigation. **Greet Kerckhofs:** Conceptualization, Methodology, Data Curation, Writing – Review & Editing, Funding acquisition, Resources, Supervision. **Wim De Borggraeve:** Conceptualization, Methodology, Data Curation, Writing – Review & Editing, Resources, Funding acquisition, Supervision. **Mark Grinstaff**: Conceptualization, Resources, Supervision.

4.1 Introduction

As mentioned in the general introduction (Section 2.5), cartilage is one of the most studied musculoskeletal tissue types in CECT. The increasing interest for the characterization of aggrecan and collagen distributions in the ECM of cartilage could be attributed to the ongoing search for methods to diagnose osteoarthritis at an early point in the disease progress. Since the disease cannot be cured, early detection is of key importance for treatment that focuses on the amelioration of the disease progression rather than on symptom relief.

4.1.1 Osteoarthritis

Osteoarthritis (OA) is one of the most common causes of disability in developed countries. Estimates suggest OA affects 7% of the global population, which corresponds to more than 500 million people worldwide, and is expected to exacerbate because of the ageing population and increasing obesity.[131] Costs associated with OA have been estimated to be $128 billion per year in the US alone.[132] OA was previously thought to be solely associated with the breakdown of articular cartilage (AC) due to mechanical loading. However, the perception about OA has changed thanks to a better fundamental knowledge and evidence-based care. Today, OA is considered a complex disorder that affects the whole joint including structural changes in the AC, ligaments, subchondral bone, synovium, capsule and periarticular muscles.[133]

Pain is the most common symptom of OA, followed by stiffness and swelling. In some cases, the disease causes joint disability and loss of function.[134] The disease is most prevalent in the knee joint, followed by the hand and the hip.[134] Depending on the affected joint, OA is associated with different mechanisms of pathology.[135] Generally speaking, OA arises from an imbalance between repair and destruction of joint tissue of which the wide range of underlying pathways are not yet completely understood. It is complex in pathogenesis which involves dysregulations in inflammatory, metabolic and mechanical factors.[136]

To date, OA is most commonly diagnosed clinically based on the late-stage symptoms such as pain. Plain radiographs are performed to evaluate structural changes (*e.g.* joint space narrowing) or to rule out other

pathologies, but are not required.[136, 137] Diagnosis based on symptoms is inherently problematic since they arise when the disease is already advanced and irreversible. At that point, clinicians are left with few treatment options. Therefore, early detection of OA is of key importance since no proven disease-modifying therapy exists yet. Despite the frequency of OA, its impact on the quality of life and the related societal costs, treatments are focused on reduction of modifiable risk factors and symptom relief. Total surgical joint replacement is recommended for patients with chronic pain and disability.

OA is most commonly linked to cartilage degradation, which increases over the course of the disease.[136] The concentration of glycosaminoglycans (GAGs) in the ECM matrix has been generally seen as a biomarker for cartilage health. Therefore, we will focus on the visualization of the GAG distribution in AC by *ex vivo* microCT in the following sections. To this end, a basic understanding of the anatomy of AC is given below.

4.1.2 Articular cartilage

Articular cartilage (AC) is the smooth, lubricating tissue layer that covers the ends of the bones in the joint. Its major role is facilitating the transmission of loads and helping to move the joint smoothly. AC is mainly composed of a dense ECM in which chondrocytes are distributed. Chondrocytes are responsible for the maintenance of the AC, including synthesis and destruction of the matrix components.[138] The regeneration of the AC matrix is hindered due to the avascular nature of this tissue. Hence, the uptake of nutrients mainly occurs via diffusion from the synovial fluid through the ECM.

The ECM principally consists of water, collagen and aggrecan (cartilage-specific proteoglycan core protein).[139] Collagen fibers are the most abundant macromolecules in the ECM, of which type II collagen is the most prominent.[140] These fibers determine the ultrastructure of AC and provide its tensile strength. Together with the aggrecan aggregates, they generally contribute to the retention of water in the ECM matrix.[141] Aggrecan aggregates consist of a central hyaluronan (hyaluronic acid backbone) with multiple aggrecan monomers noncovalently attached (Figure 4.1).[142] Each aggrecan monomer consists of a core protein with covalently attached glycosaminoglycan (GAG) chains, organized in a bottle-brush structure, that are separated from each other by 2–4 nm over the length of the aggrecan. These GAGs are long unbranched polysaccharide chains that consist of repeating disaccharides units, which contain at least one sulphate group per disaccharide. The two

most abundant disaccharide types present in GAGs are chondroitin sulfate and keratan sulfate. Due to the presence of both sulfate and carboxylate groups, aggrecans carry a fixed negative charge density. These negative charges attract positively charged ions, such as Na^+ and K^+, which create a high concentration of ions within the AC. This high ion concentration generates an osmotic pressure. As a result, water is absorbed and AC is forced to swell, which provides its viscoelastic biomechanical properties, compressive resistance and lubrication between the AC surfaces.[143]

Based on the ECM composition, the shape of the chondrocytes, and the orientation of collagen fibers and aggrecans, AC can be morphologically divided into four different zones (Figure 4.1).[139, 144, 145] From top surface to bone, the different zones are:

1. superficial or tangential zone
2. middle or transitional zone
3. deep or radial zone
4. calcified zone

The superficial zone is the thinnest layer and it has the lowest concentration of aggrecans. This zone is characterized by thin collagen fibers that are oriented parallel to the surface. The parallel alignment helps to create tensile and shear strength. Chondrocytes in this zone are densely packed and have a flattened shape. The superficial zone is covered by a thin film of synovial fluid that provides a lubricated surface for the AC.

The middle zone is the thickest layer, it is characterized by a high concentration of aggrecans and randomly oriented collagen fibers that are large in diameter. The cells are round-shaped, randomly oriented and have a low density in this zone.

The deep zone is characterized by cells that are spheroidal in shape and arranged in columns perpendicular to the articular surface. Collagen fibers are the largest in diameter in this zone, also oriented perpendicular to the articular surface. This organization provides the AC its resistance to compressive forces. The aggrecan concentration is typically the highest in this zone while the water content is the lowest.

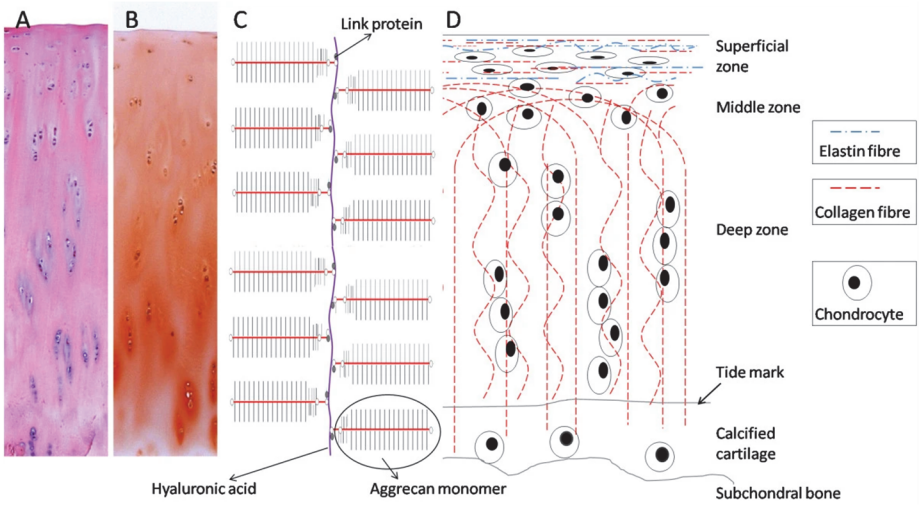


Figure 4.1 Composition of AC, divided in different zones (longitudinal view). **A** Hematoxylin and eosin staining section shows the chondrocytes and extracellular matrix distribution in articular cartilage. **B** Safranin O staining section shows that proteoglycan distribution increases from superficial zone to deep zone. **C** A schematic image of an aggrecan aggregate. **D** The schematic diagram represents the arrangements of collagen and elastin fibers within articular cartilage and changes in chondrocyte shape and arrangement with depth. Reproduced with permission from reference [146]. Copyright © 2014, Springer Nature.

The calcified zone is separated from the deep zone by a thin line, which is known as the tidemark. This zone forms the interphase between the soft AC and the bone and consists of hypertrophic chondrocytes that are dispersed in a calcified matrix. The ECM is mainly composed of type I collagen, hydroxyapatite and sodium hyaluronate.[147] Collagen fibrils from the deep zone are attached to the subchondral bone, which anchors the AC to the bone.

Due to its low metabolic activity and its avascular character, AC has a limited capacity to heal on its own.[139] Injuries or diseases like OA that degenerate the AC can affect the functioning of the joint and can lead to disability. Hence, the preservation of the AC is of major concern for the health of the joint.

In a healthy joint, processes of AC matrix degeneration and repair are balanced. In OA, the homeostatic state is disrupted and breakdown processes are increased while the aggrecan and collagen synthesis processes are suppressed.[148] OA tissue is also marked by a reduced number of chondrocytes due to suppressed cell proliferation processes. The combination of ECM

alteration induced by OA has been associated with mutations in mechanical properties of the joint.[24]

One of the early changes in the AC composition, induced by OA, is the loss of aggrecans in the ECM.[32, 149] These changes often occur before the gross morphological changes.[93] Moreover, in the earliest stage of OA, increase of GAG synthesis has been reported, when compared to normal and late-stage OA. [150] The concentration of GAGs in the ECM matrix has been accordingly seen as a biomarker for AC health.[151] Hence, CESAs that are capable to detect changes in the GAG content are of significant interest to study disease progression and support diagnosis of OA.

4.1.3 Cationic CESAs for cartilage imaging

For an overview of the recent literature regarding CESAs for microCT imaging of cartilage, the reader is referred to Section 2.5. In summary, cationic CESAs based on the triiodobenzene scaffold have been developed for imaging cartilage. More specifically, this type of CESAs is retained in the cartilage matrix due to favorable electrostatic interactions with the negatively charged GAGs. Among the reported compounds, CA4+ is the best performing cationic CESA because its partition in the cartilage most closely resembles the physiological aggrecan distribution. Moreover, Lakin *et al.* reported that the attenuation conferred by CA4+ correlated with biomechanical properties of AC (*e.g.* equilibrium moduli and stiffness).[55, 62, 64]

Previous work of the Grinstaff group showed that CA4+, bearing four primary ammonium groups, was more sensitive to changes in the GAG content compared to CA1+, which only has one primary ammonium group (Figure 4.2).[40] Meanwhile, CA4+ also showed an increased X-ray attenuation of stained AC in comparison with CA1+, which correlates with the respective iodine content.[a] As a result, an increased contrast-to-noise ratio in the final image was obtained for AC stained with CA4+.

[a] In this work, the staining solutions of CA4+6I and CA1+ had an identical iodine concentration.

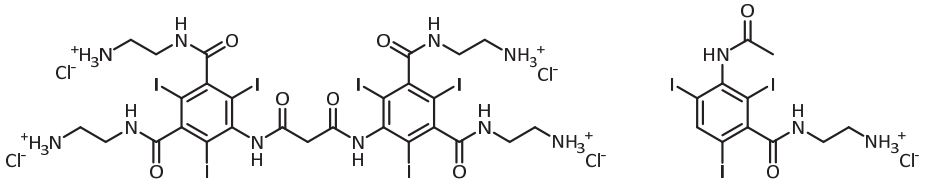


Figure 4.2 Examples of cationic CESAs for cartilage imaging, reported by the Grinstaff group. Left: CA4+ (CA4+6I)[b]. Right: CA1+.

4.2 Objectives

A review of previous literature revealed some areas for knowledge improvement. To our surprise, only a few precedents elaborate on the quantitative distribution of cationic CESAs at different AC depths, and none of them discusses the depth-dependent diffusive behavior.[42-44, 51, 52, 72, 152] Even though numerous reports exist on the evaluation of CA4+6I (CA4+) for AC imaging, very few variations in the scaffold of cationic CESAs have been studied so far.[23, 40, 50] Given their potential to evaluate GAGs, which are seen as a biomarker for AC health, we became interested to study the influence of the molecular design of CESAs on the intensity and distribution of X-ray attenuation in stained AC.

The main objective of this chapter is to expand current knowledge on cationic CESAs for microCT imaging of AC. The starting hypothesis is that the iodine content of the CESA, the CESA concentration and the staining time will show a positive trend with the gray value of stained cartilage. Moreover, it is expected that the CESA positive charge density will show a positive correlation with the affinity of the CESA towards GAGs in the cartilage matrix. To this end, compounds similar to CA4+6I are synthesized, with variations in iodine content and positive charge density. The aim is to study the influence of concentration, molecular design and staining time on the extent of X-ray attenuation of stained osteochondral plugs at different cartilage depths. The large dataset covering variations in several parameters will be analyzed in order to derive useful relationships. Additionally, the diffusive behavior at

[b] In literature, the structure shown on the left in Figure 4.2 is called CA4+, while this structure is named CA4+6I in own work.

different concentrations and depths will be investigated for all compounds studied.

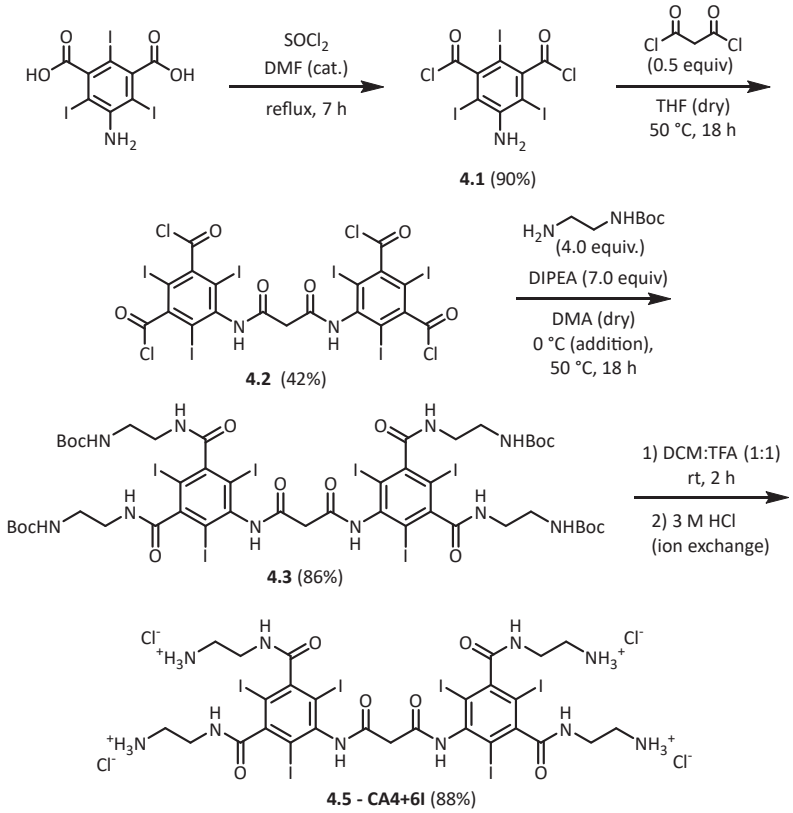
4.3 Synthesis of cationic CESAs

In general, we aim to further improve cationic CESAs to more precisely map the heterogeneous distribution of GAGs in AC. Therefore, two derivates of CA4+6I were synthesized that vary in positive charge density (CA8+6I) or iodine content (CA4+3I), discussed in Sections 4.3.2 and 4.3.3 respectively. The present study serves to provide insights into the influence of the cationic charge density and iodine content on the sensitivity of CESAs to image GAGs.

4.3.1 Synthesis of CA4+6I

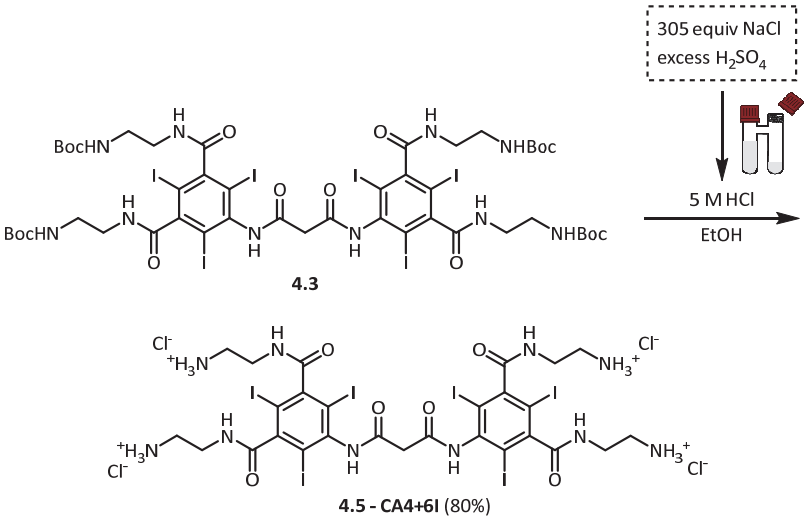
An efficient large-scale synthetic procedure for CA4+6I was described by the Grinstaff group.[69] We successfully used this procedure to synthesize CA4+6I in-house (Scheme 4.1). The synthesis started with the conversion of 5-amino-2,4,6-triiodoisophtallic acid into the corresponding diacyl chloride **4.1** by reflux in thionyl chloride. Next, **4.1** was coupled with malonyl chloride, resulting in the formation of **4.2** in a relatively low yield, which is assumed to be due to incomplete precipitation of the product. In the following step, the acyl chloride functionalized intermediate **4.2** was reacted with *N*-Boc-ethylenediamine to the corresponding amide intermediate **4.3**. After Boc deprotection using TFA, and conversion into the chloride salt by repeated dissolution in 3M HCl, CA4+6I was obtained (**4.5**). The obtained yields were slightly lower compared to the literature procedure. This can be explained by product loss during work-up and the difference in scale of the reaction.[c] The overall yield of the reaction was 29%.

[c] In literature, the synthesis was reported on 100 g scale. The synthesis was repeated in-house on 20 g scale.



Scheme 4.1 Synthesis of CA4+6I, protocol reported by Stewart *et al*, repeated in house on 20 g scale (Isolated yields).[69]

In an attempt to improve the convenience of the synthesis, the last two reaction steps of the reported CA4+6I synthesis protocol were merged. Meanwhile, the sustainability of the synthesis was ameliorated by reducing the number of synthetic steps and improving the work-up. To this end, Boc deprotection was performed in one single step using HCl gas (Scheme 4.2). By means of a two-chamber reactor, HCl was generated in one chamber by mixing NaCl and H_2SO_4 and consumed in the other chamber containing **4.3** dissolved in ethanol.[153] The conditions were chosen to obtain a 5 M HCl solution on the assumption of complete dissolution of the generated gas in ethanol. The product was obtained in 80% yield, which is comparable to the conventional procedure in Scheme 4.1.



Scheme 4.2 Synthesis of CA4+6I by Boc deprotection in one step using *ex situ* HCl generation by means of a two-chamber reactor (Isolated yields).

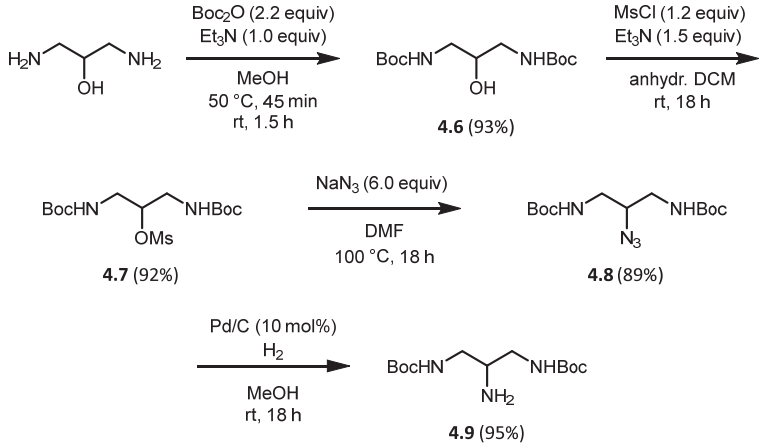
The adapted procedure obviates the need for work-up, as the product is directly obtained as an HCl salt after removal of the solvent. Despite the mentioned advantages of the shortened procedure, scalability is more challenging compared to the original procedure due to additional safety precautions.

4.3.2 Synthesis of CA8+6I

To study the influence of positive charge density on the visualization of GAGs when staining osteochondral plugs, we synthesized a compound that resembles CA4+6I, bearing eight primary ammonium groups instead of four. The acyl chloride intermediate **4.2** of the CA4+6I synthesis (Section 4.3.1) was used as a starting point. Instead of coupling *N*-Boc-ethylenediamine we wanted to couple 1,3-di-(*N*-Boc-amino)-2-aminopropane. Hence, after deprotection, the coupling of this amine linker gives rise to the double amount of primary ammonium groups compared to CA4+6I.

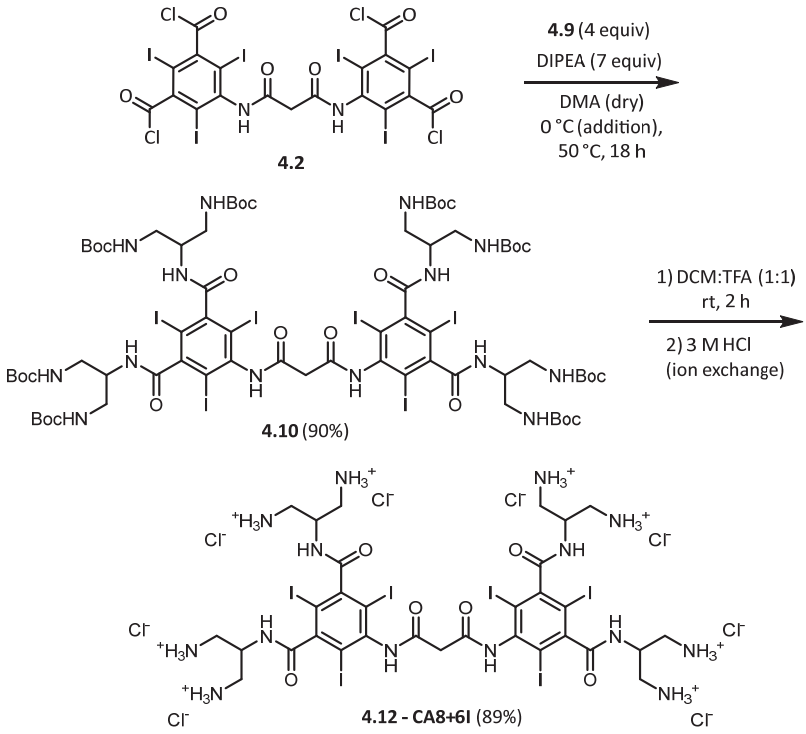
The synthesis of 1,3-di-(*N*-Boc-amino)-2-aminopropane encompasses four steps and started with the Boc protection of 1,3-diaminopropan-2-ol in the presence of an excess of di-*tert*-butyl dicarbonate (Boc_2O), yielding **4.6** (Scheme 4.3).[154] In the next three steps, the alcohol in **4.6** was converted into an amine. First mesylation was performed affording **4.7**, followed by azide

substitution (**4.8**). Finally, reduction by hydrogen gas resulted in the formation of the desired 1,3-di-(*N*-Boc-amino)-2-aminopropane (**4.9**). All intermediates were obtained in high yield and the overall yield was 72%.



Scheme 4.3 Synthesis of 1,3-di-(*N*-Boc-amino)-2-aminopropane as the amine linker for the synthesis of CA8+6I. (Isolated yields).

As shown in Scheme 4.4, the synthesis of CA8+6I is similar to CA4+6I. Therefore, it will not be discussed in detail. The overall yield (including the synthesis of **4.2**) was 30%. In addition, Boc deprotection of **4.10** by HCl gas was also performed for preparing CA8+6I using a 2-chamber reactor (not shown). The conditions were chosen to obtain a 4 M HCl, assuming that the generated gas completely dissolved in ethanol.[153] Starting from **4.10**, the end product was directly obtained as an HCl salt in 97% yield.

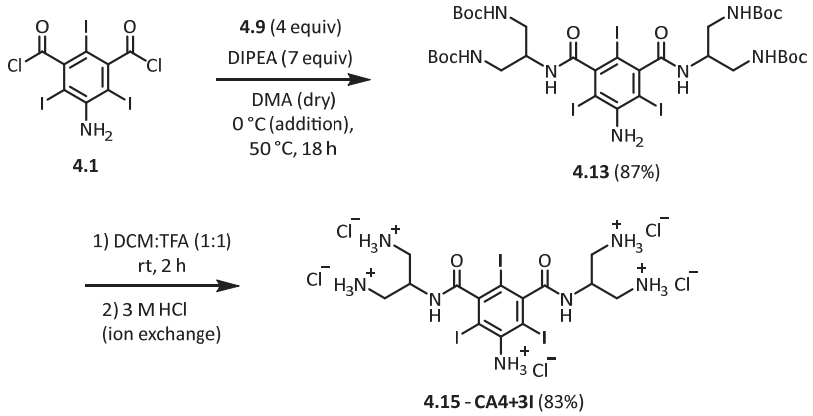


Scheme 4.4 Synthesis of CA8+6I, based on the protocol reported by Stewart *et al*.[69] (Isolated yields.)

4.3.3 Synthesis of CA4+3I

To study the influence of iodine content on the visualization of GAGs when staining osteochondral plugs, we synthesized a compound that resembles CA4+6I, bearing three iodine atoms instead of six. The acyl chloride intermediate **4.1** of the CA4+6I synthesis (Section 4.3.1) was used as a starting point, which was reacted with 1,3-di-(*N*-Boc-amino)-2-aminopropane **4.9**, yielding **4.13** (Scheme 4.5).[d] After Boc deprotection with TFA in DCM, followed by conversion into the chloride salt, the end product was obtained in good yields. The overall yield of the synthesis of CA4+3I was 65% (starting from 5-amino-2,4,6-triiodoisophtallic acid).

[d] We attempted to acylate the aniline in **4.13** to prevent protonation. However, acylation failed due to the low nucleophilicity of the aniline and steric hindrance.



Scheme 4.5 Synthesis of CA4+3I, based on the procedure for CA4+6I synthesis. (Isolated yields). The protonation of 4.15 is displayed according to physiological conditions. At low pH, the aniline will also be protonated.

4.4 Evaluation of X-ray attenuation of the CESA solutions

In this section, the X-ray attenuating properties of CA4+6I, CA8+6I and CA4+3I phantoms were evaluated. Solutions of 24 mgI/mL, 12 mgI/mL and 6 mgI/mL were prepared by dissolving CA4+6I, CA8+6I or CA4+3I in Nanopure water. Concentrations were selected identical to the concentrations used for the staining of osteochondral plugs (see next section). The gray values of the solutions were obtained by imaging 1 mL solutions using a µCT 40 (Scanco Medical AG, Switzerland).

Given that the attenuation of these compounds is principally marked by the iodine atoms, it is justifiable to use NaI as a calibrant. Hence, the obtained gray values of the CESA solutions were compared to a dilution series of NaI phantoms in order to quantify the iodine concentration based on X-ray attenuation. MicroCT images of NaI phantoms of known concentrations were acquired to construct a calibration curve (see section 7.4.4). Using this curve, averaged gray values were converted to empirical concentrations, which are displayed in Table 4.1. For every CESA, the observed empirical concentration was close to the theoretical concentration, which was our starting hypothesis.

The differences between the empirical and theoretical concentrations can be explained by errors caused by weighing of CESAs and microCT imaging. Errors related to microCT imaging could be caused by variability in conditions of the X-ray source, detector and environment (*e.g.* humidity, temperature).[155]

Besides, errors could also emerge from artefacts in the reconstructed images. For an overview of common artefacts in microCT imaging, the reader is referred to the following account.[156]

Table 4.1 Empirical concentration of CESA phantoms based on X-ray attenuation, expressed as gray value (mean ± sd).

		6 mgI/mL	12 mgI/mL	24 mgI/mL
CA4+6I	empirical conc. (mgI/mL)		11.62 ± 3.26	22.96 ± 3.91
	gray value		45.57 ± 4.84	62.41 ± 5.80
CA8+6I	empirical conc. (mgI/mL)		10.73 ± 2.41	22.64 ± 2.72
	gray value		44.26 ± 3.58	61.93 ± 4.04
CA4+3I	empirical conc. (mgI/mL)	6.90 ± 3.42	12.43 ± 3.65	23.10 ± 3.64
	gray value	38.57 ± 5.07	46.78 ± 5.42	62.61 ± 5.41

4.5 Diffusive behavior of cationic CESAs through AC

The uptake and transport of a CESA through the AC matrix generally depends on the compound charge, the compound size and the porosity of the ECM matrix.

The presence of GAGs in the ECM affords AC its negative fixed-charge density, which acts as a selective membrane. More specifically, the partitioning of charged compounds between the solute (synovial fluid or staining solution) and the AC matrix can be characterized by the Donnan equilibrium.[157] According to this model, the negative charge density of AC will increase or decrease the partitioning of positively or negatively charged CESAs, respectively. In case of cationic CESAs, the Donnan equilibrium results in an increased uptake of the CESA in the superficial zone of the AC matrix. If the affinity of the CESAs to the GAGs is sufficiently strong due to electrostatic interactions, the transport of the CESA will be accelerated towards the deeper zones. Based on diffusion studies performed by the Grinstaff group, the authors concluded that the uptake of CA4+6I obeyed the Donnan equilibrium

theory of a molecule having a positive charge of +3.7, which is close to the theoretical charge of +4.[69]

Previous work provided evidence that AC stained with CA4+6I reflects the depth-dependent aggrecan distribution in AC.[53] *Ex vivo* staining of AC with CA4+6I is dominated by electrostatic interactions with GAGs in the AC matrix. More specifically, it has been observed that CESA concentrations in the AC varies proportionately with the local GAG content (see Section 2.5).

The uptake of the CESA by AC is mainly governed by electrostatic interaction, but it is also influenced by the AC water content, collagen density, and hence, porosity of the matrix.[42] The permeability of the AC matrix reduces with increasing cartilage depth due to steric hindrance induced by both the collagen matrix and the dense aggrecans. The effective pore size is estimated to be around 6 nm in healthy cartilage. Depending on the local cartilage composition, the pore size ranges from 4 – 6 nm between GAGs to 50 – 100 nm between collagen fibrils.[158] Since the hydrodynamic radius of CA4+6I (MW = 1.5 kDa, h_r ~ 1.4 nm) is small, and the related CESAs discussed in this dissertation have a relative low molecular weight (< 1.8 kDa), we hypothesize that they are all capable to penetrate even the smallest, tortuous pore sizes in the ECM matrix.[159] Based on knowledge of solute transport in porous media, larger compounds are expected to show smaller diffusivities than smaller compounds. Given the differences in molecular weight of the studied CESAs, differences in diffusive behavior due to molecular size could be expected. However, since the differences are relatively small in comparison with the pore size of the matrix, the influence of molecular weight on the diffusivity (penetration rate) is thought to be minimal.

4.6 Staining of osteochondral plugs with cationic CESAs

To assess the staining potential of the different cationic CESA for AC imaging, bovine osteochondral plugs were stained *ex vivo* by immersion in staining solutions. Time-lapsed imaging experiments were performed to study the gray value evolution at different cartilage depths. The selected concentrations are identical to the conditions shown in Table 4.1 of the previous section. In these experiments, the gray value in the CECT images reflects the distribution of iodine, conferred by the CESAs, in the osteochondral sample. Hence,

concentrations are expressed as mgI/mL[e] unless stated otherwise. Time-lapsed CECT cross-sections of osteochondral plugs stained with CA4+6I, CA8+6I and CA4+3I are displayed in Figure 4.3. Visual comparison of identical plugs over time demonstrates the gradual increase of X-ray attenuation.

In this section, we will first discuss general trends that were observed for the obtained data. Next, the significant factors are discussed, based on the outcome of the multivariate analysis of variance (MANOVA). In doing so, the influence of parameters such as staining time, cartilage depth, CESA and concentration on the observed gray values was studied. It is important to mention that data points were excluded from the dataset due to errors related to microCT device or the staining procedure. More specific information can be found in Section 7.4.6.

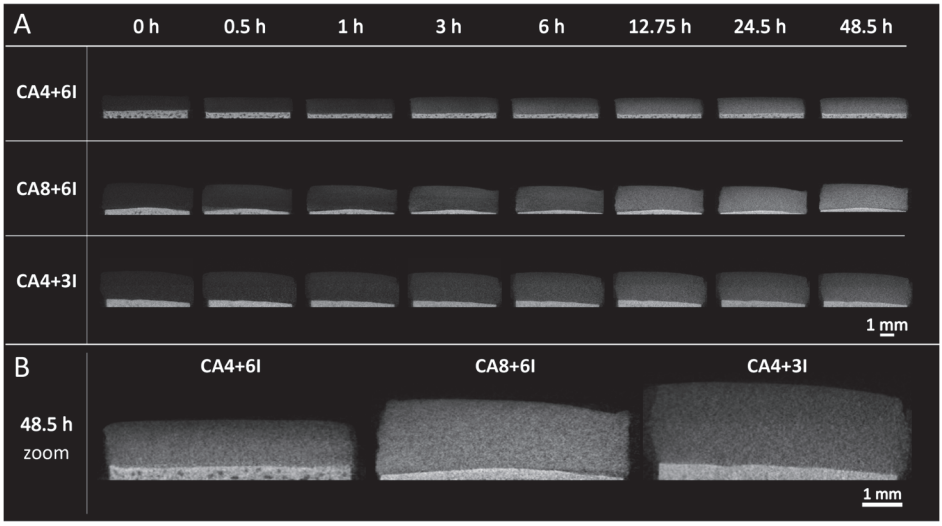


Figure 4.3 CECT images of bovine osteochondral plugs stained with different cationic CESAs. **A** Longitudinal CECT slices of osteochondral plugs before and after 0.5 h, 1 h, 3 h, 6 h, 12.75 h, 24.5 h and 48.5 h *ex vivo* staining with CA4+6I, CA8+6I and CA4+3I. **B** Enlarged CECT slices of osteochondral plugs after 48.5 h of staining. Scale bar = 1 mm. Voxel size = 18 µm. Scanning parameters: 70 kVp, 114 µA, 0.5 mm Al filter.

[e] Concentrations of CESA solutions are expressed in milligram iodine per milliliter. This implies that for the same iodine concentration, the molar concentration of CA4+3I is doubled compared to CA4+6I and CA8+6I. Conversions of mgI/mL to mg/mL and mmol/mL for every CESA is shown in Table 7.2.

4.6.1 Descriptive data analysis

General trends

The obtained data were pooled together and graphically visualized to facilitate the identification of trends (Figure 4.4)[f]. Similar 2D plots with alternative representation of the parameters are provided in Section 7.4.9 to assist in visualizing the trends. From these graphs, the following factors were found to show a positive trend with gray value (while keeping the other factors constant):

- Staining time (Figure 4.4)
- Cartilage depth at diffusion equilibrium (Figure 7.4 and Figure 7.6)
- Concentration (Figure 4.4)

A first general trend is the exponential increase of gray value that plateaus over time, which is in accordance with previous work.[40, 69, 152] Most commonly, the gray value keeps increasing over the first 12 hours and starts to level off afterwards. In literature, this gradual decay phase is often called diffusion equilibrium.[69] The diffusion characteristics will be discussed in more detail in the next Section 4.6.2.

A second general trend is the increase in gray value for increasing (cartilage) depth at diffusion equilibrium (Figure 7.4), similar to reported observations for CA4+6I stained AC.[42, 152] The partitioning of the cationic CESAs was found to be proportional to the distribution of GAGs in the AC, which are more omnipresent in the deep zone (90% depth), followed by the middle zone (50% depth).[42, 51, 69] In contrast, the opposite trend was observed for the early time points (0 – 3 hours), as can be seen in Figure 7.5. Logically, the CESA first needs to penetrate the superficial (10% depth) zone before entering the deeper zone (90% depth), which explains why the increase in gray value first appears at 10% depth. The point in time of trend reversal varies according to the CESA and concentration used.

[f] In Figure 4.4 the spline fit was used, which is a smooth, continuous function that represents the relationship between two numerical variables. The fit is based on a series of third-order polynomials in a piecewise fashion. Lambda is the smoothing argument.

A third general trend is the increase in gray value for increasing concentrations (Figure 4.4), which makes sense intuitively. The similar trend was observed in previous work on CA4+6I. [53, 72, 152] A higher concentration implicates a higher availability of CESA to stain AC, and hence a higher gray value. Although solutions of the same iodine concentration were employed, differences in gray value were observed for the different CESAs. This observation indicates that the molecular design of the cationic CESA influences the extent of gray value increase, which will be discussed in more detail below.

Next, the influence of the CESA molecular design on gray value was studied. Table 4.2 provides an overview of the cationic charge density, iodine content and molecular weight of the different CESAs. Comparing gray values for different CESAs but identical concentrations and cartilage depths revealed that CA4+3I induced the smallest gray value increase for all time points (Figure 7.6). This observation can be explained by CA4+3I having the smallest iodine content of all CESAs tested. Most often, the highest gray values were observed for samples stained with CA8+6I. Due to the higher positive charge density compared to the others, an increased uptake in the deeper zone is expected that is governed by enhanced electrostatic interactions. One might argue that this observation is counterintuitive since this compound is expected to require the least amount of molecules to saturate the negatively charged GAGs. However, this statement is valid for the case the amount of CESA present is sufficient to bind all GAGs present. Unfortunately, with the data herein we are unable to define if saturation would be achieved. Interestingly, gray values obtained for CA4+6I are most often closer to those obtained for CA8+6I than for CA4+3I.

Table 4.2 Properties of cationic CESAs. The molecules bear positive charges due to the presence of primary ammonium groups. The ratio of the positive charge density to iodine atom count is symbolized as [+]/[I].

	CA4+6I	CA4+3I	CA8+6I
Theoretical amount of positive charges	4	4	8
Amount of iodine atoms	6	3	6
Ratio [+]/[I]	0.67	1.33	1.33
Molecular weight (g/mol)	1499.876	1761.876	846.922

Altogether, the following properties show a positive trend with gray value:

- iodine content (for similar positive charge density)
- positive charge density (for similar iodine content)

In case the ratio of positive charge density to iodine content is equal, the highest increase in gray value was observed for the CESA with both the highest iodine content and positive charge density (CA8+6I).

While most of the data agrees with these trends, there remain some anomalies. In the case of CA4+3I, data points of 12 mgI/mL and 24 mg/mL are overlapping for early time points (Figure 4.4). This anomaly could be explained by the smaller number of samples for CA4+3I due to exclusion of data points, which makes the presented data less reliable (see Section 7.4.6). In the case of CA8+6I, gray values measured at 50% and 90% cartilage depth resemble each other for the later time points (Figure 7.4). Possibly this could be due to a quicker charge saturation of GAGs by CA8+6I in the deepest layer in comparison to the other CESAs. If this would be the case, oversaturation of GAGs in the middle zone (50% depth) occurs. This hypothesis seems plausible based on the lower gray value observed at 50% depth compared to 90% depth after 48 h washing in a saline solution (see Figure 4.5 in the next section).

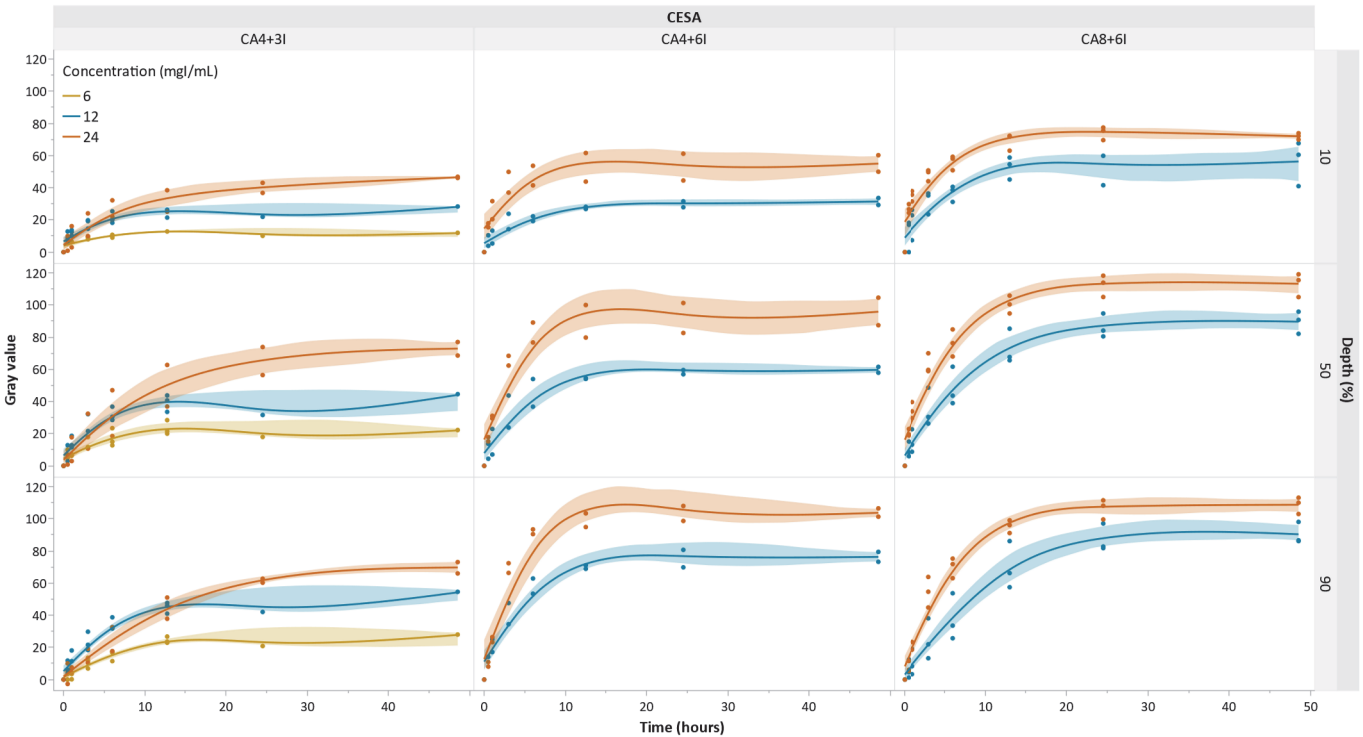


Figure 4.4 Graphical visualization of gray value analysis of osteochondral plug staining with CA4+6I, CA8+6I and CA4+3I. Smooth curves of gray value as a function of staining time (hours), classified by CESA and depth and labeled by concentration. The curves were plotted in JMP using a polynomial smoothing spline with lambda set at 0.05. The shaded regions represent the confidence of fit.

CESA removal after staining

Staining of AC by cationic CESAs is based on non-covalent interactions, which are usually reversible. Indeed, previous work provides evidence that removal of CA4+6I from osteochondral plugs is feasible by equilibrating the plugs in a saline solution. [25, 40] Interestingly, the time required to remove CA4+6I from the plugs was substantially longer compared to an anionic or neutral CESA. Bansal *et al.* reported that still 50% of the maximal X-ray attenuation conferred by CA4+6I was observed after immersion of the plugs in a saline solution for 24 h. [25, 40, g] The slower diffusion out of AC was explained by the authors as the larger affinity of CA4+6I for staining AC compared to anionic or neutral CESAs. Following this reasoning, a destaining (washing) experiment was performed. All stained AC plugs were immersed in a PBS solution and imaged by microCT. Plug stained by CA4+6I were immersed in PBS for 28.7 h, while plugs stained by CA4+3I and CA8+6I were immersed for 24 h.

Gray values observed for osteochondral plugs stained for 48.5 h were compared to those observed after washing (*i.e.* immersion in PBS) in Figure 4.5. Unfortunately, gray values observed for CA4+6I destaining could not be compared to those observed for CA4+3I and CA8+6I due to dissimilar washing times. What is striking in this chart is the complete removal of CA4+6I after 28.7 h of washing. In contrast, for none of the conditions tested, CA4+3I and CA8+6I were fully removed after 24 h of washing. Interestingly, gray values observed after CA8+6I staining and washing were markedly higher compared to CA4+3I, indicating a larger affinity of CA8+6I for AC. More specifically, after washing, the X-ray attenuation decreased by 80 – 95% in the case of CA4+3I and about 50 – 70% in the case of CA8+6I. For nearly all of the studied conditions for CA4+3I and CA8+6I, higher gray values were observed in the deeper zone compared to the superficial zone. Reasons why the deeper zone showed higher gray values are the longer distance to diffuse out of the tissue and the higher concentration of GAGs, and hence larger affinity of the CESAs for AC.

[g] Two articles reported 50% decrease of the maximal observed X-ray attenuation, conferred by CA4+6I, after 24 h immersion in saline. What is striking is that the concentration of CA4+6I used for staining 7 mm bovine osteochondral plugs was not identical; in one study 8 mgI/mL and in the other study 27 mgI/mL.

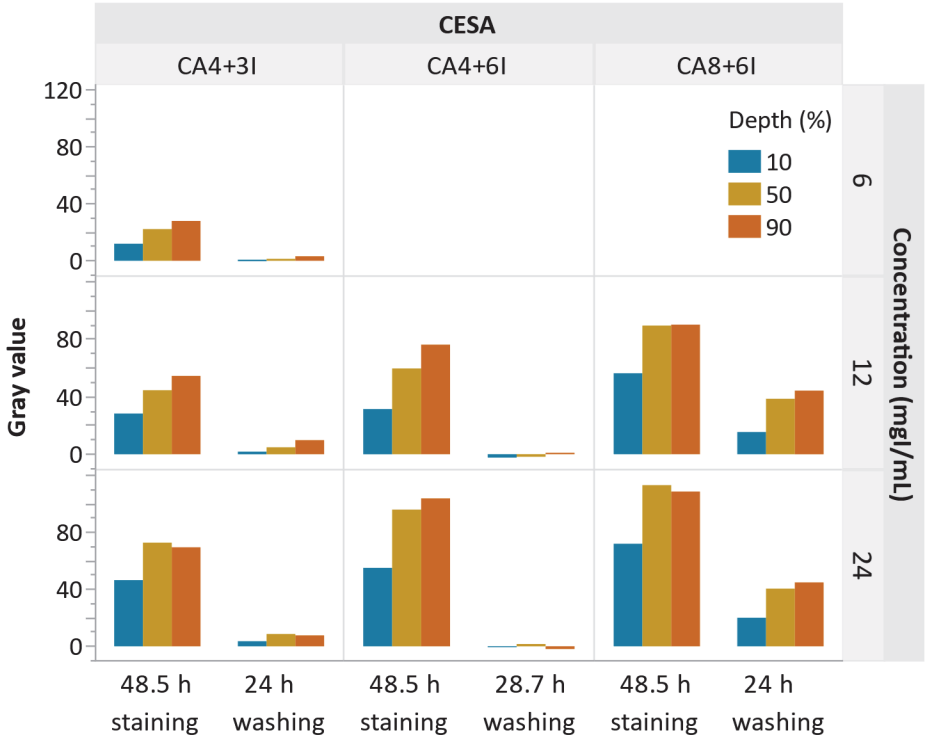


Figure 4.5 Comparison of gray values observed for plugs stained for 48.5 h, followed by immersion in PBS. Plug stained by CA4+6I were immersed in PBS for 28.7 h, while plugs stained by CA4+3I and CA8+6I were immersed for 24 h.

Iodine concentration vs molar concentration

In this section, molar concentration of the staining solutions were compared for the different CESAs, in contrast to iodine concentration as discussed above. For the same iodine concentration, the molar concentration of CA4+3I is doubled compared to CA4+6I and CA8+6I. Conversions of mgI/mL to mg/mL and mmol/mL for every CESA are shown in Table 7.2. Figure 4.6 gives an overview of the gray value increase over time for stained osteochondral plugs, classified by molar concentration and depth. In fact, the same curves are displayed as in Figure 4.4, albeit organized differently. Similar positive trends were observed between gray value and concentration, depth and staining time, which was discussed above.

Since CA4+3I possesses the same positive charge density but half of the amount of iodine atoms compared to CA4+6I, one could hypothesize the gray value observed for CA4+3I would also be half of those observed for CA4+6I. Visual comparison of the corresponding curves in Figure 4.6 suggests that this hypothesis makes sense, especially if we look at the condition of 0.032 mmol/mL. Therefore, the ratio of gray value observed for CA4+3I and CA4+6I was calculated and displayed in Table 4.3. In particular, we are mostly interested in the gray values observed for the later time points (*i.e.* after 12.75 hours, indicated in bold) to diminish variations induced by differences in penetration rate for the early timepoints. Strikingly, the ratio of iodine content is approximately reflected in the ratio of gray value.

Table 4.3 Ratio of averaged gray value observed osteochondral plugs stained with 0.032 mmol/mL solutions of CA4+3I and CA4+6I. The ratio of CA4+3I to CA4+6I is shown, categorized per depth in order to reflect the variation in iodine content in the observed gray value.

Gray value	Depth (%)	Time (hours)						
		0.5	1	3	6	12.75	24.5	48.5
$\frac{[\mathbf{CA4+3I}]}{[\mathbf{CA4+6I}]}$	10	0.57	0.46	0.41	0.45	0.47	0.41	0.51
	50	0.46	0.47	0.38	0.39	0.44	0.34	0.46
	90	0.77	0.49	0.34	0.37	0.45	0.41	0.53

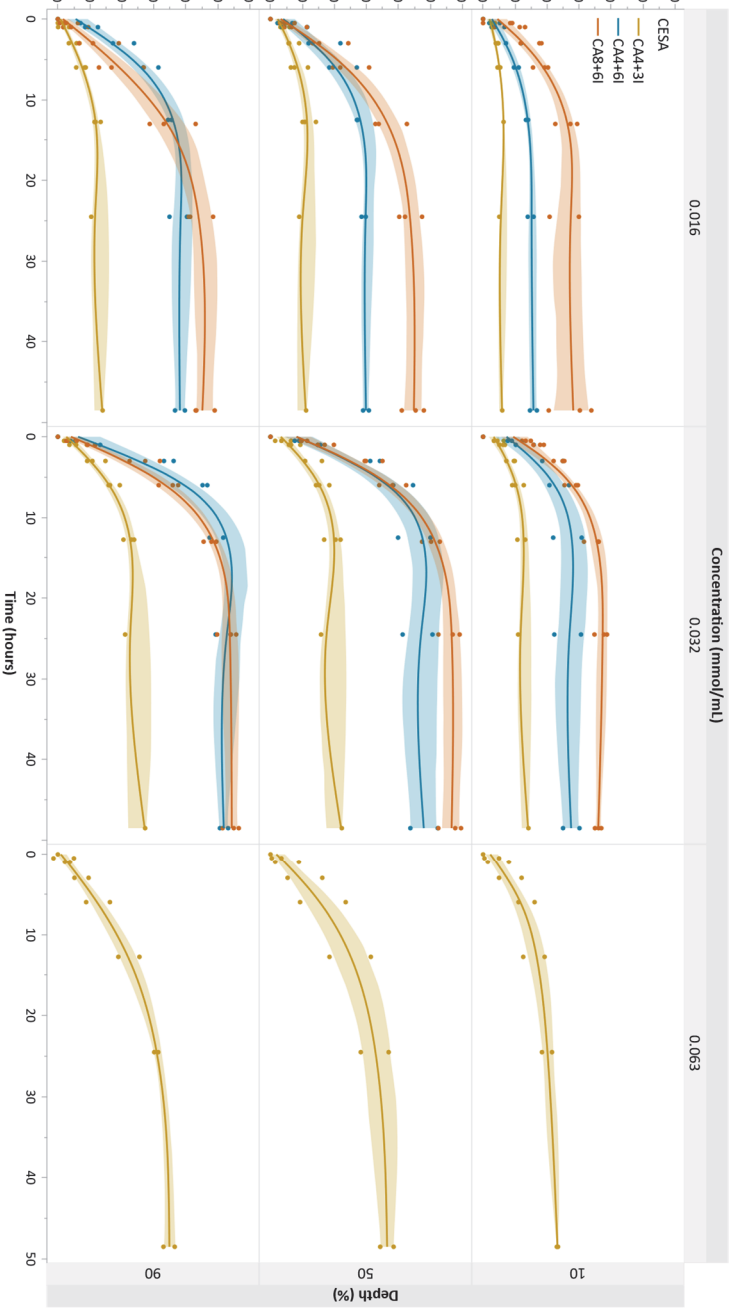


Figure 4.6 Graphical visualization of gray value analysis of osteochondral plug staining with CA4+6I, CA8+6I and CA4+3I. Smooth curves of gray value as a function of staining time (hours), classified by CESA and depth and labeled by molar concentration. The curves were plotted in JMP using a polynomial smoothing spline with lambda set at 0.05. The shaded regions represent the confidence of fit.

Gray value range

As mentioned in Section 4.1.3, previous work on the comparison between CA4+6I and CA1+, which have six and three iodine atoms respectively, showed that X-ray attenuation positively correlates with GAG content. More specifically, gray values of stained osteochondral plugs were compared with the corresponding GAG content, which was assessed by a biochemical assay. [40] The outcome of this study suggests that the broader the range of gray values covered, the higher the sensitivity of the CESA towards changes in the GAG content. [40] This can likely be explained by the fact that a wider range offers a larger palette of gray values, which facilitates the detection of small differences due to local variations in the AC matrix.

Following this reasoning, gray value profile surfaces were drawn, perpendicular to the articular surface, in the middle of AC plugs that were stained with solutions of 24 mgI/mL for 48.5 hours. As can be seen in Figure 4.7, gray value gradually increases with increasing cartilage depth, which was discussed in more detail above. Comparing CESAs with each other, the graph suggests that CA4+6I covers the widest range of gray values over the full depth of the cartilage, which was confirmed by the numerical representation of the minimum and maximum gray value in Table 4.4. The smallest range of gray values was observed for CA4+3I. Therefore, we could argue that CA4+3I is the least capable of detecting small variations in the GAG content of AC. It is interesting to note that the progression of the gray value profile of CA8+6I resembles more closely the one of CA4+6I than the one of CA4+3I. Since the covered gray value range by CA4+3I is substantially smaller than those covered by CA4+6I and CA8+6I, we hypothesize that the iodine content is of more importance than the cationic charge density to detect changes in the GAG content. However, further research is needed to support this hypothesis.

Table 4.4 Minimum and maximum gray value observed for the depth-wise profile surfaces drawn for osteochondral plugs stained with CESA solutions of 24 mgI/mL for 48.5 hours.

24 mgI/mL, 48.5 h	CA4+6I	CA4+3I	CA8+6I
minimum gray value	59	64	72
maximum gray value	155	117	157
gray value range	96	52	85

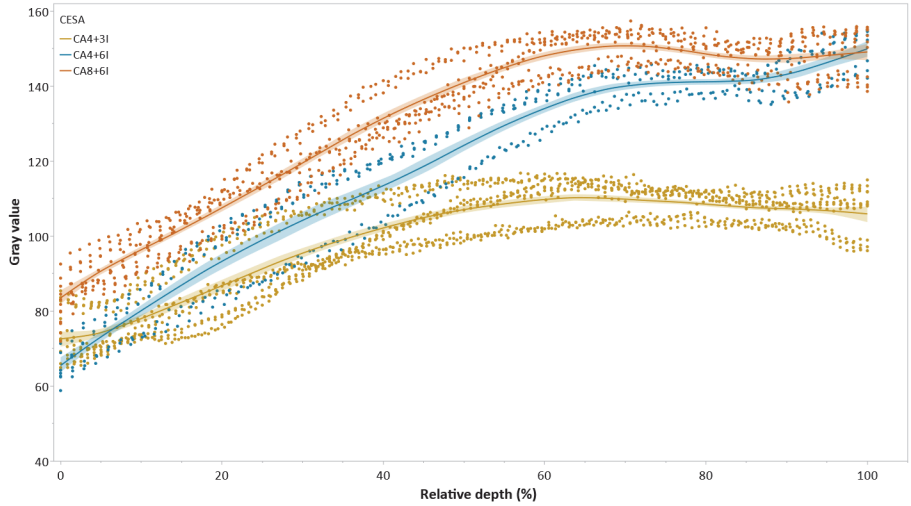


Figure 4.7 Depth wise gray value profile of osteochondral plugs stained with 24 mgI/mL CA4+6I, CA8+6I or CA4+3I after 48.5 h. The articular surface is at 0 % and the tidemark is at 100% on the x-axis. The individual dots represent gray values measured over the thickness of the cartilage. For every sample, 4 profile surfaces were drawn. The curves were plotted in JMP using a polynomial smoothing spline with lambda set at 0.05. The shaded regions represent the confidence of fit.

4.6.2 Diffusion analysis

The time to reach diffusion equilibrium depends on the composition of the ECM matrix, the CESA, the CESA concentration and the (cartilage) depth. The time to reach equilibrium, δ, which is commonly defined as 95% of the maximum gray value (GV), was calculated by fitting the following equation to the data:

$$GV = \alpha(1 - e^{t/\tau}) \qquad (4.1)$$

Where α is the maximum gray value coefficient, t the staining time and τ the penetration rate constant, *i.e.* the time required to reach 63.2% of the maximum gray value α.[69] An overview of the values obtained for α, τ and δ of the different conditions is given in Table 7.3. With some caution, insights based on the interpretation of these values are given below.

The maximum gray value α, which is closely related to the gray value at diffusion equilibrium, increases both with increasing concentration and increasing depth (Figure 4.8A). For all conditions, the highest gray values were

measured for CA8+6I, followed by CA4+6I. The lowest gray values were observed for CA4+3I. This observation agrees with the aforementioned positive trends between (i) gray value and iodine content, and (ii) gray value and positive charge density.

The influence of CESA and concentration on the time required to reach 95% of the maximum gray value (δ) is graphically visualized in Figure 4.8B. Having in mind it takes more time for a CESA to reach the deeper zone compared to the superficial zone, it is plausible that δ increases with increasing (cartilage) depth. When allocating the δ values in the graph to the respective iodine concentrations, a negative correlation was found between δ and iodine concentration in case of CA4+6I and CA8+6I. The similar trend and comparable δ values were reported for CA4+6I stained bovine plugs by Karhula *et al.* [53] Interestingly, smaller δ values were observed for CA4+6I than for CA8+6I. Surprisingly, the opposite trend was observed for CA4+3I at 10% and 50% depth. In addition, remarkably high δ values were obtained for the condition of 24 mgI/mL of CA4+3I. These anomalies could be explained by the smaller

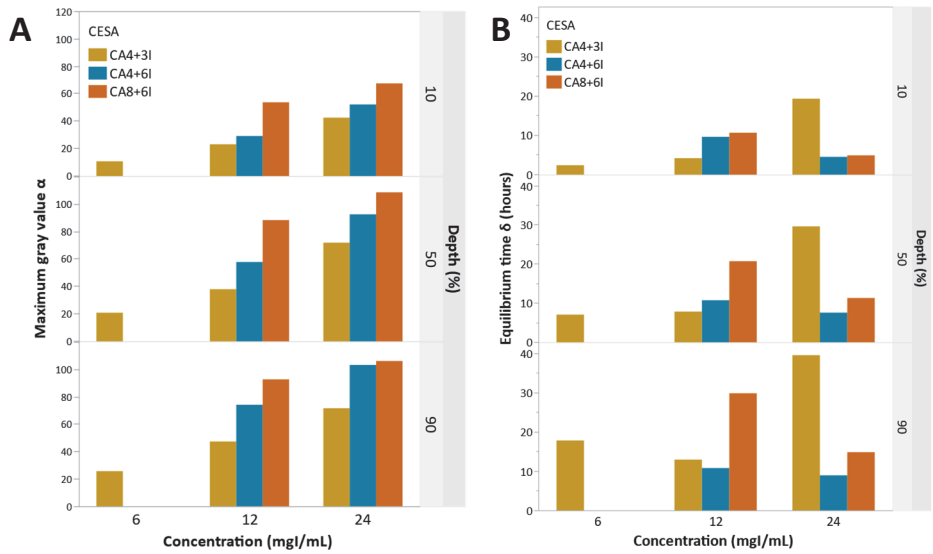


Figure 4.8 Graphical visualization of (A) α, the maximum gray value coefficient and (B) δ, the equilibrium time constant of the various conditions, categorized by iodine concentration (mgI/mL). The values of the constants were obtained by fitting equation (4.1) to the gray value data collected for stained osteochondral plugs.

number of samples due to exclusion of data points, which makes the presented data less reliable (see Section 7.4.6).

Figure 4.9 allows to compare δ values of CESAs of similar molar concentration. In doing so, the influence of the molecular weight of the CESA on the time required to reach diffusion equilibrium can be deduced. As mentioned before, remarkably high δ values were obtained in case of CA4+3I for the condition of 0.063 mmol/mL (24 mgI/mL). In case of the concentrations 0.016 mmol/mL and 0.032 mmol/mL, CA8+6I requires the most time, which is in agreement with CA8+6I having the highest molecular weight. For gray values measured at 10% and 50% depth, CA4+3I showed the smallest δ, which suggests that CA4+3I has the largest penetration rate through the AC in the superficial and middle zone. The slightly faster penetration rate in these zones of CA4+3I compared to CA4+6I and CA4+8I could be attributed to CA4+3I having the smallest size and molecular weight. This trend correlates with the general principle of a compound molecular weight being inversely proportional to its rate of diffusion. [160] Deeper in the AC matrix (90% depth), the electrostatic interactions with the GAGs most probably influence the penetration rate of

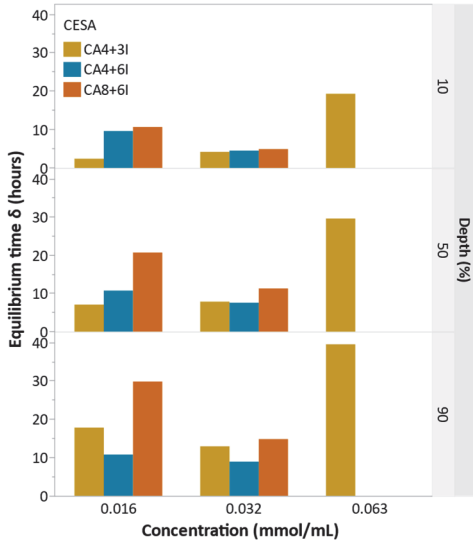


Figure 4.9 Graphical visualization of the equilibrium time constant δ of the various conditions, categorized by molar concentration. The values of the constants were obtained by fitting eq. (4.1) to the gray value data collected for stained osteochondral plugs.

the CESAs, which could be the reason why CA4+3I no longer shows the smallest δ. In terms of CESA penetration through the AC matrix, the obtained data suggest that CA4+6I possesses the most desirable trade-off between cationic charge density, iodine content and required staining time.

4.6.3 Multivariate Analysis of Variance

In this section, the experimental data were approximated by a fitted model according to the multivariate analysis of variance (MANOVA) approach using JMP®. Fitting of the data by MANOVA was performed to determine the statistical significance of the parameters involved (staining time, concentration, CESA type, cartilage depth). By implementing MANOVA, the importance of the effect on gray value for the different parameters was studied. The reader is referred to Appendix B for a brief theoretical introduction on linear model fitting. The following section is intended to provide a conceptual understanding and does not include an exhaustive discussion on the comparison of influences of the different parameters involved.

Not only main effects, but also cross effects were taken into account. Time was defined as the repeated measure. Results must be interpreted with caution due to the low sample size number, excluded data points because of errors and a MANOVA assumption that is being violated (see Section 7.4.8).

Table 4.5 represents the factors having a significant effect on gray value. The outcome of MANOVA is in line with the qualitative description of the data in Section 4.6.1. In relation to between-subject factors, significant effects over time emerged for CESA, cartilage depth and concentration. Moreover, the significant interaction effect between CESA and depth suggests that the effect of CESA on gray value differs for different depths and *vice versa*. Although no main effect was found for time, the MANOVA revealed several significant interaction effects that include time. These interaction effects indicate that the effect of CESA, concentration and depth on gray value is dependent on the staining time.

Table 4.5 Repeated-measures MANOVA with time as the repeated measure. Factors that have a significant effect on gray value are colored blue ($p < 0.05$). F represents the F-value, df the degrees of freedom and p the p-value.

Factor	F	df1, df2	p
between-subject			
CESA	46.472	2, 31	< 0.001
depth	28.071	1, 31	< 0.001
concentration	64.885	1, 31	< 0.001
CESA x depth	4.728	2, 31	0.016
CESA x concentration	2.8178	2, 31	0.075
depth x concentration	0.0012	1, 31	0.9722
within-subject			
time	1.876	2.313, 71.704	0.155
time x CESA	30.068	4.626, 71.704	< 0.001
time x depth	64.076	2.313, 71.704	< 0.001
time x concentration	29.666	2.313, 71.704	< 0.001

As mentioned in Section 4.6.1, gray values obtained for CA4+6I and CA8+6I are more closely related to each other compared to CA4+3I. If the data on CA4+3I were excluded from the MANOVA, a main effect of (staining) time became significant ($F_{1.966,\ 45.227} = 6.660$, $p = 0.003$). Likewise, interaction effects of time x CESA ($F_{1.966,\ 45.227} = 26.078$, $p < 0.001$), time x depth ($F_{1.966,\ 45.227} = 77.328$, $p < 0.001$) and time x concentration ($F_{1.966,\ 45.227} = 20.779$, $p < 0.001$) were significant. These results suggest that gray value is largely affected by time and that the gray value measured at a certain time point depends on CESA, concentration and depth.

Figure 4.10 shows the graphical representation of the Least Squares Means of gray value (gray value LSM) predicted by the model, classified per CESA. Each curve represents the overall mean per time point, averaged over depth and concentration. For all CESAs, gray value increases over time. The time-dependent influence of CA4+6I on the gray value LSM exhibits greater similarity to that of CA8+6I compared to CA4+3I, thereby indicating that the

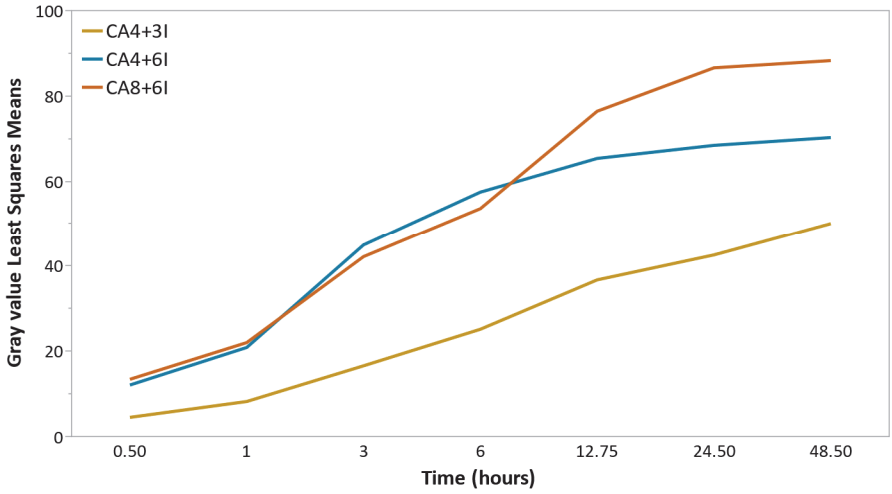


Figure 4.10 Line graph of the gray value Least Squares Means as calculated by the MANOVA approach to approximate experimental data. MANOVA assumes that the repeated measures of a same subject have a constant variance across time. Therefore, time points are specified as ordinal data.

iodine content exerts a more substantial influence on the gray value than the positive charge density. The highest increase was observed for CA8+6I, which corresponds to the descriptive data analysis in Section 4.6.1.

Table 4.6 gives an overview of the parameter estimates calculated by the JMP®. As mentioned in Appendix B, the value of the parameter estimate indicates the extent of change in gray value that is associated with a change of the corresponding factor. The comparison of estimates with each other over time suggests that depth has the lowest impact on gray value. Increasing parameter estimates over time are interpreted as changes in the corresponding factor having an increasing influence on gray value over time. This interpretation holds for the factors depth, concentration (and CA8+6I). In other words, the gray value is more influenced at a later time point by the aforementioned factors compared to an early time point. It is interesting to note that the parameter estimate corresponding to depth changes sign over time. The negative sign for the early time points means that the gray value decreases with increasing cartilage depth. This is indeed logical since the CESA did not penetrate the deeper AC zones yet. Considering the later time points, the parameter estimates indicate that an increase in cartilage depth gives rise to an increase in gray value. Moreover, the extent of increase in gray value

enlarges over time. This main effect needs to be interpreted with caution due to the presence of interaction effects between depth and CESA. However, since for all CESAs, gray value increases over time with increasing depth, the interpretation of this main effect makes sense, but keeping in mind that the extent of effect of depth on gray value differs for the different CESAs.

Table 4.6 Parameter estimates of the different factors studied for gray value LS Means in response to time based on a MANOVA model. Parameter estimates of factors that were not found significant are not shown.

Parameter estimate	0.5 h	1 h	3 h	6 h	12.75 h	24.5 h	48.5 h
intercept	6.370	4.608	1.572	0.979	9.906	7.426	10.368
CESA (CA4+3I)	-5.495	-8.817	-17.979	-20.257	-22.788	-23.293	-19.476
CESA (CA4+6I)	2.078	3.838	10.368	12.069	5.869	2.568	0.725
CESA (CA8+6I)	3.417	4.979	7.611	8.188	16.919	20.725	18.752
depth	-0.054	-0.032	0.103	0.219	0.340	0.414	0.437
concen-tration	0.360	0.792	1.566	1.878	1.820	2.107	2.084
CESA (CA4+3I) x depth (50.976)	0.044	0.004	-0.085	-0.164	-0.144	-0.178	-0.151
CESA (CA4+6I) x depth (50.976)	0.056	0.099	0.195	0.291	0.214	0.184	0.147
CESA (CA8+6I) x depth (50.976)	-0.099	-0.103	-0.111	-0.127	-0.070	-0.006	0.003

In order to compare the influence of the different factors (staining time, CESA concentration, CESA type, cartilage depth) on the gray value of stained AC, the effect size (η^2) of the parameters, as well as their 2-factor and 3-factor interactions, were computed and presented in Table 4.7. To achieve this, a generalized linear model was employed, utilizing SAS® 9.4 software to approximate the experimental data. In order to ensure consistency in the combinations of time, depth, and CESA, the dataset for the condition of 6 mgI/mL was excluded. It is important to acknowledge that the model does not adequately account for the inherent dependence of data points within the same samples. Consequently, the assumption of independence among the residuals, which represent the unexplained variability in the model, is violated. Despite this limitation, attempts to incorporate a suitable model that considers the correlation between measurements made on the same sample, such as a linear mixed model, proved challenging. Hence, although imperfect, the current linear model was utilized, given the relatively close correspondence between the estimated fixed parameters and their standard errors, which reflect parameter precision. It is worth noting that if this correspondence was not observed, the linear model would not be deemed appropriate for estimating effect sizes.

Table 4.7 Effect size of the different factors studied for gray value LS Means based on a generalized linear model. η^2 is a measure of effect size. Factors that were not found significant are not shown. Parameter estimates of factors that were not found significant are not shown.

Factor	p	η^2
time	< 0.001	0.464
CESA	< 0.001	0.124
concentration	< 0.001	0.066
depth	< 0.001	0.061
depth x time	< 0.001	0.044
CESA x time	< 0.001	0.035
CESA x depth	< 0.001	0.015
CESA x concentration	< 0.001	0.014
concentration x time	< 0.001	0.013
CESA x concentration x time	< 0.001	0.007
CESA x depth x time	0.143	0.005
depth x concentration	0.010	0.002
depth x concentration x time	0.834	0.001

Analysis of the obtained η^2 values revealed the following order of effect size on gray value: staining time > type of CESA > CESA concentration ≈ cartilage depth. This suggests that altering the staining time has a more pronounced impact on the gray value compared to modifying the concentration of the CESA solution.

4.6.4 Preferred staining condition

The optimal staining condition is defined by the information that is desired. In case knowledge on the AC volume is required, segmentation of the AC is needed. By adopting a relative low concentration of 6 mgI/mL, segmentation will be facilitated because of the more pronounced contrast difference between subchondral bone and stained AC. In contrast, visualization of the GAG distribution will be facilitated when using a relative high concentration of 24 mgI/mL. The obtained data suggest that a relative high concentration is beneficial for detecting changes in the GAG distribution because of the larger gray value range that is covered (data not shown). However, defining the optimal condition for the visualization of the GAG distribution is challenging because information is lacking about the actual GAG content in each sample. Moreover, the variations in GAG concentration and distribution over the different samples complicate the comparison between the CESAs. In general, this work would benefit from imaging at higher resolution (< 2 μm) in terms of an improved accuracy of gray value distribution and intensity. More specifically, high resolution microCT will improve the detection of local GAG variations and can reveal structural details such as chondrons[h] that are rich in GAGs. [53]

In case of CA4+6I, literature provides evidence that zones with increased X-ray attenuation correspond with high GAG content, but some nuance is in place here.[53, 69] This statement is valid in case equilibrium partitioning is predominantly determined by electrostatic interactions with GAGs and assuming that all GAGs present are saturated with CESA. However, the penetration of the CESA in the AC is also influenced by the composition of the matrix and the water content. As discussed before, the permeability of the matrix reduces with cartilage depth due to the increased steric hindrance

[h] Chondrons consist of a chondrocyte (cartilage cell) and the immediate surrounding extracellular matrix, including collagen fibers and proteoglycans. The chondrocyte is the primary cell type found in AC and is responsible for producing and maintaining the extracellular matrix.

induced by the collagen and the aggrecan network. Therefore, it could be of interest to simultaneously stain the AC matrix with a neutral CESA to map the penetration of a compound through the matrix, which mainly depends on water content and steric hindrance. In this way, the sensitivity of GAG visualization could be improved by normalizing the gray values of AC stained with a cationic CESA with those observed for a neutral CESA. Indeed, Bhattarai *et al.* showed that the sensitivity for GAGs was enhanced by quantitative dual energy microCT for simultaneous quantification of two different CESAs. [42] In this case, both CA4+6I and gadoteridol (non-ionic, gadolinium based) were used simultaneously for staining AC. Thanks to the difference in K-absorption edge, both CESA distributions in the AC matrix could be imaged at the same time by using two different X-ray voltages (50 and 100 kV). The authors were able to improve the sensitivity for GAG visualization after normalization of the gray values of CA4+6I distribution by the gray values for gadoteridol distribution. Indeed, after normalization, an improved correlation between X-ray attenuation and the AC biomechanical properties was observed. However, improved correlations were only observed for the superficial zone (10% of the cartilage thickness). Correlations between biomechanical properties and gray value distributions at the deeper zones were not improved after normalization, which could be due to the low sample size and the fact that the superficial layer controls the cartilage indentation response.

Despite improved sensitivity of CA4+6I was not accomplished after normalization by gadoteridol staining by Bhattarai *et al.*, we hypothesize this approach is still valuable. Provided that degenerated cartilage is also characterized by an higher permeability and an increased water content, this approach could be even more useful when applied to imaging osteoarthritic AC. [44, 160]

4.7 Conclusions

One of the major hallmarks for the early stage of OA is the depletion of aggrecans. Thanks to the negative charge density of the linked GAGs, positive charged CESAs are being developed to map the concentration and distribution of GAGs, and hence aggrecans, in the AC matrix. The goal of this research project was to study the influence of the molecular design of a cationic CESA on the staining potential for AC imaging.

Previous work of the Grinstaff group showed that CA4+6I, bearing four primary ammonium groups, is capable to detect GAGs in AC. Therefore, CESAs that resemble CA4+6I, but having a different iodine content (CA4+3I) or a different positive charge density (CA8+6I) were synthesized. Moreover, the synthesis protocol of CA4+6I was improved by performing the Boc deprotection with HCl gas. In this way, the protocol was shortened and the work-up became more convenient and sustainable.

Phantom solutions of identical iodine concentrations for the different CESAs were evaluated by microCT. Gray values of these solutions were compared with solutions of NaI, which served as the calibrant. In this way, empirical concentrations could be calculated based on the measured gray values. For every CESA, the observed empirical concentrations were close to the theoretical concentrations, which was our starting hypothesis.

Bovine osteochondral plugs were stained in triplicate with solutions of CA4+6I, CA4+3I and CA8+6I over time. Moreover, the influence of concentration and cartilage depth on gray value was investigated. In summary, the following factors were found to have a positive trend with gray value:

- staining time
- concentration
- cartilage depth
- iodine content of the CESA
- positive charge density of the CESA

Analysis of the obtained η^2 values revealed the following order of effect size on gray value: staining time > type of CESA > CESA concentration ≈ cartilage depth.

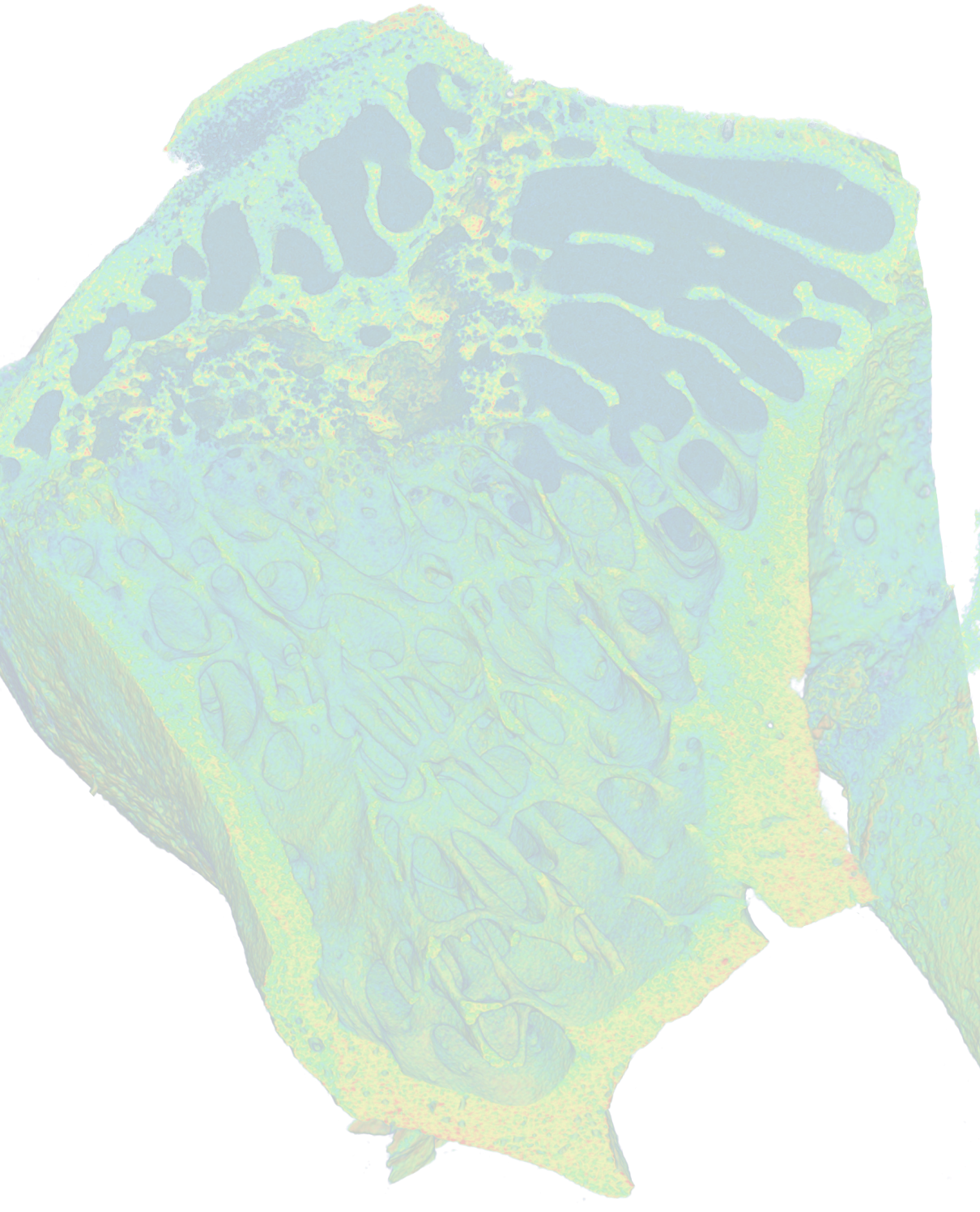
Comparing CESAs, the highest increase in gray value at diffusion equilibrium was observed for CA8+6I, followed by CA4+6I and CA4+3I. In general, gray values observed for CA8+6I and CA4+6I were more closely related compared to CA4+3I, which suggests that the CESA iodine content has a larger influence on the gray value of stained AC than the positive charge density. The data obtained from destaining experiments indicates that CA8+6I showed the highest affinity for GAGs.

Interestingly, looking at the deeper AC zone, the smallest δ value (time to reach 95% of the maximal gray value) was observed for CA4+6I. In addition, the general principle of a compound molecular weight being inversely proportional to its penetration rate was confirmed for the data obtained in the superficial and middle AC zone. Deeper in the AC matrix (90% depth), the electrostatic interaction with the GAGs most probably influences the penetration rate of the CESAs.

Defining the most optimal CESA for the visualization of the GAG distribution is challenging because information is lacking about the actual GAG content in each sample. However, according to the hypothesis that the broader the range of gray value covered, the higher sensitivity to changes in the GAG content, CA4+6I performed best.

The sensitivity of the cationic CESA could be even more improved by simultaneously staining with a non-ionic CESA. In doing so, the observed gray values for the cationic CESA can be normalized by those observed for a neutral CESA. Hence, the influence of steric hindrance and water content on diffusion can be cancelled out.

This work presents several limitations. First, the dataset was not complete due to experimental errors. Second, since we did not perform biochemical assays to determine the actual GAG content, it is hard to define the best condition for the visualization of the GAG distribution. Third, considering the statistical analysis, a MANOVA assumption was violated. Therefore, the outcome of the statistical analysis was interpreted with caution. Fourth, staining experiments were not performed on degraded AC samples to investigate the impact of a reduced GAG content on gray value.



CHAPTER 5

Protein-specific CECT

Potential for 3D visualization of protein distributions using microCT

The content of this chapter is based on unpublished work:

Vangrunderbeeck, S.; Hoffmann D.; Noppe, W.; Kerckhofs G.; De Borggraeve, W.M.

Credit authorship contribution statement

Sarah Vangrunderbeeck: Conceptualization, Investigation, Formal analysis, Data Curation, Writing – Original Draft, Writing – Review & Editing, Project administration. **Delia Hoffmann**: Conceptualization, Validation, Investigation, Data Curation, Project administration. **Wim Noppe**: Investigation, Data Curation, Formal analysis. **Greet Kerckhofs**: Conceptualization, Formal analysis, Writing – Review & Editing, Funding acquisition, Supervision. **Wim De Borggraeve**: Conceptualizatin, Formal analysis, Writing – Review & Editing, Supervision.

5.1 Introduction

Labeling and detection of the distribution of a particular protein in biological tissues is widely used in disease diagnosis by targeting specific markers. Classically, this is performed by tissue sectioning along with immunohistochemistry (IHC). Herein, the protein is recognized by means of antibodies (Abs) that are themselves labelled with a reporter (primary Abs) or that are in turn recognized by a secondary Ab that carries the reporter. [161] The most prevalent reporters are either enzymes that react with a chromogen (chromogenic immunohistochemistry, CIH) or fluorophores (immunofluorescence, IF). Hence, a broad range of Ab-enzyme conjugates is commercially available. Amongst these, horseradish peroxidase (HRP) is one of the most popular, which catalyzes oxidations by hydrogen peroxide.

Literature regarding the translation of IHC to CECT exists, albeit being premature. Only a few examples on the use of Abs for targeted CECT imaging were reported to date. Moreover, challenges related to unspecific labeling and limited tissue penetration depths seem to have hampered further improvement of targeted CECT. In 2008, pioneering work was reported by Brian D. Metscher and Gerd B. Müller who developed a procedure for 3D visualization of protein distributions in chick embryos.[108] The method relies on a whole-mount immunostaining using a primary and a secondary Ab, the latter being conjugated to an HRP enzyme. HRP catalyzes the reduction of dissolved silver ions resulting in precipitation of elemental silver in the close proximity of the secondary Ab conjugate, and hence the targeted antigen. After washing, the tissue was rendered X-ray attenuating at the sites of precipitation. The

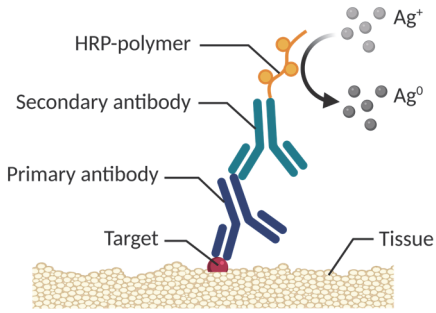


Figure 5.1 Principle of the enzyme-mediated silver reduction at the target site. The target is labeled with a primary Ab, which is on its turn is labeled with a secondary Ab, coupled to HRP. (Created with BioRender.com)

principle of the protocol is illustrated in Figure 5.1.

This approach was used to visualize the distribution of intracellular acetylated α-tubulin and of extracellular type II collagen in chick embryos, shown in Figure 5.2. Although the Ab-HRP conjugates produced an intense, non-diffusible silver precipitate at the sites of the targeted proteins, background deposition was also observed. The unspecific silver precipitation mostly occurred in cavities and on the outer surface of the sample. This unspecific staining is mainly due to non-enzymatic driven reduction of silver rather than unspecific Ab binding. Especially noteworthy about this work is the lack of validation of the experiments performed. More specifically, there is a lack of proof that all targeted proteins were labelled by HRP since the CT images were not compared to immunohistochemistry staining on tissue sections. On the same note, the observed patterns of chondrocytes in the CT images were not proven by comparison to bright-field images. Moreover, the authors did not include negative control experiments to prove that, for instance, endogenous peroxidase was successfully blocked, the secondary Ab did not bind unspecific and the increased X-ray contrast originated from the silver precipitation. Finally, the information provided in the experimental procedures is sometimes ambiguous (*e.g. '*the primary antibody was incubated overnight *or longer'*).

The same Ab-silver labeling approach was used to image and quantify subcellular structures in porous cell cultures. [162] Comparison with optical imaging reference techniques (optical projection tomography and confocal laser scanning microscopy) revealed high morphological similarity. Even though a commercially available tube-source microCT was used, the procedure is limited to porous samples with a small size (< 2 cm). Recently, Cheng and coworkers reported a method to visualize and quantify melanin distribution in whole zebrafish larvae by synchrotron radiation (SR) CT. [163] The method relies on silver reduction by endogenous melanin. Even though the need of labeling is obviated, it is interesting to note that the staining appeared highly specific to melanin. Although microCT imaging of proteins labeled by the Ab-silver method is proven to be feasible, it is important to mention that the limited tissue penetration depth of Abs entails a substantial drawback. Consequently, the current approach is limited to small samples owning an open, porous microstructure.

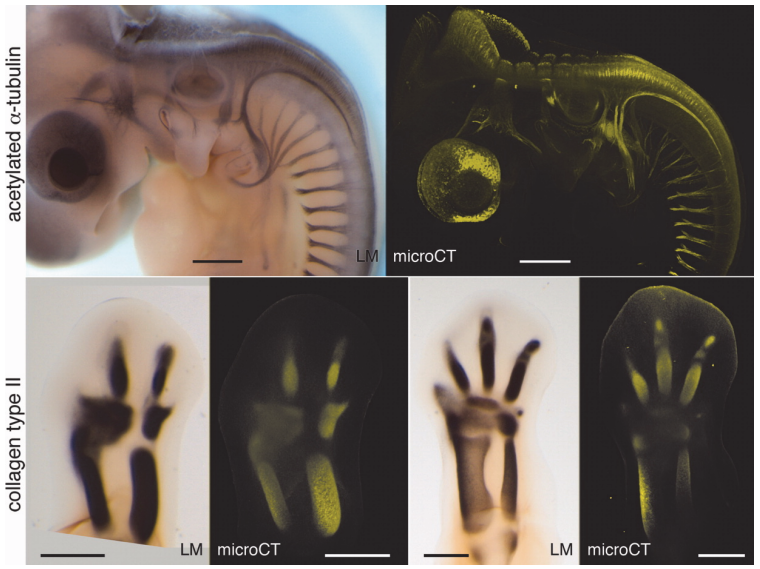


Figure 5.2 Comparison of microCT-based volume renderings and 2D stereomicroscope photographs of the Ab labeling in whole-mount chick embryos. The images of microCT volume renderings indicate the spatial extent of protein distribution in the samples. Top: Light microscopy images (LM) and volume rendering of the microCT scan (CT) showing the distribution of acetylated α-tubulin in the developing chick nervous system at stage 23. The silver staining not only depicts the positions of the cranial and spinal nerves, but also visualizes the rhombomeres and features of the central nervous system and retina. Bottom: Light microscopy images (LM) and volume rendering of the microCT scan (CT) showing the distribution of collagen type II in stage 29 chick forelimbs (left pair) and hindlimbs (right pair). The early chondrogenic domains are demonstrated in the context of the intact limb. Voxel size of all the microCT scans = 5 µm, all scale bars = 500 µm. Reprinted with permission from reference [108]. Copyright © 2011 Wiley-Liss, Inc.

In the last decade, metal nanoparticles with surface modifications have emerged as a powerful tool for targeted CECT. In this view, metal nanoparticles are commonly modified by attachment of polyethylene glycol (PEG), Abs, nucleic acids, peptides, proteins or other biomolecules. This approach is mostly investigated for diagnostic and/or therapeutic purposes in medical applications. Consequently, research in this area is mainly focused on *in vivo* X-ray CT imaging *via* intravenous injection. Besides cardiovascular diseases, studies are predominantly devoted to cancer and related biomarkers. In this regard, surface modified gold nanoparticles gained much attention due to their biocompatibility, high X-ray attenuation and established surface chemistry. The expansion of gold nanoparticles for X-ray imaging has extensively been reviewed by Mahan and Doiron. [164] Besides gold,

nanoparticles based on silver, iron, bismuth, tantalum, tungsten, gadolinium, ytterbium, platinum and lead have been studied for targeted imaging purposes. Excellent reviews by the groups of Cormode and Barber have recently summarized the latest advances in the application of nanoparticles for X-ray CT. [110, 165] Currently, *in vivo* applications of modified metal nanoparticles are still in the preclinical phase due to sub-standard performance for clinical translation. Challenges are related to the required high concentrations, retention time, unspecific bio distribution and toxicity.

The increasing attention *in vivo* imaging gained, together with the recent advances in whole-mount fluorescent immunolabeling, have probably interfered with further improvement of *ex vivo* targeted CECT. Although 3D fluorescent imaging enables visualization of multiple proteins at the same time, the protocol requires optical clearing of the tissue, which is time-consuming and could damage the tissue integrity. [166] Moreover, the imaging modality often suffers from strong background autofluorescence. [167] These limitations could be overcome by further exploiting targeted CECT. In the last couple of years, protein-specific CECT is gaining considerable attention as exemplified by the increasing number of publications on this topic. One recent example from the Lim group is the development of X-ray attenuating peptides targeting type II collagen for AC imaging. [168]

5.2 Objectives and general strategy

The ultimate goal of this research project is to combine the advantages of IHC and CECT by developing staining protocols for protein-specific CECT of biological tissues. In this regard, we aim to visualize the spatial distribution of proteins and their interrelationship with different tissue constituents. Therefore, the main objective is to develop a CESA that both contains a targeting moiety and a moiety that provides X-ray attenuation.

The major challenge of developing protein-specific CECT is the upscaling of 2D (IHC) to 3D imaging, and hence the penetration of the CESA throughout the whole tissue. Moreover, the X-ray attenuating moiety needs to be optimized to prevent unspecific staining. For this purpose, the research project was divided into three objectives:

1. Development of a protocol to improve tissue penetration
2. Development of a peptide-based targeting probe

3. Development of an X-ray attenuating substrate for HRP

As a proof of concept, CD31 was targeted. CD31 is a transmembrane protein that is often used as marker for endothelial cells bordering the lumen of blood vessels.

5.3 Development of a protocol to improve tissue penetration

One of the major hurdles in protein-specific 3D imaging is the commonly encountered scarce penetration of agents in tissues. To tackle this challenge, optimization of the staining protocol and permeabilization of the tissue are currently being studied by one of the colleagues (Dr. Delia Hoffmann – FNRS Postdoctoral fellow). Since this part of the research project is not the focus of this dissertation, results obtained are not covered. For the sake of completeness, this section only contains a brief summary of the envisaged procedures. In terms of optimization of the staining solution, the addition of salts and/or urea to the buffer could be interesting to decrease non-specific interactions between the CESA and the tissue. [169] Besides, different permeabilization protocols are being tested, including repeated freeze-thaw cycles, treatment with DMSO, delipidation methods, addition of detergent and digestion of the extracellular matrix with collagenase or hyaluronidase. [170-173]

5.4 Development of a peptide-based targeting probe

5.4.1 Ab-based probes

Protein-specific staining is most often based on Abs that specifically bind to the protein of interest. However, applying this approach to whole-mount tissue labeling suffers from slow Ab diffusion because of their large size (about 150 kDa). Indeed, whole-mount staining of murine kidney using an Ab-HRP conjugate and 3,3'-diaminobenzidine (DAB) as the revealing agent indicated a slow tissue penetration of the Abs (Figure 5.3).

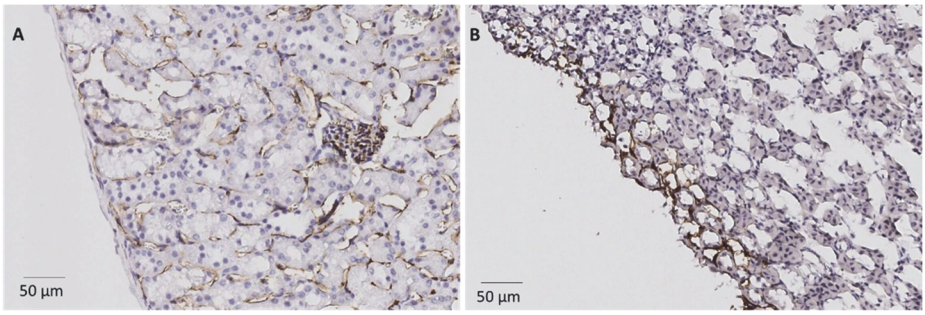


Figure 5.3 A Typical IHC staining on a murine renal cryosection performed with an anti-CD31 primary Ab, an HRP-coupled secondary Ab and revealed with DAB, giving a brown precipitate in close proximity to the antibodies. Counterstaining was performed with Mayer's hematoxylin. **B** Ab diffusion was tested on a murine kidney piece that was permeabilized with Triton X-100, blocked with fetal bovine serum and incubated for 8 days with the same anti-CD31 Ab on a shaker plate at 4°C. The tissue was frozen, sectioned and the diffused Ab was revealed with the same secondary Ab and DAB. Counterstaining was performed with Mayer's hematoxylin. The middle part of the section showed no CD31-specific staining while there was staining at the edge of the tissue, which indicates a slow diffusion.

Therefore, we aim to replace Abs by a smaller protein-specific probe. One approach to reduce the size of Abs is the enzymatic digestion between the antigen-binding fragment (Fab) and the crystallizable fragment. Since the recognition of the Ab is based on the interaction between the Fab and the antigen, the isolated Fab as such could be used as a protein-specific probe. Because of the smaller size, tissue penetration should be improved. However, the avidity of the interaction is reduced because of the single interaction compared to a complete Ab that has two Fabs. To overcome the reduced avidity, several Fabs could be oligomerized. As this approach is not the focus of this dissertation, it will not be further discussed. Instead, we will focus on the use of small peptides rather than (fragments of) Abs as targeting probes.

5.4.2 Peptide-based probes

As discussed above, the tissue penetration of Abs is challenging when staining *ex vivo*. Therefore, we wanted to reduce the size of the protein-binding probe by replacing the Ab by a short peptide sequence. In addition, this approach is interesting since the production of Abs is costly and time-consuming. Once a peptide sequence that shows the required affinity is obtained, it could be attached to a dendrimer consisting of multiple copies of iodinated arenes to confer X-ray attenuation. In case this approach does not provide sufficient X-ray attenuation for detection, a signal amplification strategy based on

enzymatic immobilization could be applied. Herein, the peptide sequence could be attached to an HRP enzyme which catalyzes the oxidation, and hence, immobilization of an X-ray attenuating substrate.

Phage display is a powerful technique to screen and identify short peptides that show affinity towards the protein of interest. The selection is based on protein-protein interactions. Herein, a library is used that consists of genetically modified filamentous bacteriophages (phages[i]). The phages are modified by inserting a foreign DNA fragment in a gene that codes for one of the coat proteins. As a result, fusion proteins are produced by the phage and the encoded peptides are displayed on the surface of the phage. [174] The physical link between the genotype (encode DNA) and the phenotype (the displayed peptide) is a fundamental concept that allows high-throughput screening. Thanks to the broad use of phage display, various combinatorial peptide libraries are generated by inserting random DNA sequences in the viral genome. Such phage libraries contain up to 10^{10} variants, providing functional access to the displayed peptides. [175] Most frequently used libraries contain peptides displayed on the pIII coat protein (3-5 copies per phage) or on the pVIII coat protein (about 2700 copies per phage). [176] A M13 bacteriophage with peptides displayed on the pIII coat proteins is illustrated in Figure 5.4.

Peptides displayed on the phage surface that show affinity to the target are then selected and enriched in a screening process, which is called biopanning. [177] In short, a library is incubated with an immobilized target. Phages that show

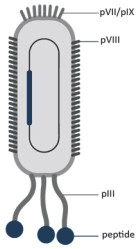


Figure 5.4 Illustration of a genetically modified M13 bacteriophage bearing displayed peptides on the pIII coat protein. (Created with BioRender.com)

[i] A phage is a virus that exclusively infects bacteria.

affinity towards the target are retained, unbound phages are removed by washing. Phages that are bound to the target are subsequently eluted and amplified in bacteria, resulting in a new library containing phages that show an increased affinity. Figure 5.5 illustrates the biopanning process using a phage library containing displayed peptides on the pIII coat protein. Three to five biopanning cycles are often required to enrich the highly specific binding phages. Finally, the resulting phages are cloned and the affinity towards the target of these individual clones is assessed by an indirect ELISA (enzyme-linked immunosorbent assay).

In short, ELISA is a plate-based technique for the detection and quantification of an antigen (the target) that is immobilized on a solid surface (Figure 5.6).[178] Next, the plate is incubated with a primary Ab that specifically bind to the immobilized target. After removing the unbound Abs by washing, the plate is incubated with a secondary Ab that specifically binds to the primary Ab. This secondary Ab is conjugated to a reporter enzyme, such as HRP. After removal of the unbound secondary Abs, detection is achieved by assessing the conjugated enzyme activity through incubation of the plate with an appropriate substrate that produces a detectable product upon reaction, which is catalyzed by the enzyme.

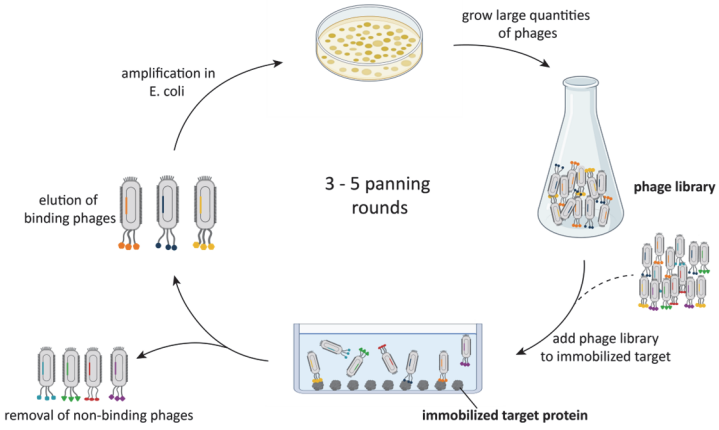


Figure 5.5 Illustration of a biopanning process to select and enrich genetically modified phages that show affinity to an immobilized target. (Created with BioRender.com)

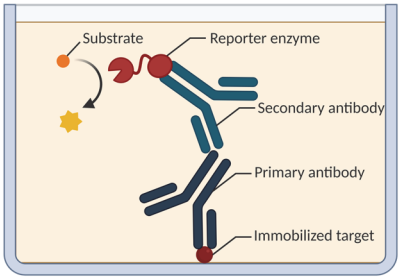


Figure 5.6 Illustration of indirect ELISA. (Created with BioRender.com)

The primary structure of the peptide inserts can be obtained by DNA sequencing of the isolated phage clones. Finally, the peptide sequence of the insert is determined by translating the DNA sequence of the coat protein bearing the insert.

In general, phage display facilitates the straightforward identification of peptide sequences that possess specific binding affinity towards the target entity. We aim to use this powerful technique to identify CD31-specific peptide sequences using a phage display library that expresses 15-mer peptides in the pIII coat protein (p3L15).

5.4.3 Selection of KLH-specific phage clones by phage display

In order to validate the technique, as a negative control, additional protein-specific probes need to be selected against a protein that is not expressed in human or mice. Therefore, we decided to start with identifying peptides that bind keyhole limpet hemocyanin (KLH) via phage display using the p3L15 library. Three biopanning rounds were performed to identify phages that bind to KLH with high affinity. These phages were cloned using TG1 cells, and 13 randomly picked clones were isolated. The DNA was isolated and subsequently subjected to replication and sequencing. Based on the DNA sequence of the isolated phage clones, the sequence of the corresponding peptide inserts could be determined. Nine unique sequences were identified (Table 5.1). The peptide inserts PI204, PI209 and PI303 could be assigned to the same family because they contain the consensus sequence PVLXXXXGSGHTVAS with no similarity to the others. Similarly, the peptide inserts PI208, PI302 and PI309 share the consensus sequence RGGXXXXCCLCLWWA.

Table 5.1 Sequences of the peptide inserts of isolated clone phages that bind to KLH, selected by phage display using the p3L15 library. Peptide sequences belonging to the same family are assigned identical colors.

Phage clone	Name peptide insert	Sequence peptide insert	Occurrence
PC201	PI201	VSFSSVPHIVVFRRS	2
PC203	PI203	SAFRSVSVSGRVLRA	1
PC204	PI204	PVLSFTRGSGHTVAS	2
PC208	PI208	RGGRGLRCCLCLWWA	1
PC209	PI209	PVLRLGQGSGHTVAS	1
PC210	PI210	TVGVGSFPRLFMHSP	1
PC302	PI302	RGGRFLLCCLCLWWA	1
PC303	PI303	PVLIFTRGSGHTVAS	3
PC309	PI309	RGGLVGLCCLCLWWA	1

Finally, the affinity of the isolated phage clones was assessed by ELISA. In brief, dilution series of KLH are incubated with the phage suspension. Next, an Ab coupled to HRP is added, which specifically binds to the phage. Lastly, a chromophore is added, which typically changes color upon reaction with HRP. We used *o*-phenylediamine as the chromophore, which is converted to 2,3-diaminophenazine upon oxidation by hydrogen peroxide catalyzed by HRP. [179] 2,3-diaminophenazine is a yellow/orange dye that show an absorbance maximum at 492 nm, detectable by an ELISA plate reader. Bovine serum albumin (BSA) was used as the negative control. The different phages clones were assessed in three different batches and the results of these assays are shown in three corresponding graphs in Figure 5.7.

As the concentration of the phages increased from 0.078 x 10^{11} phages/mL to 10.000 x 10^{11} phages/mL, an increase of absorption at 492 nm was observed for all the phage clones, indicating more phages were captured onto KLH. For none of the phages, an increase in absorbance was observed when incubated with BSA, indicating that binding did not occur between the phages and BSA. Therefore, we can conclude that all the phages tested specifically bind to KLH. It is important to note that it is impossible to compare phage clones that were assessed in different batches.

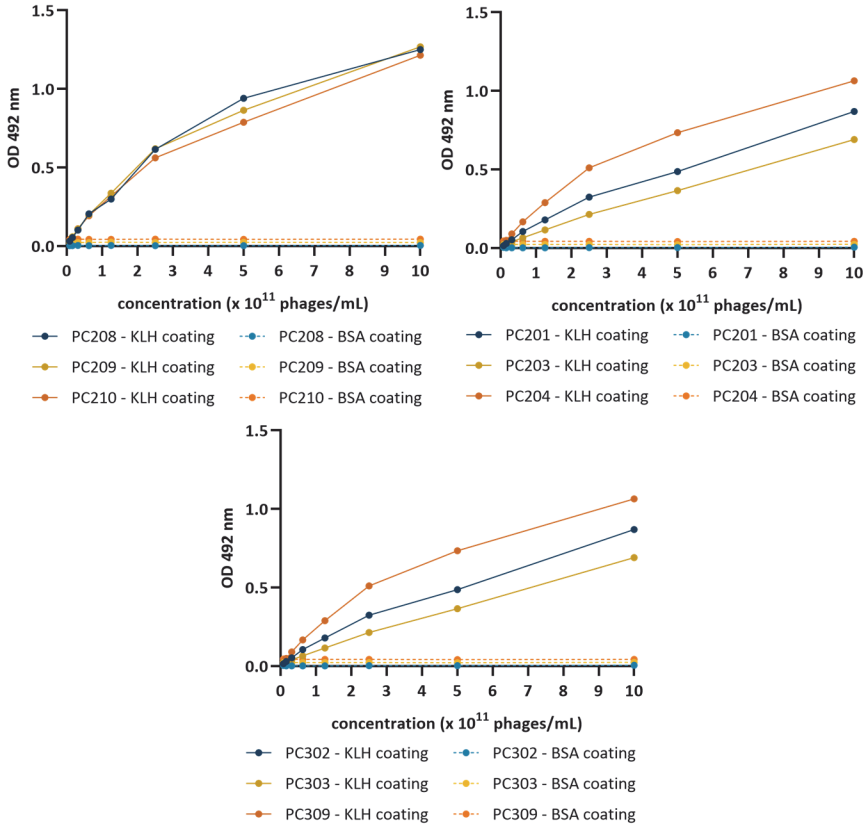


Figure 5.7 Affinity of identified phage clones for KLH and BSA assessed by ELISA.

The affinity of the phage clones towards KLH was also assessed by means of a surface plasmon resonance (SPR) biosensor. The affinity experiments were performed by Dr. Wim Noppe (IRF Life Science, KU Leuven). To this end, KLH was immobilized on the sensor surface. Next, a solution containing 5 x 10^{11} phages/mL was injected on the surface (association phase). Finally, a buffer was injected onto the surface to remove non-specifically bound components (dissociation phase). Calibration of the biosensor was performed for each phage clone individually. The obtained data were corrected for nonspecific binding and normalized to enable comparison between the different phage clones. Correction for nonspecific binding was performed by incubation of the phage clones on the sensor surface that was coated with a SuperBlock buffer. The results are shown in Figure 5.8. The deduction of the association can be readily inferred from the response of surface plasmon resonance (SPR),

denoted by the alteration in the SPR angle (referred to as the SPR response). [180] The magnitude of this shift directly corresponds to the strength of the affinity between the phage clone and HRP. [181] Notably, phage clones PC201 and PC210 exhibited the greatest affinity towards KLH. The dissociation phase is barely discernible on the curve, as there was minimal decrease in signal intensity, thereby suggesting strong binding for all investigated phages.

In the following section, the affinity of an isolated peptide sequence for KLH was analyzed and compared with the corresponding phage clone in the following section. To this end, PI210, which is the peptide sequence of PC210, was chosen to be further analyzed based on the relatively low amount of apolar aminoacids present and the observed affinity towards KLH.

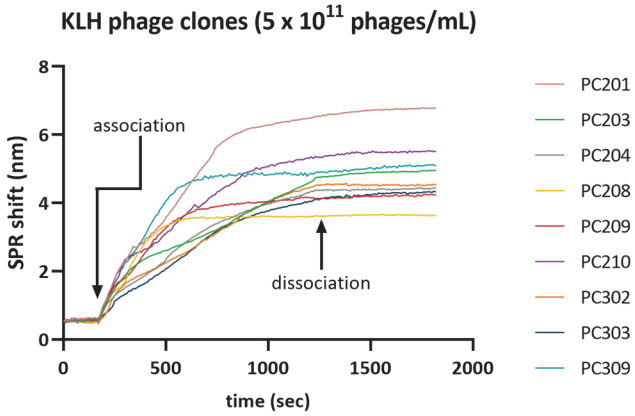
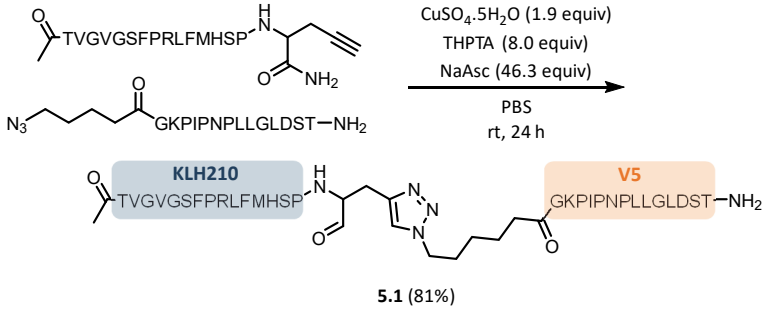


Figure 5.8 Affinity of identified phage clones for KLH assessed by biosensor.

5.4.4 Affinity comparison between phage clone and isolated peptide

The affinity towards KLH of an isolated peptide insert and the corresponding phage was studied by ELISA. As mentioned in the previous section, the peptide insert PI210 was chosen to be compared to the corresponding phage clone PC210.

In order to be detectable by ELISA, the small peptide PI210 was linked to a V5 tag to be recognizable by Abs. The V5 tag is a peptide sequence consisting of 14 amino acids (GKPIPNPLLGLDST), which is commonly used for detection by Abs. [182] PI210 attached to L-propargylglycinamide at the C-terminus and the V5-tag capped at the N-terminus with an azide were purchased as such. The



Scheme 5.1 Coupling of PI210 peptide to V5 tag via CuAAC. (Isolated yields).

PI210 was coupled to a V5 tag via the copper(I)-catalyzed alkyne-azide cycloaddition (CuAAC), as illustrated in Scheme 5.1.[183]

The binding of **5.1** was evaluated by ELISA using a mouse anti-V5, conjugated to HRP and compared to the binding of the corresponding phage clone PC210, using a mouse anti-M13, conjugated to HRP. 3,3',5,5'-tetramethylbenzidine was used as the revealing agent, which is converted to 3,3',5,5'-tetramethylbenzidine diimine upon oxidation by hydrogen peroxide catalyzed by HRP. 3,3',5,5'-tetramethylbenzidine diimine is a blue dye that shows an absorbance maximum at 450 nm, which is detectable by an ELISA plate reader.

The results of the ELISA are summarized in Figure 5.9. For comparison, the solution of 1.66 x 10^{-9} mmol/mL **5.1** contains the same amount of molecules as the amount of phages in the 10.0 x 10^{11} phages/mL solution. Specific binding to KLH was observed for the phage clone PC210. For an increasing concentration of phages, an increase in optical density (OD) was observed for the KLH coating, while none of the concentrations studied showed an increase in OD for the BSA coating. The peptide insert **5.1** did not bind specifically to KLH because a similar OD was observed for the KLH as for the BSA coating. For the highest concentration of **5.1**, an increase in background noise was observed. Although the same amount of molecules/phages are present when comparing 1.66 x 10^{-9} mmol/mL of **5.1** with 10.0 x 10^{11} phages/mL of PC210, the binding of **5.1** to KLH was not as strong as PC210. However, it is important to note that every phage clone contains 3 to 5 copies of the peptide insert, which implies that the amount of peptides present per entity is higher in case of the phage clone. Nevertheless, binding was not observed for a concentration of **5.1** that was 1000 times higher than the highest measured concentration of PC210. The reduced binding of **5.1** compared to PC210 could

be ascribed to the lower avidity. Moreover, the increased conformational flexibility of the peptide in **3.1** compared to PC210 could also play a role in decreasing the affinity.

The use of isolated peptides as probes for protein tagging requires a thorough understanding of the factors that influence protein recognition before moving on. This led to the realization of the necessity to optimize parameters such as concentration, avidity and conformational flexibility and hence, the associated time and labor. Therefore, the development of a peptide-based probe for protein-specific staining was put on hold and another strategy based on enzymatic labels was explored in the next section.

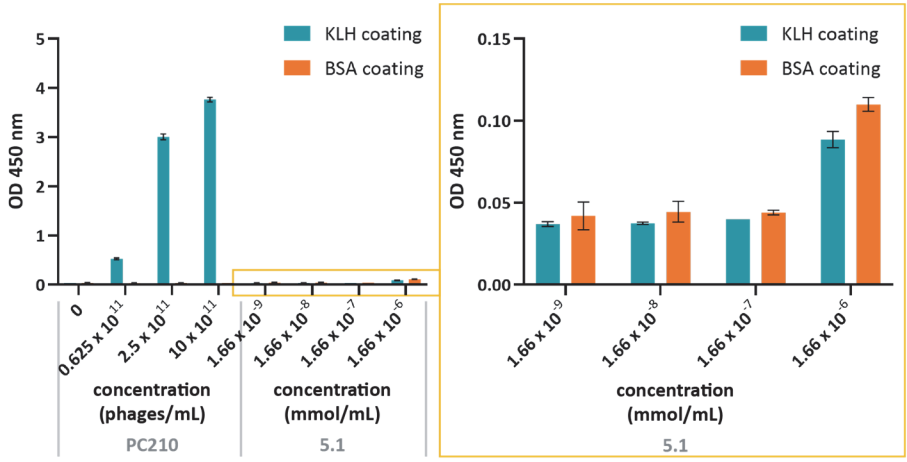


Figure 5.9 Evaluation of the binding of 5.1 compared to the corresponding phage clone PC210 by means of ELISA.

5.5 Development of an X-ray attenuating substrate for HRP

As discussed in section 5.1, precedent literature for protein-specific CECT based on HRP-labeled targets exists. This approach is interesting because it induces a local accumulation of the metal, and hence an amplification of the X-ray attenuation. Nonetheless, unspecific metal precipitation was observed in cavities and on the outer surface of the sample. Also, the use of commercial immunodetection kits often require the successive incubation of the sample with different reagents. These reagents need to penetrate the sample separately, which is time-consuming and raises the amount of parameters and

hence the complexity of the protocol. Lastly, the intense, black color of the metal precipitate could render a potential second staining more invisible in case of overlap, which complicates the analysis.

In house performed protein-specific whole-mount staining using the same enzyme metallography immunodetection kit as previously reported indicated that the silver ions did not penetrate the tissue completely.[108] Moreover, when the same kit was tested on histological sections, unspecific staining was observed. Given these observations and the reported disadvantages, we aimed to develop an X-ray attenuating compound that accumulates in close proximity of the protein of interest, which shows a good tissue penetration and no unspecific staining.

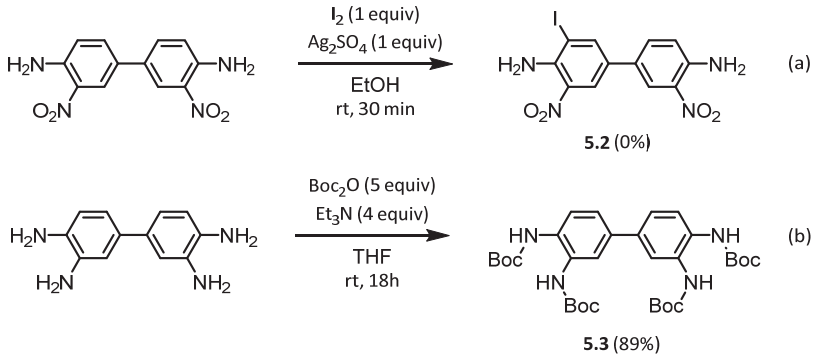
5.5.1 Iodination of 3,3'-diaminobenzidine

3,3'-diaminobenzidine tetrahydrochloride (DAB) is a commonly used chromogen in IHC to stain antigens labeled with HRP.[184] Upon oxidation by hydrogen peroxide, which is catalyzed by HRP, DAB polymerizes and forms a dark brown insoluble precipitate. Iodination of DAB was investigated to introduce X-ray attenuating properties. Iodine is considered the least reactive halogen in electrophilic aromatic substitution, hence aromatic iodination using iodine is considered challenging. Therefore, the direct introduction of iodine in aromatic compounds traditionally requires a Lewis acid or a strong oxidizing agent such as nitric acid, sulfuric acid or hydrogen peroxide.[185] Two literature procedures were employed for the iodination of DAB (Table 5.2). A first method is based on the protocols reported by Gallo *et al.* and Ferreira *et al.*, which involves the use of iodine and hydrogen peroxide for iodination of heteroaromatic compounds.[186, 187] The second method is based on the di-iodination of 2,3-diaminophenazine using iodine monochloride (ICl) and Et_3N.[188] Unfortunately, for none of the performed procedures iodinated DAB was obtained. Instead, black precipitation was observed indicating the presence of the oxidized DAB polymer.

Table 5.2 Screening of reaction conditions for the iodination of DAB. Scale of the reactions: entry 1, 1 mmol; entry 2, 1 mmol.

entry	Iodine source	Additive	Solvent	Temp. (°C)	Time	Ref.
1	I_2 (6 equiv)	H_2O_2 (4 equiv)	CH_3CN : H_2O (1:1)	80	2h	186, 187
2	ICl (2.5 equiv)	Et_3N (2.5 equiv)	THF	rt	3.5h	188

Since DAB is easily oxidized, alternative strategies were sought. One approach, based on the work published by Sy, involved the iodination of 3,3'-dinitrobenzidine using iodine and silver sulfate (Scheme 5.2a).[189] Formation of the product was not observed, even not at increased temperature (60 °C) or after a longer reaction time (3 days). Instead, brown precipitation was observed, which corresponded to a mixture of 3,3'-dinitrobenzidine and the oxidized product. Therefore, the following strategies relied on the iodination of *N,N',N'',N'''*-tetrakis(*tert*-butyloxycarbonyl)-3,3'-diamino-benzidine (**3.3**), which was obtained by mixing DAB with Boc_2O in the presence of triethylamine (Scheme 5.2b).[190] Table 5.3 gives an overview of the different conditions for the iodination of **5.3**.



Scheme 5.2 (a) Iodination of 3,3'-dinitrobenzidine and **(b)** *N*-Boc protection of DAB yielding *N,N',N'',N'''*-tetrakis(*tert*-butyloxycarbonyl)-3,3'-diamino-benzidine. (Isolated yields).

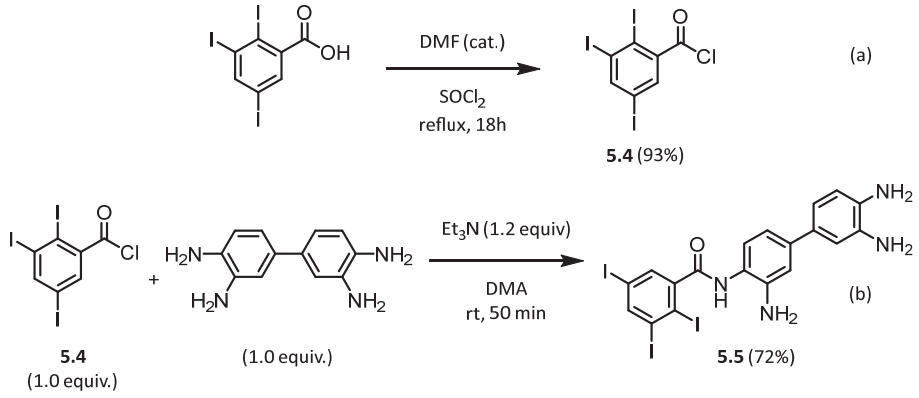
Table 5.3 Screening of reaction conditions for the iodination of *N*,*N*',*N*'',*N*'''-tetrakis(*tert*-butyloxycarbonyl)-3,3'-diamino-benzidine. Scale of the reactions: entry 1, 0.15 mmol; entry 2, 0.2 mmol; entry 3, 0.2 mmol; entry 4, 0.5 mmol.

entry	Iodine source	Additive	Solvent	Temp. (°C)	Time	Reference
1	I_2 (6 equiv)	H_2O_2 (4 equiv)	MeCN : H_2O (1:1)	80	2h	[186, 187]
2	ICl (2.5 equiv)	Et_3N (2.5 equiv)	THF	rt	3.5h	[188]
3	NIS (4 equiv)	$TsOH.H_2O$ (10 mol%)	THF : MeOH (1:1)	rt	25h	[191, 192]
4	NIS (4 equiv)	$AgNTf_2$ (10 mol%)	THF	36	4h	[193]

We were unfortunately unable to observe product formation for the studied conditions. For entries 1, 2 and 4 no conversion was observed since mainly starting material could be identified *via* NMR and LC-MS. Installing iodine on the 2- and/or 5-position of **5.3** will be less favored compared to DAB since the *N*-Boc group increases steric hindrance and it reduces the nucleophilic reactivity of the C-2 and the C-5 positions. The combination of both factors could be a plausible explanation for the failure of these reactions. Entry 3 resulted in a very complex reaction mixture, and black precipitation was observed. It is hypothesized that *p*-toluenesulfonic acid monohydrate ($TsOH.H_2O$) was able to deprotect some of the *N*-Boc groups of **5.3**, giving rise to the oxidized polymer formation. As a result, the synthesis of iodinated DAB was abandoned and a new strategy for derivatizing DAB towards an X-ray attenuating revealing agent for HRP was explored.

5.5.2 Attachment of an X-ray attenuating core to DAB

The iodination of DAB, as seen in the previous section, has some inherent drawbacks due to oxidation as the main side reaction. Therefore, a different strategy was anticipated, focusing on the attachment of an X-ray attenuation core to DAB. To this end, 2,3,5-triiodobenzene was adopted as the X-ray attenuating core. Therefore, commercially available 2,3,5-triiodiobenzoic acid was converted to the corresponding acyl chloride **5.4** by reflux in thionyl chloride (Scheme 5.3a). Next, DAB was coupled with **5.4** in the presence of Et_3N, resulting in **5.5** (Scheme 5.3b).



Scheme 5.3 Attachment of 2,3,5-triiodobenzoyl to DAB. (Isolated yields).

We wanted to test compound **5.5** as a revealing agent for antigens that were labeled with HRP. According to the IHC protocol, a 200 mM stock solution of **5.5** was made in DMSO. As a positive control, a 200 mM stock solution was made of DAB.[j] **5.5** was barely soluble in DMSO. Even if the solvent volume was doubled, a white turbid solution was obtained. Precipitation was observed when a 1:25 dilution was made in PBS. Notably, DAB dissolved in DMSO gave a transparent solution, even when it was diluted afterwards in PBS (1:25). Since **5.5** was not soluble in DMSO nor in water, it could not be tested as a revealing agents on sections.

In view of the encountered intricacies of iodination of DAB and the poor solubility of **5.5**, the derivatization of DAB towards an X-ray attenuating substrate for HRP was halted. Instead, tyramine was selected to derivatize in the next section.

5.5.3 Screening of commercially available iodinated tyrosine analogues

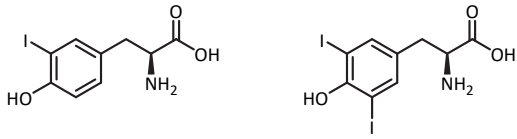
HRP is known to catalyze the oxidative dimerization of phenolic compounds. In this regard, tyramine (4-(2-aminoethyl)phenol) coupled to a reporter was adopted as a substrate for HRP.[194, 195] Upon oxidation of tyramine by hydrogen peroxide, a reactive free radical is created that can covalently bind to electron-rich residues, such as tyrosine, in close proximity of the HRP-labeled epitope.

[j] The same vial of DAB was used for the synthesis of **5.5** as for the positive control for making the stock solution in DMSO according to the IHC protocol (Sigma-Aldrich, cat# D8001, lot#WXBD3217V).

This amplification approach, known as catalyzed reporter deposition (CARD), is fundamentally different from chromogens such as DAB, since it does not rely on precipitation.

Although iodination of the phenolic moiety in tyramine could hamper the oxidative dimerization, we wanted to verify whether commercially available compounds 3-iodo-L-tyrosine (**5.6**) and 3,5-diiodo-L-tyrosine (**5.7**) could be used as a substrate for HRP (Figure 5.10). For sake of simplicity, we wanted to stain endogenous peroxidase activity instead of labeling a specific protein by means of HRP functionalized Abs. In this way, the amount of parameters is reduced since the endogenous peroxidase itself is able to oxidize (derivatives of) tyramine. Peroxidases are present in roughly all living organisms and are part of a large family of isoenzymes. Depending on the type of organism, peroxidases have a broad range of metabolic activities and distributions in tissues.[196]

Fixed murine kidneys, cut in half, were incubated at room temperature for five days with a borate buffered saline solution containing 0.0035% hydrogen peroxide and 1 mM **5.6** or **5.7**. As a negative control, borate buffered saline solution with 0.0035% hydrogen peroxide was used. After washing with PBS, the kidneys were imaged by microCT (see section 7.5.7 for scanning parameters). Representative transverse CT images are shown in Figure 5.11. Quantification of mean gray value was obtained by averaging the gray value of profile surfaces of 10 different slices. Unfortunately we were unable to observe an increase in contrast for the samples stained with **5.6** and **5.7**. Based on an equivalence test using an equivalence bound of 8[k], the mean gray value



5.6 **5.7**

Figure 5.10 3-iodo-L-tyrosine (**5.6**) and 3,5-diiodo-L-tyrosine (**5.7**).

[k] The mean gray value was obtained by averaging the gray value of profile surfaces of 10 different slices across the sample. The equivalence bound was set to be 10 times the average of the standard deviation (= 0.837) of the profile surfaces of the negative control sample (significance level $\alpha = 0.05$).

of **5.6** and of **5.7** were found to be equivalent to the mean gray value of the negative control, which means that no significant difference could be observed. An increase in contrast was even not observed when regional analyses were performed on the border of the samples stained with **5.6** and **5.7**. In order to circumvent limitations related to penetration, microCT imaging of a tissue section stained with compounds **5.6** or **5.7** could help in evaluating the staining mechanism.

The absence of staining throughout the sample could be explained by hampered penetration or difficulties with covalent attachment of **5.6**/**5.7** to the tissue, or a combination of both. Oxidation of *o*-iodo-L-tyrosine is thought to be more difficult than oxidation of L-tyrosine due to the decreased electron density. Therefore, we prefer derivatizing tyramine at the primary amine side rather than at the phenolic side, which is the subject of the next section.

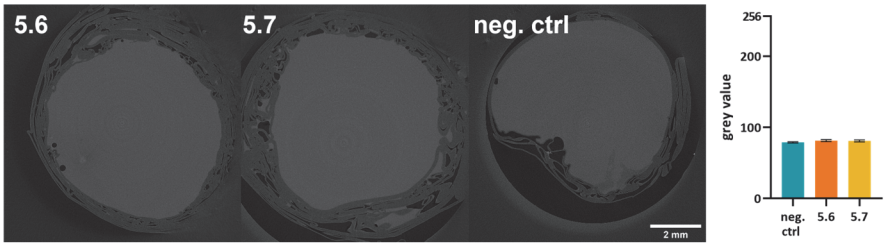
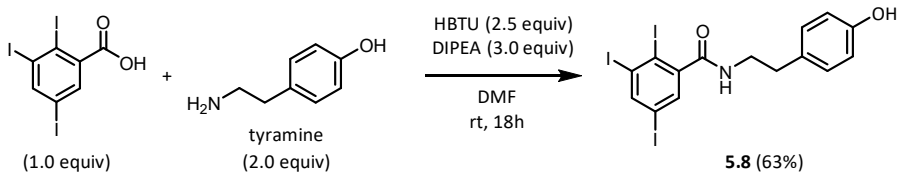


Figure 5.11 Representative transverse CT images of murine kidneys stained with compounds **5.6** (left), **5.7** (middle) and borate buffered saline as negative control (right), along with the quantification of mean gray values. Quantification of mean gray value was obtained by averaging the gray value of profile surfaces of 10 different slices. Data are represented as average ± sd. An equivalence test (two-one-sided t-tests) was performed for statistical analysis (significance level $\alpha = 0.05$).

5.5.4 Attachment of an X-ray attenuating core to tyramine

Conjugates of tyramine are commonly prepared by acylation of the primary amine with *N*-hydroxysuccinimide esters of the reporter.[197] CARD was originally disclosed by Bobrow *et al.* with biotin as the reporter.[198] At low concentrations, the authors reported that the biotinyl-tyramide was successfully covalently immobilized on a solid surface coated with proteins. Finally, they aimed to amplify the signal by coupling the biotinylated surface with streptavidin-enzyme reporters. Nowadays, a broad array of alternative reporters are commercially available. Among these, fluorophores are the most popular.

We aimed to synthesize an X-ray attenuating tyramide conjugate. In this regard, we first synthesized compound **5.8** with 2,3,5-triiodobenzyl moiety as the reporter. As illustrated in Scheme 5.4, 2,3,5,-triiobenzoic acid and tyramine are conjugated *via* the formation of an amide bond by means of a coupling reagent.



Scheme 5.4 Synthesis of 2,3,5-triiodobenzyl-tyramide conjugate using 2-(1*H*-Benzotriazole-1-yl)-1,1,3,3-tetramethyluronium hexafluorophosphate (HBTU) as the coupling reagent and N,N'-diisopropylethylamine (DIPEA) as the base. (Isolated yields).

The X-ray attenuating properties of compound **5.8** were assessed by imaging a 100 mM solution in DMSO, and compared with DMSO as a negative control (see section 7.5.7 for scanning parameters). As can be seen in Figure 5.12, a significant increase in gray value was observed for the solution containing **5.8**, compared to DMSO.

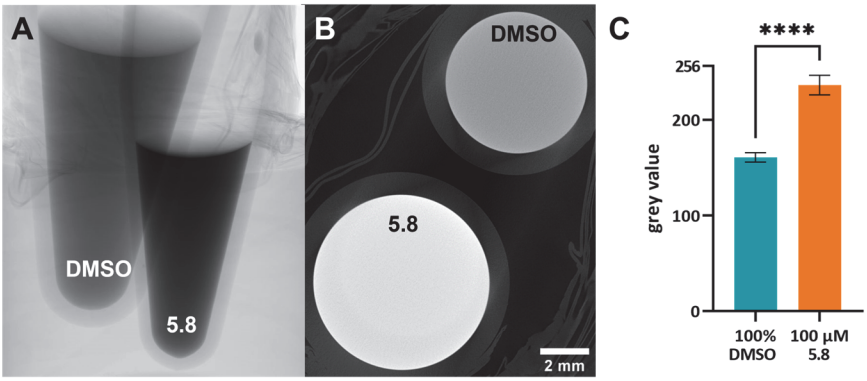
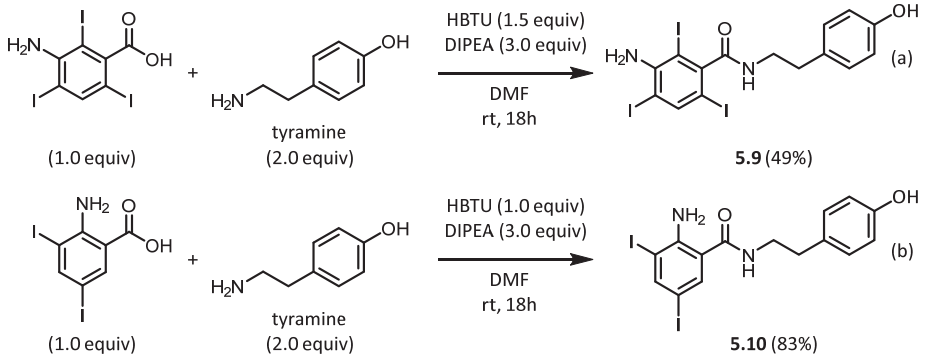


Figure 5.12 Evaluation of X-ray attenuation of compound **5.8** and comparison with DMSO by microCT. **A** Radiograph of DMSO and a 100 mM solution of **5.8** in DMSO. **B** Representative slice of a DMSO and a 100 mM solution of **5.8** in DMSO. Scale bar = 2 mm. **C** Quantification of gray value of DMSO and a 100 mM solution of **5.8** in DMSO, obtained by averaging the gray value of a profile surface of 9 different slices. Data are represented as average ± sd. An unpaired t-test was performed for statistical analysis. Significance is indicated as followed: ****p<0.0001 (significance level $\alpha = 0.05$).

Next, we attempted to use compound **5.8** as the X-ray revealing agent for an HRP-labeled tissue sample. According to the IHC protocol, the 100 mM stock solution needs to be diluted to 1 mM in PBS + 0.0035% hydrogen peroxide. However, precipitation was observed under these conditions. Alternative solvents were screened for the dilutions: water, borate buffered saline and mixtures of PBS and DMSO. The following mixtures of DMSO in PBS were tested: 20%, 40% and 60% DMSO. Unfortunately, precipitation was observed for all the screened solvents, albeit minimally for the 60% DMSO in PBS mixture. Using a solvent with a higher concentration of DMSO is not an option due to protein instability of HRP and loss of enzyme activity.[199] Due to the inability of **5.8** to penetrate the tissue, we were unable to perform the staining experiment to reveal HRP.

In order to increase its solubility in water, we wanted to modify compound **5.8**. It is appropriate to not modify the phenolic side in **5.8**, and hence its oxidation potential to prevent hampered oxidation. Therefore, we opted to add an amine to the iodinated core. The reason was twofold: introduction of both a hydrophilic group and a handle for further modification. Based on commercial availability, compounds **5.9** and **5.10** were synthesized using the same approach as for **5.8** (Scheme 5.5).

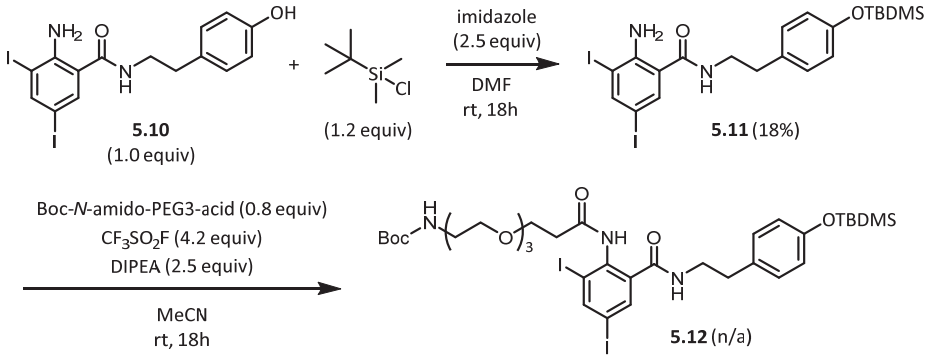


Scheme 5.5 Synthesis of **(a)** 3-amino2,4,6-triiodobenzyl-tyramide conjugate and **(b)** 2-amino-3,5-diiodobenzyl-tyramide conjugate using HBTU as the coupling reagent and DIPEA as the base. (Isolated yields).

We were unfortunately unable to dissolve **5.9** nor **5.10** in water. Even in acidic conditions (1M HCl), none of them dissolved. In an attempt to improve the water solubility of compound **5.9**, we aimed to reduce the amide. First, $LiAlH_4$ in THF was used as the reducing agent. The obtained reaction mixture was

complex since not only the corresponding amine was obtained, but also a mixture of the non-iodinated product (results not shown). In order to prevent overreduction, borane-tetrahydrofuran was tried for amide reduction. Despite the milder conditions, a mixture of compounds derived from overreduction was obtained (results not shown). Therefore, the following paragraph will discuss the attempts to improve water solubility through attachment of a short polyethylene glycol (PEG) unit.

We attempted to form the amide bond between Boc-*N*-amido-PEG3-acid and **5.9** or **5.10** by means of HBTU and DIPEA using the same conditions as in Scheme 5.5b. Sadly, analysis of both reaction mixtures by LC-MS and NMR indicated no product formation (results not shown). The absence of conversion could be attributed to the poor nucleophilicity of the electron-deficient amine along with the steric hindrance caused by the ortho-substituted iodine atom(s). In this regard, acyl fluorides sparked our interest because of their relative small size and high reactivity towards sterically hindered amines.[200, 201] Therefore, we wanted to explore activation of the carboxylic acid in Boc-*N*-amido-PEG3-acid by *in situ* acyl fluoride formation and immediate reaction with the amine of **5.9**. The acyl fluoride can be obtained by reacting this carboxylic acid with trifluoromethanesulfonyl fluoride gas (triflyl fluoride gas, CF_3SO_2F) in a two-chamber reactor.[202] First, the phenol in **5.9** needed to be protected to prevent triflate formation or esterification by reaction with triflyl fluoride gas. This was done by *tert*-butyldimethylsilyl (TBDMS) ether formation, yielding **5.11** (Scheme 5.6).[203] Second, the carboxylic acid in Boc-*N*-amido-PEG3-acid was transformed *in situ* into the acyl fluoride *via* reaction with triflyl fluoride. Triflyl fluoride gas was generated *ex situ* by mixing *N*-phenyltrifluoromethanesulfonimide and potassium bifluoride. Without isolation of the generated acyl fluoride, amidation occurred by nucleophilic attack of the amine of **5.11**.

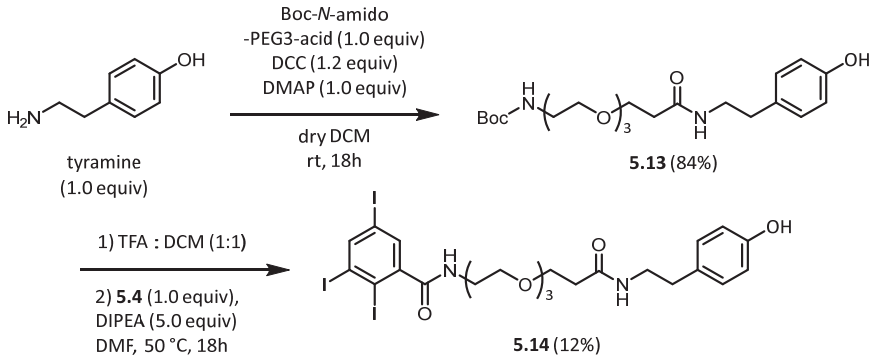


Scheme 5.6 Attempted synthesis of 2-(Boc-*N*-amido-PEG3-amido)-3,5-diiodobenzamide-tyramide conjugate. (Isolated yields).

Unfortunately, a complex reaction mixture was observed when analyzed by LC-MS. Besides the product **5.12**, starting material and other side products could be identified that hindered the reaction outcome. The origin of side product formation is probably due to a combination of deprotection of the TBDMS ether and possible subsequent triflation. Moreover, the compound consisting of **5.9** with two Boc-*N*-amido-PEG3-acyl units was also identified, which is probably a result of simultaneous esterification at the phenol and amidation at the aniline. The TBDMS deprotection is thought to be due to the fluoride-mediated cleavage of silyl ethers. Product isolation was found to be arduous, yet an alternative approach was sought that could reduce the amount of side products.

The amide bond formation with an ortho-iodine-substituted aniline has some inherent drawbacks due to the reduced reactivity, as discussed earlier. Therefore, the order of the ligation of the three different components was reversed. First, tyramine was attached to Boc-*N*-amido-PEG3-acid, using DCC as the coupling reagent, resulting in the pegylated tyramide **5.13** (Scheme 5.7). After *N*-Boc deprotection under acidic conditions, the primary amine was acylated with **5.4** in the presence of DIPEA, affording compound **5.14**.

The X-ray attenuating properties of compound **5.14** were assessed by microCT imaging of a 100 mM solution in DMSO, and compared with a 100 mM solution of tyramine in DMSO as a negative control (see section 7.5.7 for scanning parameters). As can be seen in Figure 5.13, a significant increase in gray value was observed for the solution containing **5.14**, compared to tyramine. It should be noted that that this experiment is rather a proof of concept than a representation of tissue staining since the concentration used is relative high and probably difficult to emulate in tissue staining.



Scheme 5.7 Synthesis of 2,3,5-triiodobenzamide-PEG3-tyramide conjugate. (Isolated yields).

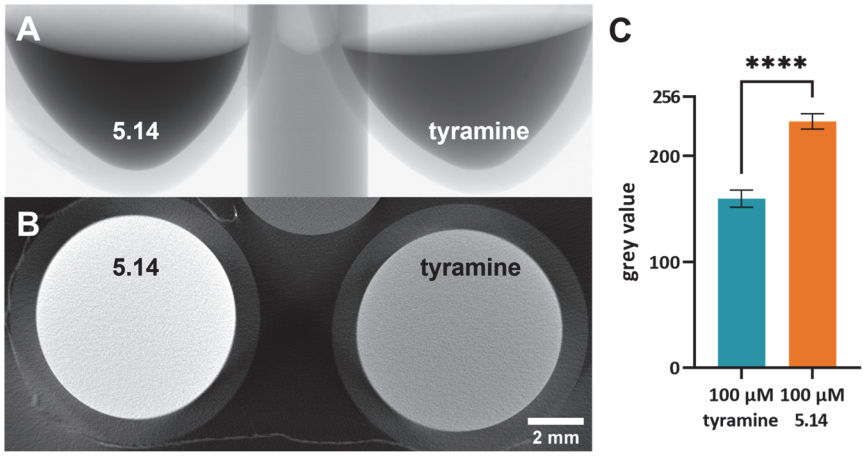


Figure 5.13 Evaluation of X-ray attenuation of compound **5.14** and comparison with tyramine by microCT. **A** Radiograph of a 100 mM solution of tyramine and a 100 mM solution of **5.14** in DMSO. **B** Representative slice of a 100 mM solution of tyramine and a 100 mM solution of **5.14** in DMSO. Scale bar = 2 mm. **C** Quantification of gray value of a 100 mM solution of tyramine and a 100 mM solution of **5.14** in DMSO, obtained by averaging the gray value of 10 different cross-sections. Data are represented as average ± sd. An unpaired t-test was performed for statistical analysis. Significance is indicated as followed: ****p<0.0001 (significance level $\alpha = 0.05$).

Next, we wanted to evaluate compound **5.14** as a CESA. For sake of simplicity, endogenous peroxidase activity was labeled instead of labeling a specific protein *via* HRP functionalized antibodies. To this end, fixed murine kidneys, cut in half, were incubated at room temperature for five days with a borated buffered saline solution containing 0.0035% hydrogen peroxide and 1 mM **5.14**. As a negative control, borated buffered saline solution with 0.0035% hydrogen peroxide was used. After washing with PBS, the kidneys were imaged by microCT.

Upon mixing the 100 mM stock solution of **5.14** with the borate buffered saline, the solution turned opaque white, which indicates that **5.14** does not dissolve completely in water. Nevertheless, the staining and imaging of the murine kidney was performed as described. Representative transverse CT images are shown in Figure 5.14.

Based on an equivalence test using an equivalence bound of 8[I], the mean gray value of the kidney stained with **5.14** were found to be equivalent to the mean gray value of the negative control, which means that no significant difference could be observed. We hypothesize that the absence of enhanced contrast is due to hampered penetration because of poor solubility. In order to circumvent limitations related to penetration, microCT imaging of a tissue section stained with compound **5.14** could help in evaluating the staining mechanism. Finally, alternative strategies to increase the water solubility of an X-ray attenuating tyramide conjugate could ultimately pave the way to evaluate these conjugates as revealing agents for HRP-labeled proteins.

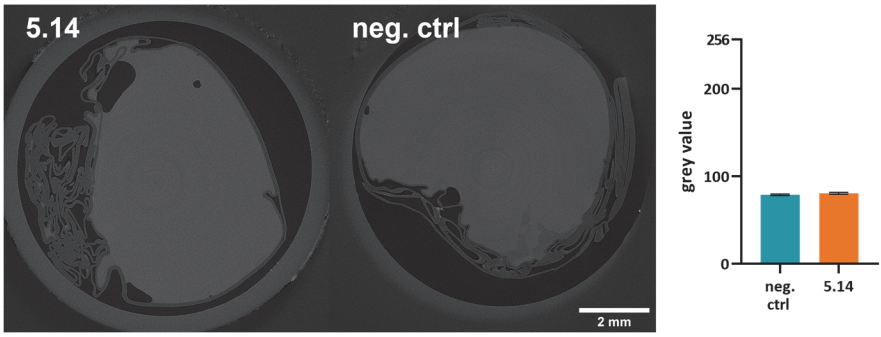


Figure 5.14 Representative transverse CT images of murine kidneys stained with compound **5.14** (left) and borate buffered saline as negative control (right), along with the quantification of mean gray values. Quantification of mean gray value was obtained by averaging the gray value of profile surfaces of 10 different slices. Data are represented as average ± sd. An equivalence test (two-one-sided t-tests) was performed for statistical analysis (significance level $\alpha = 0.05$).

5.6 Conclusions

The goal of this research project was to combine the advantages of IHC and CECT by developing staining protocols for protein-specific CECT of tissues. Central to this chapter was the development of a compound consisting of a protein-specific probe and a moiety that provides X-ray attenuation.

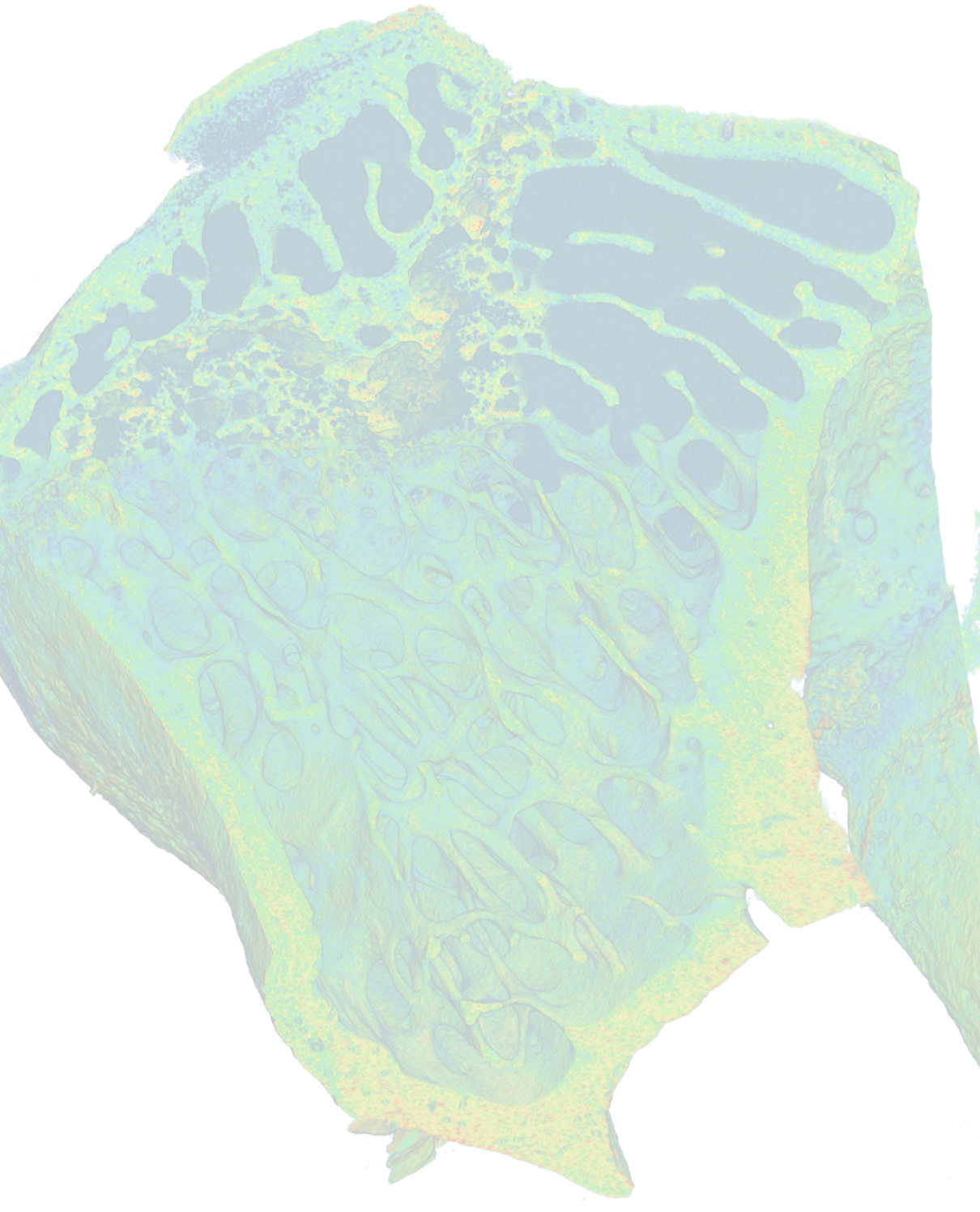
[I] The mean gray value was obtained by averaging the gray value of profile surfaces of 10 different slices across the sample. The equivalence bound was set to be 10 times the average of the standard deviation (= 0.837) of the profile surfaces of the negative control sample.

To improve tissue penetration, the use of short peptide sequences was explored as an alternative for Abs in the first part. As a proof of concept, peptide sequences that show affinity towards KLH as the negative control were identified. To this end, phage display using the p3L15 library was performed. To evaluate the binding interaction by ELISA, a peptide based on one of the identified sequences was synthesized and covalently linked to a V5 tag. Based on the obtained results we can conclude that the synthetic peptide did not bind specifically to KLH. The reduced binding could be due to the reduced avidity of the synthetic peptide **5.1** compared to the corresponding phage clone. Moreover, the peptide has an increased conformational flexibility compared to the phage clone, which could also play a role in decreasing the affinity.

In the second part, the development of the X-ray attenuating moiety of the protein-specific probe was discussed. In view of signal amplification, we opted to employ Abs conjugated to HRP for protein labeling. Herein, we wanted to develop an X-ray attenuating substrate of HRP. First, we worked on the iodination of DAB, a commonly used chromogen in IHC. Several approaches were studied to reduce the chances of DAB oxidation, which is a side reaction of iodination. Unfortunately, product formation was observed for none of the cases. Second, we attached 2,3,5-triiodobenzoyl to DAB via amide formation. The resulting product was not soluble in DMSO nor in water, which hampered further evaluation as a revealing agent. For this reason, we shifted focus towards derivatization of tyramine, which is commonly derivatized for fluorescence imaging. First, we evaluated commercially available iodinated tyramide analogues as X-ray attenuating substrates for HRP in murine kidneys. Sadly, we did not observe an increase in contrast, which could be explained by a hampered diffusion or impeded oxidation because of the presence of the iodine atoms on the phenol. Second, we synthesized a 2,3,5-triiodobenzoyl-tyramide conjugate. Evaluation by microCT revealed a contrast increase for a solution of the latter, compared to the solvent. However, the poor water solubility of the 2,3,5-triiodobenzoyl-tyramide conjugate precluded its further use as a CESA. Regrettably, the addition of an extra amine functionality on the iodinated arene did not help to improve water solubility. Finally, the addition of a short PEG moiety to the 2,3,5-triiodobenzoyl-tyramide was synthesized to increase the probability of water solubility. Although a contrast increase was observed for a solution of the latter, a whole-mount staining of a murine kidney was found to give the same result as the negative control. We hypothesized that the absence of contrast increase for the stained kidney is

due to unsuccessful penetration of the 2,3,5-triiodobenzamide-PEG3-tyramide conjugate because of incomplete water solubility.

In summary, the development of protein-specific CECT is only in the initial stage. At the one hand, increasing the avidity of the peptide-based protein-specific probe could lead to better binding, and hence a good alternative for Abs for labeling proteins. At the other hand, improving the water solubility of the tyramide-based X-ray attenuating moiety could ultimately lead to an X-ray attenuating revealing agent for HRP-labeled proteins.



CHAPTER 6

Conclusions & Outlook

This dissertation revolves around the development of CESAs for CECT imaging. Ultimately, we aim to exploit CECT as a tool for X-ray based histology of biological tissues by generating contrast differences between constituents through *ex vivo* staining. In chapter 3, POMs were explored as CESAs for bone marrow and kidney visualization. In chapter 4, cationic CESAs were synthesized and examined for cartilage imaging. In chapter 5, the goal was to develop protein-specific probes as CESAs, ultimately providing a platform to study the 3D spatial composition and organization of proteins in biological tissues. The following paragraphs provide a more detailed summary of the completed objectives, along with the future outlook, organized per chapter. Finally, a multidirectional future outlook of *ex vivo* CECT imaging in a broader context is discussed.

6.1 Polyoxometalates as CESAs

Conclusions

In chapter 3, the main goal was to assess the staining potential of WD POMs to visualize the composition of biological tissues by CECT imaging. Four different WD POMs and PTA, serving as a reference, were dissolved in PBS at equal concentrations and subsequently used to stain murine long bones and kidneys for CECT imaging. ^{31}P NMR measurements of the staining solutions performed before and after staining revealed that calcium ions interact with lacunary POM structures and induce a shift in the ^{31}P NMR resonance signals. In addition, Mono-WD POM was found to be the most stable POM species in PBS since Parent-WD POM and Hf-WD POM convert and dissociate, respectively, to it. Finally, Mono-WD POM and Hf-WD POM species showed the best diffusion and overall staining of soft tissues.

Our finding was that Mono-WD POM is the most suitable CESA of the screened POM species in terms of contrast-enhancement, penetration through the tissue, non-destructiveness, chemical stability, and ease and cost of synthesis. Compared to Hf-WD POM, the synthesis of Mono-WD POM require less steps, and hence, leads to a lower production cost. This work was further strengthened by improving the staining properties of Mono-WD POM by addition of LiCl to the staining solution to increase its solubility. We conclude that 35 mg/mL of Mono-WD POM with 3.0 mg/mL of LiCl, dissolved in PBS, results in high contrast enhancement of soft tissue without inducing substantial tissue shrinkage.

Future outlook

Although contrast enhancement was obtained, tissue shrinkage was observed for long bones that were stained with Mono-WD POM solutions containing a high level of LiCl (> 3.0 mg/mL). Therefore, the development of isotonic staining solutions containing CESAs that match the pH levels of biological tissues will be the focus of future research. This could be achieved by exchanging the POM counterions for Li^+. Counterion exchange could be performed by protonation of the POM using a strong acid, followed by a titration with a basic salting-out salt.[204] Alternatively, an ion-exchange resin could be employed.

In the past years, POMs have successfully been used as *ex vivo* CESAs within our research group. These POMs include Hf-WD POM, Mono-WD POM, Preyssler anion and zirconium-substituted Keggin POM.[22, 83, 159, 205] Expanding the applicability of WD and Keggin POMs as CESAs for microCT imaging to POMs with other geometries and/or substituted metals form an appealing extension to this work. It would be interesting to study the influence of a POM size/geometry/charge on its diffusive behaviour and stability in physiological conditions. In this view, a ring-shaped POM and POM species such as Lindqvist and Evans-Anderson could be considered. Besides, the effect of substituting one [WO_2] group by a metal atom (Cu, Hf, Zr or Fe) could be of interest in light of specific interactions with the tissue. Moreover, staining other tissue types than bone marrow, kidney, placenta or brain could lead to untapped soft tissue CECT imaging.



Figure 6.1 POM species other than Wells-Dawson and Keggin. Left: Lindqvist POM. Middle: Evans-Anderson POM. Right: Ring-shaped P_8W_{48} POM.

6.2 Cationic CESAs

Conclusions

In chapter 4, three cationic CESAs were synthesized with varying iodine content and positive charge density. Moreover, we were successful in shortening the previously reported synthesis protocol of CA4+6I, while improving the work-up. The main objective was to study the influence of the CESA concentration, its molecular design and staining time on cartilage imaging by studying the gray value evolution and diffusive behavior at different depths. We achieved this by time-lapsed CECT imaging of bovine cartilage plugs. All parameters listed showed a positive trend with gray value, demonstrating the effectiveness of the CESAs. Considering the CESA molecular design, the obtained data suggest that the iodine content has a larger effect on contrast enhancement compared to the positive charge density. Based on the data obtained from the destaining experiments, CA8+6I was found to have the highest affinity for GAGs, while CA4+6I is thought to have the highest sensitivity for detecting variations in the GAG content. Since some limitations were encountered during the experiments, repeating the imaging with a higher resolution is advisable to confirm these hypotheses.

Future outlook

This work demonstrated that variations in iodine content and positive charge density of cationic CESAs influence their diffusive behavior, GAG affinity and sensitivity to detect changes in the GAG content. Notwithstanding, the observed gray values were not yet compared to the actual GAG content, which should be determined by a biochemical assay. Ideally, the sensitivity of the cationic CESAs to detect alterations in the GAG concentration and distribution can be further explored and validated in the future. This can be achieved by comparing the actual GAG content with gray values of stained bovine cartilage plugs of different degradation levels, mimicking osteoarthritic cartilage. The actual GAG content can be assessed by performing the 1,9-dimethylmethylene blue assay after staining, or by fluorescence imaging using GAG-targeting fluorescent probes. Deeper knowledge on the diffusivity (penetration rate) can be obtained by including additional early (< 30 min) timepoints in future time-lapsed experiments. To gain more insights about the affinity between the CESAs and the GAGs, a time-lapsed destaining experiment in a saline solution could be performed to determine the half-life.

These advanced insights will help to define the most optimal CESA that should be used for cartilage imaging.

Accurate characterization of cartilage requires limited tissue destructiveness induced by staining. Therefore, comparing the cartilage volume measured before and after staining should be performed to avoid future biased analyses. The sensitivity of the cationic CESA could be improved by simultaneously staining with a non-ionic CESA. In doing so, the observed gray values for the cationic CESA can be normalized by those observed for a neutral CESA. Hence, the influence of steric hindrance and water content on diffusion can be cancelled out.

Since the positive charge density has an influence on the CESA efficacy to stain GAGs, it would be of interest to define the actual positive charge of the cationic compound in the staining solution. For instance, the charge can be experimentally determined by titration or potentiometry. If the actual charge would substantially deviate from the theoretical charge, quaternary ammonium salts could be considered instead of primary ammonium provided that solubility would not be adversely affected.

To further establish the feasibility of CECT as a tool for the evaluation of cartilage health, investigating the correlation between X-ray attenuation and the biomechanical properties is an additional future research interest. In conjunction with literature precedent on CA4+6I, it is expected that CA8+6I and CA4+3I will show a correlation between gray value and the equilibrium compressive modulus and the coefficient of friction.[8] From a clinical point of view, these insights will strengthen the efficacy of CECT as a tool for monitoring OA progression and diagnosis.

6.3 Development of protein-specific contrast-enhancing staining agents

Conclusions

The overarching goal of this research project was to combine the advantages of protein-specific immunohistochemistry and CECT by developing staining protocols for protein-specific CECT imaging of tissues.

The first part focused on the search for a probe to target proteins. Unfortunately, ELISA revealed that no specific binding was observed for the peptide selected for KLH (negative control) by phage display. The reduced binding could be due to the reduced avidity of the synthetic peptide, coupled with an increased conformational flexibility compared to the corresponding phage clone. In the second part, the development of the X-ray attenuating moiety of the protein-specific probe was discussed. Herein, we wanted to develop an X-ray attenuating substrate for HRP, which is coupled to an Ab targeting a protein of interest. Since iodination of 3,3'-diaminobenzidine was not feasible and attachment of 2,3,5-triiodobenzoyl led to insolubility in water and DMSO, we shifted focus towards derivatization of tyramine analogues. Commercially available iodinated tyrosines turned out to be incompatible with HRP-labeled kidney under the conditions studied. The poor water solubility of the 2,3,5-triiodobenzoyl-tyramide conjugate precluded its further assessment as a CESA. Regrettably, the addition of an extra amine functionality or even a PEG moiety was not sufficient to obtain complete water solubility.

The project is considered challenging due to its multifaceted nature and required expertise from different fields. Hence, the fulfillment of the main goal was not yet successful and the development of protein-specific CECT is only in its initial stage. On the one hand, increasing the avidity of the peptide-based protein-specific probe could lead to better binding, and hence a good alternative for Abs for labeling proteins. On the other hand, improving the water solubility of the tyramide-based X-ray attenuating moiety could ultimately lead to an opaque revealing agent for HRP-labeled proteins.

Future outlook

Even though conjugated antibodies are the mainstay to label specific proteins, we believe that short peptide sequences selected by phage display could be a good alternative. Before evaluating the protein-specific staining capacities of these peptides, the binding interaction towards the target needs to be further improved. It is important to note that a single peptide does not have the same avidity as a phage or an Ab. Therefore, comparing the binding of a dendrimer containing multiple copies of the selected short peptide inserts with the corresponding phage clone would be interesting. Building further on the development of a KLH-specific labeling method, the synthesis of a dendrimer bearing four copies of the KLH210 peptide and one copy of a V5 tag is proposed (Figure 6.2). The binding interactions could then be evaluated by

ELISA using a mouse anti-V5, conjugated to HRP and compared to the binding of the corresponding phage clone PC210, using a mouse anti-M13 that is conjugated to HRP.

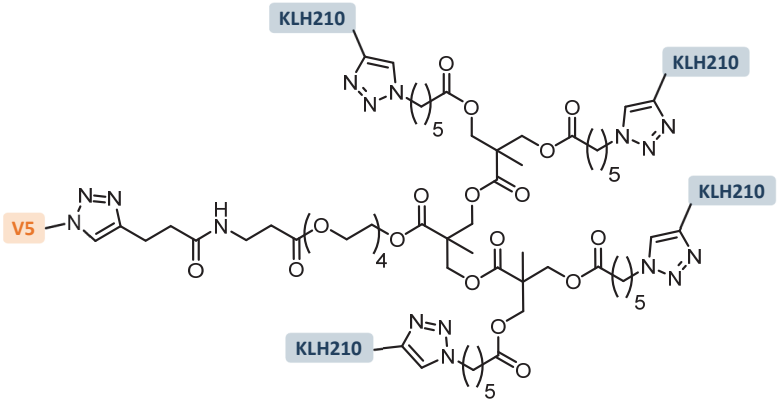


Figure 6.2 Proposed dendrimer containing 4 copies of the KLH210 peptide, which was previously selected by phage display, and one copy of a V5 tag.

Once an equal, or even stronger, binding interaction of the KLH210-decorated dendrimer could be obtained, the V5 tag could be exchanged for an attached HRP enzyme or a dendrimer which is decorated with multiple copies of iodinated arenes. Ultimately, the same approach could be performed for CD31-specific labeling.

Because of the commercial availability of fluorescent tyramide conjugates, it is more reliable to focus on the development of X-ray attenuating tyramide conjugates rather than DAB conjugates. Although we successfully synthesized X-ray attenuating conjugates of tyramine, the observed poor water solubility hindered further validation. Therefore, the addition of more hydrophilic groups could improve the water solubility by reducing the lipophilicity. Inspired by commercially available iodinated contrast agents, compounds **6.1** and **6.2** could be prepared for improved water solubility (Figure 6.3). The addition of hydroxyl functionalities could help to achieve sufficient water solubility at physiological conditions through hydrogen bonding with water molecules.

Finally, future research would benefit from improved knowledge on the diffusion of CESAs through the tissue matrix upon staining. To overcome limitations related to diffusion, staining could be performed on tissue sections

instead of (parts of) a tissue. A protocol to stain and image tissue sections has been developed, which was not yet available at the time of writing. Hence, a first future direction should be to evaluate CESAs that were discussed in this dissertation on tissue sections rather than on tissue samples. Moreover, results obtained by CECT could be compared with fluorescence imaging to validate the developed tyramide conjugates.

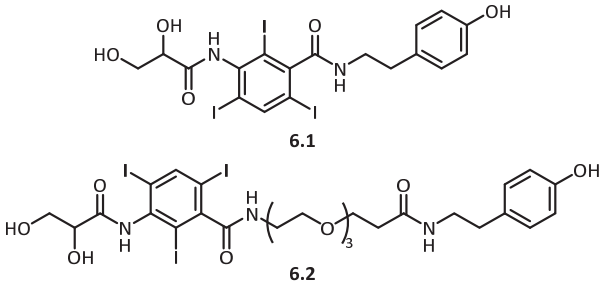


Figure 6.3 Potential X-ray attenuating tyramide analogues with additional hydroxyl functionalities for improved water solubility.

6.4 Future of *ex vivo* CECT

Although being a quite young field, *ex vivo* CECT imaging evolved substantially in the last two decades as a tool for X-ray based 3D histology of soft biological tissues. Advances in the development of CESAs combined with improvements in instrumentation are accelerating the field by enabling more accurate visualization of specific tissues and structures, not only in the research setting, but also in the preclinical practices. Owing to its multidisciplinary character, the field is expected to advance in several concurrent directions.

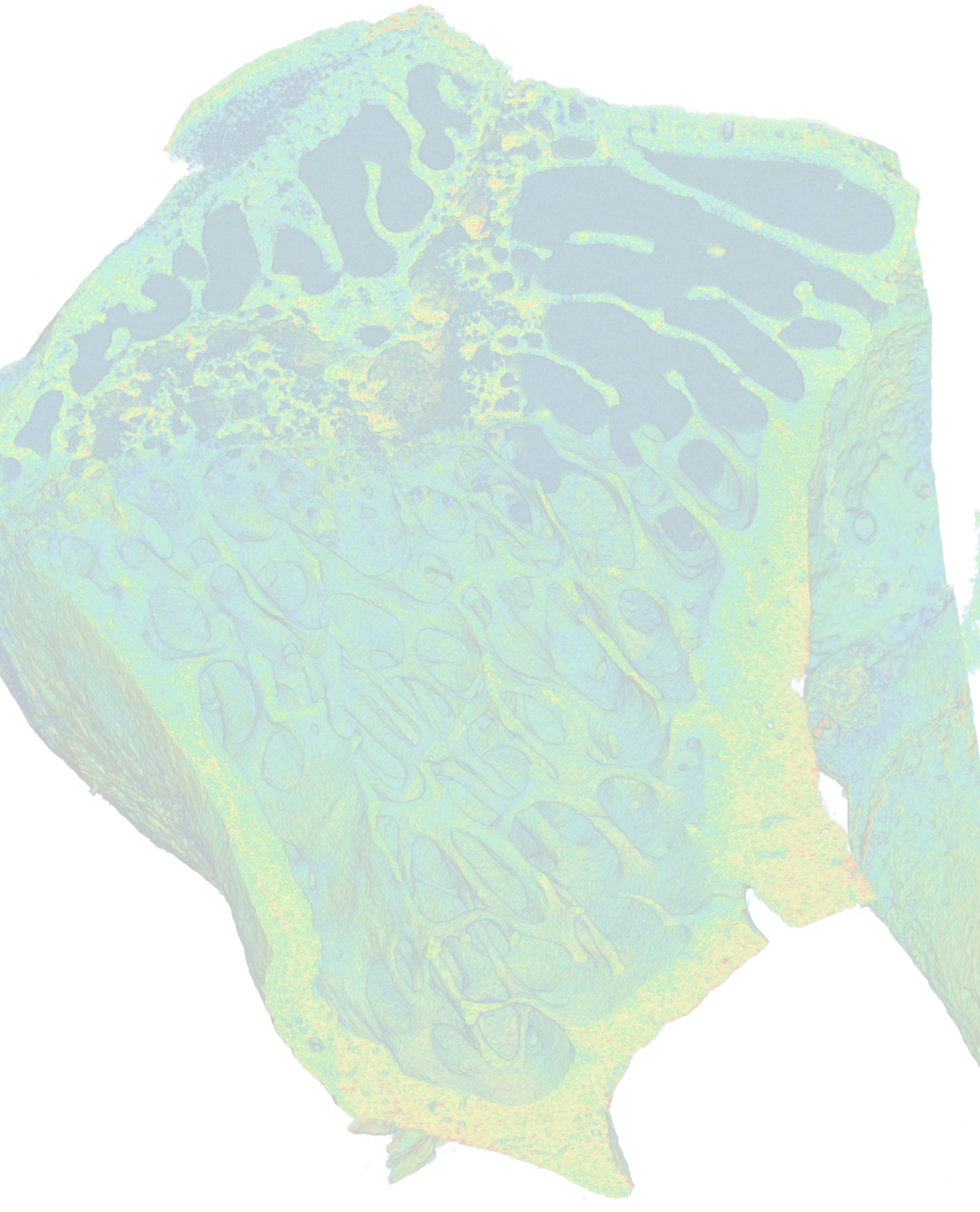
First, future research is expected to focus on the development of CESAs for emerging microCT technologies such as dual energy CT (DECT) and spectral photon-counting CT (SPCCT). On one hand, DECT allows to distinguish between materials with similar densities but a different K-edge by applying different X-ray energies. On the other hand, SPCCT provides high spatial resolution images coupled with the possibility to measure the energy of individual photons, hence facilitating quantitative assessments.

Second, the need to understand the interaction between CESAs and biological tissues has prompted research on novel CESAs to gradually shift from trial-and-error approaches to the development of CESAs tailored to staining

specific components of the tissue envisioned. Meanwhile, CESAs that are capable to render tissues X-ray attenuating without inducing tissue deformation are still sought after for general microstructure visualization. Ongoing research in *in vivo* targeting imaging is chiefly devoted to metal nanoparticles that are conjugated with targeting probes for detecting specific biomarkers. [165] In this regard, gold nanoparticles labeled with Abs that are currently being used in preclinical CT imaging could be translated to an *ex vivo* context to enable X-ray based 3D histology. In order to achieve a sufficient contrast-to-noise ratio, further progress on the development of staining protocols for improved tissue penetration and enhanced local accumulation of the contrasting moiety are required.

Third, future research on CECT would benefit from standardized protocols to perform CECT imaging. Not only staining protocols for protein-specific staining, but also protocols for general staining should be improved to more closely align with physiological conditions. Albeit protein-specific CESAs provide information about the 3D distribution of a specific target, information is lacking about the relationship between the target location and the microstructure of the tissue. For this purpose, general CESAs (*e.g.* Mono-WD POM) could be used as counterstain for the protein-specific CESAs, similar to the role of hematoxylin in IHC. In this regard, protocols for DECT would allow simultaneous imaging. Meanwhile, research on protocols that allow further contrast enhancement is being pursued, as exemplified by the development of cryogenic CECT within our own lab.[206]

Finally, the creation of an open-access, preferentially user-sourced, database of CESAs would enable the community to share experimental protocols and obtained results in a more accessible and transparent way. Over the past decade, data have been generated at increased speed. Yet, numerical details on the obtained results and experimental details of the protocols involved are often rarely findable. This lack of accessibility combined with the lack of standardized procedures substantially limits comparison of data and prevents enhanced understanding of the CESA efficacy under transparent and uniform reporting conditions. A database in which CESAs are organized by the type of sample stained, staining time, concentration, sample treatment (*e.g.* fixation, permeabilization) along with observations such as the degree of contrast enhancement, tissue deformation, degree of tissue penetration would facilitate future investigations and meta-analyses, fueling innovations in CECT imaging.



CHAPTER 7

Experimental Section

7.1 Chemical safety considerations

Safety is of major concern in a lab environment in its broadest aspects. It is crucial to limit the risk of exposure to (potentially) hazardous compounds and situations. This risk of exposure is not only of concern to the operator, but also to the surrounding environment and its individuals and ecosystems. All experimental work in this dissertation was carried out in accordance with the Code of Practice for Safety in the Lab,[207] and the Departmental Safety Brochure.[208] To comply with safety measures, experiment-dedicated risk assessments need to be prepared and regular audits are performed. When manipulating toxic or hazardous compounds, high-risk laboratory equipment and instable products special care and attention are needed. Additionally, it is of utmost importance to be especially cautious when synthesizing unknown molecules or performing novel procedures in case that unprecedent risks could occur, in addition to known safety concerns.

Working in a synthetic lab inherently implicates a higher chance of exposure to potentially dangerous compounds. Therefore, a lab coat, safety goggles and gloves were worn while performing research in the scope of this dissertation. Moreover, the experiments were done in a well-ventilated fume hood to reduce the risk of exposure to chemicals and organic solvents. More information about personal protective equipment and safety measures can be found on the web page of The Department of Chemistry, and of the HSE department (Health, Safety & Environment). Additional information and existing risk analyses can be found on a user-contributed sharepoint.[208]

The next paragraphs discuss more detailed safety concerns about chemical safety that are associated with this research.

X-ray microCT

MicroCT imaging involve X-rays, which are a type of electromagnetic radiation that have high energy and short wavelengths. Moreover, X-rays are a type of ionizing radiation that can cause damage to the DNA when passing through the human body. This damage can lead to mutations that can increase the risk of developing cancer. Exposure to high radiation levels can also lead to short-term side effects such as vomiting, fatigue, bleeding and the loss of skin and hair. The extent of damage caused by X-rays depends on the energy and duration of the exposure, the radiation dose and the part of the body that is

exposed. Although the microCT imaging was performed with a sealed source, a portable dosimeter attached to the lab coat was used to monitor radiation levels. Every month, the dosimeter is read to determine the radiation dose. The annual dose limit is are 20 mSv for occupational exposure for work performed in a radiation context according to the International Labour Organization.[209]

Chemical reagents

Some reagents used in this work are associated with specific hazards and are briefly discussed in this section. Sulfuric acid (H_2SO_4) is highly corrosive since it both acts as a very strong acid and an oxidant and warrants cautious handling. Reactions including sodium azide (NaN_3) were never brought in contact with acids to avoid the formation of hydrazoic acid, which is a strongly toxic gas. An organic azide was prepared in this work, which should be handled with care because of the potential explosion hazard. After preparation, it was stored as solution in the freezer and always used under sufficiently dilute conditions during synthesis. Although reactions involving hydrogen chloride (HCl) gas were performed in small quantities in a fume hood, it should be handled with care. This gas is corrosive, causes damage to the respiratory tract and is toxic upon inhalation. Moreover, pressure calculations should be performed before each reaction to prevent that the glassware pressure limit is exceeded.

Halogenated solvents such as dichloromethane (DCM) and chloroform ($CHCl_3$) may cause irritation of the skin, eyes and respiratory tract. Moreover, they are suspected to cause cancer and to damage certain organs and the central nervous system by prolonged or repeated exposure. Hence, breathing the vapors and skin contact should be avoided and the use of protective equipment is mandatory.

Ethers like diethyl ether (Et_2O) and tetrahydrofuran (THF) are highly flammable liquids and should be kept away from heat, sparks, hot surfaces and open flames. In addition, ET_2O is highly volatile. In the presence of light, air, heat or certain metals ethers may generate explosive peroxides. They are harmful to the human body if swallowed and may cause irritation to the skin, eyes and respiratory tract.

7.2 General experimental information

7.2.1 General information

All reagents were obtained from commercially available sources (Sigma-Aldrich, Acros organics, AK Scientific, J&K Scientific, Fisher Scientific, Fluorochem and Chinapeptides) and were used as purchased without further purification. All moisture-sensitive reactions were carried out under nitrogen atmosphere and in flame-dried glassware. Reactions were stirred magnetically with PTFE-coated magnetic stirring bars at 300 – 660 rpm. Solvents were evaporated with a rotary evaporator at a temperature of 50 °C. Final compounds were dried under high vacuum (10^{-3} mbar) at room temperature. Water was removed by lyophilization using a Virtis 2K Benchtop Freeze Dryer at – 60 °C under high vacuum (10^{-3} mbar). Yields refer to isolated compounds after chromatography, precipitation and/or crystallization.

7.2.2 Purification equipment

Analytical thin layer chromatography

Analytical thin layer chromatography (TLC) was performed by using Sigma-Aldrich 20 x 20 cm precoated, glass TLC plates with fluorescent indicator at 254 nm (article number 99571, layer thickness 250 µm, particle size 8.0-12.0 µm, average pore diameter 6 Å). Compounds were visualized by UV irradiation (254 nm) or by using a staining solution.

Column chromatography

Column chromatography was performed using ACROS silica gel, for column chromatography (60–200 µm particle size, average pore diameter of 60 Å).

Flash column chromatography

Flash column chromatography (medium pressure liquid chromatography, MPLC) was performed using a Büchi Sepacore® flash apparatus, consisting of a C-660 Büchi fraction collector, a Büchi C-615 pump manager that controls two Büchi C-605 Pump Modules, a Knauer WellChrom K-2501 spectrophotometer (operating at 254 nm) and a Linseis D120S plotter. Büchi PP cartridges (40/150 mm) were filled with ACROS ultra-pure silica gel for

column chromatography (40-60 µm particle size, average pore diameter of 60 Å) using a Büchi C-670 Cartridger. The eluent flow rate was set to 25 mL/min.

Semi-preparative reversed-phase high-performance liquid chromatography

Semi-preparative reversed-phase high-performance liquid chromatography (RP-HPLC) was performed using a Waters Delta 600 system equipped with a Waters 996 photodiode-array detector. The HPLC system was equipped with a Phenomenex Luna reversed-phase C_{18} 5 µm column (length: 150 mm, ID: 21.2 mm). Samples (injection volume: 400 µL) were run in a mixture of acetonitrile and water + 0.1% formic acid (HPLC grade, Acros Organics) using a specific gradient program. Data were acquired and processed using Agilent LC/MSD ChemStation software rev. B.04.03-SP2.

7.2.3 Analytical equipment

^{1}H nuclear magnetic resonance spectroscopy

^{1}H NMR spectra were recorded on Bruker Avance 300 spectrometer with a Bruker 300 UltraShield™ magnet system (^{1}H basic frequency of 300.13 MHz) and a 5 mm BBO BB-1H probe with z-gradients, on a Bruker Avance III HD 400 spectrometer with a Bruker Ascend™ 400 magnet system (^{1}H basic frequency of 400.17 MHz) and a 5 mm PABBO BB/19F-1H/D probe with z-gradients, and on a Bruker Avance II+ 600 spectrometer with a Bruker 600 UltraShield™ magnet system (^{1}H basic frequency of 600.13 MHz) and a 5 mm PABBO BB-1H/D probe with z-gradients. Samples were dissolved in DMSO-d_6, $CDCl_3$ or MeOH-d_4. In case of DMSO-d_6 and $CDCl_3$ the solvent was used as internal reference (DMSO-d_6: 2.50 ppm; $CDCl_3$: 7.26). In case MeOH-d_4, tetramethylsilane was used as an internal reference. Data were recorded at room temperature using Bruker TopSpin 2.1pl8 (Bruker Avance 300 spectrometer), TopSpin 3.6.1 (Bruker Avance III HD 400 and Bruker Avance II+ 600 spectrometers). The δ-values are expressed in parts per million (ppm). All spectra were processed and analyzed using Bruker TopSpin software (ver. 4.0.6) and ACD/Labs 2018.1.1 (File version S80S41). For reporting NMR data, the following acronyms are used: s (singlet), d (doublet), t (triplet), q (quartet), m (multiplet), and as combinations thereof, with “br” indicating a broadened peak(s). First-order approximations were used in the analyses and reports of the ^{1}H NMR spectra in order to retain useful information. The prefix app. denotes the apparent multiplicity of a signal, indicating the general shape and form of the multiplet in the spectrum, even though this is not theoretically

expected based on the molecular structure of the compound and/or some higher order fine structure could be observed.

^{13}C nuclear magnetic resonance spectroscopy

^{13}C NMR spectra were recorded on Bruker Avance 300 spectrometer (operating at 75 MHz, console with a Bruker 300 UltraShield™ magnet system, equipped with a 5 mm BBO BB-1H probe with z-gradients), on a Bruker Avance III HD 400 spectrometer (operating at 101 MHz, console with a Bruker Ascend™ 400 magnet system, equipped with a 5 mm PABBO BB/19F-1H/D probe with z-gradients) and on a Bruker Avance II$^+$ 600 spectrometer (operating at 151 MHz, console with a Bruker 600 UltraShield™ magnet system, equipped with a 5 mm PABBO BB-1H/D probe with z-gradients). ^{3}C-experiments were ^{1}H-decoupled using power-gated decoupling. Samples were dissolved in DMSO-*d*$_6$, $CDCl_3$ or MeOH-*d*$_4$. The deuterated solvents were used as internal reference (DMSO-*d*$_6$: 39.52 ppm, septet; $CDCl_3$ 77.16 ppm, triplet; MeOH-d$_4$: 49.00 ppm, septet). Data were recorded at room temperature using Bruker TopSpin 2.1pl8 (Bruker Avance 300 spectrometer), TopSpin 3.6.1 (Bruker Avance III HD 400 and Bruker Avance II+ 600 spectrometers). The δ-values are expressed in ppm. All spectra were processed and analyzed using Bruker TopSpin software (ver. 4.0.6) and ACD/Labs 2018.1.1 (File version S80S41).

^{31}P nuclear magnetic resonance spectroscopy

^{31}P NMR spectra were recorded on, Bruker Avance III HD 400 (operating at 162 MHz, console with a Bruker Ascend™ 400 magnet, equipped with a 5 mm PABBO BB/19F-1H/D probe with z-gradients). Solutions containing 35.0 mg of POM in 1 mL PBS with 10% D_2O were recorded, directly after dissolution and after different time increments. ^{31}P NMR spectra of the solutions after staining of long bones and kidneys were also recorded. As an external standard, 25% H_3PO_4 in D_2O in a sealed capillary was used. All spectra were processed and analyzed using Bruker TopSpin software (ver. 4.0.6). From this software spectra were exported (using the command convbin2asc) and plotted using Matlab (Mathworks, Natick, US), to generate the figure.

High-resolution mass spectrometry

High resolution mass spectra (HR-MS) were acquired on a Waters Synapt G2 HDMS quadrupole orthogonal-acceleration time-of-flight (Q-oa-ToF) mass spectrometer with an electrospray ionization (ESI) source (capillary voltage 4000 V), operating in the positive mode. Data were recorded with a resolution of 15000 (FWHM) using leucine encephalin as lock mass. Samples were prepared by dissolving the compound in methanol and diluting this solution with an acetonitrile/water mixture (1/1 v/v) to an approximate concentration of 0.1 mM. Each sample was infused at flow rate of 3 µL/min. Data were acquired and processed using Waters MassLynx™ 4.1 software.

Low resolution mass spectrometry

Low resolution mass spectra (LR-MS) were acquired using an Agilent 1 100 HPLC system or a Thermo Electron LCQ Advantage apparatus (Thermo Scientific, Erembodegem-Aalst, Belgium).

The HPLC system consists of a G1311A quaternary pump and solvent module, a G1322A vacuum degasser, a G1313A autosampler (ALS), a G1315A diode-array (DAD) detector (operating at 280 nm) and a G1316A thermostatted column compartment (TCC, kept at a constant temperature of 25 °C). The HPLC system was equipped with a Grace Prevail reversed-phase C18 3 µm column (length: 150 mm, ID: 2.1 mm) and coupled to an Agilent 6 110 single-quadrupole mass spectrometer with an electrospray ionization (ESI) source (capillary voltage: 3 500 V), operating in the positive mode. Samples (injection volume: 10 µL) were run in a mixture of methanol and water + 0.1% formic acid or a mixture of acetonitrile and water + 0.1% formic acid (HPLC grade, Acros Organics) using a specific gradient program for each compound. All samples were run at a flow rate of 0.12 mL/min. Data were acquired using Agilent LC/MSD ChemStation software rev. B.04.03-SP2 [105] and processed and analyzed using ACD/Spectrus Processor 2019.1.2.

The Thermo Finnigan LCQ Advantage apparatus allowed to acquire ESI mass spectra. The system is fed by an Agilent 1100 pump and injection system Syringe pump Syringes Flow reactor T-mixer Collector vessel58 (Agilent Technologies, Eindhoven, Netherlands). Xcalibur software was used for data analysis.

Atmospheric solids analysis probe mass spectrometry

Ambient mass spectrometry was acquired with an atmospheric pressure solid analysis probe (ASAP), combined with a single quadrupole (SQ) mass spectrometer (RADIAN^{TM} ASAP, Waters, Milford, MA). Samples were inserted as a solid or solution on a glass probe (1.9 mm diameter). Prior to sample loading, each glass probe was inserted into the ASAP source to remove possible contaminants by exposing the probe in a stream of nitrogen gas of high temperature (about 600 °C) for one minute. Samples were analyzed at a probe temperature of 450 °C with a scan speed of 2 Hz, the corona current was set at 3 µA positive mode) or 6 µA (negative mode) , and the sampling cone voltage was at 15 V (positive mode) or 20 V (negative mode). Data were acquired both in negative and in positive ion mode over a mass range of 30 – 1250 m/z with automatic internal calibration. Instrument control, data acquisition and data analysis was done using Mass Lynx v4.2 software (Waters, Milford, MA).

Infrared spectrometry

Attenuated total reflection (ATR) Fourier-transformed infrared (FT-IR) spectra were recorded on a Bruker Alpha-P FT-IR spectrometer with single reflection Platinum ATR accessory. Samples were analyzed neat in solid or liquid state without any further manipulations. The data were recorded at room temperature using Bruker OPUS 7.5 and processed and analyzed using ACD/Spectrus Processor 2019.1.2. The ν-values are reported in units of reciprocal centimeters (cm^{-1}).

Melting points

Melting points (MP) were recorded using an Electrothermal™ IA9300 digital melting point apparatus. Samples were analyzed in 1.5 mm outer diameter capillaries with a sample height of 1-2 mm. All samples were heated at a rate of 5.0 °C/min. The T_m-values values are reported in units of degrees Celsius (°C) and are uncorrected.

Osmolality

The osmotic concentration of solutions was measured by evaluating the freezing point depression, using an Advanced Instruments Single-Sample Osmometer Model 3250. Aqueous samples of 0.25 mL were measured.

pH

The pH of solution was measured using a FiveEasy pH meter F20 (Mettler Toledo) with pH micro electrodes (InLab® Micro).

SPR Biosensor

The affinity of selected phages towards the KLH protein was evaluated using the White Fox 1.0 (Fox BIOSYSTEMS, Belgium).

7.3 Chapter 3: POM screening – Experimental

7.3.1 Materials

Contrast-enhancing staining agents

The 1:2 hafnium(IV)-substituted Wells-Dawson POM $K_{16}[Hf(\alpha_2\text{-}P_2W_{17}O_{61})_2]\bullet 19H_2O$ (α_2-HfP_2W_{17} or Hf-WD POM),[210] parent Wells-Dawson POM α-/β-$K_6P_2W_{18}O_{62}\bullet 14/19H_2O$ (α/β-P_2W_{18} or Parent-WD POM),[128] monolacunary Wells-Dawson POM α_2-$K_{10}P_2W_{17}O_{61}\bullet 20H_2O$ (α_2-P_2W_{17} or Mono-WD POM) and trilacunary Wells-Dawson POM $Na_{12}[\alpha\text{-}P_2W_{15}O_{56}]\bullet 24H_2O$ (α-P_2W_{15} or Tri-WD POM) were synthesized as described in literature.[128] Phosphotungstic acid $H_3PW_{12}O_{40}$ (PTA) (Sigma Aldrich, USA) and all other chemicals were purchased from commercially available sources. Staining solutions were prepared by dissolving 35.0 mg/mL (3.5%) POM in PBS. The PBS buffer containing KH_2PO_4, NaCl and Na_2HPO_4, helps to maintain a physiological pH of 7.32 and is widely used in biological research. The PBS buffer is obtained by dissolving commercially available PBS tablets (Sigma Aldrich, USA) in water. The pH of the POM solutions was measured in PBS.

Tissue samples

The different POMs were tested as CESAs on long bones (tibiae and femurs) and kidneys of C57Bl/6 mice with an age between 15 and 28 weeks (n=3 per

POM species). As a negative control, samples kept in PBS (n=3) were used. All animal experiments were performed in accordance with the Belgian legislation and were approved by the Ethical Committee of the Faculty of Biomedical Sciences of the KU Leuven. All animals were euthanized and the long bones (tibiae and femurs) and kidneys were harvested, fixed in a 4% paraformaldehyde solution (Sigma Aldrich, USA) for 16 hours and stored in PBS at 4°C. Before staining, the distal end of the long bones was removed to allow better diffusion of the CESA into the bone marrow compartment. Samples were immersed in the staining solution for different time periods at 4°C while shaking gently: 48 hours for the long bones, 4 and 10 days for the kidneys. After staining, samples were scanned using CECT, and the remaining staining solution was collected and used for ^{31}P NMR spectroscopy.

7.3.2 Microfocus X-ray computed tomography

MicroCT scans were acquired using a Phoenix NanoTom M (GE Measurement and Control Solutions, Germany) equipped with a 180kV/15W energy nanofocus X-ray tube and a GE DXR detector (3072 x 2400 pixels). A diamond-coated tungsten target was used for all scans. The CT images have been generated at the X-ray computed tomography facilities of the Department of Development and Regeneration of the KU Leuven, financed by the Hercules Foundation (project AKUL 13/47). The microCT datasets were reconstructed with the Datos|x software (GE Measurement and Control Solutions) and exported as 16-bit XY slices (.tiff). The images were cropped to reduce the size of the dataset.

Acquisition

Prior to scanning, samples were first wrapped in parafilm, and were then imaged using a Phoenix NanoTom M. For the long bones the system was operated at a voltage of 60 kV and a current of 140 µA, and a 0.2 mm filter of aluminium was used to reduce beam hardening during the acquisition. The exposure time was 500 ms, and 1800 images were acquired over 360° using the fast scan mode (frame averaging = 1; image skip = 0), resulting in a scan time of 15 minutes. The proximal long bones were examined at 2 µm isotropic voxel size to assess the trabecular bone as well as the bone marrow tissue and adipocytes in the metaphysis. For the kidneys, a voltage of 60 kV, a current of 170 µA and a 0.1 mm filter of aluminum were used. The exposure time was 500 ms, and 2400 images were acquired over 360° using the fast scan mode (frame averaging = 1; image skip = 0). A 5.5 µm isotropic voxel size was

selected. During reconstruction (Datos|x, GE Measurement and Control Solutions), we applied a beam hardening correction of 8 and 7 for the long bones and kidneys respectively, and a Gaussian filter with a radius of 3 voxels.

Image processing and analysis

For each sample, gray value profile lines were drawn and analyzed within the structures of interest using the software tools DataViewer (Bruker Micro-CT, Kontich, Belgium) and Matlab (Mathworks, Natick, US). These profile lines were as long as possible, but still covering the same structure of interest, to average out the inherent image noise. For the long bones, profile lines were selected within the cortical bone, bone marrow tissue, adipocytes, air and parafilm. For the kidneys, profiles lines in the cortex (outer part of the kidney), the renal pelvis (central part of the kidney), air and parafilm were selected. The methodology for drawing the profile lines in the long bones is illustrated in Figure 7.1A-D. More precisely, for bone and bone marrow tissue, the profile lines were drawn in the middle of the reconstructed volumes, along the longitudinal orientation of the long bone. The bone profile lines were drawn in the cortical bone and the bone marrow tissue profile lines were indicated in the middle of the bone marrow cavity, excluding trabecular bone. For the adipocytes, the profile lines were selected in the middle of the bone marrow cavity covering five different adipocytes for each sample.

For each CECT dataset, the reconstruction software offsets the gray values within the images to the less dense voxels detected and normalizes them to the densest ones. Therefore, to make all our scans comparable in terms of grayscale, the gray values of each dataset were normalized to the average gray value of air and parafilm. These two known materials served as gray value references. Let $G_{X,i}$ be the average gray value of a tissue X in sample i. The normalized gray value associated to that tissue was noted and calculated as follows:

$$g_{X,i} = \frac{G_{X,i} - G_{A,i}}{G_{P,i} - G_{A,i}}$$

where $G_{P,i}$ and $G_{A,i}$ represent the average gray values of parafilm and air, respectively, measured within sample i.

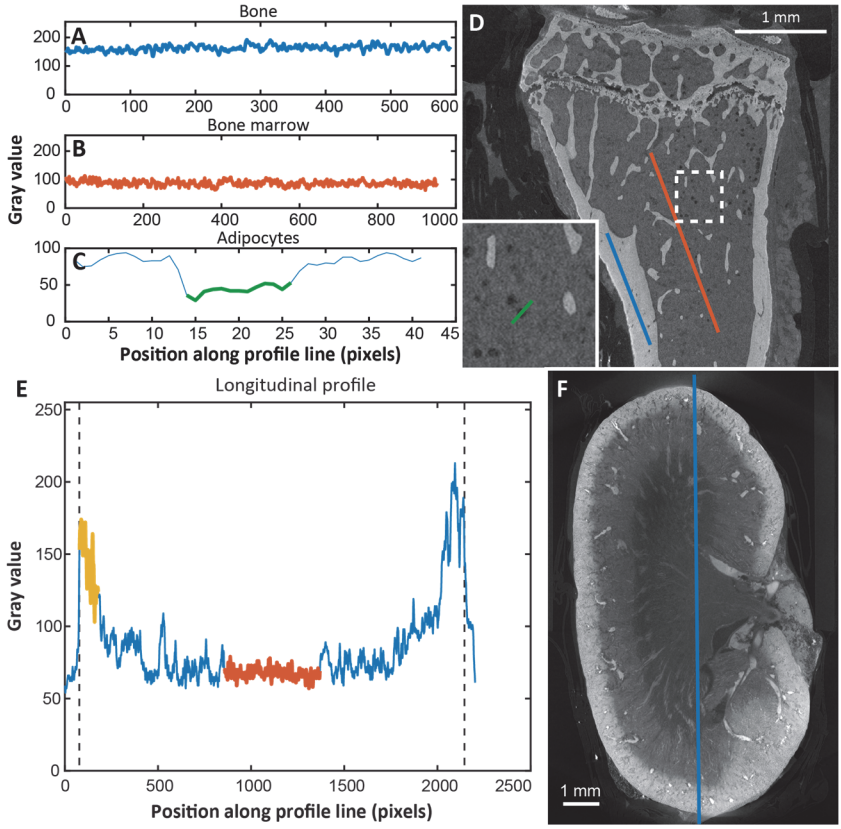


Figure 7.1 Typical profile lines drawn on a murine long bone A-D stained with Hf-WD POM and on a murine kidney E-F stained with Parent-WD POM. **A** Gray value profile line for cortical bone, corresponding to the blue line in D. **B** Gray value profile line for the bone marrow tissue, corresponding to the orange line in D. **C** Profile line drawn through the bone marrow compartment covering an adipocyte, corresponding to the green line in the insert in D. The green, thicker line in C corresponds to the gray values of the adipocyte only. **D** Longitudinal CT image of a long bone stained with Hf-WD POM. Insert = a magnification of the dotted white rectangle. The colored lines are the different profile lines. **E** Longitudinal gray value profile line corresponding to the blue line in F. The yellow and orange thick lines represent the gray values for the cortex and the renal pelvis of the kidney respectively. The vertical dotted lines represent the edges of the kidney, used to measure the kidney length. **F** Longitudinal CT image slice of a kidney stained with Parent-WD POM. The blue line is the profile line in E. Scale bar is 1 mm, voxel size is 2 µm for the long bone and 5.5 µm for the kidney. For the kidneys, the methodology to draw the profile lines is illustrated in Figures 1E-F. Briefly, longitudinal profile lines were drawn from the top of the kidney to the bottom, passing through the renal pelvis. A region of 550 µm from the top was selected to generate the cortex gray values and the middle region was manually selected for the renal pelvis gray values.

For the long bones, the contrast difference between cortical bone and bone marrow tissue, and between bone marrow tissue and adipocytes, were calculated as the absolute differences between the normalized gray values of the respective tissues. For the kidneys, the extent of diffusion through the tissue was determined by calculating the normalized contrast difference between the cortex and the renal pelvis (as previously explained). This value was then divided by the half-length of the kidney (measured from the scans).

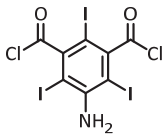
7.3.3 Statistical analysis

For the comparison in terms of contrast difference between the different POM species and PBS, a one-way ANOVA test was performed. For the extent of diffusion, we only compared similar POM species with each other for the different staining times using a one-way ANOVA test. The statistical analysis was performed using GraphPad Prism 8 software. The graphs represent the individual data points per experimental condition, along with their mean and standard deviation. Significance is indicated as following P-values: *: 0.01 to 0.05, **: 0.001 to 0.01, and ***: 0.0001 to 0.001 and ****< 0.0001 (significance level α=0.05).

7.4 Chapter 4: Cationic CESAs – Experimental

7.4.1 Synthesis

5-amino-2,4,6-triiodoisophthaloyl dichloride (compound 4.1)



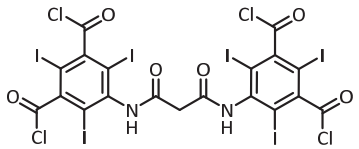
The procedure was performed as reported by Stewart *et al*.[69] The commercially available 3-amino-2,4,6-triiodoisopthalic acid (20.000 g, 35.79 mmol, 1.0 equiv) was stirred in 50 mL thionyl chloride (683.56 mmol, 19.1 equiv). A catalytic amount of DMF (0.1 mL, 1.3 mmol) was added and the mixture was refluxed for 7 h. After 7 hours, the reaction mixture was precipitated in cold water (0 °C). After filtration, the precipitation was dissolved in EtOAc and washed with saturated $NaHCO_3$ and brine. The organic layer was dried over Na_2SO_4, evaporated under reduced pressure (30 °C, not until dryness) and filtered again. Removal of residual solvent was done in

vacuo. Further purification was done by crystallization in EtOAc, resulting in **4.1** as a pale yellow powder (19.199 g, 32.23 mmol, 90%).

^{13}C NMR (101 MHz, DMSO-d_6) δ = 169.13, 150.05, 148.66, 99.79, 86.40. **LR-MS** (ESI) m/z calcd for $C_8H_3Cl_2I_3NO_2$ $[M+H]^+$ 595.7, found 595.5. **Physical appearance**: pale yellow solid.

These data are in agreement with literature data.[69, 211]

_N_,_N_'-Bis(2,4,6-triiodo-3,5-benzenedichlorocarbonyl)-malonamide (compound 4.2)

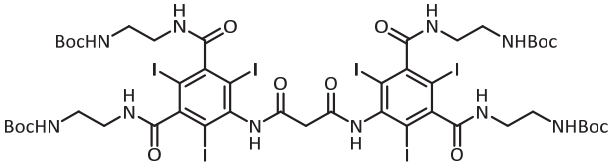


The procedure was performed as reported by Stewart *et al.*[69] Dissolution of 5-amino-2,4,6-triiodoisophthaloyl dichloride (**4.1**) (28.693 g, 48.17 mmol, 1.0 equiv) in dry THF (230 mL) under argon atmosphere was followed by the dropwise addition of malonyl chloride (2.3 mL, 23.64 mmol, 0.5 equiv). The reaction mixture was stirred overnight at 50 °C. Afterward, the reaction was cooled and left in the freezer to precipitate at -24 °C. The precipitate was filtered and washed with cold THF (2 x 100 mL). The filtrate was concentrated up to 30 % using a rotary evaporator and again left at -24 °C overnight to generate a second batch of the precipitate. After filtration and pooling of the two batches, **4.2** was obtained as a white solid (25.670 g, 42%).

^{13}C NMR (101 MHz, DMSO-d_6) δ = 169.45, 164.65, 149.15, 143.12, 98.27, 87.43, 38.98. **LR-MS** (ESI) m/z calculated for $C_{19}H_5Cl_4I_6N_2O_6$ $[M+H]^+$ 1258.3, found 1258.1 **Physical appearance**: white solid.

These data are in agreement with literature data.[69, 211]

Tetra-*tert*-butyl (((5,5′-[malonylbis(azanediyl))bis(2,4,6-triiodoisophthaloyl))tetrakis(azanediyl))tetrakis(ethane-2,1-diyl)]tetracarbamate (compound 4.3)

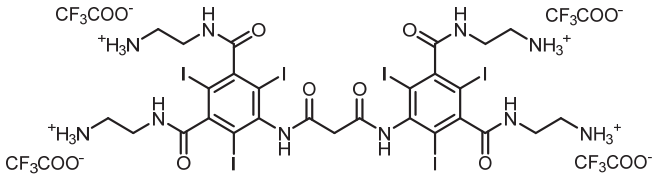


The procedure was performed as reported by Stewart *et al*.[69] **4.2** (18.820 g, 14.94 mmol, 1.0 equiv) was dissolved in anhydrous DMA (55 mL), followed by dropwise addition of dry DIPEA (18.2 mL, 104.60 mmol, 7.0 equiv) and the reaction mixture was cooled to 0 °C. The cooling was followed by the dropwise addition of *tert*-butyl-*N*-(2-aminoetyl)carbamate (10.534 g, 65.75 mmol, 4.4 equiv). Afterwards, the reaction mixture was precipitation in 1 M HCl while stirring. The obtained solid was filtered and washed thoroughly with water. After removal of water by lyophilization for three days, the product was obtained as a white solid (22.647 g, 86%).

^{1}H NMR (400 MHz, DMSO-d_6) δ = 10.26 - 10.17 (m, 2H), 8.70 - 8.33 (m, 4H), 6.87 - 6.66 (m, 4H), 3.52 (br s, 2H), 3.31 - 3.12 (m, 16H), 1.39 (s, 36H). **^{13}C NMR** (101 MHz, DMSO-d_6) rotameric mixture, resonances for minor rotamers are enclosed in parenthesis () δ = (169.27), 169.25, (169.20), 164.75, (155.53, 155.51), 155.44, 149.98, 142.68, 98.94, (98.91), (90.22), 90.19, 77.75, 42.32, 38.88, 38.85, 28.18. **LR-MS** (ESI) m/z calculated for $C_{47}H_{65}I_6N_{10}O_{14}$ $[M+H]^+$ 1754.8, found 1754.7. **Physical appearance**: white solid.

These data are in agreement with literature data.[69]

5,5′-[Malonylbis(azanediyl)]bis[*N*1,*N*3-bis(2-aminoethyl)-2,4,6-triiodoisophthalamide], trifluoroacetate salt (CA4+6I TFA salt – compound 4.4)

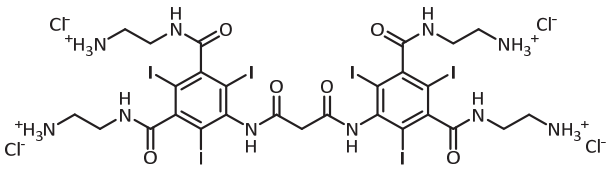


The procedure was performed as reported by Stewart *et al*.[69] Intermediate **4.3** (22.650 g, 12.91 mmol) was dissolved in a (1:1) DCM:TFA mixture (80 mL) and stirred for 1 hour at room temperature. To assure complete conversion, the reaction was stirred for an additional hour. Precipitation in diethyl ether (320 mL) was followed by filtration and washing with diethyl ether. After removal of the solvent under reduced pressure, the desired product **4.4** was obtained as a pale yellow solid (22.590 g, 97%).

^{1}H NMR (400 MHz, DMSO-d_6) δ = 10.36 - 10.17 (m, 2H), 8.88 - 8.64 (m, 4H), 8.10 (br s, 12H), 3.60 - 3.43 (m, 12H), 3.05 - 2.95 (m, 8H). **^{13}C NMR** (101 MHz, DMSO-d_6) rotameric mixture, resonances for minor rotamers are enclosed in parenthesis () δ = 169.62, (169.56), 164.77, 158.54 (q, *J* = 90.2 Hz), (158.50 (q, *J* = 90.2 Hz)), 149.56, (149.58), 142.99, 117.09 (q, *J* = 298.6 Hz), 99.31, (99.20), 99.15, 90.25, (42.45), 42.43, (37.42), 37.40, (36.62), 36.60. **LR-MS** (ESI) m/z calculated for $C_{27}H_{33}I_6N_{10}O_6$ $[M+H]^+$ 1354.7, found 1354.6. **Physical appearance**: pale yellow solid.

These data are in agreement with literature data.[69]

5,5'-[Malonylbis(azanediyl)]bis[*N*1,*N*3-bis(2-aminoethyl)-2,4,6-triiodoisophthalamide], chloride salt (CA4+6I Cl salt – compound 4.5)



Conventional procedure

The procedure was performed as reported by Stewart *et al*.[69] Exchange of the TFA ion by the Cl ion was performed by the consecutive dissolution of **4.4** (8.500 g, 4.70 mmol) in 3 M HCl (25.5 mL) and precipitation in acetone with constant vigorous stirring. Next, the two dissolution-precipitation cycles followed. After the final precipitation, the product was filtered, washed with acetone dried under reduced pressure. The product **4.5** was obtained a pale yellow powder(6.423 g, 91%).

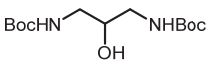
Two-chamber procedure for Boc deprotection by HCl gas

The procedure was performed as reported by Verschueren *et al.*[153] Chamber A was filled with NaCl (1.169 g, 20.00 mmol, 305.5 equiv) and chamber B was filled with **4.3** (100 mg, 0.06 mmol, 1.0 equiv). The reactor was sealed and flushed with argon, EtOH was added to chamber B (4 mL). The reaction was stirred overnight after the addition of H_2SO_4 (6.4 mL, 120.00 mmol) to chamber A. After removal of the solvent, **4.5** was as obtained as a light-yellow solid (68 mg, 80%).

^{1}H NMR (600 MHz, DMSO-d_6) δ = 10.34 - 10.22 (m, 2H), 8.88 - 8.74 (m, 4H), 8.32 - 8.15 (m, 12H), 3.57 - 3.44 (m, 10H), 3.04 - 2.91 (m, 8H). **^{13}C NMR** rotameric mixture, resonances for minor rotamers are enclosed in parenthesis () (151 MHz, DMSO-d_6) δ = 169.64, (164.61, 169.58), 164.88, (149.48), 149.45, 142.84, (100.12), 100.04, (90.70), 90.69, 42.2, (42.27), (37.44), 37.37, (36.65) 36.54. **LR-MS** (ESI) m/z calculated for $C_{27}H_{33}I_6N_{10}O_6$ $[M+H]^+$ 1354.7, found 1354.6. **Physical appearance**: pale yellow solid.

These data are in agreement with literature data.[69]

di-*tert*-butyl (2-hydroxypropane-1,3-diyl)dicarbamate (compound 4.6)



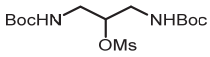
1,3-diaminopropan-2-ol (1.512 g, 16.77 mmol, 1.0 equiv) was dissolved in MeOH and triethylamine (Et_3N) (2.3 mL, 16.85 mmol, 1.0 equiv) was added. The reaction mixture was stirred and heated to 45 °C, followed by the dropwise addition of di-*tert*-butyl dicarbonate (7.939 g, 36.38 mmol, 2.2 equiv) in MeOH. After 30 min the reaction was cooled down to room temperature. The reaction was stirred for an additional 1.5 h at room temperature. After evaporation of the solvent, dissolution in diethyl ether and washing with water, the solvent was dried and evaporated under reduced pressure. The product (**4.6**) was obtained as a viscous white liquid that turned into a solid overnight (4.541 g, 93%).

^{1}H-NMR (400 MHz, DMSO-d_6) δ = 6.59 (br t, *J* = 5.2 Hz, 1H), 3.50 - 3.41 (m, 1H), 3.18 (d, *J* = 5.2 Hz, 1H), 2.99 - 2.92 (m, 2H), 2.89 - 2.82 (m, 2H), 1.47 (s, 2H), 1.38 (s, 18H). 2.90 (m, 4H), 1.38 (s, 18H). **^{13}C-NMR** (101 MHz, DMSO-d_6) δ =

156.21, 78.09, 69.35, 44.56, 28.69. **LR-MS** (ESI) m/z calculated for $C_{13}H_{27}N_2O_5$ $[M+H]^+$ 291.2, found 291.1. **Physical appearance**: viscous white liquid.

These data are in agreement with literature data.[154]

Methanesulfonic acid 2-*tert*-butoxycarbonylamino-1-(*tert*-butoxycarbonylaminomethyl)ethyl ester (compound 4.7)

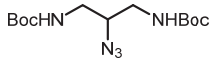


Compound **4.6** (15.970 g, 55.0 mmol, 1.0 equiv) was dissolved in anhydrous DCM (4 mL), followed by addition of 11.5 mL Et_3N (82.4 mmol, 1.5 equiv). The reaction mixture was cooled to 0 °C and methane sulfonyl chloride (11.34 g, 99.0 mmol, 1.8 equiv) was added. The mixture was stirred at room temperature for 1 h. After washing with 1 M HCl, $NaHCO_3$ and brine, the organic layers were combined and dried over anhydrous Na_2SO_4. After removal of the solvent under reduced pressure the product (**4.7**) was obtained as a white solid (18.545 g, 0.05 mmol, 92%).

^{1}H NMR (400 MHz, $CDCl_3$) δ = 5.21 (br s, 1H), 4.66 (br s, 1H), 3.68 (s, 1H), 3.52 - 3.42 (m, 2H), 3.39 - 3.28 (m, 2H), 3.09 (s, 3H), 1.43 (s, 18H). **^{13}C NMR** (101 MHz, $CDCl_3$) δ = 156.44, 80.12, 79.21, 40.96, 38.27, 28.43. **LR-MS** (ESI) m/z calculated for $C_{14}H_{29}N_2O_7S$ $[M+H]^+$ 369.1, found 369.1. **Physical appearance**: white solid.

These data are in agreement with literature data.[154]

di-*tert*-butyl (2-azidopropane-1,3-diyl)dicarbamate (compound 4.8)

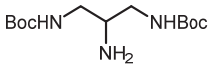


Compound **4.7** (499 mg, 1.36 mmol, 1.0 equiv) was dissolved in DMF (5 mL), followed by addition of sodium azide (507 g, 7.80 mmol). The mixture was stirred overnight at 100 °C. After removal of the solvent under reduced pressure, the residual was dissolved in EtOAc and washed with water and brine. After drying over anhydrous Na_2SO_4, removal of the solvent under reduced pressure, the product (**4.8**) was obtained as a viscous colorless liquid that solidified overnight (379 mg, 89%).

^{1}H-NMR (400 MHz, DMSO-d_6) δ = 7.05 (bs, 2H), 3.61 – 3.53 (m, 1H), 3.12 – 3.02 (6, 2H), 3.01 – 2.88 (m, 2H), 1.38 (s, 18H). **^{13}C-NMR** (101 MHz, DMSO-d_6) δ = 156.13, 78.45, 61.63, 42.26, 28.66. **LR-MS** (ESI) m/z calculated for $C_{13}H_{24}N_5O_4$ $[M+H]^+$ 314.2, found 314.2. **Physical appearance**: viscous colorless liquid.

These data are in agreement with literature data.[154]

di-*tert*-butyl (2-aminopropane-1,3-diyl)dicarbamate (compound 4.9)

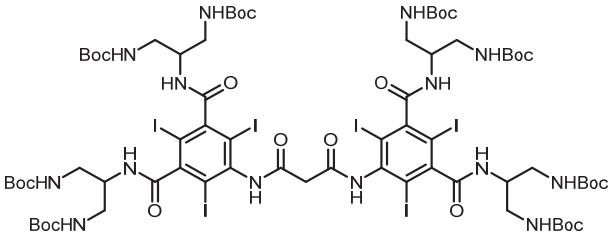


Compound **4.8** (34.860 g, 110.54 mmol) was dissolved in anhydrous EtOH (887.70 mL). Pd/C (2.100 g) was added and the mixture was hydrogenated in the presence of H_2 (balloon) for 4 days. Afterwards, the reaction mixture was filtered over Celite® 535 and washed with MeOH. Next, the solution was centrifugated to remove residual Pd/C particles. After removal of the solvent under reduced pressure, the product (**4.9**) was obtained a colorless viscous liquid (30.553 g, 95%). The liquid solidified over time.

^{1}H-NMR (400 MHz, DMSO-d_6) δ = 6.67 (bs, 2H), 2.98 – 2.85 (m, 2H), 2.81 – 2.72 (m, 2H), 2.72 – 2.62 (m, 1H), 1.39 (br s, 2H), 1.38 (s, 18H). **^{13}C-NMR** (101 MHz, DMSO-d_6) δ = 155.83, 77.60, 51.16, 44.67, 28.24. **LR-MS** (ESI) m/z calculated for $C_{13}H_{28}N_3O_4$ $[M+H]^+$ 290.2, found 290.2. **Physical appearance**: viscous colorless liquid.

These data are in agreement with literature data.[154]

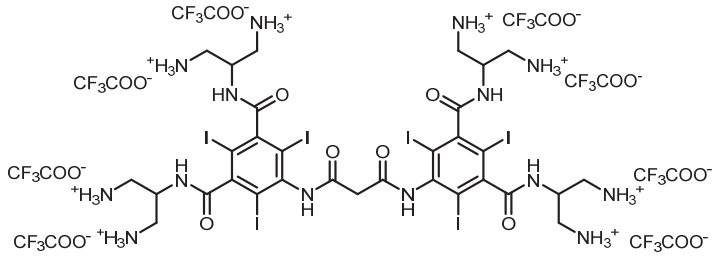
octa-*tert*-butyl (((5,5'-(malonylbis(azanediyl))bis(2,4,6-triiodoisophthaloyl))tetrakis(azanediyl))tetrakis(propane-2,1,3-triyl))octakis(λ^2-azanecarboxylate) (compound 4.10)



The procedure is based on the protocol for the synthesis of CA4+6I as reported by Stewart *et al*.[69] First, compound **4.2** (7.970 g, 6.33 mmol, 1.0 equiv) was dissolved in anhydrous DMA, followed by dropwise addition of dry DIPEA (7.7 mL, 44.30 mmol, 7.0 equiv) and the reaction mixture was cooled to 0°C. Next, di-*tert*-butyl (2-aminopropane-1,3-diyl)dicarbamate **4.9** (8.508 g, 29.40 mmol, 4.6 equiv) was added dropwise. After 30 min, the ice bath was removed and the reaction mixture was heated to 50 °C, followed by overnight stirring. Afterwards, the reaction mixture was precipitation in 1 M HCl while stirring. The obtained solid was filtered and washed thoroughly with water. After removal of water by lyophilization for three days, the product was obtained as an off-white solid (13.839 g, 90%).

^{1}H-NMR (400 MHz, DMSO-d_6) δ = 10.29 – 10.20 (m, 2H), 8.47 – 8.30 (m, 4H), 6.67 – 6.36 (m, 8H), 3.98 (br s, 4H), 3.54 (s, 2H), 3.28 – 2.99 (m, 16 H), 1.38 (s, 72H). **^{13}C-NMR** (101 MHz, DMSO-d_6) δ = 169.34, 156.05, 150.24, 141.76, 99.39, 90.11, 78.44, 49.60, 42.14, 41.01, 28.72. **HR-MS** (ESI) m/z calculated for $C_{71}H_{100}I_6N_{14}O_{22}$ $[M+4Na]^{4+}$ 588.5246, found 589.3931. **IR** (neat, cm^{-1}): v 3295 (N-H stretch, 2978 (C-H stretch), 1691 (C=O stretch), 1455 (C-H bend), 1251 (C-N stretch), 1165 (C-O stretch), 781 (C-H bend). **MP**: T_m 289.1 – 292.8 (decomposition). **Physical appearance**: off-white solid.

2,2',2'',2'''-((5,5'-(malonylbis(azanediyl))bis(2,4,6-triiodoisophthaloyl))tetrakis(azanediyl))tetrakis(propane-1,3-diaminium), trifluoroacetate salt (CA8+6I TFA salt - compound 4.11)

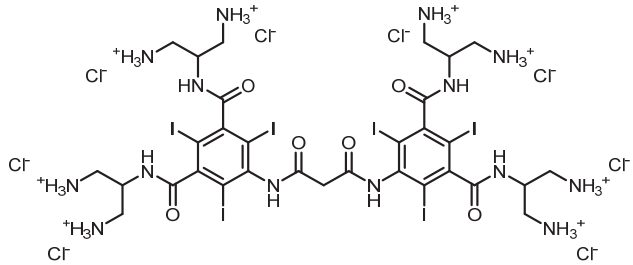


The procedure is based on the protocol for the synthesis of CA4+6I as reported by Stewart *et al*.[69] Intermediate **4.10** (13.000 g, 5.724 mmol) was dissolved in a (1:1) DCM:TFA mixture (70 mL) and stirred for 1 hour at room temperature. To assure complete conversion, the reaction was stirred for an additional hour. Precipitation in diethyl ether was followed by the removal of the solvent

under vacuum. The desired product **4.11** was obtained as a pale yellow solid (12.843 g , 5.395 mmol, 94%).

^{1}H-NMR (400 MHz, DMSO-d_6) δ = 10.48 – 10.27 (m, 2H), 9.07 – 8.70 (m, 4H), 8.32 (bs, 24H), 4.51 – 4.36 (m, 4H), 3.58 (br s, 2H), 3.22 (br s, 16H). **^{13}C NMR** (101 MHz, DMSO-d_6) rotameric mixture, resonances for minor rotamers are enclosed in parenthesis () δ = 169.95, (169.87), 165.36, (165.39), 159.39 (q, *J* = 32.3 Hz), (149.30), 149.26, 143.70 (143.75), 117.38 (q, *J* = 297.8 Hz), (100.45), 100.27, 90.76, (46.63), 46.59, (43.02), 42.93, 39.27. **HR-MS** (ESI) m/z calculated for $C_{31}H_{45}I_6N_{14}O_6$ $[M+H]^+$ 1470.7920, found 1470.7905. **IR** (neat, cm^{-1}): v 3674 (N-H stretch), 2988 (C-H stretch), 2900 (C-H stretch), 1665 (C=O stretch). **MP**: T_m 285.2 – 289.7 (decomposition). **Physical appearance**: pale yellow solid.

2,2',2'',2'''-((5,5'-(malonylbis(azanediyl))bis(2,4,6-triiodoisophthaloyl))tetrakis(azanediyl))tetrakis(propane-1,3-diaminium), chloride salt (CA8+6I Cl salt - compound 4.12)



Conventional procedure

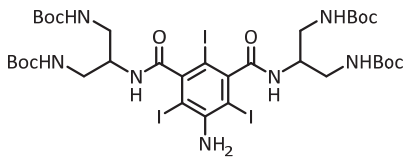
The procedure is based on the protocol for the synthesis of CA4+6I as reported by Stewart *et al*.[69] Exchange of the TFA ion by the Cl ion was performed by the consecutive dissolution of **4.11** (11.000 g, 4.62 mmol) in 3 M HCl (25 mL) and precipitation in acetone with constant vigorous stirring. Two dissolution-precipitation cycles were followed. After the final precipitation, the product was filtered, washed with acetone dried under reduced pressure. The product **4.12** was obtained a pale yellow powder (7.759 g, 95%).

Two-chamber procedure for Boc deprotection by HCl gas

The procedure was performed as reported by Verschueren *et al.*[153] Chamber A was filled with NaCl (235 mg, 4.01 mmol, 157.3 equiv) and chamber B was filled with **4.10** (58 mg, 0.03 mmol). The reactor was sealed and flushed with argon, EtOH was added to chamber B (2 mL). The reaction was stirred overnight after the addition of H_2SO_4 (1.4 mL, 27.11 mmol) to chamber A. After removal of the solvent, **4.12** was as obtained as a light-yellow solid (44 mg, 98%).

^{1}H NMR (400 MHz, DMSO-d_6) δ = 10.48 - 10.27 (m, 2H), 9.17 - 8.75 (m, 4H), 8.51 (br s, 24H), 4.58 - 4.45 (m, 4H), 3.56 (br s, 2H), 3.22 (m, 16H). **^{13}C NMR** (101 MHz, DMSO-d_6) δ = 169.79, 165.40, 149.06, 143.27, 101.48, 91.55, 46.10, 42.79, 38.95. **HR-MS** (ESI) m/z calculated for $C_{31}H_{45}I_6N_{14}O_6$ $[M+H]^+$ 1470.7920, found 1468.7261. **IR** (neat, cm^{-1}): v 3279 (N-H stretch), 2976 (C-H stretch), 2931 (C-H stretch), 1784 (C=O stretch), 1687 (C=O stretch). **MP**: T_m 286.2 – 290.5 (decomposition). **Physical appearance**: pale yellow solid.

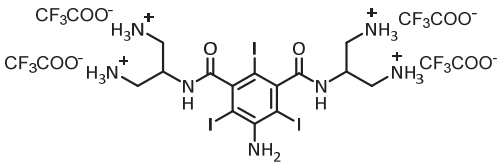
tetra-*tert*-butyl (((5-amino-2,4,6-triiodoisophthaloyl)bis(azanediyl))bis(propane-2,1,3-triyl))tetracarbamate (compound 4.13)



The procedure is based on the protocol for the synthesis of CA4+6I as reported by Stewart *et al*.[69] **4.2** (10.010 g, 16.804 mmol, 1.0 equiv) was dissolved in anhydrous DMA (20 mL) followed by dropwise addition of dry DIPEA (20.5 mL, 117.63 mmol, 7.0 equiv) and the reaction mixture was cooled to 0 °C. The cooling was followed by the dropwise addition of *tert*-butyl-*N*-(2-aminoetyl)carbamate **4.9** (10.698 g, 36.97 mmol, 2.2 equiv). Afterwards, the reaction mixture was precipitation in 1 M HCl while stirring. The obtained solid was filtered and washed thoroughly with water. After removal of water by lyophilization, the product **4.13** was obtained as a yellow solid (16.178 mg, 87%).

^{1}H NMR (400 MHz, DMSO-d_6) δ = 8.26 (br s, 2H), 6.73 – 3.36 (m, 4H), 5.55 (s, 2H), 3.97 (s, 2H), 3.29 – 2.93 (m, 8H), 1.39 (br s, 36H). **^{13}C NMR** (101 MHz, DMSO-d_6) δ = 169.84, 156.08, 149.23, 140.12, 100.15, 89.43, 78.44, 53.84, 49.56, 42.10, 28.72. **HR-MS** (ESI) m/z calculated for $C_{34}H_{54}I_3N_7O_{10}$ $[M+Cl]^-$ 1136.0766, found 1136.0762. **IR** (neat, cm^{-1}): v 3345 (N-H stretch), 2975 (C-H stretch), 1686 (C=O stretch), 1649 (C=O stretch), 1454 (C-H bend), 1249 (C-N stretch), 1163 (C-O stretch), 780 (C-H bend). **MP**: T_m 246.1 – 248.4 °C (decomposition). **Physical appearance**: yellow solid.

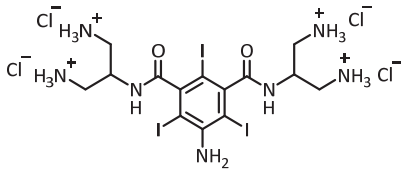
2,2'-((5-amino-2,4,6-triiodoisophthaloyl)bis(azanediyl))bis(propane-1,3-diaminium), trifluoroacetate salt (CA4+3I TFA salt – compound 4.14)



The procedure is based on the protocol for the synthesis of CA4+6I as reported by Stewart *et al*.[69] Intermediate **4.13** (9.500 g, 8.62 mmol) was dissolved in a (1:1) DCM:TFA mixture (50 mL) and stirred for 1 hour at room temperature. To assure complete conversion, the reaction was stirred for an additional hour. Precipitation in diethyl ether was followed by the removal of the solvent under vacuum. The desired product **4.14** was obtained as a yellow solid (5.741 g, 94%).

^{1}H NMR (600 MHz, DMSO-d_6) δ = 8.78 - 8.60 (m, 2H), 8.31 – 8.08 (br s, 12H), 5.64 (br s, 2H), 4.37 (dt, *J* = 6.1, 12.2 Hz, 2H), 3.26 - 3.11 (m, 8H). **^{13}C NMR** (151 MHz, DMSO-d_6) rotameric mixture, resonances for minor rotamers are enclosed in parenthesis () δ = 170.43, (170.40), 159.02 (q, *J* = 32.1 Hz, 1C), 148.78, (148.50), 148.43, 148.19, (148.11), 117.41 (q, *J* = 298.5 Hz, 1C), 80.47, (80.10), 46.51, 39.42, (39.39). **HR-MS** (ESI) m/z calculated for $C_{14}H_{22}I_3N_7O_2$ $[M+H]^+$ 701.9047, found 701.9046. **IR** (neat, cm^{-1}): v 3307 (N-H stretch), 2914 (C-H stretch), 2900 (br, N-H stretch), 1661 (C=O stretch), 1455 (C-H bend), 1266 (C-N stretch), 1181 (C-O stretch), 1127 (C-F stretch), 796 (C-H bend). **MP**: T_m 226.5 – 229.4 °C (decomposition). **Physical appearance**: yellow solid.

2,2'-((5-amino-2,4,6-triiodoisophthaloyl)bis(azanediyl))bis(propane-1,3-diaminium), chloride salt (CA4+3I Cl salt – compound 4.15)



The procedure is based on the protocol for the synthesis of CA4+6I as reported by Stewart *et al*.[69] Exchange of the TFA ion by the Cl ion was performed by the consecutive dissolution of **4.14** (11.00 mg, 9.51 mmol) in 3 M HCl (52 mL) and precipitation in acetone with constant vigorous stirring. Two dissolution-precipitation cycles were followed. After the final precipitation, the product was filtered, washed with acetone dried under reduced pressure. The product **4.15** was obtained a pale yellow solid (7.123 g, 88%).

^{1}H NMR (500 MHz, DMSO-d_6) δ = 9.12 - 8.87 (m, 2H), 8.79 - 8.36 (m, 12H), 5.52 (s, 2H), 4.55 (br s, 2H), 3.30 – 3.07 (m, 8H). **^{13}C NMR** (101 MHz, DMSO-d_6) δ = 170.63, (170.44), 148.44, 148.19, (147.95), 147.85, 81.08, 46.25, 39.30. **HR-MS** (ESI) m/z calculated for $C_{14}H_{22}I_3N_7O_2$ $[M+H]^+$ 701.9047, found 701.9053. **IR** (neat, cm^{-1}): v 3338 (N-H stretch), 2869 (br, N-H stretch), 1651 (C=O stretch), 1453 (C-H bend), 1261 (C-N stretch), 881 (C-H bend). **MP**: T_m 224.5 – 226.4 °C (decomposition). **Physical appearance**: pale yellow solid.

7.4.2 Materials

Tissue samples

Osteochondral plugs were cored at different spots on both the lateral and medial facet of the femoral groove of the stifle joint from a freshly slaughtered, skeletally mature cow (36 – 54 months). Coring resulted in plugs of 7 mm diameter and variable height, each consisting of articular cartilage, subchondral bone and trabecular bone. Coring was performed using a diamond-tipped cylindrical cutter (catalog number 102080, Starlite Industries, Rosemont, PA) irrigated with water at room temperature. The samples were frozen at – 20°C in 400 ± 20 mOsm/kg saline solution containing a preservative cocktail of protease inhibitors, antibiotics and antimycotics to minimize tissue degradation over the course of the experiment. The osteochondral plugs were harvested from femoral grooves of two different cows (10 plugs from one cow,

11 plugs from the other cow) to obtain randomized samples. Figure 7.2 shows an image of a bovine femoral groove where osteochondral plugs were harvested. For the staining experiments, the plugs were thawed and the sides of the plugs were carefully sealed using cyanoacrylate glue (Loctite, Henkel Corp., USA) to allow CESA penetration only through the articular surface.



Figure 7.2 Photo showing the locations where osteochondral plugs were harvested from a bovine femoral groove. Plugs were randomly selected after freezing.

CESA solutions

CESAs for staining osteochondral plugs were dissolved in an aqueous solution containing preservative cocktail of protease inhibitors, antibiotics and antimycotics to prevent tissue degradation over the course of the experiment. A stock solution of demineralized water was made containing 5 mM ethylenediaminetetraacetic acid (EDTA), 5 mM benzamidine HCl and 1 X Gibco antibiotic-antimycotic (Life Technologies, Carlsbad, CA). Next, the pH of the solution was adjusted to pH 7.4 ± 1.0 by addition of NaOH. Finally, the osmolality of the solution was adjusted to 400 ± 30 mOsm/kg by addition of NaCl in order to achieve iso-osmolar conditions to synovial fluid. Table 7.1 gives an overview of the solution properties after adjustment for pH and osmolality.

Table 7.1 Properties of the staining solutions.

	CA4+6I		CA8+6I		CA4+3I	
mgI/mL	pH	mOsm/kg	pH	mOsm/kg	pH	mOsm/kg
6					7.26	412
12	7.34	414	6.35	398	7.36	403
24	7.39	398	6.41	403	7.23	428

7.4.3 Microfocus X-ray computed tomography

MicroCT scans were acquired using a µCT 40 (Scanco Medical AG, Switzerland) equipped with a 70 kVp/8W X-ray tube. This system consists of an X-ray tube capable of producing cone beams detected by a charge-coupled device detector with 2048 × 256 detectors (2048 × 2048 pixels per slice). The X-ray beam was filtered with a 0.5 mm aluminum filter. CECT slices were reconstructed using the manufacturer cone beam reconstruction algorithm, and exported as 8-bit XY slices (.tiff). Beam-hardening correction was performed.

Acquisition

Solutions were imaged in Eppendorf tubes, which were attached to an airtight sample holder. The osteochondral plugs were individually positioned in an airtight sample holder. The airtight sample holder is equipped with a platform containing 8 mm holes to accommodate six plugs. Per scan, six plugs were imaged at the same time using a µCT 40. All the scans were performed at 18 µm voxel size, 70 kV source voltage, 114 µA tube current and 200 ms integration time. Per scan, 371 images were obtained. Scan duration was about 45 min. The time spent scanning was not included in the incubation times.

Image processing and analysis

Concerning the stained cartilage plugs, the histogram of the dataset with plugs stained for 48 h with CA8+6I was windowed to the dynamic range of the dataset. Meanwhile, the 8-bit Tiff slices were converted to 8-bit bmp slices. Gray value normalization was performed on all other datasets using a rubber piece and the sample holder as the external references. During normalization,

8-bit Tiff files were converted to 8-bit bmp files. Both operations were performed using in-house developed MATLAB scripts.[212, 213]

Using Avizo (Thermo Fisher Scientific, Bordeaux, France), each individual plug was extracted as a subvolume in every datasets. Next, identical plugs imaged at different time points were registered and resampled. Using DataViewer (Bruker Micro-CT, Kontich, Belgium) profile surfaces (with a width of 110 pixels and an average length of 220 pixels) were drawn at various depths, measured from the osteochondral surface. These profile surfaces covered the middle of the osteochondral plug, to average out inherent image noise. Since the samples were cored at different spots in the femoral groove, there is some variation in cartilage thickness. Due to the cartilage depth- and thickness-dependency of the GAG distribution, we decided to calculate mean gray values at relative depth distances rather than absolute depth distances.

For every individual sample, the depth dependent averaged gray values of native cartilage before immersion in the staining solution were subtracted from the averaged gray values at the different time points during staining.

7.4.4 NaI calibration curve for iodine concentration determination

A calibration curve was generated based on the measured gray values of 1mL NaI solutions of various concentrations in Nanopure water (Barnstead Nanopure Thermo Scientific, Waltham, MA). The concentrations of the NaI solutions ranged from 6 mgI/mL (0.047 mmol/mL) to 48 mgI/mL (0.378 mmol/mL). Histograms were windowed based on their dynamic range. Gray values were normalized in between different datasets using external references (rubber piece and sample holder). For each phantom, gray value profile lines were drawn within the solution at three different depths and averaged using DataViewer (Bruker Micro-CT, Kontich, Belgium). These profile lines were drawn as long as possible, still covering the solution, to average out inherent image noise. Figure 7.2 displays the NaI calibration curve.

CESA solutions were prepared by dissolving CA4+6I, CA8+6I and CA4+3I in Nanopure water (Barnstead Nanopure Thermo Scientific, Waltham, MA). Table 7.1 gives an overview of the concentrations used. The X-ray attenuating properties of the solutions were assessed by scanning 1 mL solutions using a µCT 40 (Scanco Medical AG, Switzerland). The scans were performed at 18 µm voxel size, 70 kV source voltage, 114 µA tube current and 200 ms integration

time. Histograms were windowed based on their dynamic range. Gray values were normalized in between different datasets.

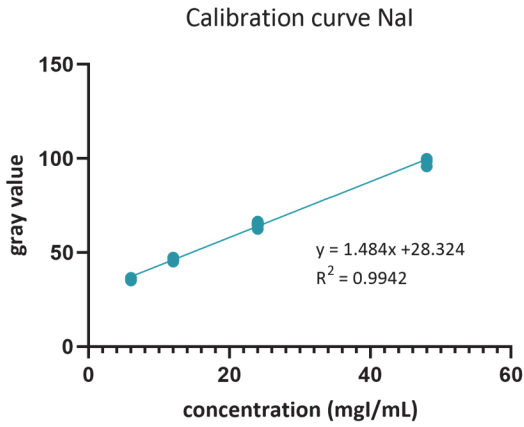


Figure 7.3 Calibration curve for NaI phantoms of concentrations 6 mgI/ml, 12 mgI/mL, 24 mgI/mL and 48 mgI/mL.

Table 7.2 Conversion table for CESA concentrations.

	CA4+6I (1499.876 g/mol)		**CA8+6I** (1761.876 g/mol)		**CA4+3I** (846.922 g/mol)	
mgI/mL	mg/mL	mmol/mL	mg/mL	mmol/mL	mg/mL	mmol/mL
6					13	0.016
12	24	0.016	28	0.016	27	0.032
24	47	0.032	55	0.032	54	0.063

For each CESA solution, gray value profile lines were drawn within the solution at three different depths and analyzed using DataViewer (Bruker Micro-CT, Kontich, Belgium). The profile lines were as long as possible, but still covering the solution, to average out inherent image noise. The way of profile line drawing is demonstrated in Figure 7.3. To illustrate the range of gray values covered, a profile line was drawn on air, the Eppendorf tube and the CA4+6I staining solution. The orange colored gray values were averaged, corresponding to the CA4+6I solution at a certain depth.

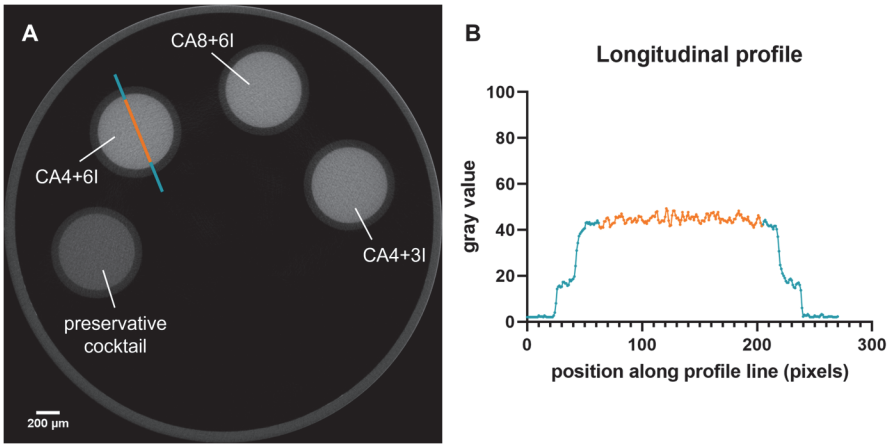


Figure 7.4 Illustration of profile line drawing to obtain averaged gray values of staining solutions. **A** Cross section of CA4+6I, CA8+6I and CA4+3I staining solutions of 12 mgI/mL. **B** Gray value profile line for the CA4+6I solution, corresponding to the blue/orange line in A.

7.4.5 Staining of osteochondral plugs with cationic CESAs

Bovine osteochondral plugs were stained by immersion in CESA staining solutions of 1.5 mL per plug. During immersion, samples were placed on a horizontal shaker plate. The plugs were taken out of the staining solution at dedicated time points (30 min, 1h, 3h, 6h, 12h30, 24h30 and 48h30) and excess liquid was removed by gently blotting on tissue paper. Next, the plugs were placed in the sample holder for imaging. Some deviations in the time points happened due to unanticipated errors related to the microCT system. One holder can accommodate six plugs. The time spent scanning was not included in the incubation times. The following concentrations were studied: 12 mgI/mL, 24 mgI/mL for CA4+6I and CA8+6I and 6 mgI/mL, 12 mgI/mL, 24 mgI/mL for CA4+6I. The experiment was performed in triplicate (n = 3) for each condition. After staining, the plugs were transferred to a PBS solution and placed on a shaker plate, in order to remove the staining solution. Plugs that were stained with CA4+3I and CA8+6I were immersed for 24 h, while plugs stained with CA4+6I were immersed for 24.67 h. The discrepancy in washing time is due to a technical failure of the microCT system.

Mean gray values were calculated based on profile surfaces that were drawn at different depths. For every individual sample, the depth-dependent averaged gray value of native cartilage (*i.e.* before immersion in the staining solution) was subtracted from the averaged gray value for each time point.

Interpretation of the data and the accompanied models requires caution because of the removal of some data points due to experimental errors (see next section), and because of cartilage variations due to differences in composition and thickness of different samples.

7.4.6 Descriptive data analysis

First, the data were inspected for anomalies. Data points were excluded from the dataset in case of mistakes during the course of the experiment (*e.g.* the improper swapping of plugs stained with CA4+3I for time points 24.5 h and 48.5 h) or in case of staining errors (*e.g.* uneven staining pattern of cartilage due to loosening of the glue in case of CA4+6I and CA4+3I). Due to temporary errors of the microCT system during the experiment, scans performed at time point 12.5 h slightly fluctuated in time. More specifically, for CA4+6I scans were performed at 12.5 h, for CA4+3I at 12.75 h and for CA8+6I at 13 h. However, the slight differences in time were assumed to be negligible, and hence, these time points were all approximated as time point 12.75 h.

Gray value range

The datasets of stained osteochondral plugs with a concentration of 24 mgI/mL and a staining time of 48.5 hours were analyzed using DataViewer (Bruker Micro-CT, Kontich, Belgium). For each plug, gray value profile surfaces having a width of 80 pixels (*i.e.* 1.440 µm) were drawn on 2 central sagittal sections in the XZ-plane and 2 central coronal section in the YZ-plane. As a result, per plug four sets of gray value profiles were obtained. The profile surfaces were as long as possible, covering the cartilage.

7.4.7 Diffusion analysis

Data were fitted using SAS via the JMP® Pro software package (v17, SAS Institute). More specifically, a nonlinear iterative fitting was carried out, using the least squares method according to Gauss-Newton using the following equation:

$$GV = \alpha(1 - e^{t/\tau}) \quad (1)$$

Where α is the maximum gray value coefficient, t the staining time and τ the penetration rate constant, *i.e.* the time required to reach 63.2% of the maximum gray value α. [69] Table gives an overview of the α and τ values

obtained for every condition, together with the Root Mean Square Error (RMSE). RMSE is the square root of the mean squared error between the fitted plot and the actual data points. This value is basically a measure of how far the points are from the fitted line, on average. When the RMSE is lower, the actual data points are closer to the fitted plot.

Table 7.3 Values of the constants obtained when fitting equation (4.1) to the gray value data collected for stained osteochondral plugs, classified per condition. α is the maximum gray value coefficient, τ the penetration rate constant, RMSE the Root Mean Square Error, δ the time required to reach 95% of the maximum gray value.

		24 mgl/mL				12 mgl/mL				6 mgl/mL			
	depth (%)	α	τ	RMSE	δ	α	τ	RMSE	δ	α	τ	RMSE	δ
CA4+6I	10	52.189	1.508	6.721	4.518	29.184	3.210	3.688	9.636				
	50	92.673	2.528	6.878	7.573	57.897	3.587	6.282	10.746				
	90	103.435	3.003	4.672	8.996	74.368	3.612	4.878	10.821				
CA8+6I	10	67.596	1.639	7.405	4.910	53.784	3.562	8.525	10.671				
	50	108.735	3.777	8.120	11.315	88.474	6.917	7.746	20.722				
	90	106.321	4.968	5.730	14.883	92.893	9.971	8.816	29.870				
CA4+3I	10	42.548	6.449	6.044	19.319	23.141	1.397	3.072	4.185	10.710	0.799	1.592	2.394
	50	71.964	9.887	9.795	29.619	38.010	2.620	4.538	7.849	20.868	2.360	3.670	7.070
	90	71.798	13.208	5.058	39.568	47.523	4.335	4.283	12.987	25.891	5.964	2.717	17.867

7.4.8 Statistical data analysis (MANOVA)

All statistics were conducted using SAS® 9.4 or SAS®- via the JMP® Pro software package (v17, SAS Institute). Statistical significance was assumed at a probability (p) value of < 0.05. For the MANOVA analysis of the data, we used a repeated measures design with time as the repeated measure. Here, gray values categorized per time point were entered as the dependent variables, while CESA, depth and concentration and their two-factor interactions were entered as factors. The repeated measures design is the most appropriate model in this case because it accounts for dependence between different time points for the same sample. MANOVA assumes that the repeated measures of a same subject have a constant variance across time. Since the differences in time between the different time points in our study are not constant, this assumption is violated. Therefore, results must be interpreted with caution. In case the sphericity assumption was not met according to Mauchly's test, the Greenhouse-Geisser correction was employed.

7.4.9 Supplementary figures

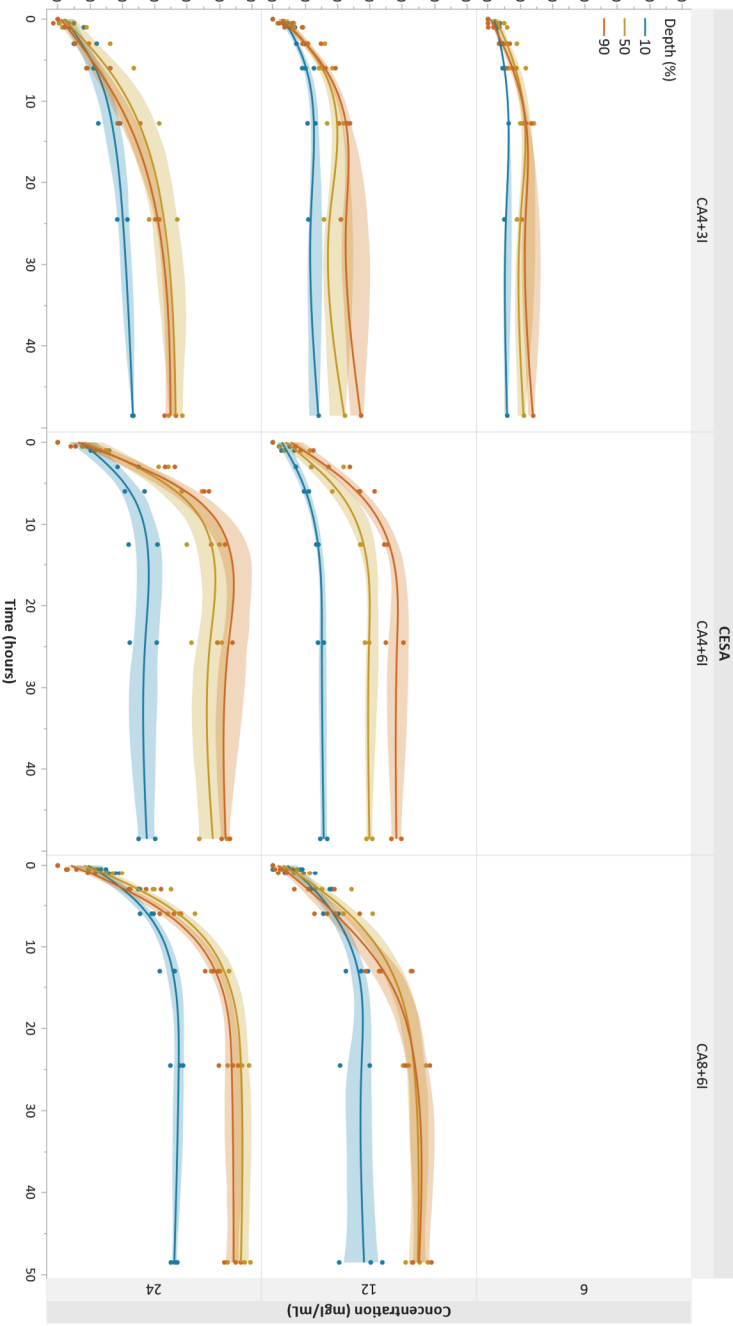


Figure 7.5 Graphical visualization of gray value analysis of osteochondral plug staining with CA4+6I, CA8+6I and CA4+3I. Smooth curves of gray value as a function of staining time (hours), classified by CESA and concentration and labeled by cartilage depth. The curves were plotted in JMP using a polynomial smoothing spline with lambda set at 0.05. The shaded regions represent the confidence of fit.

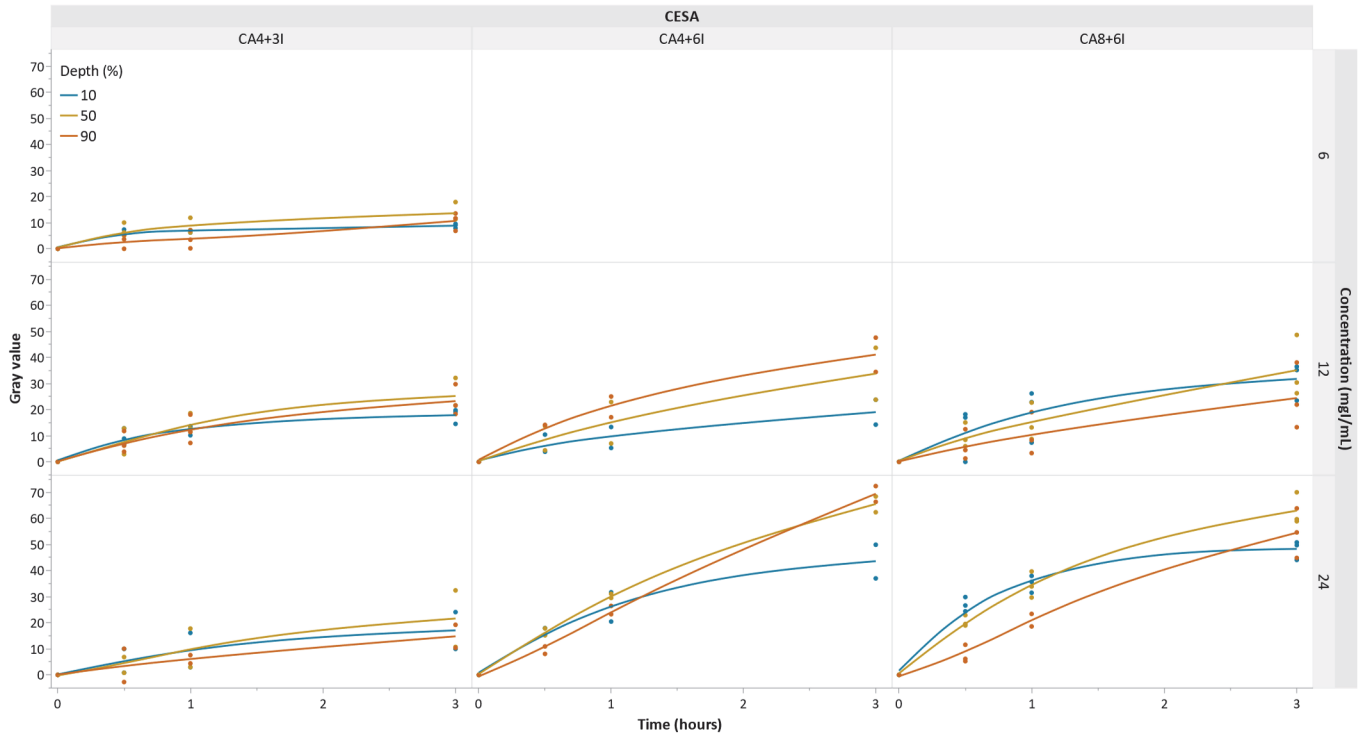


Figure 7.6 Graphical visualization of gray value analysis of osteochondral plug staining with CA4+6I, CA8+6I and CA4+3I for early time points. Smooth curves of gray value as a function of staining time (hours), classified by CESA and concentration and labeled by cartilage depth. The curves were plotted in JMP using a polynomial smoothing spline with lambda set at 0.05.

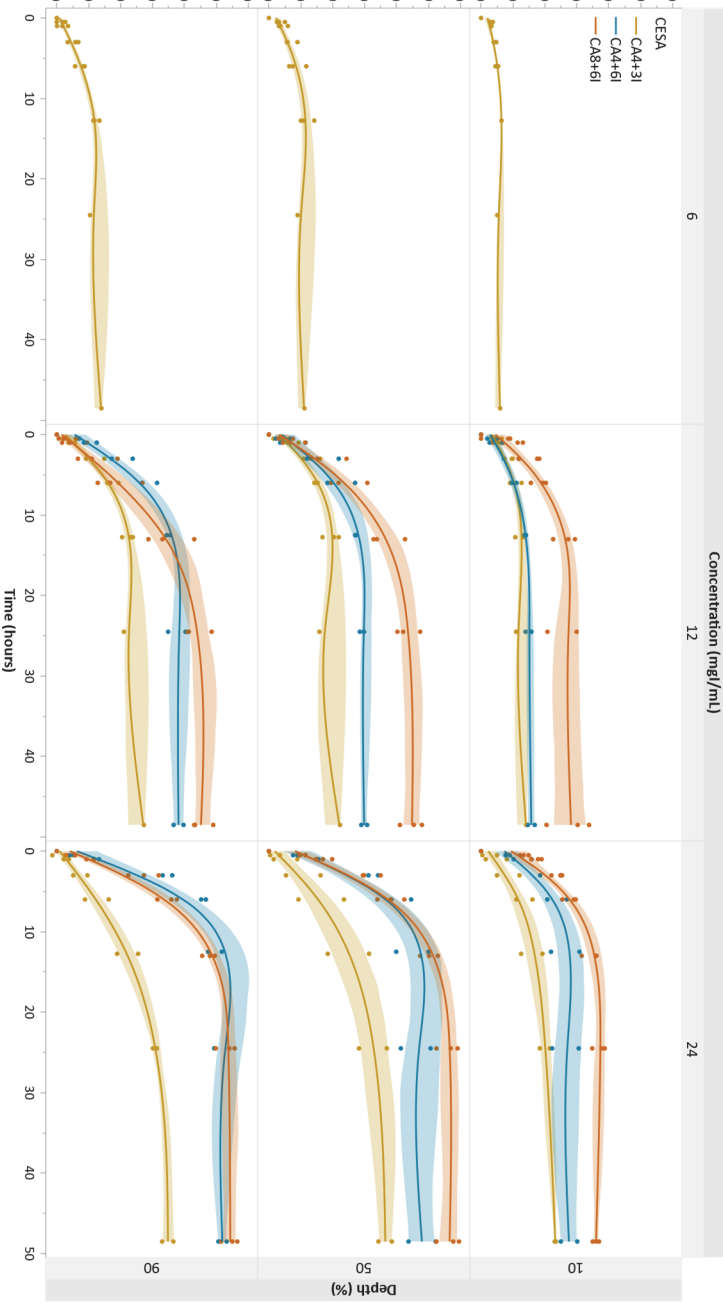
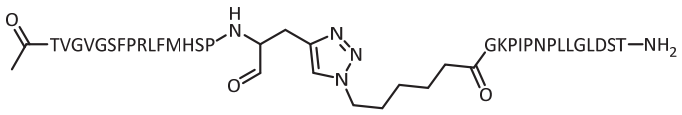


Figure 7.7 Graphical visualization of gray value analysis of osteochondral plug staining with CA4+6I, CA8+6I and CA4+3I. Smooth curves of gray value as a function of staining time (hours), classified by concentration and cartilage depth and labeled by CESA. The curves were plotted in JMP using a polynomial smoothing spline with lambda set at 0.05. The shaded regions represent the confidence of fit.

7.5 Chapter 5: Protein-specific CECT – Experimental

7.5.1 Synthesis

PI210 (compound 5.1)

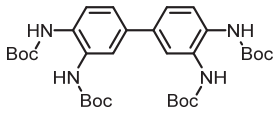


Reagents: All chemicals were purchased from commercial suppliers: Sigma Aldrich, Acros organics. The peptide sequences Ac-TVGVGSFPRLFMHSP-(L-Pra)-NH_2 (KLH210) and (6-Azido)-GKPIPNPLLGLDST-NH_2 (V5-tag) were purchased from ChinaPeptides (Shanghai, China) as HPLC-purified, custom synthesized on the 50 mg scale.

Procedure: The procedure is based on the protocol reported by Presolski S. *et al*.[183] In a 10 mL flask KLH210 (1.0 mg, 0.566 µmol, 1.0 equiv) and V5-tag (1.0 mg, 0.641 µmol, 1.0 equiv) were dissolved in PBS (1x, 6.7 mmol PO_4). $CuSO_4.5H_2O$ (0.3 mg, 1.2 µmol, 1.9 equiv) and tris(3-hydroxypropyltriazolylmethyl)amine (THPTA, 2.2 mg, 5.1 µmol, 8.0 equiv) were mixed in 85 µL demineralized water in a 2 mL tube and transferred to the reaction flask. Next, sodium ascorbate (NaAsc, 20.6 mg, 104.0 µmol, 46.3 equiv) was dissolved in 1 mL of demineralized water and 283 µL of this solution was added to the reaction flask. The flask was flushed with nitrogen and the reaction was stirred for 24 hours at room temperature. Next, the reaction mixture was transferred into a dialysis cassette (MWCO 2 kDa). The product was purified by dialysis in 500 mL PBS (0.5x, 3.35 mL PO_4) containing 1 mM ethylenediaminetetraacetic acid (EDTA) for 5 days with 2 times change of the dialysate. Next, the dialysis cassette was transferred to 500 mL demineralized water for 2 days with frequent water change. Finally, the retentate was lyophilized to obtain **5.1** as a white powder (1.72 mg, 81%).

LR-MS (ESI) $C_{152}H_{240}N_{42}O_{40}S$ m/z $[M+3H]^{3+}$ calculated: 1110.311, found: 1110.200; $[M+2H+Na]^{3+}$ calculated: 1117.638, found: 1117.300; $[M+4H]^{4+}$ calculated: 832.985, found: 832.900; $M+3H+Na]^{4+}$ calculated: 838.480, found: 838.300. **Physical appearance**: white powder.

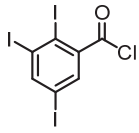
_N_,_N_',_N_'',_N_'''-tetrakis(tert-butyloxycarbonyl)-3,3'-diaminobenzidine (compound 5.3)



The Boc protection procedure is based on a protocol reported by Boz *et al*.[190] In a 250 mL flask charged with a stirring was DAB (1.071 g, 5 mmol, 1.0 equiv) dissolved in THF (150 mL) and Et_3N (2.8 mL, 20 mmol, 4.0 equiv). Next, a solution of Boc_2O (5.456 g, 25 mmol, 5.0 equiv) in THF (50 mL) was added slowly added to the reaction mixture. The flask was thoroughly purged with nitrogen and stirred overnight at room temperature under a nitrogen atmosphere. The reaction mixture was concentrated under reduced pressure and purified by flash column chromatography on silica gel (DCM/MeOH, 95/5). The product was isolated as a white solid (2.739 g, 4.456 mmol, 89%).

^{1}H NMR (400 MHz, DMSO-d_6) δ = 8.64 – 8.54 (m, 4H), 7.71 (app. s, 2H), 7.58 (app. d, *J* = 8.5 Hz, 2H), 7.32 (app. dd, *J* = 2.1, 8.5 Hz, 2H), 1.50 (s, 36H). **^{13}C NMR** (101 MHz, DMSO-d_6) δ = 153.74, 153.63, 135.81, 130.78, 129.87, 124.56, 122.53, 122.09, 80.03, 79.95, 31.14, 28.53. **HR-MS** (ESI) m/z calculated for $C_{32}H_{46}N_4O_8$ $[M+Na]^+$ 637.3208, found 637.3223. **IR** (neat, cm^{-1}): v 3302 (N-H stretch), 2977 (C-H bend), 1697 (C=O stretch), 1585 (N-H bend), 1455 (C-H bend), 1271 (C-N stretch), 1151 (C-O stretch), 769 (C-H bend). **MP**: T_m 155.1 – 157.5 °C. **Physical appearance**: white solid.

2,3,5-Triiodobenzoyl chloride (compound 5.4)



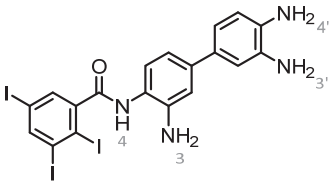
The procedure is based on the literature procedure by Samuel *et al*.[214] 2,3,5-triiodobenzoic acid (10.5 g, 0.021 mol, 1.0 equiv) was suspended in thionyl chloride (131.4 mL, 1.800 mol, 85.7 equiv) in a 250 mL flask. Subsequently, DMF (58 µL, 0.001 mol, 3.6 mol%) was added. The reaction mixture was refluxed overnight. Next, excess thionyl chloride was removed under reduced pressure. The remaining brown solid was purified by crystallization in DCM.

Product was obtained a white solid needles (10.186 g, 0.02 mol, 93%). The mother liquor fraction was reused in a second and third round of crystallization, which increased the yield.

^{1}H NMR (400 MHz, DMSO-d_6) δ = 8.32 (app. d, *J* = 1.8 Hz, 1H), 7.73 (app. d, *J* = 1.8 Hz, 1H). **^{13}C NMR** (101 MHz, DMSO-d_6) δ = 168.32, 147.53, 144.10, 135.68, 114.75, 107.35, 95.69. **Physical appearance**: white crystals.

These data are in agreement with literature data.[214]

2,3,5-triiodo-*N*-(3,3',4'-triamino-[1,1'-biphenyl]-4-yl)benzamide (compound 5.5)



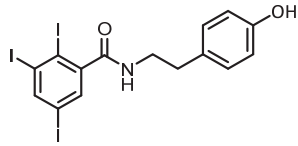
A procedure similar to the protocol reported by Sunke *et al.* was performed.[215]

A flame-dried 100 mL flask was charged with a stirring bar and DAB (190.3 mg, 0.89 mmol, 1.0 equiv), capped with a septum and purged with N_2 gas. Dry dimethylacetamide (DMA, 2.5 mL) was added to dissolve DAB. Next, Et_3N (0.148, 1.07 mmol, 1.2 equiv) was added at 0 °C. Then **5.4** (460.3 mg, 0.89 mmol, 1.0 equiv) dissolved in 2.4 mL dry DMA was slowly added over a time course of 80 min (0.03 mL/min) using a syringe pump while stirring. The reaction mixture was stirred at room temperature for 50 min. Product formation was followed by TLC. After removal of DMA under reduced pressure, the residue was precipitated when added to water. The obtained precipitate was filtered and washed with saturated aq. $NaHCO_3$ solution, brine and ethyl acetate. After drying over vacuum, an off-white solid was obtained. Due to the poor solubility, the product was used as such.

At this point, it could not be stated with certainty that compound **5.5** was obtained as displayed. Potentially, the amide formation could also happen on the position *N*-3.

^{1}H NMR (400 MHz, DMSO-d_6) δ = 9.63 – 9.39 (m, 1H), 8.32 (app. s, 1H), 7.97 – 7.85 (m, 2H), 7.62 – 7.35 (m, 1H), 7.34 – 7.09 (m, 1H), 7.02 – 6.68 (m, 1H), 6.67 – 6.48 (m, 1H), 5.20 – 4.88 (m, 1H), 4.63 – 4.38 (m, 1H). **^{13}C NMR** (101 MHz, DMSO-d_6) δ = 167.33, 147.90, 146.53, 143.31, 141.28, 135.54, 135.29, 129.95, 126.44, 124.49, 116.00, 115.06, 114.08, 113.98, 113.68, 113.26, 112.97, 108.37, 95.96. **HR-MS** (ESI) m/z calculated for $C_{19}H_{15}I_3N_4O$ $[M+Na]^+$ 718.8278, found 719.0093. **IR** (neat, cm^{-1}): v 3386 (N-H stretch), 1644 (C=O stretch), 1301 (C-N stretch), 619 (C-I stretch). **MP**: T_m 258.9 – 266.8 °C (decomposition). **Physical appearance**: off-white solid.

***N*-(4-hydroxyphenethyl)-2,3,5-triiodobenzamide (compound 5.8)**



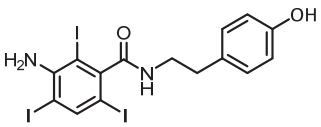
A procedure similar to the protocol reported by Mahindroo *et al.* was performed.[216]

In 100 mL flask, charged with a stirring bar, 2,3,5-triiodobenzoic acid (1.02 g, 2 mmol, 1.0 equiv), HBTU (1.896 g, 5 mmol, 2.5 equiv) were dissolved in DMF (8 mL). After addition of DIPEA (1.0 mL, 6 mmol, 3.0 equiv), the reaction mixture was stirred for 30 min at room temperature. Next, a solution of tyramine (560 mg, 4 mmol, 2.0 equiv) in DMF (1.0 mL) was added and the reaction mixture was stirred overnight at room temperature. DMF was removed under reduced pressure. The residue was dissolved in ethyl acetate and washed sequentially with HCl 1 M, saturated aq. $NaHCO_3$ and brine. The combined organic layers were dried over anhydrous Na_2SO_4, filtered and concentrated under reduced pressure. Next, the crude product was purified by flash column chromatography on silica gel (heptane/ethyl acetate, 6/4). The title compound was obtained as a white solid (0.782 g, 1.26 mmol, 63%).

^{1}H NMR (400 MHz, DMSO-d_6) δ = 9.19 (s, 1H), 8.50 (t, *J* = 5.6 Hz, 1H), 8.25 (app. d, *J* = 1.9 Hz, 1H), 7.41 (app. d, *J* = 1.9 Hz, 1H), 7.07 - 7.00 (m, 2H), 6.73 - 6.65 (m, 2H), 3.38 - 3.28 (m, 2H), 2.70 (t, *J* = 7.4 Hz, 2H). **^{13}C NMR** (101 MHz, DMSO-d_6) δ = 168.24, 156.18, 147.99, 146.37, 135.03, 130.04, 129.68, 115.58, 113.89, 108.07, 95.74, 41.42, 34.40. **HR-MS** (ESI) m/z calculated for $C_{15}H_{12}I_3NO_2$ $[M+H]^+$ 619.8080, found 619.8077. **IR** (neat, cm^{-1}): v 3305 (N-H stretch), 3219

(br, O-H stretch), 2912 (C-H stretch), 1614 (C=O stretch), 1358 (O-H bend), 1237 (C-N stretch), 1205 (C-O stretch), 735 (C-H bend), 556 (C-H stretch). **MP**: T_m 229.3 – 231.4 °C (decomposition). **Physical appearance**: white solid.

3-amino-*N*-(4-hydroxyphenethyl)-2,4,6-triiodobenzamide (compound 5.9)

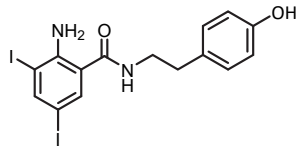


A procedure similar to the protocol reported by Mahindroo *et al.* was performed.[216]

In 100 mL flask, charged with a stirring bar, 3-amino-2,4,6-triiodobenzoic acid (1.576 g, 3.0 mmol, 1.0 equiv), HBTU (1.707 g, 4.5 mmol, 1.5 equiv) were dissolved in DMF (10 mL). After addition of DIPEA (1.568 mL, 9.0 mmol, 3.0 equiv), the reaction mixture was stirred for 10 min at room temperature. Next, a solution of tyramine (0.84 g, 6.0 mmol, 2.0 equiv) in DMF (5.0 mL) was added and the reaction mixture was stirred overnight at room temperature. DMF was removed under reduced pressure. The residue was dissolved in ethyl acetate and washed sequentially with HCl 1 M, saturated aq. $NaHCO_3$ and brine. The combined aqueous phases were extracted with DCM three times. The organic layers were combined and dried over anhydrous Na_2SO_4, filtered and concentrated under reduced pressure. Next, the crude product was purified by flash column chromatography on silica gel (DCM/MeOH, 99/1 + 0.1% Et_3N). The title compound was obtained as a yellow solid (0.927 g, 1.46 mmol, 49%).

^{1}H NMR (400 MHz, DMSO-d_6) δ = 9.18 (s, 1H), 8.49 (t, J = 5.6 Hz, 1H), 7.98 (s, 1H), 7.10 – 7.03 (m, 2H), 6.72 – 6.65 (m, 2H), 5.36 (s, 2H), 3.37 – 3.31 (m, 2H), 2.76 (t, *J* = 7.5, 2H). **^{13}C NMR** (101 MHz, DMSO-d_6) δ = 169.90, 156.13, 149.15, 147.85, 146.68, 129.96, 129.77, 115.64, 82.30, 81.48, 76.93, 41.48, 34.42. **HR-MS** (ESI) m/z calculated for $C_{15}H_{13}I_3N_2O_2$ $[M+H]^+$ 634.8190, found 634.8175. **IR** (neat, cm^{-1}): v 3313 (N-H stretch), 3216 (br, O-H stretch), 2913 (C-H stretch), 1641 (C=O stretch), 1589 (N-H bend), 1372 (O-H bend), 1293 (C-N stretch), 1226 (C-N stretch), 1172 (C-O stretch), 718 (C-H bend), 566 (C-I stretch). **MP**: T_m 220.5 – 222.4 °C (decomposition). **Physical appearance**: light yellow, off-white solid.

2-amino-*N*-(4-hydroxyphenethyl)-3,5-diiodobenzamide (compound 5.10)

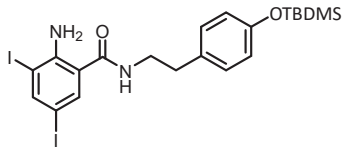


A procedure similar to the protocol reported by Mahindroo *et al.* was performed.[216]

In 100 mL flask, charged with a stirring bar, 2-amino-3,5-diiodobenzoic acid (1.587 g, 4 mmol, 1.0 equiv), HBTU (1.517 g, 4 mmol, 1.0 equiv) were dissolved in DMF (10 mL). After addition of DIPEA (2.1 mL, 12 mmol, 3.0 equiv), the reaction mixture was stirred for 10 min at room temperature. Next, a solution of tyramine (1.12 g, 8.0 mmol, 2 equiv) in DMF (5 mL) was added and the reaction mixture was stirred overnight at room temperature. DMF was removed under reduced pressure. The residue was dissolved in ethyl acetate and washed sequentially with HCl 1 M, saturated aq. $NaHCO_3$ and brine. The organic layers were combined and dried over anhydrous Na_2SO_4, filtered and concentrated under reduced pressure. Next, the crude product was purified by flash column chromatography on silica gel (DCM/MeOH, 98/2 + 0.1% Et_3N). Further purification was performed by crystallization in DCM. The title compound was obtained as off-white crystals (1.695 g, 3.34 mmol, 83%).

^{1}H NMR (400 MHz, DMSO-d_6) δ = 9.18 (s, 1H), 8.56 (t, *J* = 5.5 Hz, 1H), 7.95 (d, *J* = 1.9 Hz, 1H), 7.73 (d, *J* = 1.9 Hz, 1H), 7.08 - 6.96 (m, 2H), 6.75 - 6.63 (m, 2H), 6.46 (s, 2H), 3.41 - 3.34 (m, 2H), 2.70 (t, *J* = 7.6 Hz, 2H). **^{13}C NMR** (101 MHz, DMSO-d_6) δ = 167.22, 156.13, 148.40, 148.04, 136.77, 129.98, 129.90, 118.69, 115.60, 88.04, 76.72, 41.61, 34.52. **HR-MS** (ESI) m/z calculated for $C_{15}H_{14}I_2N_2O_2$ $[M+H]^+$ 508.9221, found 508.9224. **IR** (neat, cm^{-1}): v 3448 (N-H stretch), 3335 (N-H stretch), 3168 (br, O-H stretch), 2919 (C-H stretch), 1597 (N-H bend), 1365 (O-H bend), 1248 (C-N stretch), 1229 (C-H stretch), 1183 (C-O stretch), 731 (C-H bend), 551 (C-I stretch). **MP**: T_m 200.5 – 202.3 °C (decomposition). **Physical appearance**: white crystals.

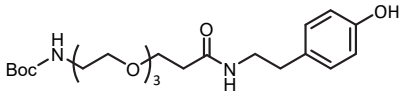
2-amino-*N*-(4-((tert-butyldimethylsilyl)oxy)phenethyl)-3,5-diiodobenzamide (compound 5.11)



tert-Butyldimethylsilyl chloride (186.8 mg, 1.2 mmol, 1.2 equiv) was added to a stirring solution of **5.10** (508.9 mg, 1.0 mmol, 1.0 equiv) and imidazole (170.5 mg, 2.5 mmol, 2.5 equiv) in 3 mL of DMF at room temperature. The mixture was stirred at room temperature overnight. Analysis of the reaction mixture by LC-MS indicated incomplete conversion. Therefore, the temperature was raised to 60 °C and the reaction mixture was stirred one extra night. Despite the incomplete conversion, even at higher temperatures, the reaction was stopped. The reaction mixture was cooled down and DMF was removed under reduced pressure. The residual was dissolved in a big volume of DCM due to poor solubility. Next, the organic phase was washed with saturated aq. $NaHCO_3$. The aqueous phase was extracted three times with DCM. The organic phases were combined and DCM was removed under reduced pressure. Due to presence of precipitation, the crude product was coated on celite and purified by flash column chromatography on silica gel (isohexane/ethyl acetate, 9/1) to afford the product as a white solid (112.6 mg, 0.18 mmol, 18%). Compound **5.10** was recovered and isolated (263.8 mg). The yield based on the converted **5.10** was 46%. The low yield is due to a leakage during column chromatography, incomplete conversion and the poor solubility of **5.11**.

^{1}H NMR (400 MHz, DMSO-d_6) δ = 8.57 (t, *J* = 5.5 Hz, 1H), 7.95 (d, *J* = 2.0 Hz, 1H), 7.71 (d, *J* = 2.0 Hz, 1H), 7.17 - 7.05 (m, 2H), 6.81 - 6.73 (m, 2H), 6.45 (s, 2H), 3.43 - 3.35 (m, 2H), 2.75 (t, *J* = 7.4 Hz, 2H), 0.98 - 0.92 (s, 9H), 0.21 - 0.13 (s, 6H). **^{13}C NMR** (101 MHz, DMSO-d_6) δ = 166.76, 153.39, 147.91, 147.57, 136.27, 132.16, 129.70, 119.63, 118.17, 87.55, 76.21, 40.84, 33.99, 25.58, 17.91, -4.50. **HR-MS** (ESI) m/z calculated for $C_{21}H_{28}I_2N_2O_2Si$ $[M+H]^+$ 623.0086, found 623.0084. **IR** (neat, cm^{-1}): v 3426 (N-H stretch), 3333 (N-H stretch), 2929 (C-H stretch), 2857 (C-H stretch), 1629 (C=O stretch), 1603 (N-H bend), 1362 (C-N stretch), 1324 (C-N stretch), 1247 (Si-C stretch), 1192 (C-O stretch), 911 (Si-O stretch), 866 (C-H bend), 776 (C-H bend), 534 (C-I stretch). **Physical appearance**: white solid.

tert-butyl(15-(4-hydroxyphenyl)-12-oxo-3,6,9-trioxa-13-azapentadecyl)carbamate (compound 5.13)

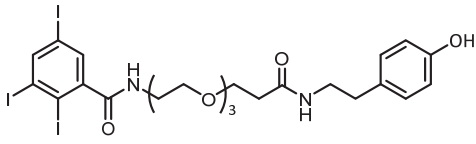


A procedure similar to the protocol reported by Zhang *et al.* was performed.[217]

A flame-dried flask of 50 mL, containing a stirring-bar, was filled withBoc-*N*-amido-PEG3-acid (93.7 mg, 0.29 mmol, 1.0 equiv), 4-dimethylaminopyridine (DMAP, 35.6 mg, 0.29 mmol, 1.0 equiv) and dicyclohexylcarbodiimide (DCC, 72.2 mg, 0.29 mmol, 1.2 equiv) and 12 mL dry DCM. After 30 min stirring at room temperature, tyramine (40.0 mg, 0.29 mmol, 1.0 equiv) was added and the reaction mixture was stirred overnight at room temperature. The reaction was stopped and the white crystals (= *N,N'*-dicyclohexylurea) were removed by filtration. Next, the crude mixture was diluted with DCM and washed subsequently with 1M HCl (three times), saturated aq. $NaHCO_3$ and brine. The organic phase was dried over anhydrous Na_2SO_4 , filtered and the solvent was removed under reduced pressure. Afterwards, a small amount of DCM was added and the residue was stored overnight at 0°C. Next, white crystals were removed by filtration. The solvent was removed under reduced pressure, and the process of removal of *N,N'*-dicyclohexylurea by recrystallization from DCM and filtration was performed once more. Finally, the desired compound was isolated as a yellow oil (108.1 mg, 0.25 mmol, 84%).

^{1}H NMR (400 MHz, $CDCl_3$) δ = 7.08 – 7.01 (m, 2H), 6.86 - 6.79 (m, 2H), 8.50 (br s, 1H), 5.08 (br s, 1H), 3.72 - 3.46 (m, 14H), 3.37 - 3.26 (m, 2H), 2.75 (t, J = 6.6 Hz, 2H), 2.50 - 2.41 (m, 2H), 1.46 (s, 9H)**. ^{13}C NMR** (101 MHz, $CDCl_3$) δ = 171.77, 155.24, 155.14, 129.84, 129.76, 115.64, 70.40, 70.29 (br s, 2C), 70.12, 67.27, 66.50, 40.59, 40.34, 36.67, 34.60, 28.43. **ASAP-MS** $C_{22}H_{36}N_2O_7$ m/z $[M+H]^+$ calculated: 441.260 found: 441.3. **Physical appearance**: yellow oil.

_N_-(15-(4-hydroxyphenyl)-12-oxo-3,6,9-trioxa-13-azapentadecyl)-2,3,5-triiodobenzamide (compound 5.14)



A 50 mL flask was charged with a stirring bar and compound **5.13** (103.4 mg, 0.24 mmol) was dissolved in a 1 : 1 mixture of DCM and trifluoroacetic acid (2 mL : 2 mL). The mixture was stirred at room temperature for 2 hours. Afterwards, the solvent was removed under reduced pressure. In order to remove excess trifluoroacetic acid, the mixture was coevaporated with MeOH twice to remove residual TFA. Afterwards, the residue was dried *in vacuo* to yield the crude compound (**5.13a**, 3-(2-(2-(2-aminoethoxy)ethoxy)ethoxy)-*N*-(4-hydroxyphenethyl)propanamide) as a yellow oil (66.3 mg, 0.195 mmol, 83%). **ASAP-MS** $C_{17}H_{28}N_2O_5$ m/z $[M+]^{+\cdot}$ calculated: 340.200 found: 340.2; $M+H]^+$ calculated: 341.207 found: 341.2.

A flame-dried 25 mL flask was charged with a stirring bar and filled with compound **5.4** (2,3,5-triiodobenzoyl chloride, 54.5 mg, 0.105 mmol, 1 equiv). Next, it was dissolved in 1 mL dry DMF and DIPEA (92 µL, 0.526 mmol, 5 equiv) was added. While stirring, the crude amino-PEG3-tyramide **5.13a** (37.7 mg, 0.105 mmol, 1 equiv) dissolved in 0.5 mL DMF was dropwise added over a time course of 15 min at room temperature using a syringe pump (0.03 mL/min). The reaction mixture was stirred overnight at 50 °C. Afterwards, the mixture was cooled to room temperature, and the solvent was removed under reduced pressure. The residue was purified by semipreparative RP-HPLC at a flow rate of 10 mL/min for 55 min. (Solvent A, H_2O + 0.1% HCOOH; solvent B, MeCN; 40% B ⟶ 55% B, 15 min; 55% B, 15 min; 55% B ⟶ 100% B 25 min). The retention time of the product was 20.6 min. The appropriate fractions were pooled, solvent was removed under reduced pressure and lyophilized to afford the desired product as a yellow oil (16.3 mg, 0.016 mmol, 15%).

^{1}H NMR (400 MHz, MeOH-d_4) δ = 8.31 (app. d, *J* = 2.0 Hz, 1H, 7.58 (app. d, *J* = 1.8 Hz, 1H), 7.09 - 7.01 (m, 2H), 6.77 - 6.69 (m, 2H), 3.73 - 3.54 (m, 2H), 3.54 - 3.49 (m, 2H), 3.40 - 3.34 (m, 2H), 2.77 - 2.66 (m, 2H), 2.41 (t, *J* = 6.2 Hz, 2H). **^{13}C NMR** (101 MHz, MeOH-d_4) δ = 172.47, 169.83, 155.52, 148.80, 147.13, 134.85, 129.86, 129.40, 114.87, 111.52, 105.88, 93.30, 70.24, 70.06, 69.89, 69.88, 68.72, 66.92, 40.91, 39.55, 36.31, 34.26. **HR-MS** (ESI) m/z calculated for $C_{24}H_{29}I_3N_2O_6$ $[M+H]^+$ 822.9238, found 822.9225. **Physical appearance**: yellow oil.

7.5.2 Phage display library

The random peptide library p3L15 displaying linear 15-mer peptides was kindly provided by Dr. G.P. Smith (University of Missouri, Columbia, MO, USA)

consisting of about 2 x 108 primary transformants. Peptides are expressed at the N-terminus of the pIII coat protein.

7.5.3 Phage display protocol

The biopanning procedure was performed as described earlier.[218] In the next paragraphs, the protocol for one round of biopanning is described. The protocol of the following rounds is identical to the first one. Phage display commonly involves three to five rounds of biopanning. The phage display against KLH was performed with three rounds of biopanning.

A solution of keyhole limpet hemocyanin (KLH) with a concentration of 10 µg/ml in phosphate-buffered saline (PBS) was coated (50 µL/well) at room temperature (RT) on a sterile 96 well plate, followed by incubation overnight at 4°C on a shaker plate. After discarding the coating solution the plate was washed twice with 100 µL PBS containing 0.5% Tween-20 (TPBS). Post-coating was performed with a 1% (wt/vol) solution of BSA in PBS for at least one hour at RT (200 µL/well). As a negative control, wells were coated with a solution of 0.1% BSA, 0.5% TPBS and 2.5×10^{12} phages (p3L15 library) in PBS for one hour at room temperature (50 µL/well). After washing all wells (BSA post-coated and negative control) twice with TPBS, a solution of 0.1% BSA, 0.5% TPBS and 2.5×10^{12} phages (p3L15 library) in PBS was added to all the coated wells (50 µL/well), and the plate was incubated overnight at 4 °C on a shaker plate. After removal of the phage suspension and careful washing with TPBS (six times, 200 µL/well), the bound phages were eluted by incubating wells with 0.2 M glycine, pH 2.2 at room temperature on a shaker plate for 10 min (100 µL/well). The eluate was transferred to a sterile Eppendorf tube and neutralized by adding 1 M Tris pH 8.0, vortexed and kept on ice until infection (19 µL/tube).

An overnight *E. coli* K91 BluKan cell culture (containing 20 mg/mL kanamycine in NZY-tetracycline-medium) was diluted 100 times and grown in NZY-tetracycline-medium at 37°C on a shaker until the OD^{600} was about 0.45. To 100 µl eluted phage solution, 200 µl of 'starved'[m] *E. coli* K91 BluKan cell culture

[m] Starved *E. coli* K91 BluKan cells were prepared by removing the cell culture medium after OD^{600} was about 0.45. Cell culture medium was removed by centrifugation (1750 rpm) and removal of the supernatant. The remaining pellet was suspended in a 30 mL 80 mM NaCl and incubated for 45 min at 37 °C on a shaker plate. After centrifugation

and 20 mL NZY-tetracycline-medium were added and incubated overnight at 37 °C on a shaker plate for phage infection.

After incubation, the infected cell culture was centrifuged (8000 rpm) at 4 °C for 20 min. The supernatant was transferred to a sterile 50 mL falcon tube and a solution of 20 %PEG6000 in 2.5M NaCl was added with a volume equal to ¼ of the supernatant volume, followed by incubation on ice for at least two hours. Next, the content of the falcon tube was centrifugated (3200 rpm) for 20 min at 4 °C. The supernatant was carefully removed and the remaining pellet was dissolved in 1 mL miliQ water with 300 µL of the 20 %PEG6000 in 2.5M NaCl solution. After incubation on ice for one hour, the solution was centrifugated (13400 rpm) for 5 min at 4 °C. The supernatans was removed and the pellet was dissolved in 250 µL sterile PBS buffer. Finally, the solution was centrifugated (13400 rpm) for 90 seconds at room temperature. The supernatant contains the purified phage solution after one round of biopanning against KLH, dissolved in PBS. The concentration could be determined by measuring the absorbance at 269 nm. The supernatant was removed and stored at −20 °C until further use.

After three rounds of biopanning, single clone phages were prepared. Therefore, 900 µL of TG1 *E.coli* cells grown in Luria broth (LB) medium with OD^{600} of about 0.45 were mixed with 100 µL of a 10^8 phages/mL solution and incubated for 45 min at 37 °C. Next, 100 µL of this solution was plated on tetracycline containing agar plates. After overnight incubation at 37°C, the grown colonies were isolated and identified through DNA sequencing. All selected phages were finally stored in PBS-5% glycerol (w/v%) at −20 °C until further use.

7.5.4 Elisa protocol for the identified phage clones

Wells of a 96 well plate with flat bottom were coated with 100 µL of a 20 µg/mL solution of KLH (EDM Milipore, # 374805) in PBS, or with 100 µL of a 1% BSA (Sigma-Aldrich, #SLBW6771) solution in PBS and the plate was incubated overnight at 4°C. Next, the unbound proteins were washed three times by immersing the plate in the washing buffer (3 x PBS – 0.1% Tween20). Next, protein blocking was done by adding 300 µL/well of a 4% milk solution in PBS and incubating for it at least two hours at room temperature on a

(1750 rpm) and removal of the supernatant, the pellet was resuspended in 1 mL NAP-buffer and stored at 4 °C until infection.

shaker plate. Afterwards, the plate was washed three times by immersing it in the washing buffer. Next, 100 µL of the phage solutions were added to the plate and incubated for two hours at room temperature on a shaker plate. The following concentrations were used, obtained by serial dilution (n=1 for KLH, n=1 for BSA): (i) 10.0 x 10^{11} phages/mL, (ii) 5 x 10^{11} phages/mL, (iii) 2.5 x 10^{11} phages/mL, (iv) 1.25 x 10^{11} phages/mL, (v) 0.625 x 10^{11} phages/mL, (vi) 0.313 x 10^{11} phages/mL, (vii) 0.156 x 10^{11} phages/mL and (viii) 0.078 x 10^{11} phages/mL. Dilutions of the phage solution were made using PBS - 0.4% milk. Afterwards, the plate was washed 12 times with the washing buffer to remove unbound phage. Next, 100 µl of a 1:5000 diluted solution containing the mouse anti-M13 mAb, conjugated to HRP (GE Healthcare, #27-9421-01) was added to every well and the plate was incubated for one hour at room temperature. The dilutions of the mouse anti-M13 mAb were made using PBS - 0.4% milk. Afterwards, the plate was washed 12 times with the washing buffer to remove unbound antibodies. The revealing solution was prepared by dissolving 10 mg *o*-phenylenediamine dihydrochloride (OPD, ThermoFisher, #34005) in a solution consisting of 10 mL 0.1M citric acid, 10 mL 0.2M sodium phosphate dibasic dodecahydrate and 8 µL 35% hydrogen peroxide. Revealing was performed by incubating the plate with the revealing solution for 4 minutes in the dark, 160 µL/well. Immediately after, 50 µL/well of 4M sulfuric acid was added to stop the reaction. Finally, the plate was read at 492 nm using an ELISA plate reader.

7.5.5 Elisa protocol for the comparison of phage & peptide insert

The affinity for KLH (keyhole limped hemocyanin) of the isolated peptide insert (PI210) was evaluated by ELISA and compared to the affinity of the corresponding phage clone PC21. BSA (bovine serum albumin) was used as a negative control.

16 wells of a 96 well plate with flat bottom were coated with 100 µL of a 20 µg/mL solution of KLH (EDM Milipore, # 374805) in PBS, 16 other wells were coated with 100 µL of a 1% BSA (Sigma-Aldrich, #SLBW6771) solution in PBS and the plate was incubated overnight at 4°C. Next, the unbound proteins were washed by immersing the plate in the washing buffer (3 x PBS – 0.1% Tween20). After removal of the washing buffer, protein blocking was done by adding 200 µL/well of a 4% milk solution in PBS and incubating for it at least two hours at room temperature on a shaker plate. Afterwards, the plate was washed by immersing it in the washing buffer. Next, 100 µL of the solutions containing PC210/PI210 were added to the plate and incubated for two hours

at room temperature on a shaker plate. Dilutions of the PC210/PI210 solutions were made using PBS - 0.4% milk. For the phages clone PC210, the following concentrations were used (n=2 for KLH, n=2 for BSA): (i) 10.0 x 10^{11} phages/mL, (ii) 2.5 x 10^{11} phages/mL and (iii) 0.625 x 10^{11} phages/mL. For PI210, the following concentrations were used (n=2 for KLH, n=2 for BSA) (i) 1.66 x 10^{-6} mmol/mL, (ii) 1.66 x 10^{-7} mmol/mL, (iii) 1.66 x 10^{-8} mmol/mL and (iv) 1.66 x 10^{-9} mmol/mL. For comparison, the solution of 1.66 x 10^{-9} mmol/mL PI210 contains the same amount of peptide molecules as the amount of phages of the solution 10.0 x 10^{11} phages/mL. Afterwards, the plate was washed 6 times with the washing buffer to remove unbound PC210/PI210. Secondary antibodies were diluted in PBS - 0.4% milk, 100 µL were added and incubated for 1 hour at room temperature on a shaker plate. For the phage wells a dilution of 1:5000 of the mouse anti-M13 mAb, conjugated to HRP(GE Healthcare, #27-9421-01) was used. For the PP01 wells a dilution of 1:1000 of the mouse anti-V5, conjugated to HRP (Thermo Fisher, #R961-25) was used. Afterwards, the plate was washed 6 times with the washing buffer to remove unbound antibodies. Next, revealing was performed by incubating the plate with 3,3',5,5'-tetramethylbenzidine (TMB, Sigma-Aldrich, #T4444) for 4 minutes in the dark, 100 µL per well. Immediately after, 100 µL/well of 1M HCl was added to neutralize the reaction. Finally, the plate was read at 450 nm using an ELISA plate reader.

7.5.6 Protocol for staining kidneys with compounds 3.6, 3.7 or 3.14

A 100 mM stock solution of **3.6** was prepared by dissolving 26.4 mg (0.086 mmol) of **3.6** in 960 µL of a 100 mM aqueous Na_2CO_3 solutions. A 50 mM stock solution of **3.7** was prepared by dissolving 20.3 mg (0.043 mmol) of **3.7** in 866 µL of a 100 mM aqueous Na_2CO_3 solutions. A 100 mM stock solution of **3.14** was prepared by dissolving 13.5 mg (0.016 mmol) in 164 µL DMSO. Next, solutions were prepared in Eppendorf tubes consisting of 1 mL borate buffered saline with 0.0035% H_2O_2 and 1 mM of the tyramide analogue. As a negative control, 1 mL borate buffered saline with 0.0035% H_2O_2 was used. Fixed murine kidneys were cut in two equal pieces, transferred to the Eppendorf tubes (one piece per condition) and incubated overnight at room temperature on a shaker plate. The solutions were refreshed after two days. After 5 days of incubation, the kidney pieces were quickly dried on a tissue paper and rinsed with PBS 1X. The kidney pieces were then washed by placing them in a 40 mL PBS 1X solution, while shaken overnight at room temperature in the absence of light. Afterwards, the kidney pieces were taken out of the

solution, dried on a tissue paper and wrapped in parafilm for microCT scanning.

7.5.7 Microfocus X-ray computed tomography

MicroCT scans were acquired using a Phoenix NanoTom M (GE Measurement and Control Solutions, Germany) equipped with a 180kV/15W energy nanofocus X-ray tube and a GE DXR detector (3072 x 2400 pixels). A diamond-coated tungsten target was used for all scans. The CT images have been generated at the X-ray computed tomography facilities of the Department of Development and Regeneration of the KU Leuven, financed by the Hercules Foundation (project AKUL 13/47). The microCT datasets were reconstructed with the Datos|x software (GE Measurement and Control Solutions) and exported as 16-bit XY slices (.tiff). The images were cropped to reduce the size of the dataset.

Acquisition

During reconstruction (Datos|x, GE Measurement and Control Solutions), the images were cropped to reduce the size of the dataset. The inline median, ROI CT filter that are implemented in the software, were applied.

For the solution of **3.6** and the DMSO control the system was operated at a voltage of 60 kV and a current of 570 µA. The voxel size was 10.67 µm. The exposure time was 500 ms, and 1400 images were acquired over 360° using the fast scan mode (frame averaging = 1; image skip = 0), resulting in a scan time of 12 minutes.

For the solution of **3.12** and the tyramine control the system was operated at a voltage of 60 kV and a current of 200 µA. The voxel size was 10.0 µm. The exposure time was 500 ms, and 500 images were acquired over 360° using the fast scan mode (frame averaging = 1; image skip = 0), resulting in a scan time of 4 minutes and 10 seconds.

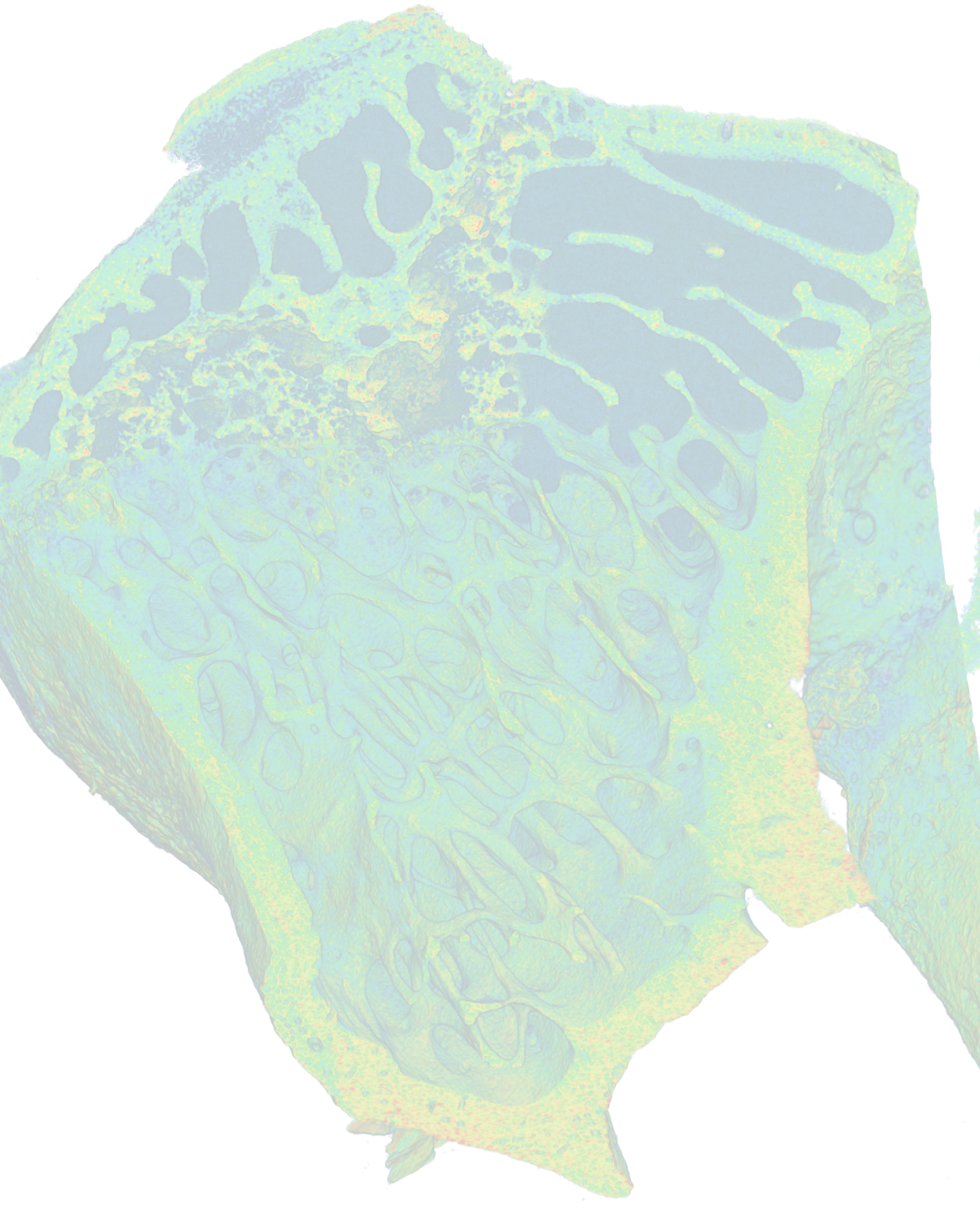
For the kidney pieces, stained with compounds **3.6**, **3.7**, **3.14** or the corresponding negative control the system was operated at a voltage of 60 kV and a current of 191 µA. The voxel size was 3.714 µm. A 0.1 mm aluminum filter was used. The exposure time was 500 ms, and 2400 images were acquired over 360° using the fast scan mode (frame averaging = 1; image skip = 0), resulting in a scan time of 20 minutes.

Quantification of gray value of a 100 mM solution of tyramine and a 100 mM solution of 3.14 in DMSO, obtained by averaging the gray value of 10 different cross-sections.

Image processing and analysis

The dataset of scanned solutions **3.6** and **3.12** of 16-bit Tiff files was converted to 8-bit bmp files with automatic histogram windowing to the dynamic range of the dataset using an in-house developed MATLAB script. For each solution, gray value profile lines were drawn of 10 different cross-sections and analyzed using DataViewer (Bruker Micro-CT, Kontich, Belgium). The profile lines were as long as possible, but still covering the solution, to average out the inherent image noise. The gray values were averaged over the different cross-sections.

The dataset of the kidney piece stained with **3.14** of 16-bit Tiff files was converted to 8-bit bmp files with automatic histogram windowing to the dynamic range of the dataset. Gray value normalization was performed on all other datasets (of kidney pieces) using a ceramic bead (Al_2O_3) and parafilm as the external references. During normalization, 16-bit Tiff files are converted to 8-bit jpg files. Both operations were performed using an in-house developed MATLAB script.[212, 213]



Appendix A

Theoretical background on
X-ray microfocus computed tomography

A.1 Introduction

X-ray computed tomography (CT) is a 3D imaging modality that was introduced in the early 1970s.[1] Herein, the penetration power of X-rays is exploited to create two-dimensional (2D) radiographs (projections) of a sample at sequential angles. Samples can be visualized as a 3D volume that can be virtually sliced in any desired direction and orientation. Hence, the internal architecture can be visualized at a microscopic level in a non-destructive way.

The non-destructive nature of this technique has led to its widespread use as a diagnostic tool in medical applications. Within this set-up, the imaging device typically rotates around the specimen. Conventional medical CT devices employ X-ray energies between 80 and 140 keV and commonly achieve resolutions ranging from 1 mm to 100 µm.[155] Besides the clinical context, CT is generally used in industry and research to examine and characterize samples. In case of non-living samples, the radiation dose is not limited with respect to health. Hence, higher resolutions can be obtained by using higher X-ray doses. Moreover, the resolution can also be increased by placing the sample as close as possible to the source. In this regard, higher resolution could be obtained when using microCT in the micrometer range (voxel size ≥ 0.1 µm) and X-ray nanofocus tomography (nanoCT) in the nanometer range (voxel size down to 300 nm). In most of these set-ups, the X-ray source and detector are static and the sample rotates.

In this appendix, some background on microCT is given, which serves to understand the principles of microCT and parameters used in this work.

A.2 Instrumentation and parameters

MicroCT imaging performed in the context of this dissertation was done using a laboratory-based X-ray system. Such a system consists of three fundamental components: the X-ray source, the detector and the sample stage (Figure A.1A). Most commonly, the source is a microfocus X-ray tube where X-rays are generated by collision of a beam of accelerated electrons on a metal target (*e.g*. molybdenum or tungsten).[219] More specifically, upon heating of a tungsten filament by applying a current (anode), electrons are emitted and accelerated towards a metal target (cathode) by an applied potential difference (kVp) in vacuum (Figure A.1B).[220]

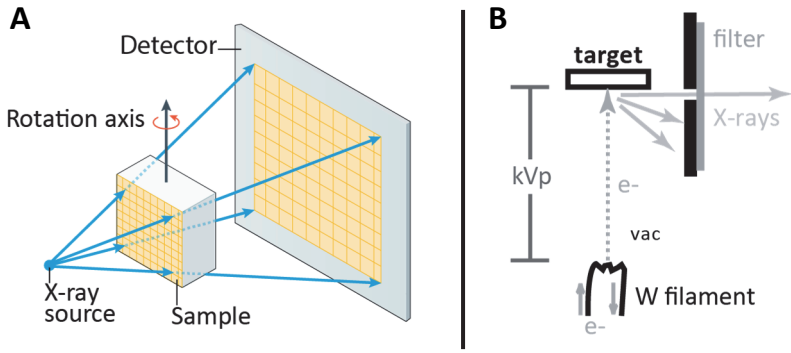


Figure A.1 A Typical configuration of a laboratory X-ray CT system with a cone beam design. Reproduced with permission from reference [155]. Copyright © 2021, Springer Nature Limited. **B** Schematic representation of an X-ray reflection source tube. Upon heating of the filament, electrons are thermionically emitted and accelerated by a tube potential (kVp) in vacuum. The electron beam generates X-rays when bombarding the target. Reproduced with permission from reference [219]. Copyright © 2008, Taylor & Francis Group LLC.

By means of lenses, the electron beam is focused on a small site on the target, called the focal spot. In general, the focal spot size of microfocus X-ray tube sources is in the range of 1 – 20 µm.[221] Upon collision, the electrons decelerate because of interaction with the nuclei of the target material. Consequently, (part of) their kinetic energy is converted into photons producing a polychromatic beam, which is known as Bremsstrahlung.[1] Besides the continuous spectrum, sharp characteristic photon energy peaks are also produced that depend on the type of target material (Figure 7.5). These characteristic peaks originate from the direct collision of high-energetic electrons with shell electrons of the target. Herein, an inner shell (mostly K shell) electron is ejected, emitting a photon with an energy equal to its binding energy. In addition, the empty vacancy in the inner shell could be refilled with an outer shell electron. As a consequence, the residual energy is released as a photon. Therefore, the choice of the type of target material depends on the desired range of X-ray energies.[1] Overall, only a small portion (± 1%) of the electron beam energy is converted into X-ray radiation, the majority of the energy is released as heat.

Microfocus X-ray tube sources generate a polychromatic spectrum of X-ray energies. The X-rays are emitted in all directions, referred as a cone beam design. Since X-rays are generated by conversion of the kinetic energy of the accelerated electrons, the highest energy of the spectrum is set by the applied potential.[155] The X-ray photon flux (intensity) depends on the tube current and

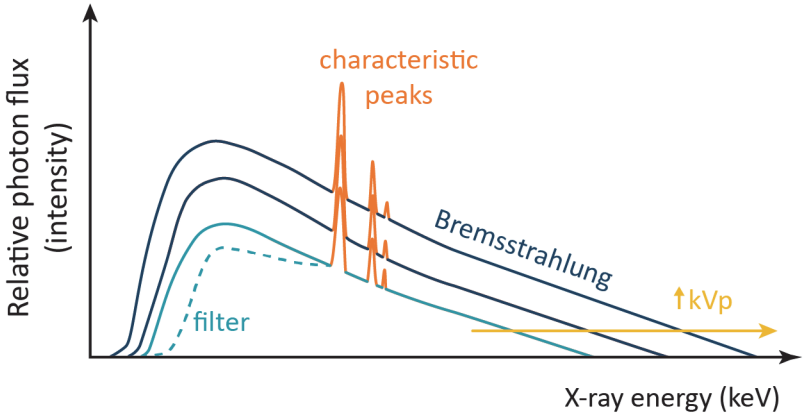


Figure A.2 Schematic representation of X-ray tube spectra with a tungsten anode. Each curve represents the spectrum at a specific tube voltage kVp, and consists of a continuous spectrum (Bremsstrahlung) and characteristic peaks. The yellow arrow indicates the shift of the continuous spectrum to higher X-ray energies when the tube voltage is increased. Increasing the tube voltage indirectly also increase the tube current, and hence the photon flux. The dotted blue line shows the effect of using a metal filter.

indirectly on the tube voltage. The higher the tube current, the higher the filament temperature, which results in an increase in electron beam incident on the target, and hence an increased focal spot size. This in turn results in an increase of the X-ray photon flux, but it does not influence the highest energy of the photons. Increasing the photon flux leads to increasing the temporal resolution, and hence in reducing the acquisition time. However, an increased focal spot size leads to an increase in diameter of the generated X-ray beam (*i.e.* the effective focal spot size), which negatively affects the spatial resolution due to blurring and geometric unsharpness.[221]

Varying the tube voltage (kVp) allows to adapt the range of X-ray energies to the intended contrast difference, which depends on the sample material (Figure A.2) On the one hand, too low energy can lead to inadequate sample penetration, and hence poor X-ray detection. On the other hand, too high energy can result in poor attenuation, and hence poor contrast difference (see section A.3). The optimal range of X-ray energies depends on the sample size and the sample composition in terms of low/high atomic number materials. Consequently, nanoCT systems operate at soft (< 1 keV) or moderate (5-30 keV) X-ray energies, while microCT systems typically work with high energies (30-300 keV). Because of limited dose, clinical CT systems operate at ranges of 80-140 keV. In contrast, industrial CT systems are capable of operating at very

high X-ray energies (> 400 keV), resulting in hard X-rays.[155] Metallic filters (*e.g.* an 0.1 mm thick aluminum plate*)* in front of the X-ray source are commonly used to absorb soft X-rays that do not penetrate the sample, and hence 'harden' the beam. As a result, oversaturation of the detector in the periphery is reduced, which reduces scatter and beam hardening artefacts.[156]

The sample is mounted on the sample stage, which rotates during X-ray acquisition. In most cases, the sample rotates continuously over 180 ° or 360°. It is crucial the sample does not move during acquisition to prevent image blurring. Most commonly the position of the sample, and sometimes also the position of the detector, relative to the source could be changed, which enables geometric magnification. To ensure a complete reconstruction, it is common practice to make sure that the full width of the sample fits within the field of view of the detector.[222]

The X-ray detector records the pattern of X-ray intensities that passes the sample for every projection. In this regard, two prominent parameters that affect image quality are the angular increment (*i.e.* the number of radiographs) and the acquisition time per radiograph.[222] X-ray detectors regularly consist of a scintillator and metal-oxide semiconductors. The scintillator converts X-rays into visible light. The metal-oxide semiconductors convert the light signals into electrons for digital processing, resulting in a 2D radiograph.[155]

Finally, 2D cross-sections (slices) are created by recovering the spatial distribution of attenuating entities through mathematically compiling the set of radiographs. The most commonly used algorithm for reconstruction is the filtered backprojection.[223, 224]

A.3 Principles of X-ray attenuation

Interactions of X-rays with matter can change the intensity and phase of the X-rays. Attenuation contrast imaging is based on the change in intensity while phase contrast imaging is based on the change of the phase. Attenuation contrast imaging is appropriate for visualizing samples bearing different components that attenuate differently, and forms the centerpiece of this dissertation.

The attenuation coefficient of a material defines its ability to absorb or scatter X-rays upon passing through. In general, attenuation of X-rays depends on anobject thickness, electron density and relative density.[220] While passing through a material, the transmitted X-ray intensity (number of photons per second) decays exponentially compared to the initial X-ray intensity. The transmitted intensity of an X-ray beam that traverses a sample consisting of n different materials (i = 1, …, n) can be described by the Beer-Lambert law:

$$I = I_0 e^{-\sum_{i=1}^{n} \mu_i x_i} \quad \text{(A1)}$$

where I_0 is the incident X-ray intensity, I is the X-ray intensity after interactions with the sample, μ_i the linear attenuation coefficient of material i, and x_i the path length of the X-ray beam through material i. Since the linear attenuation coefficient linearly increases with the material physical density ρ, the mass attenuation coefficient μ_m is often reported for convenience:

$$\mu_m = \frac{\mu_i}{\rho} \quad \text{(A2)}$$

The mass attenuation coefficient is expressed in cm^2/g and depends on the atomic number Z of the material constituents and the energy of the incident X-ray beam E. Since the Beer-Lambert law is only valid for monochromatic X-rays, eq. (A1) needs to be adapted in case polychromatic X-rays are used:

$$I = \sum_{0}^{E_{max}} I_0(E) e^{-\sum_{i=1}^{n} \mu_i x_i} \quad \text{(A3)}$$

where $I_0(E)$ is the incident X-ray intensity of the polychromatic beam with energies E and μ_m the mass attenuation coefficient of material i.[225] Yet, eq. (A1) is generally used in practice for sake of simplicity.

Attenuation of X-rays is caused by the interaction of X-ray photons with materials. In general, these interactions are explained by four major types of mechanisms: the photoelectric effect, Compton scattering, Rayleigh scattering and pair production (Figure A.4).[1, 220, 225, 226] Since the pair production effect only occurs at X-ray energies above the capacity of laboratory-based X-ray systems (> 1 meV), its contribution is considered negligible and will not be further discussed.

The total X-ray attenuation of a material is defined by its linear attenuation coefficient, which is governed by the combined contributed of the interactions listed. Therefore, the total linear attenuation coefficient is formulated as:

$$\mu = \mu_{PE} + \mu_{CS} + \mu_{RS} \qquad (A4)$$

Where μ_{PE} is attenuation coefficient due to photoelectric effect, μ_{CS} the attenuation coefficient due to Compton scattering and μ_{RS} the attenuation coefficient due to Rayleigh scattering. The relative proportion of μ_{PE}, μ_{CS} and μ_{RS} depends on the energy of the incident X-ray beam E and on the atomic number of the material. The individual contribution of each interaction mechanism to the total attenuation coefficient is illustrated in Figure A.3**.** for three different materials (carbon, aluminum and tungsten). This figure shows that the Compton scattering becomes more prominent for carbon (Z = 6) at energies higher than 25 keV (Figure A.3A). Likewise, Compton scattering is most dominant for aluminum (Z = 13) for energies above 50 keV (Figure A.3B). The magnitude of the Compton scattering decreases with increasing atomic number, which is illustrated when comparing the attenuation coefficient of tungsten (Z = 74) with the one of carbon and aluminum. Moreover, the magnitude of the photoelectric effect decreases promptly with increasing photon energy, and increases with increasing atomic number. Indeed, in the case of tungsten the contribution of the photoelectric effect is most dominant

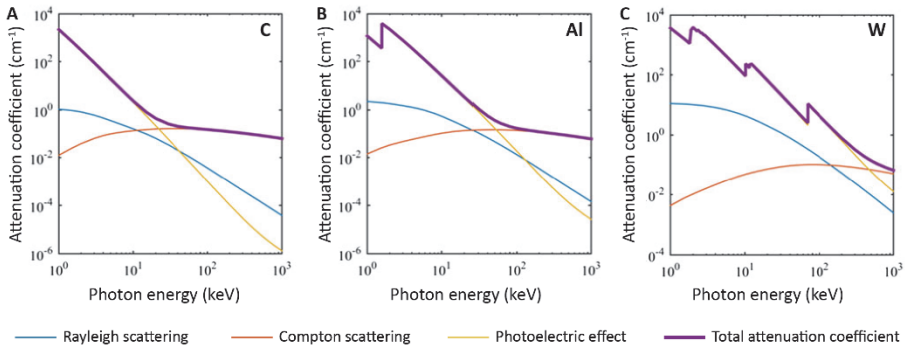


Figure A.3 Contribution of the different interaction mechanisms to the total attenuation coefficient for **A** carbon, **B** aluminum and **C** tungsten, which depends on the photon energy. Values of attenuation coefficients were obtained from the National Institute of Standards and Technology (NIST) online database.[227] Reproduced with permission from reference [225]. Copyright © 2018, Springer.

for a large range of energies (Figure A.3C).

A.3.1 Photoelectric effect (PE)

The PE is the phenomenon of a photon being absorbed by an atom, which results in expelling one of its inner shell (K or L) electrons. The kinetic energy of the expelled electron is equal to the difference between the energy of the incident photon and its binding energy. As a result, one of the atom outer shell electrons can refill the empty spot created by the expelled electron, which results in the generation of a characteristic X-ray with an energy that is equal to the difference in binding energies of the involved electrons. In case the energy of the expelled electron is high enough, another electron can be ejected resulting in additional ionization and X-ray generation. The secondary ejected electron is called an Auger electron (not shown in Figure A.4). The PE is most prominent when the energy of the incident X-ray is ≤ 100 keV.[228]

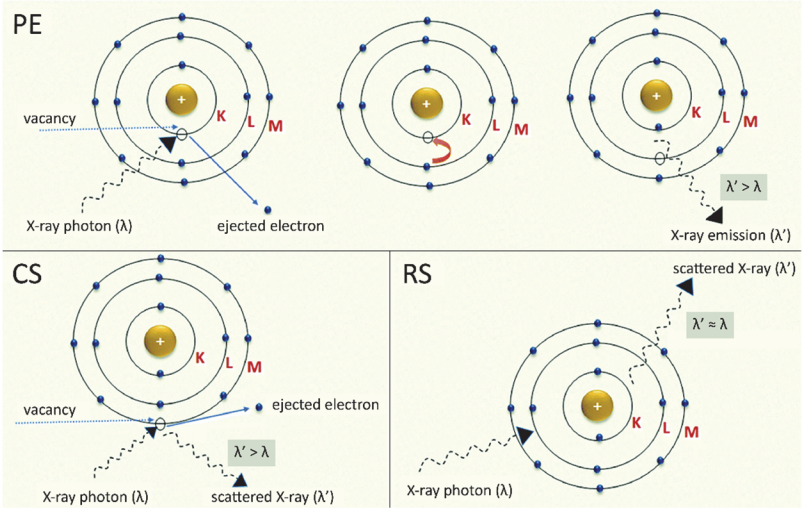


Figure A.4 Schematic representation of the most common X-ray interactions with matter (λ symbolizes the wavelength of the incident X-ray, λ' of the emitted X-ray): photoelectric effect (PE), Compton scattering (CS) and Rayleigh scattering (RS). Reproduced with permission from reference [220]. Copyright © 2021, Royal Society of Chemistry.

The linear attenuation coefficient related to the photoelectric effect (μ_{PE}) is formulated as:

$$\mu_{PE} \propto \frac{\rho Z^3}{{E_p}^3} \qquad (A5)$$

where ρ is the physical density of the material constituents, Z the atomic number of the material constituents and E_p the energy of the incident X-ray beam. The probability of the PE is mainly dependent on the atomic number of the material constituent atoms. Therefore, materials having a high atomic number are used for shielding X-rays.

Interestingly, an increased PE occurs at X-ray energies that are slightly higher than the binding energy of an atom K-shell electrons. Consequently, in that energy range, photons are significantly more absorbed. This particular energy level, known as the K-edge value, is specific for every atom, which is sometimes exploited to generate a relative increase in contrast in the final image.

A.3.2 Compton scattering (CS)

The inelastic scattering that occurs when an incident photon of the X-ray beam interacts with an outer shell electron of an atom is known as CS. In contrast to the PE, the photon is not absorbed but scattered. Hence, the energy of the photon is decreased, the wavelength shifted and the direction changed. Meanwhile, the outer shell electron is expelled with a kinetic energy that is equal to the difference in energy of the photon before and after collision. Whereas at low X-ray energy the PE mostly outperforms CS, at higher X-ray energy the contribution of CS becomes more prominent. The contribution of CS to the linear equation coefficient can be written as follows:

$$\mu_{CS} \propto \frac{\rho Z}{A} \qquad \text{(A6)}$$

where ρ is the physical density, Z the atomic number and A the atomic mass of the material constituents. The probability of CS depends on the electron density of the material atoms rather than on the atomic number.[220]

A.3.3 Rayleigh scattering (RS)

RS, also known as coherent scattering, is the interaction of low energy incident X-ray photons (< 30 keV) with the electrons of the material atoms.[220, 225] The interaction is considered elastic since no electron is expelled and the photons' energy loss is negligible. After interaction, the photons' direction changes

while its energy and wavelength are virtually unchanged. The linear attenuation coefficient of the RS contribution is described as:

$$\mu_{RS} \propto \frac{\rho Z}{E_p^2} \quad \text{(A7)}$$

where ρ is the physical density, Z the atomic number of the material constituents and E_p the energy of the incident X-ray beam.

A.4 Measurement of attenuation

The unit of a material radiodensity in the reconstructed 2D or 3D image mostly depends on the application. For industrial or research purposes, the radiodensity is often expressed as gray value. For clinical applications, radiodensity is commonly measured in terms of Hounsfield unit. In the framework of this thesis, radiodensity is expressed as gray value.

A.4.1 Gray value

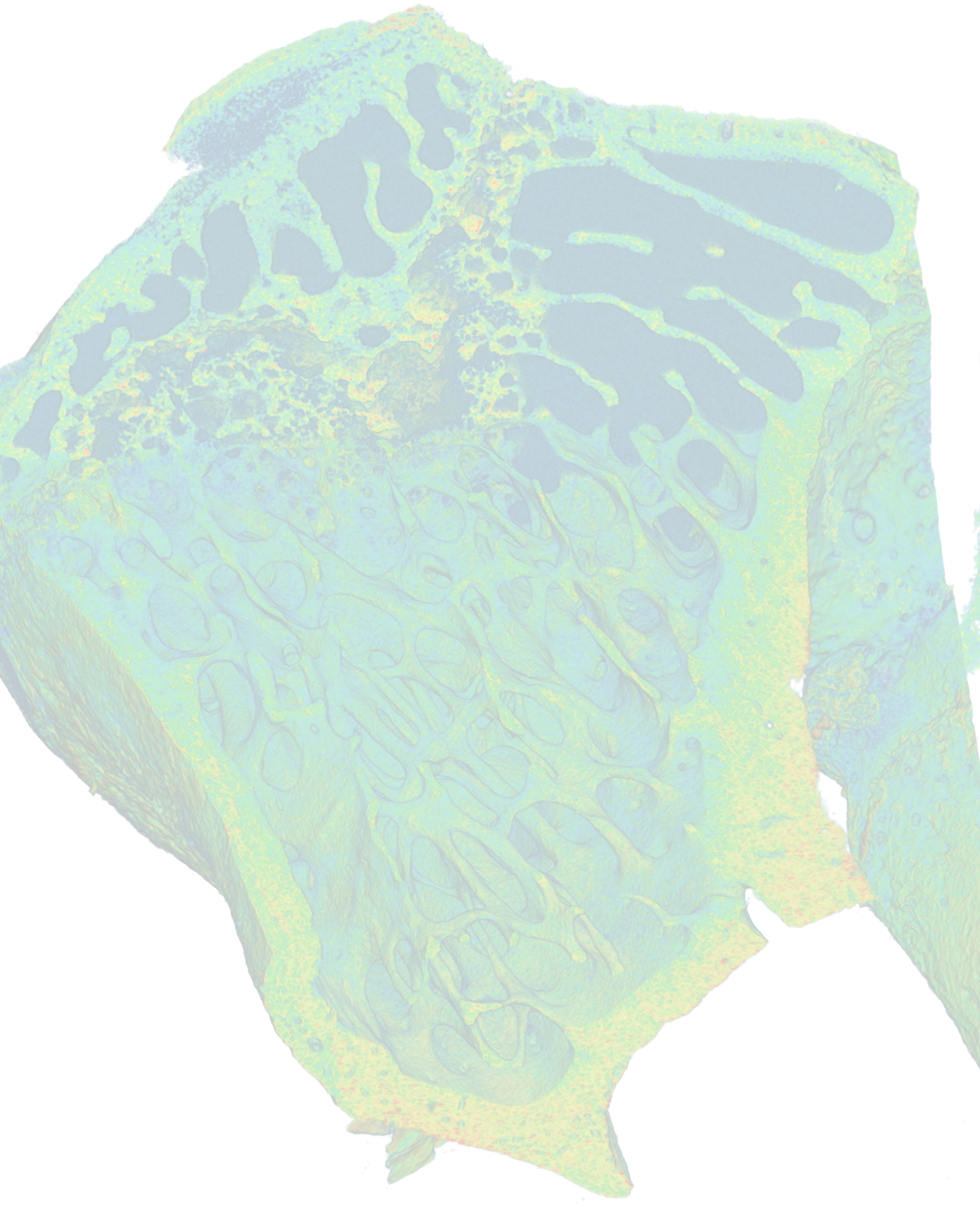
Quantification of radiodensity in gray value is based on the brightness of pixels (2D) or voxels (3D) in the digital image, which is correlated to the attenuation of the material. Images are typically stored with 8 bits per pixel, which allows 256 (2^8) shades of gray. For microCT images shown in this dissertation black (gray value 0) corresponds to the lowest and white (gray value 255) corresponds to the highest radiodensity.

A.4.2 Hounsfield unit

Hounsfield unit (HU) is a relative quantitative unit for radiodensity of materials, most often in a biological/clinical context. As a reference, water is defined as having 0 HU and air as -1000 HU at standard temperature and pressure. [1] Therefore, the HU of a material is defined as:

$$HU = 1000 \frac{\mu_i - \mu_{water}}{\mu_{water}} \quad \text{(A8)}$$

where μ_i is the linear attenuation coefficient of material i and μ_{water} the linear attenuation coefficient of water.



Appendix B

Brief theoretical background on statistical modelling

In this section, the mathematical principles JMP® employs are briefly summarized and some definitions of statistical terms are given to help interpretation of the data generated by the software.[229]

JMP® builds models based on an equation to approximate experimental data and examines the relationship between dependent and independent variables. For instance, in case data can be described by a simple linear regression model, the response variable of the model (Y) depends on a single factor (x), which can be approximated with the following linear equation:

$$Y = \beta_0 + \beta_1 x + U \qquad \text{(B1)}$$

Where β_0 is the y-intercept, β_1 the slope and U the error term, called the residual. β_1 is also called the main effect or the linear effect. In general, the residual is the difference between the experimental data and the data estimated by the model. The origin of the residual can be attributed to an experimental error or a lack of fit of the model to approximate the data, or a combination of both.

Models consist often of multiple factors and combinations therefore that influence the output of Y. Hence, in case of combinations, these factors also have an influence on each other, which are called interaction or cross effects. Moreover, exponential effects (*e.g.* quadratic) could also be included in the model. In case of a two-factor model, the equation of the model could look as follows:

$$Y = \beta_0 + \beta_1 x_1 + \beta_2 x_2 + \beta_{12} x_1 x_2 + \beta_{11} x_1^2 + \beta_{22} x_2^2 + U \qquad \text{(B2)}$$

Based on this approach JMP® will build a model to fit the experimental data. One of the most common methods to estimate unknown parameters (*i.e.* β_0, β_1, β_2, β_{12}, β_{11}, and β_{22}) is the least squares method. A good fit is obtained if all residuals are close to zero, because this mean the regression curve approximates the data points closely. Hence, the software tries to minimize the sum of the residuals by minimizing the sum of the squared residuals, which results in the **least squares estimation** of the regression model. The value of the estimate of the parameters β_i, calculated by the software reflects the influence of the corresponding factor on the output of the system.

REFERENCES

1 Haidekker, M. A. Computed Tomography. In *Medical Imaging Technology*.Springer New York, **2013**; pp 37-53.

2 Li, Z.; Clarke, J. A.; Ketcham, R. A.; Colbert, M. W.; Yan, F. An investigation of the efficacy and mechanism of contrast-enhanced X-ray Computed Tomography utilizing iodine for large specimens through experimental and simulation approaches. *BMC Physiol.* **2015**, *15*, 1-16.

3 Early, C. M.; Morhardt, A. C.; Cleland, T. P.; Milensky, C. M.; Kavich, G. M.; James, H. F. Chemical effects of diceCT staining protocols on fluid-preserved avian specimens. *PLoS One* **2020**, *15* (9), 1-24.

4 Dawood, Y.; Hagoort, J.; Siadari, B. A.; Ruijter, J. M.; Gunst, Q. D.; Lobe, N. H. J.; Strijkers, G. J.; de Bakker, B. S.; van den Hoff, M. J. B. Reducing soft-tissue shrinkage artefacts caused by staining with Lugol's solution. *Sci. Rep.* **2021**, *11* (1), 1-12.

5 Neues, F.; Epple, M. X-ray Microcomputer Tomography for the Study of Biomineralized Endo- and Exoskeletons of Animals. *Chem. Rev.* **2008**, *108* (11), 4734-4741.

6 Veuthey, T.; Herrera, G.; Dodero, V. I. Dyes and stains: from molecular structure to histological application. *Front. Biosci.-Landmark* **2014**, *19*, 91-112.

7 Silva, J.; Zanette, I.; Noel, P. B.; Cardoso, M. B.; Kimm, M. A.; Pfeiffer, F. Three-dimensional non-destructive soft-tissue visualization with X-ray staining micro-tomography. *Sci. Rep.* **2015**, *5*, 1-7.

8 Lakin, B. A.; Grasso, D. J.; Shah, S. S.; Stewart, R. C.; Bansal, P. N.; Freedman, J. D.; Grinstaff, M. W.; Snyder, B. D. Cationic agent contrast-enhanced computed tomography imaging of cartilage correlates with the compressive modulus and coefficient of friction. *Osteoarthr. Cartil.* **2013**, *21* (1), 60-68.

9 Tratwal, J.; Labella, R.; Bravenboer, N.; Kerckhofs, G.; Douni, E.; Scheller, E. L.; Badr, S.; Karampinos, D. C.; Beck-Cormier, S.; Palmisano, B.*; et al.* Reporting Guidelines, Review of Methodological Standards, and Challenges Toward Harmonization in Bone Marrow Adiposity Research. Report of the Methodologies Working Group of the International Bone Marrow Adiposity Society. *Front. Endocrinol.* **2020**, *11*, 1-36.

10 Martins de Souza e Silva, J.; Utsch, J.; Kimm, M. A.; Allner, S.; Epple, M. F.; Achterhold, K.; Pfeiffer, F. Dual-energy micro-CT for

quantifying the time-course and staining characteristics of ex-vivo animal organs treated with iodine- and gadolinium-based contrast agents. *Sci. Rep.* **2017**, *7* (1), 1-10.

11 Albertini, G.; Giuliani, A.; Komlev, V.; Moroncini, F.; Pugnaloni, A.; Pennesi, G.; Belicchi, M.; Rubini, C.; Rustichelli, F.; Tasso, R.*; et al.* Organization of Extracellular Matrix Fibers Within Polyglycolic Acid-Polylactic Acid Scaffolds Analyzed Using X-Ray Synchrotron-Radiation Phase-Contrast Micro Computed Tomography. *Tissue Eng., Part C* **2009**, *15* (3), 403-411.

12 Verboven, P.; Kerckhofs, G.; Mebatsion, H. K.; Ho, Q. T.; Temst, K.; Wevers, M.; Cloetens, P.; Nicolaï, B. M. Three-Dimensional Gas Exchange Pathways in Pome Fruit Characterized by Synchrotron X-Ray Computed Tomography. *Plant Physiol.* **2008**, *147* (2), 518-527.

13 Johnson, J. T.; Hansen, M. S.; Wu, I.; Healy, L. J.; Johnson, C. R.; Jones, G. M.; Capecchi, M. R.; Keller, C. Virtual histology of transgenic mouse embryos for high-throughput phenotyping. *PLoS Genet.* **2006**, *2* (4), 471-477.

14 Litzlbauer, H. D.; Neuhaeuser, C.; Moell, A.; Greschus, S.; Breithecker, A.; Franke, F. E.; Kummer, W.; Rau, W. S. Three-dimensional imaging and morphometric analysis of alveolar tissue from microfocal X-ray-computed tomography. *Am. J. Physiol. Lung Cell Mol. Physiol.* **2006**, *291* (3), L535-L545.

15 Ribi, W.; Senden, T. J.; Sakellariou, A.; Limaye, A.; Zhang, S. Imaging honey bee brain anatomy with micro-X-ray-computed tomography. *J. Neurosci. Methods* **2008**, *171* (1), 93-97.

16 Metscher, B. D. MicroCT for Developmental Biology: A Versatile Tool for High-Contrast 3D Imaging at Histological Resolutions. *Dev. Dyn.* **2009**, *238* (3), 632-640.

17 Metscher, B. D. MicroCT for comparative morphology: simple staining methods allow high-contrast 3D imaging of diverse non-mineralized animal tissues. *BMC Physiol.* **2009**, *9* (1), 1-14.

18 Wong, M. D.; Dorr, A. E.; Walls, J. R.; Lerch, J. P.; Henkelman, R. M. A novel 3D mouse embryo atlas based on micro-CT. *Development* **2012**, *139* (17), 3248-3256.

19 Jahn, H.; Oliveira, I. D.; Gross, V.; Martin, C.; Hipp, A.; Mayer, G.; Hammel, J. U. Evaluation of contrasting techniques for X-ray imaging of velvet worms (Onychophora). *J. R. Microsc. Soc.* **2018**, *270* (3), 343-358.

20 Schulz-Mirbach, T.; Heß, M.; Metscher, B. D. Sensory epithelia of the fish inner ear in 3D: studied with high-resolution contrast enhanced microCT. *Front. Zool.* **2013**, *10* (1), 1-11.
21 Pauwels, E.; Van Loo, D.; Cornillie, P.; Brabant, L.; Van Hoorebeke, L. An exploratory study of contrast agents for soft tissue visualization by means of high resolution X-ray computed tomography imaging. *J. R. Microsc. Soc.* **2013**, *250* (1), 21-31.
22 Kerckhofs, G.; Stegen, S.; van Gastel, N.; Sap, A.; Falgayrac, G.; Penel, G.; Durand, M.; Luyten, F. P.; Geris, L.; Vandamme, K.*; et al.* Simultaneous three-dimensional visualization of mineralized and soft skeletal tissues by a novel microCT contrast agent with polyoxometalate structure. *Biomaterials* **2018**, *159*, 1-12.
23 Joshi, N. S.; Bansal, P. N.; Stewart, R. C.; Snyder, B. D.; Grinstaff, M. W. Effect of Contrast Agent Charge on Visualization of Articular Cartilage Using Computed Tomography: Exploiting Electrostatic Interactions for Improved Sensitivity. *J. Am. Chem. Soc.* **2009**, *131* (37), 13234-13235.
24 Palmer, A. W.; Guldberg, R. E.; Levenston, M. E. Analysis of cartilage matrix fixed charge density and three-dimensional morphology via contrast-enhanced microcomputed tomography. *Proc. Natl. Acad. Sci. U.S.A.* **2006**, *103* (51), 19255-19260.
25 Bansal, P. N.; Stewart, R. C.; Entezari, V.; Snyder, B. D.; Grinstaff, M. W. Contrast agent electrostatic attraction rather than repulsion to glycosaminoglycans affords a greater contrast uptake ratio and improved quantitative CT imaging in cartilage. *Osteoarthr. Cartil.* **2011**, *19* (8), 970-976.
26 van Tiel, J.; Siebelt, M.; Waarsing, J. H.; Piscaer, T. M.; van Straten, M.; Booij, R.; Dijkshoorn, M. L.; Kleinrensink, G. J.; Verhaar, J. A. N.; Krestin, G. P.*; et al.* CT arthrography of the human knee to measure cartilage quality with low radiation dose. *Osteoarthr. Cartil.* **2012**, *20* (7), 678-685.
27 Boulocher, C.; Magnier, L.; Roger, T.; Viguier, E.; Chereul, E. Preliminary study: non destructive evaluation of early cartilage morphological changes in a rabbit model by equilibrium partitioning of an ionic contrast agent by microcomputed tomography (EPIC-µCT). In *World Congress on Osteoarthritis*, 2012; Osteoarthritis and Cartilage: Vol. 20, p S66.
28 Kerckhofs, G.; Sainz, J.; Marechal, M.; Wevers, M.; Van de Putte, T.; Geris, L.; Schrooten, J. Contrast-Enhanced Nanofocus X-Ray

Computed Tomography Allows Virtual Three-Dimensional Histopathology and Morphometric Analysis of Osteoarthritis in Small Animal Models. *Cartilage* **2014**, *5* (1), 55-65.

29 Kerckhofs, G.; Sainz, J.; Wevers, M.; Van de Putte, T.; Schrooten, J. Contrast-enhanced Nanofocus Computed Tomography Images The Cartilage Subtissue Architecture in Three Dimensions. *Eur. Cells Mater.* **2013**, *25*, 179-189.

30 Yoo, H. J.; Hong, S. H.; Choi, J. Y.; Lee, I. J.; Kim, S. J.; Choi, J. A.; Kang, H. S. Contrast-enhanced CT of Articular Cartilage: Experimental Study for Quantification of Glycosaminoglycan Content in Articular Cartilage. *Radiology* **2011**, *261* (3), 805-812.

31 Freedman, J. D.; Ellis, D. J.; Lusic, H.; Varma, G. V.; Grant, A. K.; Lakin, B. A.; Snyder, B. D.; Grinstaff, M. W. dGEMRIC and CECT Comparison of Cationic and Anionic Contrast Agents in Cadaveric Human Metacarpal Cartilage. *J. Orthop. Res.* **2020**, *38* (4), 719-725.

32 Bansal, P. N.; Joshi, N. S.; Entezari, V.; Grinstaff, M. W.; Snyder, B. D. Contrast Enhanced Computed Tomography can predict the glycosaminoglycan content and biomechanical properties of articular cartilage. *Osteoarthr. Cartil.* **2010**, *18* (2), 184-191.

33 Entezari, V.; Bansal, P. N.; Stewart, R. C.; Lakin, B. A.; Grinstaff, M. W.; Snyder, B. D. Effect of Mechanical Convection on the Partitioning of an Anionic Iodinated Contrast Agent in Intact Patellar Cartilage. *J. Orthop. Res.* **2014**, *32* (10), 1333-1340.

34 Kallioniemi, A. S.; Jurvelin, J. S.; Nieminen, M. T.; Lammi, M. J.; Toyras, J. Contrast agent enhanced pQCT of articular cartilage. *Phys. Med. Biol.* **2007**, *52* (4), 1209-1219.

35 Cockman, M. D.; Blanton, C. A.; Chmielewski, P. A.; Dong, L.; Dufresne, T. E.; Hookfin, E. B.; Karb, M. J.; Liu, S.; Wehmeyer, K. R. Quantitative imaging of proteoglycan in cartilage using a gadolinium probe and microCT. *Osteoarthr. Cartil.* **2006**, *14* (3), 210-214.

36 Kulmala, K. A. M.; Karjalainen, H. M.; Kokkonen, H. T.; Tiitu, V.; Kovanen, V.; Lammi, M. J.; Jurvelin, J. S.; Korhonen, R. K.; Toyras, J. Diffusion of ionic and non-ionic contrast agents in articular cartilage with increased cross-linking-Contribution of steric and electrostatic effects. *Med. Eng. Phys.* **2013**, *35* (10), 1415-1420.

37 Silvast, T. S.; Kokkonen, H. T.; Jurvelin, J. S.; Quinn, T. M.; Nieminen, M. T.; Toyras, J. Diffusion and near-equilibrium distribution of MRI and CT contrast agents in articular cartilage. *Phys. Med. Biol.* **2009**, *54* (22), 6823-6836.

38 Taylor, C.; Carballido-Gamio, J.; Majumdar, S.; Li, X. J. Comparison of quantitative imaging of cartilage for osteoarthritis: T2, T1 rho, dGEMRIC and contrast-enhanced computed tomography. *Magn. Reson. Imaging* **2009**, *27* (6), 779-784.

39 Grinstaff, M.; Joshi, N.; Bansal, P. Cationic Contrast Agents And Methods Of Use Thereof. US20110158909A1, 2009.

40 Bansal, P. N.; Joshi, N. S.; Entezari, V.; Malone, B. C.; Stewart, R. C.; Snyder, B. D.; Grinstaff, M. W. Cationic Contrast Agents Improve Quantification of Glycosaminoglycan (GAG) Content by Contrast Enhanced CT Imaging of Cartilage. *J. Orthop. Res.* **2011**, *29* (5), 704-709.

41 Benders, K. E. M.; Malda, J.; Saris, D. B. F.; Dhert, W. J. A.; Steck, R.; Hutmacher, D. W.; Klein, T. J. Formalin fixation affects equilibrium partitioning of an ionic contrast agent-microcomputed tomography (EPIC-µCT) imaging of osteochondral samples. *Osteoarthr. Cartil.* **2010**, *18* (12), 1586-1591.

42 Bhattarai, A.; Honkanen, J. T. J.; Mylller, K. A. H.; Prakash, M.; Korhonen, M.; Saukko, A. E. A.; Viren, T.; Joukainen, A.; Patwa, A. N.; Kroger, H.*; et al.* Quantitative Dual Contrast CT Technique for Evaluation of Articular Cartilage Properties. *Ann. Biomed. Eng.* **2018**, *46* (7), 1038-1046.

43 Bhattarai, A.; Makela, J. T. A.; Pouran, B.; Kroger, H.; Weinans, H.; Grinstaff, M. W.; Toyras, J.; Turunen, M. J. Effects of human articular cartilage constituents on simultaneous diffusion of cationic and nonionic contrast agents. *J. Orthop. Res.* **2021**, *39* (4), 771-779.

44 Bhattarai, A.; Pouran, B.; Makela, J. T. A.; Shaikh, R.; Honkanen, M. K. M.; Prakash, M.; Kroger, H.; Grinstaff, M. W.; Weinans, H.; Jurvelin, J. S.*; et al.* Dual contrast in computed tomography allows earlier characterization of articular cartilage over single contrast. *J. Orthop. Res.* **2020**, *38* (10), 2230-2238.

45 Boos, M. A.; Grinstaff, M. W.; Lamande, S. R.; Stok, K. S. Contrast-Enhanced Micro-Computed Tomography for 3D Visualization and Quantification of Glycosaminoglycans in Different Cartilage Types. *Cartilage* **2021**, *13* (2_suppl), 486S-494S.

46 Dourthe, B.; Nickrnanesh, R.; Wilson, D. R.; D'Agostino, P.; Patwa, A. N.; Grinstaff, M. W.; Snyder, B. D.; Vereecke, E. Assessment of healthy trapeziometacarpal cartilage properties using indentation testing and contrast-enhanced computed tomography. *Clin. Biomech.* **2019**, *61*, 181-189.

47 Freedman, J. D.; Lusic, H.; Snyder, B. D.; Grinstaff, M. W. Tantalum Oxide Nanoparticles for the Imaging of Articular Cartilage Using X-Ray Computed Tomography: Visualization of Ex Vivo/In Vivo Murine Tibia and Ex Vivo Human Index Finger Cartilage. *Angew. Chem. Int. Ed.* **2014**, *53* (32), 8406-8410.

48 Gao, X. Q.; Patwa, N. A.; Deng, Z. H.; Utsunomiya, H.; Grinstaff, W. M.; Ruzbarsky, J. J.; Snyder, D. B.; Ravuri, S.; Philippon, J. M.; Huard, J. Influence of fixation on CA4+contrast enhanced microCT of articular cartilage and subsequent feasibility for histological evaluation. *Am. J. Transl. Res.* **2021**, *13* (8), 8921-8937.

49 Garcia, J. P.; Longoni, A.; Gawlitta, D.; J.W.P. Rosenberg, A.; Grinstaff, M. W.; Töyräs, J.; Weinans, H.; Creemers, L. B.; Pouran, B. Contrast enhanced computed tomography for real-time quantification of glycosaminoglycans in cartilage tissue engineered constructs. *Acta Biomater.* **2019**, *100*, 202-212.

50 Honkanen, J. T. J.; Turunen, M. J.; Freedman, J. D.; Saarakkala, S.; Grinstaff, M. W.; Ylarinne, J. H.; Jurvelin, J. S.; Toyras, J. Cationic Contrast Agent Diffusion Differs Between Cartilage and Meniscus. *Ann. Biomed. Eng.* **2016**, *44* (10), 2913-2921.

51 Honkanen, M. K. M.; Matikka, H.; Honkanen, J. T. J.; Bhattarai, A.; Grinstaff, M. W.; Joukainen, A.; Kroger, H.; Jurvelin, J. S.; Toyras, J. Imaging of proteoglycan and water contents in human articular cartilage with full-body CT using dual contrast technique. *J. Orthop. Res.* **2019**, *37* (5), 1059-1070.

52 Honkanen, M. K. M.; Saukko, A. E. A.; Turunen, M. J.; Xu, W. J.; Lovric, G.; Honkanen, J. T. J.; Grinstaff, M. W.; Lehto, V. P.; Toyras, J. Triple Contrast CT Method Enables Simultaneous Evaluation of Articular Cartilage Composition and Segmentation. *Ann. Biomed. Eng.* **2020**, *48* (2), 556-567.

53 Karhula, S. S.; Finnila, M. A.; Freedman, J. D.; Kauppinen, S.; Valkealahti, M.; Lehenkari, P.; Pritzker, K. P. H.; Nieminen, H. J.; Snyder, B. D.; Grinstaff, M. W.*; et al.* Micro-Scale Distribution of CA4+ in Ex vivo Human Articular Cartilage Detected with Contrast-Enhanced Micro-Computed Tomography Imaging. *Front. Phys.* **2017**, *5*, 1-8.

54 Lakin, B. A.; Ellis, D. J.; Shelofsky, J. S.; Freedman, J. D.; Grinstaff, M. W.; Snyder, B. D. Contrast-enhanced CT facilitates rapid, non-destructive assessment of cartilage and bone properties of the human metacarpal. *Osteoarthr. Cartil.* **2015**, *23* (12), 2158-2166.

55 Lakin, B. A.; Patel, H.; Holland, C.; Freedman, J. D.; Shelofsky, J. S.; Snyder, B. D.; Stok, K. S.; Grinstaff, M. W. Contrast-enhanced CT using a cationic contrast agent enables non-destructive assessment of the biochemical and biomechanical properties of mouse tibial plateau cartilage. *J. Orthop. Res.* **2016**, *34* (7), 1130-1138.
56 Lawson, T.; Joenathan, A.; Patwa, A.; Snyder, B. D.; Grinstaff, M. W. Tantalum Oxide Nanoparticles for the Quantitative Contrast-Enhanced Computed Tomography of Ex Vivo Human Cartilage: Assessment of Biochemical Composition and Biomechanics. *ACS Nano* **2021**, *15* (12), 19175-19184.
57 Mashiatulla, M.; Moran, M. M.; Chan, D.; Li, J.; Freedman, J. D.; Snyder, B. D.; Grinstaff, M. W.; Plaas, A.; Sumner, D. R. Murine articular cartilage morphology and compositional quantification with high resolution cationic contrast-enhanced CT. *J. Orthop. Res.* **2017**, *35* (12), 2740-2748.
58 Nelson, B. B.; Makela, J. T. A.; Lawson, T. B.; Patwa, A. N.; Barrett, M. F.; McIlwraith, C. W.; Hurtig, M. B.; Snyder, B. D.; Moorman, V. J.; Grinstaff, M. W.*; et al.* Evaluation of equine articular cartilage degeneration after mechanical impact injury using cationic contrast-enhanced computed tomography. *Osteoarthr. Cartil.* **2019**, *27* (8), 1219-1228.
59 Nelson, B. B.; Makela, J. T. A.; Lawson, T. B.; Patwa, A. N.; Snyder, B. D.; McIlwraith, C. W.; Grinstaff, M. W.; Goodrich, L. R.; Kawcak, C. E. Cationic contrast-enhanced computed tomography distinguishes between reparative, degenerative, and healthy equine articular cartilage. *J. Orthop. Res.* **2021**, *39* (8), 1647-1657.
60 Nelson, B. B.; Stewart, R. C.; Kawcak, C. E.; Freedman, J. D.; Patwa, A. N.; Snyder, B. D.; Goodrich, L. R.; Grinstaff, M. W. Quantitative Evaluation of Equine Articular Cartilage Using Cationic Contrast-Enhanced Computed Tomography. *Cartilage* **2021**, *12* (2), 211-221.
61 Newton, M. D.; Hartner, S. E.; Timmons, S.; Delaney, N. D.; Pirrone, M. G.; Baker, K. C.; Maerz, T. Contrast-enhanced CT of the intervertebral disc: A comparison of anionic and cationic contrast agents for biochemical and morphological characterization. *J. Orthop. Res.* **2017**, *35* (5), 1067-1075.
62 Nickmanesh, R.; Stewart, R. C.; Snyder, B. D.; Grinstaff, M. W.; Masri, B. A.; Wilson, D. R. Contrast-enhanced computed tomography (CECT) attenuation is associated with stiffness of intact knee cartilage. *J. Orthop. Res.* **2018**, *36* (10), 2641-2647.

63 Oh, D. J.; Lakin, B. A.; Stewart, R. C.; Wiewiorski, M.; Freedman, J. D.; Grinstaff, M. W.; Snyder, B. D. Contrast-enhanced CT imaging as a non-destructive tool for ex vivo examination of the biochemical content and structure of the human meniscus. *J. Orthop. Res.* **2017**, *35* (5), 1018-1028.

64 Paakkari, P.; Inkinen, S. I.; Honkanen, M. K. M.; Prakash, M.; Shaikh, R.; Nieminen, M. T.; Grinstaff, M. W.; Makela, J. T. A.; Toyras, J.; Honkanen, J. T. J. Quantitative dual contrast photon-counting computed tomography for assessment of articular cartilage health. *Sci. Rep.* **2021**, *11* (1), 1-11.

65 Saukko, A. E. A.; Sarin, J. K.; Nykanen, O.; Nissi, M. J.; te Moller, N. C. R.; Weinans, H.; Mancini, I. A. D.; Visser, J.; Brommer, H.; van Weeren, P. R.*; et al.* Dual-contrast computed tomography enables detection of equine posttraumatic osteoarthritis in vitro. *J. Orthop. Res.* **2022**, *40* (3), 703-711.

66 Saukko, A. E. A.; Turunen, M. J.; Honkanen, M. K. M.; Lovric, G.; Tiitu, V.; Honkanen, J. T. J.; Grinstaff, M. W.; Jurvelin, J. S.; Toyras, J. Simultaneous Quantitation of Cationic and Non-ionic Contrast Agents in Articular Cartilage Using Synchrotron MicroCT Imaging. *Sci. Rep.* **2019**, *9*, 1-9.

67 Stewart, R. C.; Bansal, P. N.; Entezari, V.; Lusic, H.; Nazarian, R. M.; Snyder, B. D.; Grinstaff, M. W. Contrast-enhanced CT with a High-Affinity Cationic Contrast Agent for Imaging ex Vivo Bovine, Intact ex Vivo Rabbit, and in Vivo Rabbit Cartilage. *Radiology* **2013**, *266* (1), 141-150.

68 Stewart, R. C.; Nelson, B. B.; Kawcak, C. E.; Freedman, J. D.; Snyder, B. D.; Goodrich, L. R.; Grinstaff, M. W. Contrast-Enhanced Computed Tomography Scoring System for Distinguishing Early Osteoarthritis Disease States: A Feasibility Study. *J. Orthop. Res.* **2019**, *37* (10), 2138-2148.

69 Stewart, R. C.; Patwa, A. N.; Lusic, H.; Freedman, J. D.; Wathier, M.; Snyder, B. D.; Guermazi, A.; Grinstaff, M. W. Synthesis and Preclinical Characterization of a Cationic Iodinated Imaging Contrast Agent (CA4+) and Its Use for Quantitative Computed Tomography of Ex Vivo Human Hip Cartilage. *J. Med. Chem.* **2017**, *60* (13), 5543-5555.

70 Zhang, H. L.; Belev, G.; Stewart, R. C.; Grinstaff, M. W.; Snyder, B. D.; Wilson, D. R. Protocol development for synchrotron contrast-enhanced CT of human hip cartilage. *Med. Eng. Phys.* **2019**, *73*, 1-8.

71 Lakin, B. A.; Grasso, D. J.; Stewart, R. C.; Freedman, J. D.; Snyder, B. D.; Grinstaff, M. W. Contrast Enhanced CT Attenuation Correlates with the GAG Content of Bovine Meniscus. *J. Orthop. Res.* **2013**, *31* (11), 1765-1771.

72 Honkanen, M. K. M.; Saukko, A. E. A.; Turunen, M. J.; Shaikh, R.; Prakash, M.; Lovric, G.; Joukainen, A.; Kroger, H.; Grinstaff, M. W.; Toyras, J. Synchrotron MicroCT Reveals the Potential of the Dual Contrast Technique for Quantitative Assessment of Human Articular Cartilage Composition. *J. Orthop. Res.* **2020**, *38* (3), 563-573.

73 Michalak, G. J.; Walker, R.; Boyd, S. K. Concurrent Assessment of Cartilage Morphology and Bone Microarchitecture in the Human Knee Using Contrast-Enhanced HR-pQCT Imaging. *J. Clin. Densitom.* **2019**, *22* (1), 74-85.

74 ter Voert, C. E. M.; Kour, R. Y. N.; van Teeffelen, B. C. J.; Ansari, N.; Stok, K. S. Contrast-enhanced micro-computed tomography of articular cartilage morphology with ioversol and iomeprol. *J. Anat.* **2020**, *237* (6), 1062-1071.

75 Nieminen, H. J.; Ylitalo, T.; Karhula, S.; Suuronen, J. P.; Kauppinen, S.; Serimaa, R.; Hæggström, E.; Pritzker, K. P.; Valkealahti, M.; Lehenkari, P.*; et al.* Determining collagen distribution in articular cartilage using contrast-enhanced micro-computed tomography. *Osteoarthr. Cartil.* **2015**, *23* (9), 1613-1621.

76 Kwon, K. A.; Bax, D. V.; Shepherd, J. H.; Cameron, R. E.; Best, S. M. Avoiding artefacts in MicroCT imaging of collagen scaffolds: Effect of phosphotungstic acid (PTA)-staining and crosslink density. *Bioact. Mater.* **2022**, *8*, 210-219.

77 Karhula, S. S.; Finnila, M. A.; Lammi, M. J.; Ylarinne, J. H.; Kauppinen, S.; Rieppo, L.; Pritzker, K. P.; Nieminen, H. J.; Saarakkala, S. Effects of Articular Cartilage Constituents on Phosphotungstic Acid Enhanced Micro-Computed Tomography. *PLoS One* **2017**, *12* (1), e0171075.

78 Nieminen, H. J.; Gahunia, H. K.; Pritzker, K. P. H.; Ylitalo, T.; Rieppo, L.; Karhula, S. S.; Lehenkari, P.; Haeggstrom, E.; Saarakkala, S. 3D histopathological grading of osteochondral tissue using contrast-enhanced micro-computed tomography. *Osteoarthr. Cartil.* **2017**, *25* (10), 1680-1689.

79 Borges, P. D.; Forte, A. E.; Vincent, T. L.; Dini, D.; Marenzana, M. Rapid, automated imaging of mouse articular cartilage by microCT for early detection of osteoarthritis and finite element modelling of joint mechanics. *Osteoarthr. Cartil.* **2014**, *22* (10), 1419-1428.

80 Zhu, Y.; Ponjevic, D.; Matyas, J. R.; Boyd, S. K. Contrast-enhanced x-ray microscopy of articular cartilage. *Connect. Tissue Res.* **2021**, *62* (5), 542-553.

81 Netzer, C.; Scharen, S.; Geurts, J. Phosphotungstic acid-enhanced micro computed tomography for three-dimensional visualization and analysis of collagen distribution in human osteochondral tissues. *Osteoarthr. Cartil.* **2018**, *26*, S432-S432.

82 Kun-Darbois, J. D.; Manero, F.; Rony, L.; Chappard, D. Contrast enhancement with uranyl acetate allows quantitative analysis of the articular cartilage by microCT: Application to mandibular condyles in the BTX rat model of disuse. *Micron* **2017**, *97*, 35-40.

83 de Bournonville, S.; Vangrunderbeeck, S.; Ly, H. G. T.; Geeroms, C.; De Borggraeve, W. M.; Parac-Vogt, T. N.; Kerckhofs, G. Exploring polyoxometalates as non-destructive staining agents for contrast-enhanced microfocus computed tomography of biological tissues. *Acta Biomater.* **2020**, *105*, 253-262.

84 Schulz-Mirbach, T.; Hess, M.; Metscher, B. D. Sensory epithelia of the fish inner ear in 3D: studied with high-resolution contrast enhanced microCT. *Front. Zool.* **2013**, *10*,

85 Cox, P. G.; Jeffery, N. Reviewing the Morphology of the Jaw-Closing Musculature in Squirrels, Rats, and Guinea Pigs with Contrast-Enhanced MicroCT. *Anat. Rec.* **2011**, *294* (6), 915-928.

86 Jeffery, N. S.; Stephenson, R. S.; Gallagher, J. A.; Jarvis, J. C.; Cox, P. G. Micro-computed tomography with iodine staining resolves the arrangement of muscle fibres. *J. Biomech.* **2011**, *44* (1), 189-192.

87 Scheller, E. L.; Doucette, C. R.; Learman, B. S.; Cawthorn, W. P.; Khandaker, S.; Schell, B.; Wu, B.; Ding, S. Y.; Bredella, M. A.; P.K., F.*; et al.* Region-specific variation in the properties of skeletal adipocytes reveals regulated and constitutive marrow adipose tissues. *Nat. Commun.* **2015**, *6*, 1-15.

88 Scheller, E. L.; Troiano, N.; VanHoutan, J. N.; Bouxsein, M. A.; Fretz, J. A.; Xi, Y. G.; Nelson, T.; Katz, G.; Berry, R.; Church, C. D.*; et al.* Use of Osmium Tetroxide Staining with Microcomputerized Tomography to Visualize and Quantify Bone Marrow Adipose Tissue In Vivo. *Methods of Adipose Tissue Biology, Pt A* **2014**, *537*, 123-139.

89 Balint, R.; Lowe, T.; Shearer, T. Optimal Contrast Agent Staining of Ligaments and Tendons for X-Ray Computed Tomography. *PLoS One* **2016**, *11* (4), 1-15.

90 Sartori, J.; Köhring, S.; Witte, H.; Fischer, M. S.; Löffler, M. Three-dimensional imaging of the fibrous microstructure of Achilles tendon entheses in Mus musculus. *J. Anat.* **2018**, *233* (3), 370-380.
91 Shearer, T.; Rawson, S.; Castro, S. J.; Balint, R.; Bradley, R. S.; Lowe, T.; Vila-Comamala, J.; Lee, P. D.; Cartmell, S. H. X-ray computed tomography of the anterior cruciate ligament and patellar tendon. *Muscles Ligaments Tendons J.* **2014**, *4* (2), 238-244.
92 Rossetti, L.; Kuntz, L. A.; Kunold, E.; Schock, J.; Muller, K. W.; Grabmayr, H.; Stolberg-Stolberg, J.; Pfeiffer, F.; Sieber, S. A.; Burgkart, R.*; et al.* The microstructure and micromechanics of the tendon-bone insertion. *Nat. Mater.* **2017**, *16* (6), 664-670.
93 Xie, L.; Lin, A. S. P.; Guldberg, R. E.; Levenston, M. E. Nondestructive assessment of sGAG content and distribution in normal and degraded rat articular cartilage via EPIC-μCT. *Osteoarthr. Cartil.* **2010**, *18* (1), 65-72.
94 Xie, L.; Lin, A. S. P.; Levenston, M. E.; Guldberg, R. E. Quantitative assessment of articular cartilage morphology via EPIC-μCT. *Osteoarthr. Cartil.* **2009**, *17* (3), 313-320.
95 Jin, L. H.; Choi, B. H.; Kim, Y. J.; Oh, H. J.; Kim, B. J.; Yin, X. Y.; Min, B. H. Nondestructive Assessment of Glycosaminoglycans in Engineered Cartilages Using Hexabrix-Enhanced Micro-Computed Tomography. *Tissue Eng. Regener. Med.* **2018**, *15* (3), 311-319.
96 Saukko, A. E. A.; Honkanen, J. T. J.; Xu, W. J.; Vaananen, S. P.; Jurvelin, J. S.; Lehto, V. P.; Toyras, J. Dual Contrast CT Method Enables Diagnostics of Cartilage Injuries and Degeneration Using a Single CT Image. *Ann. Biomed. Eng.* **2017**, *45* (12), 2857-2866.
97 Quintarelli, G.; Zito, R.; Cifonelli, J. A. On Phosphotungstic acid Staining.1. *J. Histochem. Cytochem.* **1971**, *19* (11), 641-647.
98 Nemetschek, T.; Riedl, H.; Jonak, R. Topchemistry of the Binding of Phosphotungstic Acid to Collagen. *J. Mol. Biol.* **1979**, *133* (1), 67-83.
99 Cawthorn, W. P.; Scheller, E. L.; Learman, B. S.; Parlee, S. D.; Simon, B. R.; Mori, H.; Ning, X. M.; Bree, A. J.; Schell, B.; Broome, D. T.*; et al.* Bone Marrow Adipose Tissue Is an Endocrine Organ that Contributes to Increased Circulating Adiponectin during Caloric Restriction. *Cell Metabolism* **2014**, *20* (2), 368-375.
100 Gargiulo, P.; Helgason, T.; Ramon, C.; Jonsson, H.; Carraro, U. CT and MRI assessment and characterization using segmentation and 3D modeling techniques: applications to muscle, bone and brain. *Eur. J. Transl. Myol.* **2014**, *24* (1), 55-62.

101 Aslanidi, O. V.; Nikolaidou, T.; Zhao, J. C.; Smaill, B. H.; Gilbert, S. H.; Holden, A. V.; Lowe, T.; Withers, P. J.; Stephenson, R. S.; Jarvis, J. C.*; et al.* Application of Micro-Computed Tomography With Iodine Staining to Cardiac Imaging, Segmentation, and Computational Model Development. *IEEE Trans. Med. Imaging* **2013**, *32* (1), 8-17.

102 Buytaert, J.; Goyens, J.; De Greef, D.; Aerts, P.; Dirckx, J. Volume Shrinkage of Bone, Brain and Muscle Tissue in Sample Preparation for Micro-CT and Light Sheet Fluorescence Microscopy (LSFM). *Microsc. Microanal.* **2014**, *20* (4), 1208-1217.

103 Vickerton, P.; Jarvis, J.; Jeffery, N. Concentration-dependent specimen shrinkage in iodine-enhanced microCT. *J. Anat.* **2013**, *223* (2), 185-193.

104 Schneider, P.; Krucker, T.; Meyer, E.; Ulmann-Schuler, A.; Weber, B.; Stampanoni, M.; Muller, R. Simultaneous 3D Visualization and Quantification of Murine Bone and Bone Vasculature Using Micro-Computed Tomography and Vascular Replica. *Microsc. Res. Tech.* **2009**, *72* (9), 690-701.

105 Hu, J. Z.; Cao, Y.; Wu, T. D.; Li, D. Z.; Lu, H. B. High-resolution three-dimensional visualization of the rat spinal cord microvasculature by synchrotron radiation micro-CT. *Med. Phys.* **2014**, *41* (10), 1-8.

106 Bentley, M. D.; Ortiz, M. C.; Ritman, E. L.; Romero, J. C. The use of microcomputed tomography to study microvasculature in small rodents. *Am. J. Physiol. Regul. Integr. Comp. Physiol.* **2002**, *282* (5), R1267-R1279.

107 Leyssens, L.; Pestiaux, C.; Kerckhofs, G. A Review of Ex Vivo X-ray Microfocus Computed Tomography-Based Characterization of the Cardiovascular System. *Int. J. Mol. Sci.* **2021**, *22* (6), 1-26.

108 Metscher, B. D.; Muller, G. B. MicroCT for Molecular Imaging: Quantitative Visualization of Complete Three-Dimensional Distributions of Gene Products in Embryonic Limbs. *Dev. Dyn.* **2011**, *240* (10), 2301-2308.

109 Cormode, D. P.; Naha, P. C.; Fayad, Z. A. Nanoparticle contrast agents for computed tomography: a focus on micelles. *Contrast Media Mol. Imaging* **2014**, *9* (1), 37-52.

110 Koc, M. M.; Aslan, N.; Kao, A. P.; Barber, A. H. Evaluation of X-ray tomography contrast agents: A review of production, protocols, and biological applications. *Microsc. Res. Tech.* **2019**, *82* (6), 812-848.

111 van Leeuwenhoeck, A. Observations, communicated to the publisher by Mr. Antony van Leewenhoeck, in a dutch letter of the 9th Octob.

1676. here English'd: concerning little animals by him observed in rain-well-sea- and snow water; as also in water wherein pepper had lain infused. *Phil. Trans.* **1675**, *12* (133), 821-831.

112 Rodrigues, P. V.; Tostes, K.; Bosque, B. P.; de Godoy, J. V. P.; Neto, D. P. A.; Dias, C. S. B.; Fonseca, M. D. Illuminating the Brain With X-Rays: Contributions and Future Perspectives of High-Resolution Microtomography to Neuroscience. *Front. Neurosci.* **2021**, *15*, 1-13.

113 Styner, M.; Thompson, W. R.; Galior, K.; Uzer, G.; Wu, X.; Kadari, S.; Case, N.; Xie, Z. H.; Sen, B.; Romaine, A.*; et al.* Bone marrow fat accumulation accelerated by high fat diet is suppressed by exercise. *Bone* **2014**, *64*, 39-46.

114 Sonnaert, M.; Kerckhofs, G.; Papantoniou, I.; Van Vlierberghe, S.; Boterberg, V.; Dubruel, P.; Luyten, F. P.; Schrooten, J.; Geris, L. Multifactorial Optimization of Contrast-Enhanced Nanofocus Computed Tomography for Quantitative Analysis of Neo-Tissue Formation in Tissue Engineering Constructs. *PLoS One* **2015**, *10* (6), 1-17.

115 Farcasiu, D.; Li, J. Q. Acidity Measurements on a Heteropolyacid Hydrate in Acetic-Acid Solution - a Case of 3 Hydrons Ionizing Independently, Rather Than Consecutively. *J. Catal.* **1995**, *152* (1), 198-203.

116 Kirby, J. F.; Baker, L. C. W. Effects of counterions in heteropoly electrolyte chemistry. 1. Evaluations of relative interactions by NMR on Kozik salts. *Inorg. Chem.* **1998**, *37* (21), 5537-5543.

117 Sadakane, M.; Ostuni, A.; Pope, M. T. Formation of 1 : 1 and 2 : 2 complexes of Ce(III) with the heteropolytungstate anion alpha(2)-P2W17O61 (10-), and their interaction with proline. The structure of Ce-2(P2W17O61)(2)(H2O)(8) (14-). *J. Chem. Soc., Dalton Trans.* **2002**. (1), 63-67.

118 Degenhardt, K.; Wright, A. C.; Horng, D.; Padmanabhan, A.; Epstein, J. A. Rapid 3D Phenotyping of Cardiovascular Development in Mouse Embryos by Micro-CT With Iodine Staining. *Circ. Cardiovasc. Imaging* **2010**, *3* (3), 314-138.

119 West, M. J. Tissue Shrinkage and Stereological Studies. *Cold Spring Harb. Protoc.* **2013**, *2013* (3), 207-212.

120 5 - Disturbances of Free Water, Electrolytes, Acid-Base Balance, and Oncotic Pressure. In *Veterinary Medicine (Eleventh Edition)*, Constable, P. D., Hinchcliff, K. W., Done, S. H., Grünberg, W. Eds.W.B. Saunders, **2017**; pp 113-152.

121 Absillis, G.; Parac-Vogt, T. N. Peptide bond hydrolysis catalyzed by the Wells-Dawson Zr(alpha2-P2W17O61)2 polyoxometalate. *Inorg. Chem.* **2012**, *51* (18), 9902-9910.
122 Ly, H. G.; Absillis, G.; Parac-Vogt, T. N. Amide bond hydrolysis in peptides and cyclic peptides catalyzed by a dimeric Zr(IV)-substituted Keggin type polyoxometalate. *Dalton Trans.* **2013**, *42* (30), 10929-10938.
123 Boglio, C.; Hasenknopf, B.; Lenoble, G.; Remy, P.; Gouzerh, P.; Thorimbert, S.; Lacote, E.; Malacria, M.; Thouvenot, R. Sensing the chirality of Dawson lanthanide polyoxometalates [alpha1-LnP2W17O61]7- by multinuclear NMR spectroscopy. *Chemistry* **2008**, *14* (5), 1532-1540.
124 Dupre, N.; Remy, P.; Micoine, K.; Boglio, C.; Thorimbert, S.; Lacote, E.; Hasenknopf, B.; Malacria, M. Chemoselective catalysis with organosoluble Lewis acidic polyoxotungstates. *Chemistry* **2010**, *16* (24), 7256-7264.
125 Smith, B. J.; Patrick, V. A. Quantitative Determination of Aqueous Dodecatungstophosphoric Acid Speciation by NMR Spectroscopy. *Aust. J. Chem.* **2004**, *57* (3), 261-268.
126 Zhu, Z.; Tain, R.; Rhodes, C. A study of the decomposition behaviour of 12-tungstophosphate heteropolyacid in solution. *Can. J. Chem.* **2003**, *81* (10), 1044-1050.
127 Sokolov, M. N.; Chubarova, E. V.; Peresypkina, E. V.; Virovets, A. V.; Fedin, V. P. Complexes of Zr-IV and Hf-IV with monolacunary Keggin- and Dawson-type anions. *Russ. Chem. Bull.* **2007**, *56* (2), 220-224.
128 Ginsberg, A. P. *Inorganic Syntheses*; Wiley, **1990**.
129 Lyon, D. K.; Miller, W. K.; Novet, T.; Domaille, P. J.; Evitt, E.; Johnson, D. C.; Finke, R. G. Highly oxidation resistant inorganic-porphyrin analog polyoxometalate oxidation catalysts. 1. The synthesis and characterization of aqueous-soluble potassium salts of .alpha.2-P2W17O61(Mn+.cntdot.OH2)(n-10) and organic solvent soluble tetra-n-butylammonium salts of .alpha.2-P2W17O61(Mn+.cntdot.Br)(n-11) (M = Mn3+,Fe3+,Co2+,Ni2+,Cu2+). *J. Am. Chem. Soc.* **1991**, *113* (19), 7209-7221.
130 Roberts, J. K. M.; Wadejardetzky, N.; Jardetzky, O. Intracellular pH measurements by phosphorus-31 nuclear magnetic resonance. Influence of factors other than pH on phosphorus-31 chemical shifts. *Biochemistry* **1981**, *20* (19), 5389-5394.

131 Hunter, D. J.; March, L.; Chew, M. Osteoarthritis in 2020 and beyond: a Lancet Commission. *Lancet* **2020**, *396* (10264), 1711-1712.
132 Hunter, D. J.; Nevitt, M.; Losina, E.; Kraus, V. Biomarkers for osteoarthritis: Current position and steps towards further validation. *Best Pract. Res., Clin. Rheumatol.* **2014**, *28* (1), 61-71.
133 Brandt, K. D.; Radin, E. L.; Dieppe, P. A.; van de Putte, L. Yet more evidence that osteoarthritis is not a cartilage disease. *Ann. Rheum. Dis.* **2006**, *65* (10), 1261-1264.
134 Long, H. B.; Liu, Q.; Yin, H. Y.; Wang, K.; Diao, N. C.; Zhang, Y. Q.; Lin, J. H.; Guo, A. Prevalence Trends of Site-Specific Osteoarthritis From 1990 to 2019: Findings From the Global Burden of Disease Study 2019. *Arthritis Rheumatol.* **2022**, *74* (7), 1172-1183.
135 Hunter, D. J.; Bierma-Zeinstra, S. Osteoarthritis. *Lancet* **2019**, *393* (10182), 1745-1759.
136 Abramoff, B.; Caldera, F. E. Osteoarthritis Pathology, Diagnosis, and Treatment Options. *Med. Clin. North Am.* **2020**, *104* (2), 293-311.
137 Katz, J. N.; Arant, K. R.; Loeser, R. F. Diagnosis and Treatment of Hip and Knee Osteoarthritis A Review. *JAMA - J. Am. Med.* **2021**, *325* (6), 568-578.
138 Buckwalter, J. A.; Mow, V. C.; Ratcliffe, A. Restoration of Injured or Degenerated Articular Cartilage. *J. Am. Acad. Orthop. Surg.* **1994**, *2* (4), 192-201.
139 Fox, A. J. S.; Bedi, A.; Rodeo, S. A. The Basic Science of Articular Cartilage: Structure, Composition, and Function. *Sports Health* **2009**, *1* (6), 461-468.
140 Akkiraju, H.; Nohe, A. Role of Chondrocytes in Cartilage Formation, Progression of Osteoarthritis and Cartilage Regeneration. *J. Dev. Biol.* **2015**, *3* (4), 177-192.
141 Buckwalter, J.; Mankin, H. Articular cartilage: part I. *J. Bone Jt. Surg.* **1997**, *79* (4), 600-611.
142 Ulrich-Vinther, M.; Maloney, M. D.; Schwarz, E. M.; Rosier, R.; O'Keefe, R. J. Articular Cartilage Biology. *J. Am. Acad. Orthop. Surg.* **2003**, *11* (6), 421-430.
143 Han, E.; Chen, S. S.; Klisch, S. M.; Sah, R. L. Contribution of Proteoglycan Osmotic Swelling Pressure to the Compressive Properties of Articular Cartilage. *Biophys. J.* **2011**, *101* (4), 916-924.
144 Bhosale, A. M.; Richardson, J. B. Articular cartilage: structure, injuries and review of management. *Br. Med. Bull.* **2008**, *87* (1), 77-95.

145 Camarero-Espinosa, S.; Rothen-Rutishauser, B.; Foster, E. J.; Weder, C. Articular cartilage: from formation to tissue engineering. *Biomater. Sci.* **2016**, *4* (5), 734-767.
146 He, B.; Wu, J. P.; Kirk, T. B.; Carrino, J. A.; Xiang, C.; Xu, J. High-resolution measurements of the multilayer ultra-structure of articular cartilage and their translational potential. *Arthritis Res. Ther.* **2014**, *16* (2), 205.
147 Wang, W. Y.; Ye, R. X.; Xie, W. Q.; Zhang, Y. Y.; An, S. B.; Li, Y. S.; Zhou, Y. Roles of the calcified cartilage layer and its tissue engineering reconstruction in osteoarthritis treatment. *Front. Bioeng. Biotechnol.* **2022**, *10*, 1-12.
148 Hauser, R. A. The acceleration of articular cartilage degeneration in osteoarthritis by nonsteroidal anti-inflammatory drugs. *Journal of Prolotherapy* **2010**, *2* (1), 305-322.
149 Fan, F.; Li, X. F.; Ren, P. L.; Cai, X. R.; Yan, Y.; Fan, Y. B.; Niu, H. J.; Ieee. Correlations between X-ray Attenuation and GAG Content of Different Cartilage Layers Based on Contrast Agent Enhanced Micro-CT. In *37th Annual International Conference of the IEEE-Engineering-in-Medicine-and-Biology-Society (EMBC)*, Milan, ITALY, Aug 25-29, 2015; 2015.pp 6366-6369.
150 Venkatesan, N.; Barre, L.; Bourhim, M.; Magdalou, J.; Mainard, D.; Netter, P.; Fournel-Gigleux, S.; Ouzzine, M. Xylosyltransferase-I Regulates Glycosaminoglycan Synthesis during the Pathogenic Process of Human Osteoarthritis. *PLoS One* **2012**, *7* (3), 1-9.
151 Grushko, G.; Schneiderman, R.; Maroudas, A. Some Biochemical and Biophysical Parameters for the Study of the Pathogenesis of Osteoarthritis: a Comparison Between the Processes of Ageing and Degeneration in Human Hip Cartilage. *Connect. Tissue Res.* **1989**, *19* (2-4), 149-176.
152 Fantoni, S.; Gabucci, I.; Cardarelli, P.; Paterno, G.; Taibi, A.; Cristofori, V.; Trapella, C.; Bazzani, A.; Assenza, M.; Bonacorsi, A. Z.*; et al.* A Cationic Contrast Agent in X-ray Imaging of Articular Cartilage: Pre-Clinical Evaluation of Diffusion and Attenuation Properties. *Diagnostics* **2022**, *12* (9), 1-17.
153 Verschueren, R. H.; Gilles, P.; Van Mileghem, S.; De Borggraeve, W. M. Solvent-free N-Boc deprotection by ex situ generation of hydrogen chloride gas. *Org. Biomol. Chem.* **2021**. 5782-5787.
154 Odell, L. R.; Chau, N.; Mariana, A.; Graham, M. E.; Robinson, P. J.; McCluskey, A. Azido and Diazarinyl Analogues of Bis-Tyrphostin as

Asymmetrical Inhibitors of Dynamin GTPase. *ChemMedChem* **2009**, *4* (7), 1182-1188.
155 Withers, P. J.; Bouman, C.; Carmignato, S.; Cnudde, V.; Grimaldi, D.; Hagen, C. K.; Maire, E.; Manley, M.; Du Plessis, A.; Stock, S. R. X-ray computed tomography. *Nat. Rev. Methods Primers* **2021**, *1* (1), 1-21.
156 Davis, G. R.; Elliott, J. C. Artefacts in X-ray microtomography of materials. *Mater. Sci. Technol.* **2006**, *22* (9), 1011-1018.
157 Bajpayee, A. G.; Grodzinsky, A. J. Cartilage-targeting drug delivery: can electrostatic interactions help? *Nat. Rev. Rheumatol.* **2017**, *13* (3), 183-193.
158 Zanon, J.; Klapars, A.; Buchwald, S. L. Copper-catalyzed domino halide exchange-cyanation of aryl bromides. *J. Am. Chem. Soc.* **2003**, *125* (10), 2890-2891.
159 Balcaen, T.; Piens, C.; Mwema, A.; Chourrout, M.; Vandebroek, L.; Des Rieux, A.; Chauveau, F.; De Borggraeve, W. M.; Hoffmann, D.; Kerckhofs, G. Revealing the three-dimensional murine brain microstructure by contrast-enhanced computed tomography. *Front. Neurosci.* **2023**, *17*, 1-15.
160 DiDomenico, C. D.; Bonassar, L. J. How can 50 years of solute transport data in articular cartilage inform the design of arthritis therapeutics? *Osteoarthr. Cartil.* **2018**, *26* (11), 1438-1446.
161 Sanderson, T.; Wild, G.; Cull, A. M.; Marston, J.; Zardin, G. 19 - Immunohistochemical and immunofluorescent techniques. In *Bancroft's Theory and Practice of Histological Techniques (Eighth Edition)*, Suvarna, S. K., Layton, C., Bancroft, J. D. Eds.Elsevier, **2019**; pp 337-394.
162 Tamminen, I.; Lehto, K.; Hannula, M.; Ojansivu, M.; Johansson, L.; Kellomaki, M.; Miettinen, S.; Aula, A.; Ihalainen, T.; Hyttinen, J. A tube-source X-ray microtomography approach for quantitative 3D microscopy of optically challenging cell-cultured samples. *Commun. Biol.* **2020**, *3* (1), 1-13.
163 Katz, S. R.; Yakovlev, M. A.; Vanselow, D. J.; Ding, Y. F.; Lin, A. Y.; Parkinson, D. Y.; Wang, Y. X.; Canfield, V. A.; Ang, K. C.; Cheng, K. C. Whole-organism 3D quantitative characterization of zebrafish melanin by silver deposition micro-CT. *eLife* **2021**, *10*, 1-21.
164 Mahan, M. M.; Doiron, A. L. Gold Nanoparticles as X-Ray, CT, and Multimodal Imaging Contrast Agents: Formulation, Targeting, and Methodology. *J. Nanomater.* **2018**, *2018*, 1-16.

165 Hsu, J. C.; Nieves, L. M.; Betzer, O.; Sadan, T.; Noel, P. B.; Popovtzer, R.; Cormode, D. P. Nanoparticle contrast agents for X-ray imaging applications. *Wiley Interdiscip. Rev. Nanomed. Nanobiotechnol.* **2020**, *12* (6), 1-89.
166 Hong, S. H.; Herman, A. M.; Stephenson, J. M.; Wu, T.; Bahadur, A. N.; Burns, A. R.; Marrelli, S. P.; Wythe, J. D. Development of barium-based low viscosity contrast agents for micro CT vascular casting: Application to 3D visualization of the adult mouse cerebrovasculature. *J. Neurosci. Res.* **2020**, *98* (2), 312-324.
167 Renier, N.; Wu, Z. H.; Simon, D. J.; Yang, J.; Ariel, P.; Tessier-Lavigne, M. iDISCO: A Simple, Rapid Method to Immunolabel Large Tissue Samples for Volume Imaging. *Cell* **2014**, *159* (4), 896-910.
168 Fowkes, M. M.; Das Neves Borges, P.; Cacho-Nerin, F.; Brennan, P. E.; Vincent, T. L.; Lim, N. H. Imaging articular cartilage in osteoarthritis using targeted peptide radiocontrast agents. *PLoS One* **2022**, *17* (5), 1-15.
169 Gleave, J. A.; Lerch, J. P.; Henkelman, R. M.; Nieman, B. J. A Method for 3D Immunostaining and Optical Imaging of the Mouse Brain Demonstrated in Neural Progenitor Cells. *PLoS One* **2013**, *8* (8), 1-12.
170 Sillitoe, R. V.; Hawkes, R. Whole-mount immunohistochemistry: A high-throughput screen for patterning defects in the mouse cerebellum. *J. Histochem. Cytochem.* **2002**, *50* (2), 235-244.
171 Messal, H. A.; Almagro, J.; Thin, M. Z.; Tedeschi, A.; Ciccarelli, A.; Blackie, L.; Anderson, K. I.; Miguel-Aliaga, I.; van Rheenen, J.; Behrens, A. Antigen retrieval and clearing for whole-organ immunofluorescence by FLASH. *Nat. Protoc.* **2021**, *16* (1), 239-262.
172 Miyawaki, T.; Morikawa, S.; Susaki, E. A.; Nakashima, A.; Takeuchi, H.; Yamaguchi, S.; Ueda, H. R.; Ikegaya, Y. Visualization and molecular characterization of whole-brain vascular networks with capillary resolution. *Nat. Commun.* **2020**, *11* (1), 1-11.
173 Joyner, A.; Wall, N. Immunohistochemistry of Whole-Mount Mouse Embryos. *Cold Spring Harb. Protoc.* **2008**.
174 Smith, G. P. Filamentous fusion phage: novel expression vectors that display cloned antigens on the virion surface. *Science* **1985**, *228* (4705), 1315-1317.
175 Wu, C. H.; Liu, I. J.; Lu, R. M.; Wu, H. C. Advancement and applications of peptide phage display technology in biomedical science. *J. Biomed. Sci.* **2016**, *23* (8), 1-14.

176 Bazan, J.; Calkosinski, I.; Gamian, A. Phage displaya powerful technique for immunotherapy 1. Introduction and potential of therapeutic applications. *Hum. Vaccines Immunother.* **2012**, *8* (12), 1817-1828.
177 Parmley, S. F.; Smith, G. P. Antibody-selectable filamentous fd phage vectors: affinity purification of target genes. *Gene* **1988**, *73* (2), 305-318.
178 Engvall, E.; Perlmann, P. Engvall E, Perlmann P. Enzyme-linked immunosorbent assay, Elisa. 3. Quantitation of specific antibodies by enzyme-labeled anti-immunoglobulin in antigen-coated tubes. *J Immunol.* **1972**, *109* (1), 129-135.
179 Bystryak, S.; Acharya, C. Detection of HIV-1 p24 antigen in patients with varying degrees of viremia using an ELISA with a photochemical signal amplification system. *Clin. Chim. Acta* **2016**, *456*, 128-136.
180 Schasfoort, R. B. M. Chapter 1 Introduction to Surface Plasmon Resonance. In *Handbook of Surface Plasmon Resonance (2)*.The Royal Society of Chemistry, **2017**; pp 1-26.
181 Knez, K.; Noppe, W.; Geukens, N.; Janssen, K. P. F.; Spasic, D.; Heyligen, J.; Vriens, K.; Thevissen, K.; Cammue, B. P. A.; Petrenko, V.*; et al.* Affinity Comparison of p3 and p8 Peptide Displaying Bacteriophages Using Surface Plasmon Resonance. *Anal. Chem.* **2013**, *85* (21), 10075-10082.
182 Li, Y. Commonly used tag combinations for tandem affinity purification. *Biotechnol. Appl. Biochem.* **2010**, *55* (2), 73-83.
183 Presolski, S. I.; Hong, V. P.; Finn, M. G. Copper-Catalyzed Azide-Alkyne Click Chemistry for Bioconjugation. *Curr. Protoc. Chem. Biol.* **2011**, *3* (4), 153-162.
184 Nakane, P. K.; Pierce, G. B. Enzyme-labeled antibodies: preparation and application for the localization of antigens. *J. Histochem. Cytochem.* **1966**, *14* (12), 929-931.
185 Hanson, J. R. Advances in the direct iodination of aromatic compounds. *J. Chem. Res.* **2006**. (5), 277-280.
186 Gallo, R. D. C.; Ferreira, I. M.; Casagrande, G. A.; Pizzuti, L.; Oliveira-Silva, D.; Raminelli, C. Efficient and eco-friendly synthesis of iodinated aromatic building blocks promoted by iodine and hydrogen peroxide in water: a mechanistic investigation by mass spectrometry. *Tetrahedron Lett.* **2012**, *53* (40), 5372-5375.
187 Ferreira, I. M.; Casagrande, G. A.; Pizzuti, L.; Raminelli, C. Ultrasound-Promoted Rapid and Efficient Iodination of Aromatic and

Heteroaromatic Compounds in the Presence of Iodine and Hydrogen Peroxide in Water. *Synth. Commun.* **2014**, *44* (14), 2094-2102.
188 Lindner, B. D.; Engelhart, J. U.; Tverskoy, O.; Appleton, A. L.; Rominger, F.; Peters, A.; Himmel, H. J.; Bunz, U. H. F. Stable Hexacenes through Nitrogen Substitution. *Angew. Chem. Int. Ed.* **2011**, *50* (37), 8588-8591.
189 Sy, W. W. Iodination of aromatic amines with iodine and silver sulfate. *Synth. Commun.* **1992**, *22* (22), 3215-3219.
190 Boz, S.; Stohr, M.; Soydaner, U.; Mayor, M. Protecting-Group-Controlled Surface Chemistry - Organization and Heat-Induced Coupling of 4,4 '-Di(tert-butoxycarbonylamino)biphenyl on Metal Surfaces. *Angew. Chem. Int. Ed.* **2009**, *48* (17), 3179-3183.
191 Boger, D. L.; Brunette, S. R.; Garbaccio, R. M. Synthesis and evaluation of a series of C3-substituted CBI analogues of CC-1065 and the duocarmycins. *J. Org. Chem.* **2001**, *66* (15), 5163-5173.
192 Tietze, L. F.; Panknin, O.; Major, F.; Krewer, B. Synthesis of a novel pentagastrin-drug conjugate for a targeted tumor therapy. *Chem. Eur. J.* **2008**, *14* (9), 2811-2818.
193 Racys, D. T.; Sharif, S. A. I.; Pimlott, S. L.; Sutherland, A. Silver(I)-Catalyzed Iodination of Arenes: Tuning the Lewis Acidity of N-Iodosuccinimide Activation. *J. Org. Chem.* **2016**, *81* (3), 772-780.
194 Warford, A.; Akbar, H.; Riberio, D. Antigen retrieval, blocking, detection and visualisation systems in immunohistochemistry: A review and practical evaluation of tyramide and rolling circle amplification systems. *Methods* **2014**, *70* (1), 28-33.
195 Speel, E. J. M.; Hopman, A. H. N.; Komminoth, P. Amplification methods to increase the sensitivity of in situ hybridization: Play CARD(S). *J. Histochem. Cytochem.* **1999**, *47* (3), 281-288.
196 Khan, A. A.; Rahmani, A. H.; Aldebasi, Y. H.; Aly, S. M. Biochemical and pathological studies on peroxidases -an updated review. *Glob. J. Health Sci.* **2014**, *6* (5), 87-98.
197 Hopman, A. H. N.; Speel, E. J. M.; Ramaekers, F. C. S. Preparation of tyramide conjugates. Netherlands EP97204097A, 1999.
198 Bobrow, M. N.; Litt, G. J.; Shaughnessy, K. J.; Mayer, P. C.; Conlon, J. The use of catalyzed reporter deposition as a means of signal amplification in a variety of formats. *J. Immunol. Methods* **1992**, *150* (1-2), 145-149.
199 Santucci, R.; Laurenti, E.; Sinibaldi, F.; Ferrari, R. P. Effect of dimethyl sulfoxide on the structure and the functional properties of

horseradish peroxidase as observed by spectroscopy and cyclic voltammetry. *Biochim. Biophys. Acta, Protein Struct. Mol. Enzymol.* **2002**, *1596* (2), 225-233.

200 Smedley, C. J.; Barrow, A. S.; Spiteri, C.; Giel, M. C.; Sharma, P.; Moses, J. E. Sulfur-Fluoride Exchange (SuFEx)-Mediated Synthesis of Sterically Hindered and Electron-Deficient Secondary and Tertiary Amides via Acyl Fluoride Intermediates. *Chem. Eur. J.* **2017**, *23* (42), 9990-9995.

201 Due-Hansen, M. E.; Pandey, S. K.; Christiansen, E.; Andersen, R.; Hansen, S. V. F.; Ulven, T. A protocol for amide bond formation with electron deficient amines and sterically hindered substrates. *Org. Biomol. Chem.* **2016**, *14* (2), 430-433.

202 Li, B. Y.; Voets, L.; Van Lommel, R.; Hoppenbrouwers, F.; Alonso, M.; Verhelst, S. H. L.; De Borggraeve, W. M.; Demaerel, J. SuFEx-enabled, chemoselective synthesis of triflates, triflamides and triflimidates. *Chem. Sci.* **2022**, *13* (8), 2270-2279.

203 Tanaka, S. Y.; Tagashira, N.; Chiba, K.; Yasuda, M.; Baba, A. Germanium(II)-mediated reductive Mannich-type reaction of alpha-bromoketones to N-alkylimines. *Angew. Chem. Int. Ed.* **2008**, *47* (35), 6620-6623.

204 Schmid, P.; Hohenschutz, M.; Grass, X.; Witzmann, M.; Touraud, D.; Diat, O.; Pfitzner, A.; Bauduin, P. Counterion effect on a-Keggin polyoxometalates in water: The peculiar role of H+ on their salting-in effect and co-assembly with organics. *J. Mol. Liq.* **2022**, *359*,

205 De Clercq, K.; Persoons, E.; Napso, T.; Luyten, C.; Parac-Vogt, T. N.; Sferruzzi-Perri, A. N.; Kerckhofs, G.; Vriens, J. High-resolution contrast-enhanced microCT reveals the true three-dimensional morphology of the murine placenta. *Proc. Natl. Acad.* **2019**, *116* (28), 13927-13936.

206 Maes, A.; Pestiaux, C.; Marino, A.; Balcaen, T.; Leyssens, L.; Vangrunderbeeck, S.; Pyka, G.; De Borggraeve, W. M.; Bertrand, L.; Beauloye, C.*; et al.* Cryogenic contrast-enhanced microCT enables nondestructive 3D quantitative histopathology of soft biological tissues. *Nat. Commun.* **2022**, *13* (1), 6207-6207.

207 https://admin.kuleuven.be/sab/vgm/kuleuven/en/riskactivities/cs (accessed.11/05/2022).

208 https://www.groupware.kuleuven.be/sites/hsecorefacilities/ (accessed.11/05/2022).

209 Niu, S. *Radiation protection of workers*; **2011**.

210 Kato, C. N.; Shinohara, A.; Hayashi, K.; Nomiya, K. Syntheses and X-ray crystal structures of zirconium(IV) and hafnium(IV) complexes containing monovacant wells-Dawson and Keggin polyoxotungstates. *Inorg. Chem.* **2006**, *45* (20), 8108-8119.
211 Wharton, T.; Wilson, L. J. Highly-iodinated fullerene as a contrast agent for X-ray imaging. *Bioorg. Med. Chem.* **2002**, *10* (11), 3545-3554.
212 *contrast-team/histogram-windowing: Initial release*; Zenodo: 2022. https://doi.org/10.5281/zenodo.7034265 (accessed 01/2022).
213 *Relative normalization of microCT datasets for grey value comparison*; Zenodo: 2023. https://doi.org/10.5281/zenodo.7688929 (accessed 01/2022).
214 Samuel, R.; Girard, E.; Chagnon, G.; Dejean, S.; Favier, D.; Coudane, J.; Nottelet, B. Radiopaque poly(epsilon-caprolactone) as additive for X-ray imaging of temporary implantable medical devices. *RSC Advances* **2015**, *5* (102), 84125-84133.
215 Sunke, R.; Adepu, R.; Kapavarapu, R.; Chintala, S.; Meda, C. L. T.; Parsa, K. V. L.; Pal, M. Vinylic amino group activation: a new and general strategy leading to functionalized fused heteroaromatics. *Chem. Commun.* **2013**, *49* (34), 3570-3572.
216 Mahindroo, N.; Connelly, M. C.; Punchihewa, C.; Kimura, H.; Smeltzer, M. P.; Wu, S.; Fujii, N. Structure-Activity Relationships and Cancer-Cell Selective Toxicity of Novel Inhibitors of Glioma-Associated Oncogene Homologue 1 (Gli1) Mediated Transcription. *J. Med. Chem.* **2009**, *52* (14), 4277-4287.
217 Zhang, B.; Huang, X. C.; Wang, H. S.; Gou, S. H. Promoting antitumor efficacy by suppressing hypoxia via nano self-assembly of two irinotecan-based dual drug conjugates having a HIF-1 alpha inhibitor. *J. Mater. Chem. B* **2019**, *7* (35), 5352-5362.
218 Brigati, J. R.; Samoylova, T. I.; Jayanna, P. K.; Petrenko, V. A. Phage Display for Generating Peptide Reagents. *Curr. Protoc. Protein Sci.* **2008**, *51* (1), 18.19.11-18.19.27.
219 Stock, S. R. *MicroComputed Tomography: Methodology and Applications*; CRC Press, **2008**.
220 Sneha, K. R.; Sailaja, G. S. Intrinsically radiopaque biomaterial assortments: a short review on the physical principles, X-ray imageability, and state-of-the-art developments. *J. Mater. Chem. B* **2021**, *9* (41), 8569-8593.

221 Ametova, E.; Probst, G.; Dewulf, W. X-ray Computed Tomography Devices and Their Components. In *Industrial X-Ray Computed Tomography*, Carmignato, S., Dewulf, W., Leach, R. Eds.Springer International Publishing, **2018**; pp 69-98.
222 du Plessis, A.; Broeckhoven, C.; Guelpa, A.; le Roux, S. G. Laboratory x-ray micro-computed tomography: a user guideline for biological samples. *GigaScience* **2017**, *6* (6), 1-11.
223 Webb, S.; Sutcliffe, J.; Burkinshaw, L.; Horsman, A. Tomographic reconstruction from experimentally obtained cone-beam projections. *IEEE Trans. Med. Imaging* **1987**, *6* (1), 67-73.
224 Ramachandran, G. N.; Lakshminarayanan, A. V. Three-dimensional Reconstruction from Radiographs and Electron Micrographs: Application of Convolutions instead of Fourier Transforms. *Proc. Natl. Acad. Sci. U.S.A.* **1971**, *68* (9), 2236-2240.
225 Hermanek, P.; Rathore, J. S.; Aloisi, V.; Carmignato, S. Principles of X-ray Computed Tomography. In *Industrial X-Ray Computed Tomography*, Carmignato, S., Dewulf, W., Leach, R. Eds.Springer International Publishing, **2018**; pp 25-67.
226 Schäfers, K. P.; Bolwin, K.; Büther, F.; Hermann, S.; Jacobs, A. H.; Kösters, T.; Kuhlmann, M.; Schäfers, M.; Viel, T. 1.10 - High-Resolution Small Animal Imaging. In *Comprehensive Biomedical Physics*, Brahme, A. Ed.Elsevier, **2014**; pp 181-211.
227 https://www.nist.gov/pml/xcom-photon-cross-sections-database (accessed.25/11/2022).
228 Aichinger, H.; Dierker, J.; Joite-Barfuß, S.; Säbel, M. Interaction of Photons with Matter. In *Radiation Exposure and Image Quality in X-Ray Diagnostic Radiology: Physical Principles and Clinical Applications*.Springer Berlin Heidelberg, **2012**; pp 21-31.
229 Goos, P.; Meintrup, D. *Statistics with JMP: Hypothesis Tests, ANOVA and Regression*; Wiley, **2016**.

PUBLICATIONS & PRESENTATIONS

Peer-reviewed Journal Articles

0000-0001-6682-9936

Gilles, P.; Veryser, C.; Vangrunderbeeck, S.; Ceusters, S.; Van Meervelt, L.; De Borggraeve, W. M. Synthesis of N-Acyl Sulfamates from Fluorosulfates and Amides. *J. Org. Chem.* **2019**, *84* (2), 1070-1078. doi: 10.1021/acs.joc.8b02785

de Bournonville, S.; Vangrunderbeeck, S.; Kerckhofs, G. Contrast-Enhanced MicroCT for Virtual 3D Anatomical Pathology of Biological Tissues: A Literature Review. *Contrast Media Mol. Imaging* **2019**, *2019*, 1-9. doi: 10.1155/2019/8617406

de Bournonville, S.[†]; Vangrunderbeeck, S.[†]; Ly, H. G. T.; Geeroms, C.; De Borggraeve, W. M.; Parac-Vogt, T. N.[*]; Kerckhofs, G.[*] Exploring Polyoxometalates as Non-invasive Staining Agents for Contrast-Enhanced Microfocus Computed Tomography of Soft Biological Tissues. *Acta Biomater.* **2020**, *105*, 253-262. doi: 10.1016/j.actbio.2020.01.038 ([†] Authors contributed equally and join the first authorship, [*] Authors contributed equally and join the last authorship)

Vangrunderbeeck, S.; Balcaen, T.; Veryser, C.; Steurs, G.; De Borggraeve, W. M. Carbonylation Chemistry Applied to the Synthesis of Benzimidazo[2,1-b]quinazolin-12-ones. *Eur. J. Org. Chem.* **2022**, *2022* (2), e202101136. doi: 10.1002/ejoc.202101136

Maes, A.; Pestiaux, C.; Marino, A.; Balcaen, T.; Leyssens, L.; Vangrunderbeeck, S.; Pyka, G.; De Borggraeve, W. M.; Bertrand, L.; Beauloye, C.*; et al.* Cryogenic contrast-enhanced microCT enables nondestructive 3D quantitative histopathology of soft biological tissues. *Nat. Commun.* **2022**, *13* (1), 6207. doi: 10.1038/s41467-022-34048-4

Oral Presentations

International Symposium on SupraBiomolecular Systems (SUPRABIO) 2021, online.
Title: Polyoxometalates as Non-destructive Staining Agents for ex-vivo Contrast-Enhanced Microfocus Computed Tomography (CECT).

Chemistry Conference For Young Scientists (ChemCYS) 2020, Blankenberge, Belgium.
Title: Exploring Polyoxometalates as Non-invasive Staining Agents for Contrast-Enhanced Microfocus Computed Tomography of Biological Tissues.

Belgian Symposium on Tissue Engineering (BSTE) 2019, Hasselt, Belgium.
Title: Exploring Polyoxometalates as Non-invasive Staining Agents for Contrast-Enhanced Microfocus Computed Tomography of Soft Biological Tissues.

International Conference on Tomography of Materials & Structures (ICTMS) 2019, Cairns, Australia.
Title: Development of Novel Non-invasive Contrast Agents for Contrast-Enhanced MicroCT of Biological Tissues.

Poster Presentations

Merck Organic Chemistry Symposium (MOCS) 2018, Blankenberge, Belgium.
Title: Synthesis of N-Acyl Sulfamates from Fluorosulfates and Amides**.**

Merck Organic Chemistry Symposium (MOCS) 2017, Blankenberge, Belgium.
Title: Safe and Convenient CO Generation and its Applications in Organic Chemistry.

Awards

Award for Best Oral Presentation
BSTE - Belgian Symposium on Tissue Engineering 2019

Prize for 3th Best Oral Presentation - session Life Sciences
ChemCYS - Chemistry Conference for Young Scientists 2020

KU LEUVEN
FACULTY OF SCIENCE
DEPARTMENT OF CHEMISTRY
SUSTAINABLE CHEMISTRY FOR METALS AND MOLECULES
Celestijnenlaan 200F – box 2404
B-3001 HEVERLEE, BELGIUM
tel. +32 16 37 44 02
sarah.vangrunderbeeck@kuleuven.be
chem.kuleuven.be/moldesigns

UC LOUVAIN
ECOLE POLYTECHNIQUE DE LOUVAIN
INSTITUTE OF MECHANICS, MATERIALS AND CIVIL ENGINEERING
Mechatronic, Electrical Energy, and Dynamic Systems
Place du Levant 2 – box L5.04.02
B-1348 LOUVAIN-LA-NEUVE, BELGIUM
sarah.vangrunderbeeck@uclouvain.be
www.contrast-team.be

